INFLUENCE OF HYDRODYNAMICS ON CARBON STEEL EROSION-CORROSION AND INHIBITOR EFFICIENCY IN SIMULATED OILFIELD BRINES

by

Tendayi Zvandasara

THESIS SUBMITED IN FULFILLMENT OF THE REQUIREMENTS
FOR THE DEGREE OF DOCTOR IN PHILOSOPHY
TO THE FACULTY OF ENGINEERING
DEPARTMENT OF MECHANICAL ENGINEERING
UNIVERSITY OF GLASGOW

December 2009

ABSTRACT

Corrosion within the oil and gas sector is an ongoing concern for operators. The challenging nature of extraction and processing fluids is an unavoidable cause of severe metallic corrosion. With modern emphasis on health, safety and the environment, the case for managing corrosion has become an imperative agenda. Whilst new and more effective methods of mitigation are key, an interim solution is improving the value of current methods. A literature survey carried out within this project has revealed CO_2 corrosion as contributing to most corrosion related failures within the industry. The corrosion behaviour in CO_2 containing environments is complex partly due to the wide range of prevailing conditions such as temperature, CO_2 concentration and flow conditions.

For oil and gas transportation pipelines, internal corrosion mitigation can be achieved by the use of chemical inhibitors. Inhibitors have been established to be effective but are by no means a complete solution. Issues such as their effectiveness in high velocity and high shear flow are a main consideration for their function. The hydrodynamic nature of the flowing fluids can affect inhibitor efficiency by either slowing the rate of formation of the inhibitive layer or causing degradation of well-formed inhibitive layers. A combined effect may also be active.

The corrosion behaviour of carbon steel in simulated oilfield conditions is investigated in this project with emphasis on conditions of varying velocity, impinging flow and consequently shear stress. Since inhibition is the main mitigation technique for fluid related corrosion, the efficiency of a commercially used inhibitor is, in this case assessed in the abovementioned conditions. To simulate both impingement and flow, a jet impingement apparatus is used in conjunction with a segmented-electrode specimen set up to separately study the erosion-corrosion behaviour of different hydrodynamic zones under the jet. Corrosion rates are measured by gravimetric analysis and results are also evaluated with electrochemistry. Additionally, galvanic interactions between the different hydrodynamic zones have been investigated. Visual and light-optical microscopic examinations are also used to assess variable effects within the zones.

Under such conditions, the corrosion rates have been found to be significantly higher in impingement zones. Aerated conditions have shown a significant variation in corrosion behaviour between impingement and non-impingement zones. The results in CO_2 saturated brines are consistent but with evidence of different relations between hydrodynamics and the corrosion rate. The inhibitor has been shown to be effective in CO_2 saturated brines and significantly influenced by both inhibitor concentration and hydrodynamic conditions. Inhibitor efficiency has also shown a complex dependence on concentration and establishes a need to evaluate optimum inhibitor concentrations before field application. Evaluation of the mass loss results against electrochemistry has shown a large discrepancy between the two methods. This rather surprising result suggests solid-free flow is not entirely free of erosion and synergistic effects.

This comprehensive study has not only improved current knowledge on the relation between hydrodynamics and inhibitor efficiency but also indicates a critical need to evaluate suitability of current monitoring methods. Electrochemical methods are increasingly used as a method of choice and while they contribute significant monitoring data, they are observed to be unable, alone, to monitor erosion and synergy. An industry review on their suitability to monitor solid-free flow corrosion is recommended.

ACKNOWLEDGEMENTS

I am delighted to have an opportunity to thank the following named individuals. In particular, this thesis would have not been possible without the assistance of my parents, family, Maggie Black and the financial assistance of the Engineering Faculty. From the Faculty of Engineering my special thanks go to Mrs Patricia Duncan and Professor Frank Cotton. Finally, I would like to thank Dr Trevor Hodgkiess who above all has been an excellent supervisor and mentor.

Dr Graham Green
Miss Marilyn Dunlop
Mr Bernard Hoey
Mr Brian Robb
Mr Denis Kearns
Mr Gordon Hicks
Mr Kenny McLaren
Clariant Chemicals, Aberdeen

Table of Contents

LIST OF FIGURES

1.0 INTRODUCTION AND OUTLINE OF THESIS

1.1 Introduction

Within the petroleum industry, various production inhibitors are available for specific applications to help control corrosion. Inhibitors often function in an adsorption manner, forming a thin protective film on the material surface hence preventing any subsequent material deterioration due to interaction with its environment.

This thesis investigates the influence of hydrodynamics on the efficiency of a corrosion inhibitor in simulated oil field environments. The main themes presented are corrosion assessments by mass loss techniques, corrosion assessments by electrochemical techniques and galvanic activity between various hydrodynamic zones.

Chapter 2 presents the basic corrosion principles related to this project. Chapter 3 presents the literature review of the main issues examined in this thesis. The issues addressed focus on internal CO_2 corrosion of offshore oil and gas pipelines and its mitigation by use of chemical inhibition.

Chapter 4 presents the experimental techniques and methods of analysing and assessing corrosion behaviour.

Chapters 5 presents results of corrosion monitoring by mass loss (Gravimetric analysis) and Chapter 6 presents results in similar conditions but monitored by electrochemistry.

Chapter 7 presents results of the galvanic assessments and Chapter 8 is the discussion.

Chapter 9 is the conclusions and recommendations.

Finally, an appendix containing graphs is presented.

2.0 BASIC CORROSION PRINCIPLES

2.1 Introduction

Corrosion is the natural surface deterioration of a metals, by interaction with its environment.

2.2 Basic Thermodynamics of Corrosion

Metallic corrosion occurs because virtually all metals are unstable (high energy) and have a tendency to revert to their more stable (lower energy) states by combination with elements present in their environment. The possibility of this combination or reaction occurring can be linked thermodynamically to the free energy change for the reaction. The Gibbs free energy change, ΔG, can therefore be used as a measure of the possibility of corrosion occurring. Values of free energy change can be obtained from the relationship given in Equation 2-1.

$$\Delta G = -nF\Delta E \qquad \text{Equation 2-1}$$

n = no of electrons passed;

F = Faradays constant, 96500 coulombs/equivalent;

$\Delta E = E - E_0$;

E_0 is the equilibrium electrode potential.

Equation 2-1 indicates that the thermodynamic tendencies for corrosion can be discussed in terms of an electrochemical parameter, E, called the electrode potential.

2.3 Electrochemical Basics of Aqueous Corrosion

The basic electrochemical mechanism of aqueous corrosion involves the occurrence of an anodic reaction and simultaneous cathodic reaction. These two reactions are always coupled to form a complete electrode process. The full electrode process is completed by electron release and consequently metal dissolution (oxidation) and

electron reception (reduction). For any metal (M) the anodic reaction or oxidation process is given by Equation 2-2

$$M \rightarrow M^{n+} + ne^{-}$$ Equation 2-2

The ensuing cathodic reaction in acidic environments is usually the reduction of hydrogen ions given by Equation 2-3.

$$2H^{+} + 2e^{-} \rightarrow H_2$$ Equation 2-3

Or in aerated acidic environments the reaction is given by Equation 2-4.

$$4H^{+} + O_2 + 4e^{-} \rightarrow 2H_2O$$ Equation 2-4

Should the environment be neutral and aerated, then the reaction is usually that of oxygen reduction given by Equation 2-5.

$$O_2 + 4e^{-} + 2H_2O \rightarrow 4OH^{-}$$ Equation 2-5

The corrosion process on a metallic component therefore involves current flow between anodic and cathodic sites. This current is usually referred to as the corrosion current, I_{corr}, and is a measure of the corrosion rate of the steel component. The relationship between I_{corr} and the corrosion rate, expressed in engineering units (e.g. mm/year) is obtained from Faraday's law and is discussed later.

2.4 Forms of Aqueous corrosion

In general, aqueous corrosion can occur in two forms, general surface corrosion and localised corrosion. Several factors including environment and material property can govern forms of aqueous corrosion.

2.4.1 General Surface Corrosion

General surface corrosion is corrosion occurring uniformly over the entire exposed surface of a metal or structure. Oil and gas pipelines normally suffer severe levels of general corrosion due to the aggressive chemical and physical nature of the environment. In particular, hydrocarbon systems using carbon steels or low alloy steels often include corrosion enhancing features such as high temperatures, high pressure, CO_2-content, H_2S-content, oxygen content, acidity, electrolyte conductivity and biological activity.

It is of intent to focus this study on the corrosion mechanisms of some of the above conditions in relation to carbon steel corrosion and corrosion inhibition efficiency.

2.4.2 Localised Corrosion

Localised corrosion involves intense corrosion attack at localised parts of a material or equipment. This type of corrosion often causes higher corrosion rates within these localised sites and it is typical to have the rest of the material corroding at a lower rate. The main types of localised corrosion are galvanic corrosion, pitting, erosion, crevice corrosion and intergranular corrosion. Factors which could influence this type of attack are given below:

- Breakdown of corrosion protection;
- Inconsistent material surface properties;
- Local accumulation of corrosive species.

2.5 Erosion-Corrosion

Erosion-corrosion is a complex process involving corrosion and mechanical wear. The total mass loss in erosion-corrosion occurring in aqueous environments is often described by Equation 2-6.

$$T = E + C + S \qquad \textbf{Equation 2-6}$$

Where

T is the total mass loss

E is the mass loss attributed to pure erosion
C is the mass loss attributed to pure corrosion
S is the mass loss attributed to a complex interaction between erosion and corrosion. This loss is often termed "synergy"

Although it is often considered that mechanical mechanisms (contributing to "E") are only prevalent when solid particles are present in flowing aqueous environments, a number of studies (see later) have demonstrated that mechanical erosion/cavitation damage can also contribute to the total mass loss in solid-free flowing liquids. As Equation 2-6 indicates, the rate of corrosion in erosion-corrosion processes can be more significant than might be considered from simple electrochemical dissolution processes ("C") because there are instances where the contribution of "S" to the total material loss are substantial. Detailed erosion-corrosion mechanisms that are relevant to this project are considered in Chapter 3.

2.6 Corrosion Monitoring

Corrosion monitoring is the use of any method or methods which can deduce or predict the amount of corrosion actively occurring on any elements of a structure or entire equipment. Recording data and analysing historical corrosion trends is also a key part of corrosion monitoring and can be effectively used to manage corrosion.

Aqueous corrosion is the most common form of corrosion. As corrosion mainly involves electron transfer, most modern methods of corrosion monitoring are based on analysing the rate of electron transfer. Such methods employ direct and indirect techniques of measuring the rate of electron transfer.

2.6.1 Corrosion Monitoring Techniques

The main aim of corrosion monitoring is to directly or indirectly measure the corrosion current density. Current methods that use this form of assessment include Linear Polarisation Resistance (LPR), Tafel Approach (Full Polarisation), AC Impedance and Electrochemical Current Noise.

Other methods such as weight loss measurements are more direct and tend to yield additional information about the corrosion process and mechanisms.

2.6.1.1 Corrosion Coupons

Corrosion coupons are made from the same material grade as the equipment to ensure the measured corrosion rate is simulating that of the actual structure. These coupons are of known weight and area. The coupons are then exposed to the service conditions for a known period and removed. The coupons are then inspected, cleaned and stripped to their bare metal for reweighing. The total material loss can then be used to calculate the corrosion rate in mm/year. Corrosion coupons possess various advantages.

Corrosion coupons are inexpensive in comparison to other monitoring methods. The end result can also give a good indication of the life expectancy of the equipment. In addition, coupons can also be configured to simulate other metallurgical variations such as welding, surface microstructure and effect of heat treatment. Finally, coupons can also give physical evidence on the corrosion mechanism i.e. pitting and any presence of microbial organisms.

2.6.1.2 Electrochemical Noise Monitoring (ENM)

This method can be widely used to monitor most forms of corrosion. ENM involves measuring the noise resulting from fluctuations in current or potential. No perturbations are applied to the test system. The variation in noise during the test is proportional to the corrosion rate.

2.6.1.3 DC Polarisation (Linear Polarisation Technique)

The linear polarisation technique avoids any problems of possible specimen surface modification or even destruction by imposing small perturbations in potential of about 20 mV more negative or 20 mV more positive than $E_{corr,}$ (the potential of a freely corroding material). These small perturbations are achieved by supplying a small current using an external DC electrical source (potentiostat) and then analysing the potential/current density data using polarisation theory. For values of potential restricted to 20mv, a plot of potential/current density would yield a straight line of gradient R_p (Polarisation Resistance). For these small shifts of ΔE from $E_{corr,}$ i.e. 20mv, the value of R_p is given by Equation 2-7.

$$\mathbf{R_p = \Delta E/\Delta I} \qquad \text{Equation 2-7}$$

Corrosion theory shows that the corrosion current, i_{corr} is inversely proportional to the polarisation resistance as shown by Equation 2-8

$$I_{corr} = B\Delta I/\Delta E \qquad \text{Equation 2-8}$$

Where B= Stern-Geary constant $= b_a b_c / 2.3(b_a + b_c)$

Therefore, for the above moderate shifts in potential, the gradient of the polarisation/current density plot will yield a value of R_p. From Equations 2-7 and 2-8, we can therefore deduce that $1/R_p$ is proportional to i_{corr}. i_{corr} can then be used as a measure of corrosion rate.

2.6.1.4 Faraday Based Technique (Tafel Extrapolation of Polarisation Curves)

The Tafel extrapolation method evaluates the corrosion rate of a corroding specimen by extrapolating a polarisation curve to the relevant current density and E_{corr}. Polarisation curves are plotted as log (current density) as a function of potential and the linear parts of such plots are normally extrapolated back to E_{corr}. This region, from which the extrapolation can be carried out is called the Tafel region.

For a reasonable Tafel region to be established on a polarisation curve, the range of polarisation is typically in values in excess of 150 mV away from E_{corr}. As these polarisation perturbations tend to be excessive, they normally alter the surface condition of the specimen. Consequently, polarisation curves of this nature can only be carried out once per specimen and tend to be left till the end of the testing period. For a repeat test the specimen needs to be ground past the damaged surface or a new specimen of similar material and condition needs to be used as a replacement.

Once the corrosion current density of the specimen is established through Tafel extrapolation, the equivalent corrosion rate, say in g/s can be determined through Faraday's law given in Equation 2-9.

$$\frac{dm}{dt} = \frac{iAM}{nF} \qquad \text{Equation 2-9}$$

Where

$\frac{dm}{dt}$ = *equivalent loss in g/s*

i = Extrapolated corrosion current density
A = Area of specimen in cm^2
M = Molecular Mass of material, g/mole
n = Valency of metal ion reaction
F = Faraday's constant, 96500 coulombs/equivalent

From Equation 2-9, the weight loss in g/s can then be converted to a loss in g/year, assuming uniform loss. This loss in g/year can then be converted into mm/year through Equation 2-10.

$$\textbf{Loss (mm/year)} = (10)\frac{L}{\rho A} \qquad \text{Equation 2-10}$$

Where
L = Corrosion rate in g/year
ρ = density of material in g/cm^3
A = Area of specimen in cm^2

2.6.2 Benefits of Corrosion Monitoring

The presence of corrosion on any equipment can bring about undesirable problems in equipment reliability, equipment availability and operational safety. Some significant benefits of corrosion monitoring include:

- Improvements in operational reliability of equipment;
- Provision of information relating corrosion rates and service conditions;
- Helps predict any failures;
- Increases the service life of any equipment;
- Financial benefits related to equipment procurement and maintenance;

- Maximises operational safety;
- Maximises profitability;
- Provides data essential for any corrosion solutions.

Within the oil and gas industry, any supply disruptions can easily affect market prices and consumer confidence. Corrosion management and monitoring is therefore vital in preventing any environmental and financial impacts of corrosion related leakages.

2.7 Corrosion Mitigation

Corrosion cannot be entirely eliminated but can be managed effectively. Current corrosion management techniques are:

- Anodic Protection;
- Cathodic Protection;
- Coatings;
- Corrosion Inhibition;
- Design Considerations;
- Material selection.

2.7.1 Materials Selection

The nature of the offshore oil and gas industry is such that operational demands for materials selected require properties such as strength, toughness, weldability, and corrosion resistance. Materials selected for pipelines have to be able to contain corrosive fluids at high pressures. High strength materials capable of fabrication to large wall thicknesses are therefore preferred. The fundamental criteria considered when selecting materials for pipeline construction include but are not limited to the following:

- Availability;
- Corrosion Resistance;
- Cost;
- Mechanical Properties;
- Weldability and ease of fabrication.

Low alloy steels such as carbon steel are often used as they have low cost, good availability, good mechanical properties and ease of fabrication. One lacking property of such materials is their corrosion resistance. Low alloy steels therefore need to be deployed with additional corrosion preventative measures such as corrosion allowances, protective coatings, cathodic protection and use of chemical inhibitors for internal corrosion mitigation.

In some cases, extremely aggressive corrosion conditions such as high levels of gases like CO_2 and H_2S, presence of seawater and presence of corrosion causing microbial organisms such as SRB's (Sulphate Reducing Bacteria) can often mean the selection of low alloy steels supplemented by corrosion mitigation techniques such as coatings and inhibitors becomes ineffective. In such cases, high alloy steels commonly known as corrosion resistant alloys (CRA's) may be selected instead. Metallic CRA's commonly used in the offshore oil and gas industry include:

- Austenitic stainless steels such as 316L (UNS S31603);
- Duplex stainless steels containing typically 22 % Cr (UNS S31803);
- Duplex stainless steels containing typically 25 % Cr (UNS S32750 or UNS S32760);
- High nickel alloys;
- Martensitic stainless steels.

2.7.2 Corrosion Inhibition

Corrosion inhibitors are often injected with production fluids to help reduce internal corrosion by adsorbing themselves onto the metal surface and forming a protective barrier. The nature of inhibition is reliant on the formation of protective films: mechanisms such as high velocities and shear stresses at the wall can be responsible for low inhibitor efficiency. Such mechanisms can affect inhibitor efficiency by either preventing film formation or stripping already formed protective films.

Inhibitors contain molecules that act by attracting themselves to metal surfaces and the presence of these molecules in larger numbers often increases their efficiency. Inhibitor effectiveness is therefore affected by concentration, with different inhibitors often requiring optimum concentration for peak efficiency. The fundamental

contribution of any inhibitor is in essence blocking one or both electrode reactions involved in corrosion.

The effectiveness of inhibitors is often described by their efficiency which is defined in Equation 2-11.

$$IE(\%) = \frac{UninhibitedCR - inhibitedCR}{UninhibitedCR} X100 \qquad \textbf{Equation 2-11}$$

Where CR is the corrosion rate and IE is the inhibitor efficiency.

3.0 LITERATURE REVIEW

3.1 Introduction

This section reviews previous studies and work relating to the main issues examined within this thesis. This project mainly focuses on current issues involving corrosion of offshore oil and gas pipelines and focuses on CO_2 corrosion and its mitigation by use of corrosion inhibitors.

Corrosion inhibitors are widely used in the oil and gas industry to tackle internal CO_2 corrosion of pipelines. One issue with corrosion inhibitors is their film efficiency in conditions of high velocity and shear stresses. Inhibitor efficiency may be affected through lack of film formation due to high shear forces or destruction of pre-formed protective films by such forces and velocities.

Shear stresses and velocities are therefore common in the evaluation of inhibitor efficiency in flowing conditions. Experimental techniques commonly used to simulate such involve mass transport. Methods of introducing variable mass transport effects include the rotating cylinder or disk, jet impingement and flow loops. Conditions involving flowing corrosive solutions have repeatedly been reported to cause mechanical damage especially in situations where the flow contains solid particles. As discussed earlier in Chapter 2, solid-free corrosive flow may also involve mechanical damage through interactive processes between corrosion and erosion ("synergy"). This being the case, non-Faraday material loss may be expected in such conditions.

A bibliographic assessment of currently recognised concepts involving mass transport, CO_2 corrosion, erosion-corrosion and inhibition is presented within this chapter. The literature discussion focuses on areas considered central to the approach taken within this thesis and forms a basis to investigate the "effect of hydrodynamics and erosion-corrosion on the efficiency of corrosion inhibitors in simulated oilfield CO_2 environments".

3.2 Mass Transport Systems

The oil and gas industry has very few methods of handling and transporting produced fluids. The most common and economically viable method is use of metallic

pipelines. Produced fluids are however very corrosive and for carbon steel pipelines, corrosion control and corrosion monitoring are essential activities to ensure integrity and optimisation. An essential part of managing corrosion is acquisition of quantitative information on corrosion mechanisms. Parameters useful in managing and reducing corrosion include temperature, pressure, pH, concentration of CO_2 and H_2S, ionic content and flow hydrodynamics. The effects of most of these parameters are evaluated in laboratories and the results have to be correlated to actual field conditions. Since the purpose of pipelines is mass transportation, the most important parameter that is commonly simulated in most laboratory systems is flow. Various laboratory systems are currently used to simulate mass transportation and have reasonably reported correlation to actual field systems. This section assesses the characteristics of current mass transfer systems and looks at some of the parameters used to best correlate laboratory results to actual field conditions.

3.2.1 Laboratory Experimental Systems

For most cases of corrosion, relative motion between the corroding metal and its environment can enhance or inhibit corrosion processes occurring in static conditions and may also introduce various types of attack such as erosion-corrosion (Poulson, 1993). Heitz, (1996) identified four main mechanisms to the combined action of corrosion and flow as:

- Cavitation;
- Erosion-corrosion (combined action of flow mechanical forces and chemical/electrochemical forces);
- Mass transport controlled corrosion;
- Phase transport controlled corrosion.

Cavitation damage is reported as occurring when variations in pressure resulting from velocity changes or sudden changes in flow geometry in areas such as pipe bends and tees causes formation of bubbles in regions of the liquid where the pressure is lower. Postlethwaite, et al. (1994). Cavitation damage is also reported to cause deep, sharp-edged craters on the metal surface Heitz, (1996) whilst others Heeg, et al. (1998) have suggested cavitation causes increases in mass transfer and shear stress.

Mass transport controlled corrosion is corrosion controlled by the supply of reactive species to the metal of the surface. Poulson, (1990) reported correlation of mass transfer with surface roughness of metals. Mass transportation can also play an important role when inhibiting a system. For example, the rate of delivery of inhibitor molecules may be controlled by mass transportation effects and can result in inadequate delivery of inhibitor molecules due to mass transport related limitations. Such limitations would result in weaker inhibitor films and consequently affect efficiency. Laboratory testing systems simulating effects such as flow influenced corrosion therefore need to be carefully considered in order to ensure that results realistically simulate actual field flow mechanisms.

A publication by NACE T-5A-31 (1995) identifies two key issues to consider when one has to select an appropriate laboratory system for assessing flow enhanced corrosion. These issues are:

a. Identification of a suitable manner of correlating bench-top results to full scale systems – current methods include mass transfer coefficients and hydrodynamic shear stress at the wall;
b. Identification of experimental systems for which these quantities are well defined.

For all laboratory flow systems, hydrodynamic parameters play an important role in facilitating correlation of laboratory results to actual field conditions. Such parameters and their effects are considered below:

Wall shear stress

Wall shear stress is defined as the isothermal pressure loss in impingementfluid flow with incremental length due to fluid friction resulting from contact with a stationery wall Efird, et al. (1993). For pipe flow, the shear stress is defined by Equation 3-1

$$\tau_w = \left(\frac{\Delta P}{\Delta L}\right)\left(\frac{d}{4}\right) \qquad \text{Equation 3-1}$$

Velocity – Higher velocities may result in erosion damage and may also play an important role in the rate of delivery of reactive species. Higher velocities can also

influence protective film persistency by inducing high shear stresses. Commonly, localised CO_2 corrosion has been linked to partial breakdown of protective corrosion product films such as iron carbonate due to fluid flow for example by Han, et al. (2007). The authors continue that these localised film breakdowns can cause severe galvanic corrosion due to presence of small anodic sites (film breakdown site) and large cathodes (remainder of surface with protective film). Such galvanic activity is discussed later.

Mass Transfer Coefficients – Often expressed as the non dimensional Sherwood number (Sh=kd/D), where k is the mass transfer coefficient (ms^{-1}), d is the length (m) and D is the mass diffusivity (m^2s^{-1}). Mass transfer as discussed earlier can have a significant influence on corrosion rates and may depend on solution chemistry and flow conditions Wang, et al. (1998).

Systems that currently simulate the above hydrodynamic parameters and are used for assessing flow induced corrosion are detailed as follows:

Flow Loop Systems;
Jet Impingement;
Rotating cylinder;
Rotating Disk.

Whilst there are attributes and disadvantages with all these approaches, the method adopted in this present work has been jet impingement technique. This has been a commonly used method of studying erosion-corrosion in laboratories and has been used significantly by researchers such as Neville, et al., (1999), Andrews, et al., (1999), Neville, et al., (2000) Neville, et al., (2001), Hu, et al., (2002), Hu, et al., (2003), Neville, et al., (2004), Wang, et al., (2004), Hussain, et al., (2005), Schmitt, et al., (2005), Hussain, et al., (2007), Neville, et al., (2007), Tang, et al., (2008).

Characteristics of this method including definitions of shear stress for a submerged impinging jet are presented below.

3.2.1.1 Jet Impingement Characteristics

The jet impingement system normally comprises of a submerged jet impinging at 90° to a flat specimen. Corrosion rates obtained using the jet impingement method have

been shown to have good correlation to pipe flow Efird, et al. (1993) and operating systems Efird, (2000) based on wall shear stress. Efird, et al. (1993) obtained a general equation for correlating jet impingement corrosion of carbon steel to pipe flow as shown in Equation 3-2.

$$R_{corr} = a\tau_w^{\ b} \qquad \textbf{Equation 3-2}$$

Where R_{corr} is the carbon steel corrosion rate (mm/yr);
a is the coefficient for the test method, in this case 6.8 for jet impingement and 7.7 for pipe flow;
b is 0.10 ± 0.02 for jet impingement and pipe flow.

The nature of the flow in a submerged impinging jet (Figure 3-1) depends on the flow Reynolds number. For an impinging jet, the Reynolds number, Re is given by Equation 3-3 Menendez, et al. (2005), Demoz, et al. (2004), Yapici, et al. (1999) whilst the shear stress value peaks at a position of r/d=1 Yapici, et al. (1999). The critical Reynolds number for transition from laminar to impingement flow for an impinging jet is 2000 Efird, et al. (1993)

$$\textbf{Re} = \textbf{dv}/\boldsymbol{\gamma} \qquad \textbf{Equation 3-3}$$

Where

d = nozzle diameter (m)

v = solution velocity (m/s)

γ = Kinematic viscosity of fluid (m^2/s)

From Figure 3-1, the nozzle geometry of an impinging jet has been described as having significant influence on the flow hydrodynamics especially at small stand-off distances, H, Jambunathan, et al. (1992). This variation in velocity also produces a variation in shear stress as shown in the following section.

Figure 3-1

Hydrodynamic characteristics of jet impingement on a flat plate showing four characteristic regions taken from (Efird, 2000)

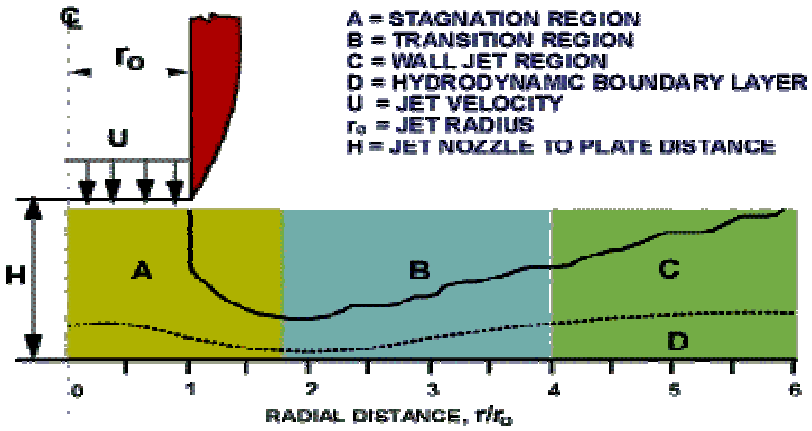

3.2.1.1.1 Governing Equations for Submerged Jet Impingement

The original equation for the wall shear stress variation with radial distance (Equation 3-4) was proposed by Giralt, et al., (1976). Efird, (2000) recalculated this equation to include the jet radius (Equation 3-5) instead of the jet diameter as the normalising factor.

$$\tau_w = 0.047\rho U^2 \,\mathrm{Re}^{-0.182}\left(\frac{r}{d}\right)^{-2} \qquad \textbf{Equation 3-4}$$

$$\tau_w = 0.179\rho V^2 \,\mathrm{Re}^{-0.182}\left(\frac{r}{r_o}\right)^{-2.0} \qquad \textbf{Equation 3-5}$$

Where

$$\mathrm{Re} = \frac{2r_o v}{\gamma}$$

Efird, (2000) again defined the friction on a smooth surface in the wall jet region

$$f = \frac{2\tau_w}{\rho U_m^{\ 2}} = 0.0315\left[\frac{U_m \delta_m}{\upsilon}\right]^{-0.182}$$ **Equation 3-6**

Where

The velocity at the edge of the boundary layer U_m is given by

$$U_m = 0.048\frac{r_o V_o}{\delta_m}$$

and the boundary layer thickness δ_m is given by: $\delta_m = 0.02r$

The above friction parameter is shown to be related to the shear stress.

For the jet impingement method, a jet to specimen stand off distance, H of 2 mm - 7 mm must be applied in order for the flow equations to apply and give good reproducibility Efird, (2000). One main advantage of the method which has been identified by the author is the wide range of wall shear stress and a continuously variable wall shear stress. For this project, the jet to specimen stand off distance has been set as 5 mm.

3.2.2 Shear Induced Removal of Films

Iron carbonate protective films have been shown to break down or be partially removed due to hydrodynamic shearing forces Han, et al., (2007). Wen, et al. (2007) also reported a failure of SRB biofilms to adhere onto metal surfaces in low fluid flow. This was due to preventative shear effects on the metal surface at velocities equivalent to 3 m/s.

3.3 CO_2 Corrosion

3.3.1 Introduction

Carbon dioxide corrosion of carbon steel results from the practice of pumping CO_2 saturated water into wells to enhance oil recovery and reduce the viscosity of the pumped fluid Heuer and Stubbins (1999), Hesjevick and Olsen (2003), Seal, et al.

(2000). Carbon dioxide dissolves in the presence of a water phase, forming carbonic acid, which is corrosive to carbon steel Lopez, et al. (2003). CO_2 corrosion in hydrocarbon production and transportation pipelines is difficult to understand, predict and control Villarreal, et al. (2006)

The enhanced corrosion rate of pipeline steels under conditions where CO_2 is present has been a problem in the oil and gas industry for years Linter and Burstein (1999). CO_2 corrosion has caused wide spread failures to equipment and remains one of the most common corrosive environments for the oil and gas industry Hesjevick and Olsen (2003), Fang, et al.(2006). CO_2 corrosion leads to failure of pipelines and equipment and results in great economic loss and calamitous accidents Zhang, et al. (2006).

Moiseeva, (2005) reports oilfield conditions favouring CO_2 corrosion as a pH of 2-8 and temperatures ranging from 15-200^{o}C. The author also reports carbon dioxide corrosion as temperature dependent and when temperatures are below 20^{o}C, corrosion rates become independent of flow rates.

3.3.2 Mechanisms of CO_2 Corrosion

When CO_2 dissolves in water at a high temperature and high pressure, carbonic acid is formed (Sun and Nesic (2008), Lopez, et al. (2003)). Carbonic acid has been suggested by Zhang, et al. (2006) as being more corrosive to carbon steel than a strong acid (such as HCl) at the same pH value.

Nordsveen, et al. (2003) observe the presence of CO_2 as increasing carbon steel corrosion by increasing the rate of the hydrogen evolution reaction (Equation 3-7). In CO_2 solutions with pH values greater than 4, the presence of H_2CO_3 enables hydrogen evolution at faster rates thus, leading to higher corrosion rates than would be found in a solution of a strong acid at the same pH. Another publication Nesic, et al. (2003) recognises and confirms formation of protective iron carbonate films which account for reductions in corrosion rate. Situations favourable to formation of this film are high bulk pH, high temperature, high partial pressure of CO_2, high Fe^{2+} concentration and low velocities.

Effects of pH on corrosion in CO_2 containing environments have also been reported with corrosion rates decreasing with increasing pH Hesjevick, et al., (2003) whilst others Fajardo, et al., (2008) found no effects on corrosion due to increased pH.

Song, et al. (2004) suggests the corrosion mechanisms for carbon dioxide corrosion are not well understood because the corrosion process is complex. In a solution boundary layer on the steel surface, the corrosion process involves CO_2 dissolution, hydration and diffusion, carbonic acid (H_2CO_3) dissociation, ionic interactions between carbonic and iron species, ferrous carbonate ($FeCO_3$) precipitation and electrochemical (anodic and cathodic) reactions.

The anodic and cathodic reactions of CO_2 corrosion of carbon steel are summarised by Equations 3-7 to 3-11. Zhang, et al., (2006) suggest that at low pH, H^+ reduction (Equation 3-7) is the dominant cathodic process because of the high concentration of H^+. When pH increases to between 4 and 6, the direct reductions of HCO_3^- and H_2CO_3 become important (Equations 3-8 and 3-9). Nesic, et al., (1996) also confirm H_2CO_3 reduction as the dominant cathodic reaction at a pH of 5. At high overpotential, Zhang, et al., (2006) suggest the dominant cathodic reaction changes to direct water reduction (Equation 3-10). The anodic reaction is mainly the dissolution of iron (Equation 3-11).

$$2H^+ + 2e^- \rightarrow H_2$$ **Equation 3-7**

$$2H_2CO_3 + 2e^- \rightarrow 2HCO_3^- + H_2$$ **Equation 3-8**

$$2HCO_3^- + 2e^- \rightarrow 2CO_3^{2-} + H_2$$ **Equation 3-9**

$$2H_2O + 2e^- \rightarrow 2OH^- + H_2$$ **Equation 3-10**

$$Fe \rightarrow Fe^{2+} + 2e^-$$ **Equation 3-11**

Han, et al., (2007) reported that during these processes of CO_2 corrosion, a protective corrosion scale ($FeCO_3$) is formed on the surface of the steel with the potential, E_{corr}, of the film covered surface increasing (less negative) and leaving the surface acting as a cathode in relation to a bare surface. Dugstad, (1998) reported the corrosion rates of carbon steel in CO_2 environments as depending on the formation of protective $FeCO_3$ films. The presence of mill scale or rust from tube manufacturing was suggested to also increase the protectiveness of films. Experiments were carried out at temperatures of 40, 60, 80 and 120°C. Film formation was best achieved at 80°C. Figures 3-2 and 3-3 taken from Dugstad, (1998) show the temperature-dependent contrast in film structure at 60 and 80°C.

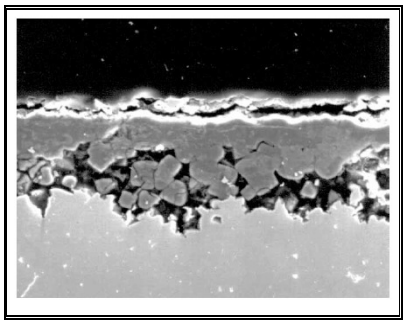

Figure 3-2, Iron Carbonate embedded in carbide film, 60°C, 10-100 times supersaturation. (Dugstad, 1998)

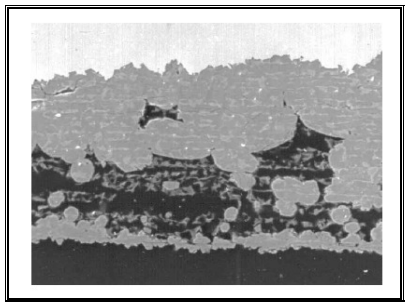

Figure 3-3, Iron Carbonate embedded in carbide film, 80°C, 10-100 times supersaturation. (Dugstad, 1998)

In a later publication, Han, et al., (2008), spontaneous passivation of mild steel in CO_2 solutions is reported. The passivation was temperature dependent with the time taken to reach self-passivation taking longer at lower temperatures due to slower process kinetics. This passivation effect was also found to be affected by pH and

CO_2 concentration. Nesic, et al., (1995) indicated formed films in CO_2 corrosion as reducing corrosion rates by acting as a barrier to mass transportation. This observation was at temperatures of 50°C and 80°C whilst Guo, et al., (1999) additionally reported protective film formation at a higher temperature of 100°C.

Dugstad, et al., (2001) reported a correlation between steel microstructure and formation of protective carbonate films. Steels with higher amounts of chromium and in the quenched and tempered condition showed better abilities to form protective films.

Mora-Mendoza, et al., (2002) reported formation of Fe_3C at pH 5.5. The iron carbide had no protective characteristics with corrosion rates increasing with time. Iron carbide formation in CO_2 environments has also been acknowledged by Chokshi, et al., (2005).

Dayalan, et al., (1998) modelled a critical flow velocity of about 15 m/s to which carbonate films would fail to form in solid-free flow. At such velocities, modelled corrosion rates increased to over 25 mm/year from corrosion rates of less than 5 mm/year at velocities of 10 m/s or below.

3.3.3 De Waard CO_2 Corrosion Prediction

The most significant method of predicting CO_2 corrosion is the de Waard and Milliams approach (Nesic, et al., (2005)). Originally presented in 1975 and utilising the combined effect of CO_2 partial pressure and temperature Olsen, (2005), the method has been revised with the most significant revision being in 1993 de Waard, (1993). The revised 1993 version is commonly used as a basis of CO_2 prediction models Marsh, et al., (2007) Hedges, (2005). The most significant CO_2 corrosion models developed from this empirical approach include models such as CASSANDRA (BP) and Hydrocor (SHELL) Marsh, et al., (2007). The 1993 de Waard revision is given by Equation 3-12.

$$\log(V_{cor}) = 5.8 - \frac{1710}{273 + t} + 0.67 \log(pCO_2) \qquad \textbf{Equation 3-12}$$

Where

V_{cor} is the corrosion rate in mm/yr

t is the temperature (K)

pCO_2 is the partial pressure of CO_2, given by $pCO_2 = \frac{\%CO_2}{100} \times P$

Where P is the system total pressure.

The NORSOK M-506 (M-506, 2005) model is based on experimental research and testing.

3.3.4 Supersaturation

For a given chemical process (e.g. formation of iron carbonate), supersaturation is defined as the species concentration in excess of the solubility limit Poulson, (1993) Sun, et al., (2006) Sun, et al., (2008) or the degree of departure from thermodynamic equilibrium Han, et al., (2007). As the degree of supersaturation increases, iron carbonate films form more easily Dugstad, (1998), Nafday, et al., (2005), Sun, et al., (2008), Fajardo, et al., (2008).

Iron carbonate films slow down the corrosion process by formation of a diffusion barrier for species involved in corrosion Wang, et al., (2003), Sun, et al., (2006), Fajardo, et al., (2008). Iron carbonate scale growth then depends on precipitation Sun, et al., (2006).

The equation for supersaturation as defined by van Hunnik, et al., (1996), Pots, et al., (2000) and Chokshi, et al., (2005), is given by Equation 3-13.

$$SS = \frac{C_{Fe^{2+}} C_{CO_3^{2-}}}{K_{sp}}$$ **Equation 3-13**

Where

SS is the supersaturation

K_{sp} is the solubility limit

$C_{Fe^{2+}}$ is the concentration of ferrous ions

$C_{CO_3^{2-}}$ is the carbonate ion concentration

Provided the supersaturation remains high, films will remain protective once formed Dugstad, (1998)

The species involved in iron carbonate formation and defined in iron carbonate supersaturation (Equation 3-13) are ferrous Fe^{2+} and carbonate CO_3^{2-} ions. The source of ferrous ions for iron carbonate formation has been identified as both that released from the steel surface and those supplied through the bulk solution Sun, et al., (2008). Concentrations of dissolved iron Fe^{2+} typically have to be in the order of >1 ppm in order to make iron carbonate film formation likely Nordsveen, et al., (2003). Ramachandran, et al., (2000) identify the lack of iron Fe^{2+} concentration below saturation conditions as responsible for lack of corrosion product films.

Chokshi, et al., (2005) evaluated the effect of supersaturation on corrosion rates in stagnant CO_2 environments without inhibitor. Tests were carried out at 80°C. Higher degrees of supersaturation produced lower corrosion rates with their effect in reducing corrosion rates being more prompt. A supersaturation level of 150 produced the lowest final corrosion rate of 0.1 mm/year after 19 hours exposure as demonstrated in Table 3-1.

Table 3-1

Corrosion Rates with degree of Supersaturation, compiled from Chokshi, et al., (2005)

Supersaturation	Experimental Time (hrs)	Final Corrosion Rate (mm/year)
7	45	0.650
9	19	1.800
30	85	0.027
37	87	0.130
150	19	0.100

Tests at 80°c and in stagnant conditions

The authors also established a link between the concentration of iron (Fe^{2+}) and the degree of supersaturation achieved. Higher degrees of supersaturation were also observed at higher pH values as shown in Table 3-2.

Table 3-2

Effect of Bulk Fe^{2+} Concentration on Degree of Supersaturation Achieved, compiled from Chokshi, et al., (2005)

pH	Fe^{2+} Concentration (ppm)	Supersaturation
6.30	10	7
6.30	50	37
6.60	10	30
6.60	50	150

3.3.5 Scaling Tendency

The scaling tendency (ST) as defined by Sun, et al., (2006) is shown in Equation 3-14.

$$ST = \frac{PR}{CR}$$ **Equation 3-14**

Where PR is the precipitation rate and CR is the corrosion rate.

From the above equation, the scaling tendency (ST) increases with increasing precipitation rate (PR) and decreases with increasing corrosion rate (CR). Nesic, et al., (2002) observed film conditions linked to scaling tendency as shown in Table 3-3.

Table 3-3

Scaling Tendency likelihood compiled from Nesic, et al., (2002)

Scaling Tendency	Observation (Condition)
ST<<1	Porous and unprotective carbonate films likely to form
ST>>1	Dense protective carbonate films likely to form

The observation of porous and unprotective carbonate films at scaling tendencies of less than 1 was also confirmed by Nesic, et al., (2003) with the explanation that at scaling tendencies of less than 1, the precipitation rate is less than the corrosion rate. Therefore, the rapidly corroding metal creates voids faster than precipitation can fill them leading to porous unprotective films. van Hunnik, et al., (1996) identified a minimum temperature of 80°C required to enable repair of damaged or porous films. At lower temperatures, scale repair would only be possible if the value of pH exceeds 6. The researchers also recognise the need to have the scaling tendency exceed a critical value before $FeCO_3$ films start to form. The critical value of scaling tendency was shown to decrease with increasing carbon content of the metal.

3.3.6 Precipitation Rate

The precipitation rate of iron carbonate has been identified as the controlling factor to protective film formation (Dugstad, 1998) .The precipitation rate as defined by van Hunnik, et al., (1996) is given in Equation 3-15.

$$PR = k_r \frac{A}{V} k_{sp} (SS - 1)(1 - SS^{-1}) \qquad \textbf{Equation 3-15}$$

Where

PR is precipitation rate

SS is Iron carbonate supersaturation

k_{sp} is solubility product of $FeCO_3$

k_r is Kinetic constant which obeys Arrhenius law

Arrhenius Law: $K_r = e^{A - \frac{B}{RT}}$ *taken from (van Hunnik, et al., 1996)*

Where R is the gas constant (J/K.mol)

T is the temperature (K)

A and B are constants

Iron carbonate precipitation is described as a function of iron carbonate supersaturation, the solubility limit, temperature (via the constant Kr which obeys Arrhenius law) and the electrode surface area to solution volume ratio is (A/V) Sun, et al., (2004) Sun, et al., (2006). The above equation for precipitation rate, PR has been shown to have a correlation to testing done by the authors in 2004 (Sun, et al.,

2004) although the authors identify an over prediction of precipitation by the equation, particularly at high surface area-to-solution volume.

Chokshi, et al., (2005) demonstrated an increase in precipitation rate with supersaturation during experiments. Calculated precipitation rates using the van Hunnik (van Hunnik, et al., 1996) equation were however significantly higher than experimental levels of precipitation.

A method of measuring precipitation rates in CO_2 corrosion, suggested by Sun and Nesic (Sun, et al., 2006) would be use of the mass loss technique. This would involve determining the mass of carbonate films by weighing the sample prior to using a product removal technique such as Clarke's solution. Reweighing the sample afterwards would help estimate the amount of carbonate film formation on the sample surface.

3.3.7 Chemical Reaction Classification in CO_2 Corrosion

It is well known that homogenous chemical reactions are those occurring everywhere in the solution and heterogeneous chemical reactions are those occurring only at the metal surface Nesic, et al., Aberdeen (2004) Nesic, et al., (2004)

Table 3-4

Classification of Chemical Reactions in CO_2 Corrosion compiled from (Nesic, et al., Aberdeen 2004), (Nesic, et al., 2004)

Homogenous	Heterogeneous
Hydration	Precipitation
Dissociation	

3.3.8 Galvanic Effects in CO_2 Corrosion

Given that CO_2 environments cause formation of protective carbonate films, localised corrosion in environments dominated by CO_2 can be caused by local defects in the protective film surface Han, et al., (2007) Han, et al., (2008).

These localised corrosion effects may also form where a differential effectiveness of product films may occur on any material surface. In particular, regions or zones on any material surface where local parameters such as hydrodynamics, temperature, surface finish, shear stresses and species concentration may play an important role in variable film formation. The galvanic couple in such a setup is likely to be as follows:

- Anode – zone where the carbonate protective film is less effective;
- Cathode – zone where the protective film is more effective.

The open circuit potential difference between the bare steel anode and film covered cathode is identified as the driving force for propagation of localised CO_2 corrosion Han, et al., (2007). Experiments by the authors have also noted that the coupled potential of the two zones is determined by the larger surface area cathode. The authors also identify two main steps involved in localised corrosion process as initiation and propagation.

Shadley, et al., (1998) particularly identified environments in which protective corrosion product films are able to form as containing high potential for pitting and mesa-type corrosion (a local corrosion attack).

3.3.8.1 Drivers for Galvanic Effects in CO_2 corrosion

Han, et al., (2008) recognise a difference in E_{corr}, or open circuit potential may act as a driving force for local galvanic corrosion. This difference in surface potential may be caused by damage in film layers and variable film formation. The surface acting as the anode is usually of a much smaller surface area compared to the cathode. In a previous publication (Han, et al., 2007) the researchers identify the region lacking in protective films as corroding at much higher rates or in orders of magnitude larger than film covered areas. This form of localised CO_2 corrosion was observed as to only propagate at a range of 0.5 - 2 iron carbonate supersaturation

The following sequence to galvanic corrosion has been summarised by the above authors Han, et al., (2008):

1. Steel is exposed to a corrosive environment;
2. When the solubility limit is exceeded, a ferrous carbonate film can form;
3. Local pH (beneath the carbonate film) increases;

4. As a consequence, a ferrous hydroxide film may form increasing potential;
5. Ferrous carbonate film is mechanically or chemically damaged resulting in localised corrosion;
6. Ferrous hydroxide layer is exposed to bulk solution where pH is lower;
7. Due to exposure to lower pH, $Fe(OH)_2$ film dissolves and locally depassivates steel surface;
8. Potential difference is established between surrounding passive surfaces with protective carbonate films and the exposed bare area;
9. Bare steel patch corrodes at much higher rate due to galvanic effect.
10. Corrosion and passive film dissolution occurs in lateral direction and causes pit growth.

3.4 Erosion-Corrosion

3.4.1 Synergy

The overall material loss in erosion-corrosion (the combined interactive effect of erosion and corrosion) Wang, et al., (2004) Neville, et al., (2003) results in material losses larger than the sum of their individual components. This combined effect is termed synergy Neville, et al., (2001). Guidelines for numerically assessing this increased material loss are given in (G119-09, ASTM). In this standard, synergy is defined as: The change in material wastage resulting from interaction between wear and corrosion. Numerically, (G119-09, ASTM) this is defined by Equation 3-21.

$$T = W_0 + C_0 + S \qquad \textbf{Equation 3-16}$$

Where

T=Total mass loss due to all effects

Wo = material loss under pure erosion conditions (in absence of corrosion) - usually ascertained by applying cathodic protection to samples in situ;

Co= corrosion rate in the absence of erosion;

S= Synergy (increase in material loss due to corrosion and erosion interactions).

Erosion-corrosion has also been identified as a tribo-corrosion mechanism Neville, et al., (2003), Wood, (2006) and has been identified as causing numerous failures in the oil and gas industry Guo, et al., (2006) with failures amounting to up to 15 % Feyerl, et al., (2008). Wang, et al., (2004) reported consequences of such failures as resulting in economic loss, increased downtime and maintenance costs.

With most piping systems operating in impingementflow, in addition to localized corrosion, erosion-corrosion can also occur, often attributed to multiphase flow Neville, et al., (2009).

Hu, et al., (2008) recognised erosion-corrosion in solid free flowing media as a little understood or recognised mechanism of material loss. The nature of erosion-corrosion is such that there are mechanical, electrochemical and interactive processes contributing to the overall material loss The material loss can therefore be caused by several mechanisms including electrochemical dissolution (pure corrosion), mechanical erosion caused by fluid flow and/or impingement of particles or fluid. While erosion is mechanical and corrosion electrochemical, these two processes acting together termed “synergy” can contribute significantly higher material losses than sum of the individual processes acting separately. The authors identify this synergistic effect as erosion enhancing corrosion or corrosion enhancing erosion.

It is therefore reasonable to classify any flowing system under either individual corrosion or erosion mechanisms as having a likely possibility of synergy. Systems undergoing corrosion in the absence of solids can therefore have synergy and individual components of erosion.

The equation representing the total weight loss due to components of pure corrosion, pure erosion and synergy is given by Equation 3-17 taken from (Hodgkiess, et al., 2005).

$$TWL = C + E + S \qquad \textbf{Equation 3-17}$$

Where TWL is the total material loss

C is the material loss due to pure corrosion

E is the material loss due to pure Erosion

S is the synergy the erosion increase due to corrosion

A more detailed definition of the above equation would be as follows:

$$T = E + C + E_C + C_E$$

Where E is the pure erosion component, C is the corrosion rate in the absence of erosion-corrosion such as in static conditions, E_C is the extra erosion enhanced by corrosion processes and C_E is the extra corrosion enhanced by erosion effects. The combined components (E_C+C_E) is S in equation 3-17.

3.4.2 Erosion-corrosion in solid-free flow

Significantly, Guo, et al., (2006) identified non-Faraday related material loss in solid-free flow. The non-Faraday component was not related to mechanical damage since this component was absent under cathodic protection and hence zero corrosion. The non-Faraday loss is therefore related to corrosion and is indicative of synergistic effects where corrosion (electrochemical loss) enhances mechanical damage. Critically, a disparity between electrochemical and mass loss monitoring techniques was established with mass loss techniques always containing higher material loss rates than Faraday or electrochemical techniques. The amount of non-Faraday material loss was also found to decrease with increasing material hardness.

Neville, et al., (1999) assessed values of erosion, corrosion and synergy in both solid- free and solid loaded flow. Tests were carried out on cast iron and the results are given in Table 3-5.

Table 3-5

Components of weight loss during flow in 3.5% NaCl at 17 m/s Neville, et al., (1999)

Mechanism	Erosion % (E)	Corrosion % (C)	Synergy % (S)
Solid Free	16.4	24.1	59.5
Liquid - Solid 18°C	55.2	9.4	35.4
Liquid - Solid 50°C	37.9	6.7	55.4

As shown above, the amount of synergy plays an important role in the total amount of material loss, even in situations with solid-free flow. Through other publications Hu, et al., (2003), material loss due to mechanical effects is also recognised in solid-free flow.

Andrews, et al., (1999) found no significant erosion-corrosion damage on 13 Cr steel samples under impinging 30 g/L NaCl flow at 150 m/s, CO_2 and 100°C. Similar tests on carbon steel demonstrated severe erosion-corrosion with weight loss determined corrosion rates of over 35 mm/year.

3.4.3 Synergy Effects

Despite the lack of a wide understanding of erosion and synergy in solid free flow, studies sometimes focusing on erosion involving solid particles have recognised or presented results where erosion and synergy are observed in zero particle loading. Such observations have been noted in publications as early as 1995, Neville, et al., (1995).

Hu, et al., (2008) carried out an extensive attempt to predict erosion-corrosion and show synergy as having a significant effect on the overall material loss. An impinging jet mechanism was used by the researchers. Tests were carried out in a CO_2 solution containing 100 000 mg/L Cl^-. The test coupons were API 5L grade X65 pipeline material. The tests were conducted using a recirculating jet impingement method with the nozzle to specimen distance kept at 5 mm. The results from the study are summarised as follows:

Results at 7 and 14 m/s flow-induced corrosion show no difference between solid-free flow and flow containing 30 mg/L sand. When higher solid loadings of 100 mg/L and 200 mg/L are applied, there is a small increase in total thickness loss but the difference at the three sand loadings and the solid-free flow remains very small. In addition, the result at 30 mg/L which best matches the total thickness loss in zero solids has a thickness loss due to pure erosion of 0.33 mm/yr and a total thickness loss (all mechanisms) of 4.9 mm/yr. The small erosion contribution in comparison to the total material loss (all mechanisms) is noted. No pure corrosion results are presented at this velocity. The authors then increase the velocity to 20 m/s with 200 mg/L sand and measure values of pure erosion (material loss under cathodic protection) and pure corrosion (material loss via electrochemistry). Summarised results of the synergistic components towards the total material loss by all mechanisms are shown in Table 3-6 and are compiled from the publication.

Table 3-6

Erosion + Corrosion and Synergy contributions at 20 m/s and 200 mg/L, compiled from Hu, et al., (2008)

Temperature	E + C (mm/yr)	T (mm/yr)	S (mm/yr)	S/(E+C)	% Synergy
20°C	<5	~12	>7	~1.4	~58.3
40°C	<5	~20	>15	~3.0	~75.0
50°C	<5	~24	>19	~3.8	~79.2
60°C	<5	~29	>24	~4.8	~82.8

More recently, Neville, et al., (2009) evaluated mitigation of carbon steel erosion-corrosion by the use of corrosion inhibitors. The authors assessed two unidentified inhibitors (only referred to as inhibitor A and inhibitor B) and their effectiveness at reducing erosion-corrosion. Results were also compared to type 316L Stainless Steel. Tables 3-7 and 3-8 summarise their findings of tests carried out in simulated produced water with 0.1% sand loading. Tests were carried out at 20 m/s and 50°C. Both inhibitors showed an ability to reduce erosion-corrosion. Inhibitor A had peak efficiency at 50 ppm concentration and inhibitor B had peak efficiency at 100 ppm. At concentrations higher than peak values, both inhibitors show a reduction in efficiency. Inhibitor B showed the best effect at reducing Erosion-Corrosion. 316 Stainless steel results showed an erosion corrosion rate of about 14 mm/yr. The result may support ideas that carbon steel corrosion can be controlled to levels

comparable to the use of corrosion resistant alloys such as 316L Stainless Steel. Inhibitor B achieved a corrosion rate of 14 mm/yr at 100 ppm. It is however noted that a corrosion rate of 14 mm/year is by no means a remarkable result.

Table 3-7

Erosion-corrosion rates for tests with Inhibitor A, compiled from Neville, et al., (2009)

Inhibitor Concentration (ppm)	Carbon Steel Erosion-Corrosion Rate (mm/yr)	Inhibitor Erosion-Corrosion Efficiency (%)
0	33	0
25	22	3.8
50	17	50.0
100	24	26.9
150	27	19.2

Table 3-8

Erosion-corrosion rates for tests with inhibitor B, compiled from Neville, et al., (2009)

Inhibitor Concentration (ppm)	Carbon Steel Erosion-Corrosion Rate (mm/yr)	Inhibitor Erosion-Corrosion Efficiency (%)
0	33	0
25	27	19.2
50	24	26.9
100	14	57.7
150	17	50.0

In contrast, Dave, et al., (2008) carried out inhibitor assessments in flowing 2 % NaCl with CO_2 and 1% sand at a test temperature of 135^{o}F (57^{o}C). The inhibitor tested was an oil dispersible amidoamine fatty acid type inhibitor. Inhibitor concentrations considered were 50 ppm, 100 ppm and 150 ppm. A submerged jet with an average velocity of 13 m/s was used by the authors with the test specimen being 1018 carbon steel (AISI 1018). Results from this publication are shown in Figure 3-4. Tests at the

lower inhibitor concentration of 50 ppm showed the least efficiency through both LPR and weight loss. Higher inhibitor concentrations of 100 and 150 ppm showed better performance unlike experiments done by Neville, et al., (2009) as shown in Table 3-7 where 50 ppm of inhibitor A showed best efficiency. This mechanism where the inhibitor shows a peak value of efficiency and develops lower efficiencies at concentrations above the peak is termed by Neville, et al., (2009) as the "peak value phenomenon".

Figure 3-4

Comparison of LPR and Weight Loss results in impinging 2 % NaCl with 1 % sand taken from (Dave, et al., 2008)

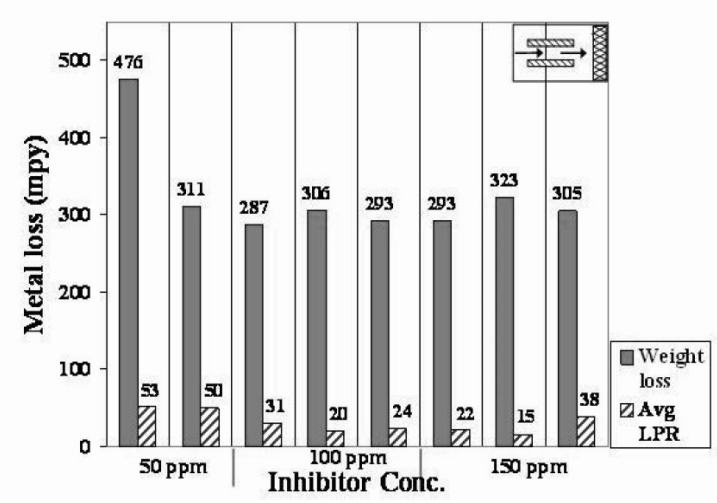

Although the results in Figure 3-4 are in flowing fluid containing 1% sand, a surprisingly large variation between LPR and weight loss results is also observed. Such a difference between weight loss and LPR is indicative of large synergistic material loss. A conversion of worst case results at 50 ppm would yield a weight loss corrosion rate of about 12.1 mm/year compared to an approximate LPR corrosion rate of 1.3 mm/year. Such a variation in material loss emphasises the extent of erosion and synergy or may be due to inaccuracy in constants used to convert polarisation resistance results to corrosion currents (i_{corr}).

In static conditions, some agreement between gravimetric and Faraday monitoring techniques have been reported by Tebbji, et al., (2007). Field data by Place Jr, (1998) also shows a discrepancy between corrosion coupon data and ER probes in

actual field locations. Coupons had corrosion rates of 0.22 MPY compared to ER probe corrosion rates of 0.04 MPY. Tests were in inhibitor conditions.

Testing by George, et al., (2004) also showed a discrepency between results obtained by linear polarisation resistance (LPR) and weight loss (WL). Results from WL were consistently higher than LPR with an example being a LPR value of about 4.5 mm/year compared to a WL value of about 6.5 mm/year at 60°C, pH 4 CO_2 solution at velocity of 1000 rpm by rotating cylinder. Such a discrepency would amount to about 30% synergistic loss in solid free flow.

From the above observations, it appears that such discrepencies are more common than expected and lessens the probability of inaccuracy with calculations and conversions of electrochemical data to equivalent corrosion rates. Such observations support concepts of non electrochemical losses in erosion-corrosion.

Hu, et al., (2002) demonstrated synergistic effects in corrosion resistant alloys such as 25 Cr duplex (Tables 3-9 and 3-10). The values of synergy noted through these experiments are significantly less than those obtained with carbon steel. Tests are carried out in 3.5 % NaCl at a temperature of 18°C. From the results, it is noted that the percentage levels of synergy and corrosion are lower compared to levels for carbon steel presented earlier in this project as corrosion resistant alloys (CRA) will have a lower component of pure corrosion and hence result in a lower level of synergy.

Table 3-9

CRA material loss and TWL components at 150-200 mg/L Solid loading at 17 m/s taken from Hu, et al., (2002)

Material	TWL (mg)	Erosion (%)	Corrosion (%)	Synergy (%)
UNS S31254	6.7	83.6	3.7	12.7
UNS S32750	6.2	95.2	2.6	2.2
UNS S32654	5.3	92.4	2.3	5.3

Table 3-10

CRA material loss and TWL components at 600-640 mg/L Solid loading at 17 m/s taken from Hu, et al., (2002)

Material	TWL (mg)	Erosion (%)	Corrosion (%)	Synergy (%)
UNS S31254	14.6	82.2	11	6.8
UNS S32750	14.1	86.5	6.8	6.7
UNS S32654	13.5	92.6	6	1.4

In another publication by the authors Hu, et al., (2004), UNS S32654 was also established as having better resistance to erosion-corrosion than UNS S31654.

Ramakrishma, et al., (2006) carried out flow loop experiments on erosion-corrosion of carbon steel in 1% NaCl solution purged with CO_2. Results at a flow velocity of 2 m/s and 2 wt % slurry concluded that interactions between corrosion and erosion enhanced individual metal loss rates. The dominant mechanism in synergy was the enhancement of erosion by corrosion.

Meng, et al., (2007) identified the contributors to synergy as velocity, solid loading and the interactive effect of solid loading and velocity.

Work by Hodgkiess, et al., (2005) also reported significant synergy losses in copper nickel alloys with maximum values of synergy in Cu-10Ni being 69 % and max values for high strength Cu/Ni being 77 % Tests were in sold-free NaCl.

3.5 CO_2 Corrosion Inhibition

Internal corrosion prevention using chemical treatment is one of the most cost effective solutions for using mild steel as the preferred material for construction of pipelines and well tubing in oilfield operations Ramachandran, et al., (1998). Corrosion inhibitors have also been the favoured mechanism for corrosion control in downhole applications Rincon, (2008)

The flow parameters currently favored for assessing the effect of flow on corrosion rates, inhibitor films formation and film stability is shear stress at the wall. Most inhibitors are however, only evaluated in stagnant conditions or low flow of < 1m/s

Neville, et al., (2003). Multiphase flow as commonly found in pipelines induces high shear stresses at the wall and may interfere with inhibitor performance Pritchard, et al., (1998)

The corrosion inhibition of a metal may involve physisorption or chemisorption of the inhibitors to the metal surface and subsequent interference with cathodic, anodic or both reactions Ali, et al., (2005). The authors comment on pipeline corrosion inhibitor molecules as typically consisting of polar head groups that interact with a metal surface (accomplished through electrostatic attraction between the hydrophilic inhibitor head, and metal surfaces) and hydrocarbon tails that repel water (hydrophobic).

Duda, et al., (2005) presented results showing inhibitor surface coverage dependent on inhibitor tail length and concentration. Higher surface coverages were achieved with higher inhibitor molecule concentrations. However, inhibitors with the most solvophobic tails showed weaker coverage and hence weaker inhibition characteristics if concentration exceeded critical values. This mechanism where inhibitor efficiency weakens at concentrations above optimum has already been earlier discussed and has been recognised as the “peak value phenomenon”.

Henry, et al., (2005) identify molecules such as quaternary salts as typically having polar head groups that interact with the metal polar surface and long hydrocarbon tails that repel water. These long chain hydrophobic tails have also been implied by Lopez, et al., (2005) to form protective porous films with a bilayer model being the film structure.

Petersen, et al., (2004) establish Inhibitor effectiveness at reducing ultrasonic cavitation damage. The inhibitor tested achieved a reduction in corrosion rates to under 0.4 mm/yr compared to uninhibited rates above 12 mm/year

Hedges, (1996) presented environmental issues with inhibitors including imidazoline based inhibitors. Concern with inhibitors was indicated to their toxicity, biodegradability and bioaccumulation. Inhibitor chemistries such as amines and imidazolines were identified as being toxic to marine crustacean *Tisbe battagliai* at low concentrations of less than 5ppm. The author emphasised development of

environmentally friendly corrosion inhibitors and identified patented chemistries with high effectiveness and lower toxicity levels. However, Kolts, et al., (1998) reported a lack of effectiveness in green inhibitor testing. Inhibitor performance was highly dependent on temperature especially at temperatures above 90^{o}C. These inhibitors also performed better in static conditions with inhibitor performance weakened significantly in flow velocities of 4 m/s.

Work by Heeg, et al., (1998) discussed two important factors in inhibitor mechanisms:

i. Persistency – the lifetime of the film;
ii. Efficiency – ratio of inhibited to uninhibited corrosion rate.

These two mechanisms have been found to depend on four major factors for multiphase flow:

i. Chemical composition of the multiphase flow;
ii. Erosive nature of the flow;
iii. Type of adsorption on metal surface (physisorption, chemisorption, packing order and roughness of the substrate);
iv. Wall shear stress.

3.5.1 Imidazoline Inhibitors

Tan, et al., (1996) and Ramachandran, et al., (1998) identified imidazolines, amides and amido-amines and their salts as having been successfully and commonly used to inhibit corrosion in CO_2 environments. Ramachandran, et al., (1998) identify the most important parameters in determining corrosion inhibition of mild steel in brine-containing systems as their bulk solution properties such as hydrophobicity and transportation of active species from the solution to the metal phase.

Chen, et al., (2000) suggest imidazoline based inhibitors as having high inhibition ability in acidic media, hence their popular use. Others for example Nesic, et al., (1995) have found poor inhibition by imidazolines in conditions where there was a presence of surface films.

3.5.2 Concentration Effects

A major issue with corrosion inhibitors is the largely variable concentrations required to achieve peak efficiency. Various studies have shown that inhibitors can be effective from optimum concentrations as low as 5 ppm to concentrations well over 1000 ppm Jeyaprabha, et al., (1998). As already discussed earlier, researchers such as Neville, et al., (2009) have recognised this concentration effect and the phenomenon termed "peak value phenomenon" where inhibitors develop lower effeciencies if concentrations are increased above optimum levels. This issue is crucial and is considered within this project.

Hesjevick, et al., (2003) reported concentrations of 20 ppm as being typical for application in oil and gas systems with the tested inhibitor achieving corrosion rates of less than 0.1 mm/year. Increasing pH did however adversely affect the inhibitor efficiency. It is however noted that higher pH values have tended to offer better protective film formation as discussed earlier in work by Chokshi, et al., (2005). Higher pH values are shown to achieve better degrees of iron carbonate supersaturation hence achieving more protective films. Work by Chokshi, et al., (2005) in stagnant conditions also identified a varied concentration effect between two unspecified inhibitors. Both inhibitors reduced corrosion rates by slowing anodic and cathodic reactions.

Although optimum concentrations are often evaluated in labs, field conditions may however require a different concentration to that established as effective during the qualification. Results from (Neville, et al., 2009) show that increasing concentration above the peak value actually worsens the inhibitor efficiency and hence the corrosion rate. Proper qualification of the inhibitor is therefore extremely important.

Jiang, et al., (2005) established a concentration effect linked to the velocity. Best efficiency concentrations depended on the flow velocity with velocities of 0-5 m/s requiring 150 mg/L and velocities of 7 m/s and 9 m/s requiring concentrations of 300mg/L in order to achieve best efficiency. In another publication (Jiang, et al., 2005), similar observations are noted with the optimum concentration for an imidazoline based inhibitor in flowing conditions of 5 m/s established as 200 mg/L. Static conditions required 100 mg/L for optimum efficiency.

Altoe, et al., (1996) identified the stability of inhibitor films as flow dependant and strongly affected by the residual concentration of the inhibitor in the solution. Higher concentrations of inhibitor were deemed necessary at high velocities. In contrast, Bommersbach, et al., (2006) found better inhibitor film formation in faster flow.

(Foss, et al., 2009) reported enhanced inhibitor performance in environments with oil. The structure of the inhibitor film was strongly influenced by the presence of oil and gave better protectiveness. The enhanced protectiveness of the inhibitor film in the presence of oil was attributed to coadsorption effects rather than formation of stable inhibitor films. Nesic, et al., (1995) found no major improvement in imidazoline based inhibitor performance in the presence of oil. (Gulbrandsen, et al., 1998) carried out tests using an imidazoline-based inhibitor in CO_2 environments. Best inhibitor efficiency was achieved at 20 ppm concentration. Increasing inhibitor concentration to 200 ppm initiated pitting corrosion.

3.5.3 Erosion-corrosion Inhibition

Neville, et al., (2009) focused on the inhibition properties of two commercial (unspecified) inhibitors in erosion-corrosion environments. The work involved establishing inhibitor effectiveness at reducing both mechanical and electrochemical processes of carbon steel material loss. A jet impingement was used with a flow velocity of 20 m/s. The nozzle stand of distance was 5 mm with the jet normal to the specimen surface. The results of this work are summarised in the previous section (section 3.4.3) on synergy. Sand loading was 0.1%. Tests of 316 (UNS S 31603) samples without inhibitor showed a yearly corrosion rate of nearly 14 mm/year which as discussed earlier is by no means a good result for a corrosion resistant alloy (CRA).

A previous study by the above researchers Neville, et al., (2003) assessed three unspecified inhibitors (only identified as CGO, CRO and CRW) in erosion-corrosion flow at concentrations of 100 ppm Inhibitors CGO and CRO are identified as oil soluble inhibitors and inhibitor CRW as an inhibitor for high shear systems. Tests were carried out in CO_2 environments with 1 % silica loading and performed by rotating cylinder electrode (RCE). All three inhibitors had an effect of shifting the potential of the steel in the positive direction with the most effective inhibitor having the largest shift in potential as detailed in Table 3-11.

Table 3-11

E_{corr} and R_p values for inhibitors in static and flow (6000 rpm) taken from (Neville, et al., 2003)

Inhibitor	Time (mins)	E_{corr} (V, SCE) Static	E_{corr} (V, SCE) at 6000 rpm	R_p ($\Omega.cm^2$) Static	R_p ($\Omega.cm^2$) at 6000 rpm
No Inhibitor	0	-0.704	-0.439	556	483
No Inhibitor	30	-0.704	-0.458	429	348
No Inhibitor	60	-0.703	-0.449	668	466
Inhibitor CGO	0	-0.626	-0.444	891	615
Inhibitor CGO	30	-0.691	-0.444	1690	810
Inhibitor CGO	60	-0.689	-0.437	1537	545
Inhibitor CRO	0	-0.690	-0.471	524	469
Inhibitor CRO	30	-0.695	-0.423	667	500
Inhibitor CRO	60	-0.695	-0.415	740	666
Inhibitor CRW	0	-0.598	-	883	-
Inhibitor CRW	30	-0.597	-0.140	2083	84985
Inhibitor CRW	60	-0.598	-0.171	2052	80000

It is also noticed that in flowing conditions, the value of R_p increased above static values for the most effective inhibitor CRW indicating lower corrosion rates at 6000 rpm compared to static conditions. This effect was reported as a result of a reduction in charge transfer by the inhibitor film. As expected, R_P values decreased, showing an increase in corrosion rates from static to flow without inhibitor. The effective inhibitor CRW also reduced erosion-corrosion to efficiencies of nearly 90 % when combined with cathodic protection. Efficiency values without cathodic protection were just below 40 %. The work by the authors obviously progresses information related to erosion-corrosion and inhibition but may be limited by the short test durations of 1 hour or less which, in opinion do not reflect real field situations where continuous inhibition normally occurs for much longer periods such as years.

In 2005, Ramachandran, et al., (2005) acknowledged the use of oilfied inhibitors in prevention of erosion-corrosion. Advances in development of such inhibitors were also reported with various inihbitors showing varying abilities and effects when inhibiting erosion-corrosion. Earlier work, Ramachandran, et al., (2002) focused on inhibitor performance in prevention of erosion-corrosion caused by impingement of particles. A numerical estimation of wear due to particle impingement was presented with modifications to account for inhibitor effects.

Work by (Wang, et al., 2005) demonstrated inhibitor reductions of erosion-corrosion by both mass loss and electrochemical analysis. The results did however show littlle correlation between both techniques again suggesting mechanical metarial losses.

3.5.4 Corrosion Inhibitor Availability

Hedges, et al., (2000) comment on the failings involved with the corrosion efficiency model (Equation 2-11 of Chapter 2) especially with respect to the design of new pipelines. Marsh, et al.,(2007) point out that using efficiency essentially examines the ratio of the inhibited and uninhibited corrosion rate and expresses this as a percentage. The problem with this approach is that efficiencies of 98% can be achieved in laboratory testing but in actual field situations, the limiting factors are not the ability of an inhibitor to reduce the corrosion rate but lack of inhibitor injection due to limitations such as the following:

1. Pump Failures;

2. Logistics;
3. Other Issues.

Rippon, (2001) identified a long list of reasons limiting availability some of which are identified below

1. Incorrect inhibitor arrives at site;
2. Inhibitor runs out on platform due to inadequate stock levels;
3. Wrong inhibitor loaded into tank by operators;
4. Inhibitor tank allowed to run empty;
5. Inhibitor incorrectly diluted;
6. Inhibitor pump breakdowns;
7. Power failures affecting inhibitor pump while production continues;
8. Power failure which stops all production.

To account for such limitations, McMahon, et al., (2007) adopt the inhibitor availability model (see Equation 3-18) and identify the approach as assuming the inhibited corrosion rate as unrelated to the uninhibited corrosivity of the system and that all systems can be inhibited to 0.1 mm/year. Rippon, (2001) proposes other values for target inhibition rates depending on the temperature profile of the system as given in Table 3-12. In the inhibitor availability concept presented by Marsh, et al., (2007), field performance of an inhibitor is determined based on the summation of total metal loss over field life, assuming inhibited corrosion and uninhibited corrosion. The actual metal loss in mm/ yr can then be worked out from Equation 3-18.

$$CR = \left(\frac{Availability(\%)}{100} * TICR \right) + \left(1 - \left(\frac{Availability(\%)}{100} \right) * UCR \right)$$ **Equation 3-18**

Where CR is metal loss in mm/yr

TICR is the target inhibited corrosion rate (0.05mm/yr, 0.1mm/yr etc)

UCR is the uninhibited corrosion rate in mm/yr

An inhibitor availability of 100% would then give the target corrosion rate in mm/yr.

Table 3-12

Recommended Inhibited Corrosion Rates compiled from (Rippon, 2001)

Temperature Range, °C	Inhibited Corrosion Rate, mm/yr
Up to 70°C	0.05
>70°C and ≤120°C	0.1
>120 °C and ≤150 °C	0.2
Above 150°C	Inhibition not recommended without specific testing

3.5.5 Preferential Weld Corrosion

Although inhibitors have been shown to have beneficial effects with regard to general CO_2 corrosion, inhibitors are also associated with unwanted effects with regard to preferential corrosion of welds within pipelines. This form of corrosion transpires through galvanic mechanisms between the parent metal and the weld and is often associated with varied inhibition of the two regions. The severity of preferential weld corrosion occurs when the parent metal (often a large surface) is the cathode in relation to the weld metal which acts as the anode. The smaller surface area of the weld metal compared to the parent metal means galvanic current densities can lead to sacrificial corrosion of the weld metal at significantly faster rates in comparison to the rest of the structure.

Turgoose, et al., (2005) identified conditions which best suit this form of corrosion as having weld consumables typically depositing 1% Ni weld metal and low conductivity conditions. The researchers also concluded this mechanism to arise due to the inability of the inhibitor tested to protect the weld metal whilst protecting the parent metal. This observation has also been observed by others such as Alawadhi, et al., (2008) as detailed below.

Studies involving inhibitors have focused on preferential corrosion as inhibitors have been found to inhibit parent metals well and act in a less effective manner on the weld metal. Such an effect has been clearly demonstrated in recent work by Alawadhi, et al., (2008) where tests in uninhibited conditions showed the weld metal and heat affected zone of welded X65 pipeline steel acting as the cathode in relation

to the parent material. In inhibited conditions involving 30 ppm of a "green" inhibitor and flowing conditions, a switch in the setup was observed with the weld metal and heat affected zone becoming anodic and the parent metal acting as a cathode. This effect is also linked to the combination of flow and inhibition as in similar inhibited environments but in static conditions, no reversal was observed. The situation was also observed to be worse in inhibited flow at higher temperatures such as 70°C which presents a dilemma as most pipelines operate in such environments. The authors concluded the behaviour as attributed to variable corrosion product film formation with less protective films forming on the weld metal than on the other regions of the weld. Table 3-13 is a review of some findings by the authors.

Table 3-13

Galvanic activity between weld and parent metal of X65 pipeline steel, compiled from Alawadhi, et al., (2008)

Test Conditions	Weld Metal	Parent Metal	HAZ
Uninhibited + Flow	Cathode	Anode	Anode
Inhibited + Static	Cathode	Anode	-
Inhibited + Flow	Anode	Cathode	Anode

To add to the emphasis of the problem, recent testing by Vera, et al., (2009) evaluated inhibitor performance at reducing galvanic corrosion and preferential corrosion of X65 carbon steel coupled to Alloy 625 in CO_2 saturated brines at 66°C. Three inhibitors at 150 concentration are assessed with only one inhibitor able to reduce the galvanic currents whilst showing no evidence of preferential weld corrosion. All three inhibitors did however show effectiveness at reducing uniform corrosion.

3.6 Conclusions

The literature review has demonstrated the extreme complexity of corrosion behavior of steels in CO_2 – containing brines. This complexity is obvious partly due to the wide range of prevailing environmental conditions such as temperature, CO_2 concentration and flow conditions.

One important factor in CO_2 corrosion of carbon steel, which has been clearly demonstrated, is iron carbonate film formation. Films containing iron carbonate

(often referred to as scale) have been well discussed as having corrosion protective characteristics. However, conditions where this scale fails to form are remarked by Garber, et al., (1998) as producing reported failures in as little as six months into service. Iron carbonate formation has also been shown to vary with supersaturation, temperature and precipitaiton. The degree of iron carbonate supersaturation achieved has been shown to directly affect film formation with higher degrees of supersaturation resulting in better film formation. Scaling tendency which is linked to the supersaturation through precipitation has also been shown to affect the structure of the film with scaling tendencies of less than 1 resulting in porous unprotective films. Scaling tendencies greater than 1 have been linked to dense protective carbonate films.

Turning to hydrodynamic influences with relation to flowing corrosive fluids, it is very clear from literature that mechanical damage mechanisms are involved during erosion-corrosion in liquid/solid flowing environments. In addition, complex interactions between erosion and corrosion porcesses (often termed synergy) can contribute largely to the total material losses. These synergistic effects have been shown to make up the majority of the material loss by all mechanisms with the pure corrosion and erosion components being in most cases, relatively small.

Numerous tests involving solid containing fluids have been carried out and most seem to agree on the observation that synergistic effects make up the majority of material losses. On the other hand, It has become apparent in some fairly recent studies such as Neville and Hodgkiess in 1999 that similar phenomenon, involving synergy can be present during aqueous solid-free erosion-corrosion. This mechanism seems to have attracted little attention although research by the above authors indicated synergistic effects amounting to 59.5 % of the total material loss in solid-free flow conditions. Since then, the issue has been little attended to as the bulk of work addressing synergy related material loss has concentrated on flowing fluids containing solid particles. This issue requires added research to confirm levels of synergy in solid-free flow. Should high levels of synergy, as reported by some previous workers exist in solid-free flow, then an experimental strategy that does not rely on electrochemical techniques only, becomes very desirable as this avoids the issue of corrosion rates being underestimated and provides additional information on the mechanisms contributing to the total material losses.

Corrosion monitoring using electrochemical techniques is inadequate as it can only assess material losses due to electrochemical mechanisms. This would consequently mean that corrosion rates assessed by such techniques in conditions involving flowing fluids underestimte the actual material losses involved. It is therefore of question whether Faraday related corrosion monitoring techniques are appropriate in conditions of flow especially solid-free flow.

Inhibitors have been found to be effective at inhibiting corrosion including erosion-corrosion. Although this is no doubt a very beneficial effect, major areas of concern arise in relation to the influence of hydrodynamic conditions on the efficiency of inhibitors. This does not simply relate to issues such as inhibitor film formation and persistency but is also likely to involve galvanic interactions between different hydrodynamic zones on a uniform steel surface. An additional feature to which inhibitor performance has been linked, involves galvanic interactions between different zones of welded components. This mechanism is an undesirable feature of inhibition and as discussed earlier can also be linked to hydrodynamics. This study will address such mechanisms considering such galvanic activity between various hydrodynamic zones and inhibitor action under such conditions.

This project aims to address the issue of inhibition in conditions of variable shear. As identified in this Chapter, one current issue with flowing corrosive fluids is the probability of material losses from mechanisms other than pure electrochemical dissolution. This project aims to address the existence of such mechanisms in solid-free flow simulating oilfield conditions.

The impingement jet method has been illustrated as one of the main and common methods of monitoring erosion-corrosion in laboratories. The jet impingement is well characterised and equations for evaluating shear stress are well defined. The method has also been extensively favored in studies involving erosion-corrosion. The (Efird, et al., 1993) and (Efird, 2000) specimen setup provides a good means of monitoring in-situ variable shear stresses.

4.0 EXPERIMENTAL TECHNIQUES AND RESULTS ANALYSIS

4.1 Introduction

This section details the experimental techniques, apparatus, chemicals and methods used to investigate the influence of hydrodynamics and shear on the efficiency of a commercial CO_2 corrosion inhibitor. A jet impingement setup is used as the mass transport system. As defined earlier in Chapter 3, the shear stress for a submerged jet impinging on a flat surface is well defined. The hydrodynamic variables used to assess the results are shear stresses that are varied by velocity and radial position along the test specimens.

The inhibitor used in the experiments was a commercial inhibitor provided by Clariant Services. The inhibitor trade name was CORRTREAT 727. All tests are carried out in 3.5% NaCl solutions at a temperature of 50^{o}C. Results are analysed by mass loss, Linear Polarisation Resistance (LPR), Tafel Extrapolation and galvanic current measurements by means of a zero resistance ammeter.

Post test analysis of corroded specimens included TalySurf surface profiling and microscopy. The tests rigs used are two identical recirculating jet impingement rigs with variable velocities. Results obtained from these experiments are presented in Chapters 5, 6, 7 and a discussion in Chapter 8. Table 4-1 summarises the test equipment used, tests procedures, test conditions and corrosion monitoring techniques.

Table 4-1

Summary of testing procedures and equipment

	Gravimetric (Mass Loss)						Electrochemical					
Test electrode	Carbon steel						Carbon steel					
Test Solution	3.5 wt % NaCl						3.5 wt % NaCl					
Test temperature	50°C						50°C					
Test velocities (m/s)	8 m/s			2 m/s			8 m/s			2 m/s		
Average shear stress in zone (Pascal's)	Im	I	O	Im	I	O	Im	I	O	Im	I	O
	183	5.9	2.2	15	0.5	0.17	183	5.9	2.2	15	0.5	0.17
Test conditions	1-7						1-5					
Test Apparatus	OHAUS AS120s electronic scales with balance accuracy 0.0001g. Test coupons located in T, I, O zones. Taylor Hobson Pneumo form TalySurf series 2 surface profiling machine. Olympus BH2-UMA light optical microscope.						Electrodes Reference – Calomel Reference Counter – Platinum counter electrode Working – Carbon steel specimens in T, I, O zones Precision 16 Bit Ramp Generator Ministat Potentiostat Zero resistance ammeter (ZRA) for measurement of galvanic currents between specimens in T, I, O zones.					
Corrosion monitoring technique(s)	Mass losses converted to equivalent corrosion rates						LPR					
							Tafel Extrapolation					
							Zero Resistance ammeter (Galvanic)					

Test conditions:

1) Aerated
2) CO_2 saturated
3) CO_2 saturated with 100ppm inhibitor
4) CO2 saturated with 150ppm inhibitor
5) CO2 saturated with 200ppm inhibitor
6) CO2 saturated with 1000ppm inhibitor
7) CO2 saturated with 1500ppm inhibitor

Im – Impingement (Impingement zone specimen)
I – Intermediate zone specimen
O – Outer zone specimen

LPR is performed by small anodic and cathodic polarisation perturbations of 20 mV from E_{corr}. Scan rate is set at 12 mV/min. Current response is noted and potential/current density plot is generated. Best fit gradient of plot corresponds to polarisation resistance Rp. i_{corr} is proportional to Rp through Equation 2-8

Tafel Extrapolation is performed by 200 mV full anodic polarisations from E_{corr}. Scan rate is set at 12 mV/min. Potential/current response is recorded then plotted on E/log i plot. Tafel region (straight line next to E_{corr}) is identified and extrapolated back to E_{corr} where corresponding current density is i_{corr}. Current density, $i_{corr,}$ is then converted to equivalent mass loss using Faraday's Law (Equation 2-9).

Galvanic Interactions are measured by a zero resistance ammeter connection between electrodes in T, I, O zones.

4.2 Jet Impingement Rigs

Two identical recirculating jet impingement rigs are used to deliver impinging flow at velocities of 8 m/s and 2 m/s. A variation in velocity is achieved by use of a smaller pump for the 2 m/s rig. The rigs will be referred to as rig 1 and rig 2. The corresponding velocities for the rigs are 8 m/s for rig 1 and 2 m/s for rig 2. Figure 4-1 shows a schematic representing the impingement rigs. The rigs recirculate 3.5 % NaCl solution dissolved at least overnight in distilled water. The standoff distance between the nozzle and the specimen surface is always kept at 5 mm. The jet nozzle is always normal to the specimen surface and is always fully submerged at its exit point. The nozzle diameters are 1 mm for both rigs. The velocities of both rigs are checked prior to every test. For the CO_2 saturated tests, the CO_2 is supplied to both rigs through rubber tubing then dispersed in the recirculating fluids by means of an aquatic fine filter. This ensures the CO_2 bubbles are of fine nature and dissolve easily.

Figure 4-1

Schematic of recirculating jet impingement rig and apparatus

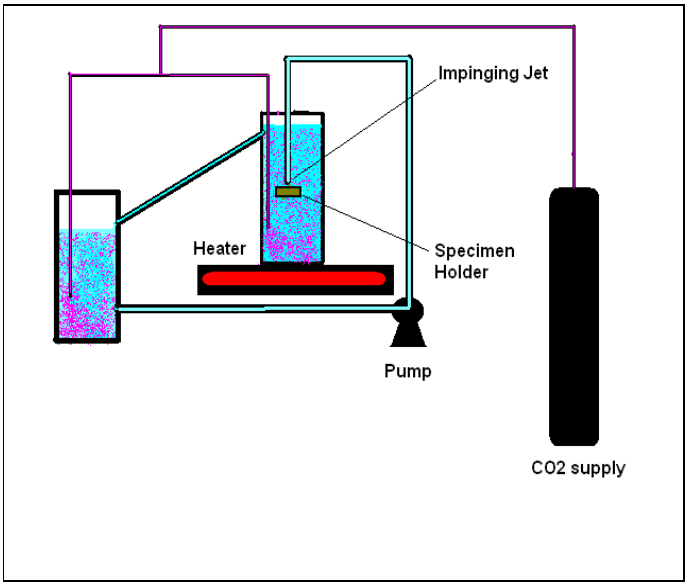

4.3 Inhibitor

The inhibitor used in this project is a commercially available CO_2 corrosion inhibitor. The inhibitor is supplied by Clariant Production UK Ltd and has a trade name of CORRTREAT 727. The compositional information and ingredients is given in Table 4-2

Table 4-2

CORRTREAT 727 Compositional Ingredients

Ingredient	Minimum (%)	Maximum (%)
2-Butoxy Ethanol	30.0	60.0
Acetic Acid	1.0	5.0
Thioglycolic Acid	0.2	2.0
Imidazoline	5.0	10.0
Imidazoline Ethoxylate	5.0	10.0

4.4 Tests Specimens

The material used for the test specimens is carbon steel. The material chemical composition and expected properties are given in Table 4-3

Table 4-3

Material Grade Properties

	C % max	Si % max	Mn % max	P % max	S % max	N % max	Cu % max
Chemical Composition	0.24	0.55	1.60	0.035	0.035	0.012	0.55
Min Yield Strength (MPa)	355						
Tensile Strength (MPa)	510 to 680						

4.4.1 Electrochemistry Specimen

Figure 4-2 shows a picture of the prepared electrochemistry specimen. The specimen is prepared by moulding machined specimens in epoxy resin to form a solid specimen with an even surface. All three coupons are machined from one solid bar of

starting material to ensure no difference in metallurgy or specimen chemistry. An electrochemical connection is made on each specimen by welding an electrical connection to each specimen prior to moulding in resin. The electrical connection has a colour code system in order to distinguish the specimens. The specimen is ground down to 600 grit before every test.

Figure 4-2

Electrochemistry Coupons embedded in epoxy resin.

4.4.1.1 Shear Stress Values

The shear stresses of the zones are calculated from the Efird, (2000) (Page 17) equation for shear stress of a submerged impinging jet. The values of shear are calculated at each radial position and an average is taken for each zone. For both rigs, the impingement zones are located in the impingement zone with the intermediate and outer zones located in the wall jet region. Figures 4-3 to 4-8 show the values of shear stress in each zone and at both velocities.

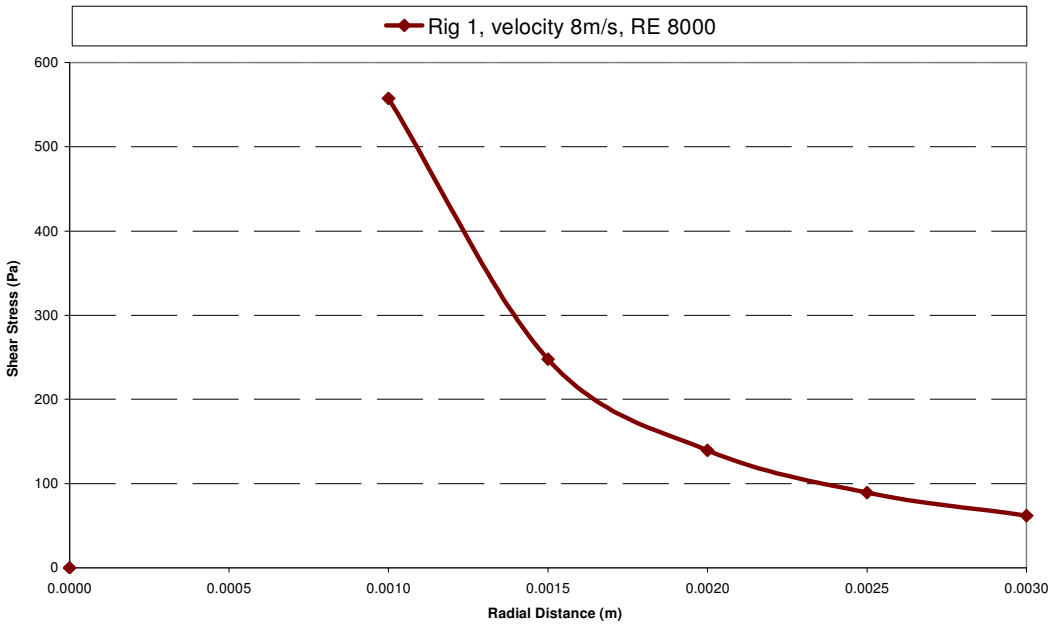

Figure 4-3. Shear stress distribution for the impingement specimen at 8 m/s. Calculated from Efird (2000) equation.

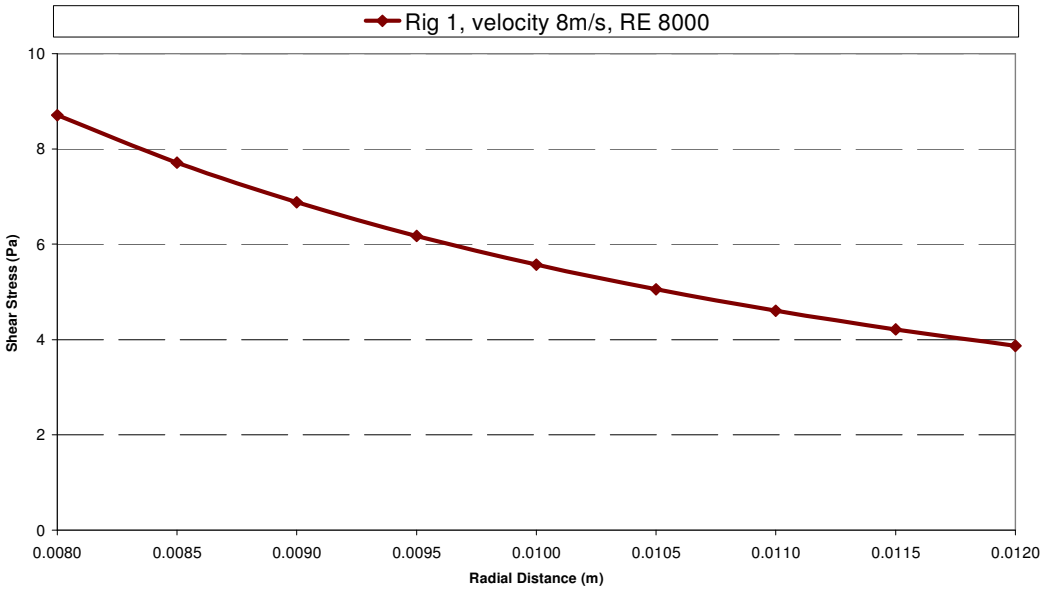

Figure 4-4. Shear stress distribution for the intermediate zone specimen at 8 m/s. Calculated from Efird (2000) equation.

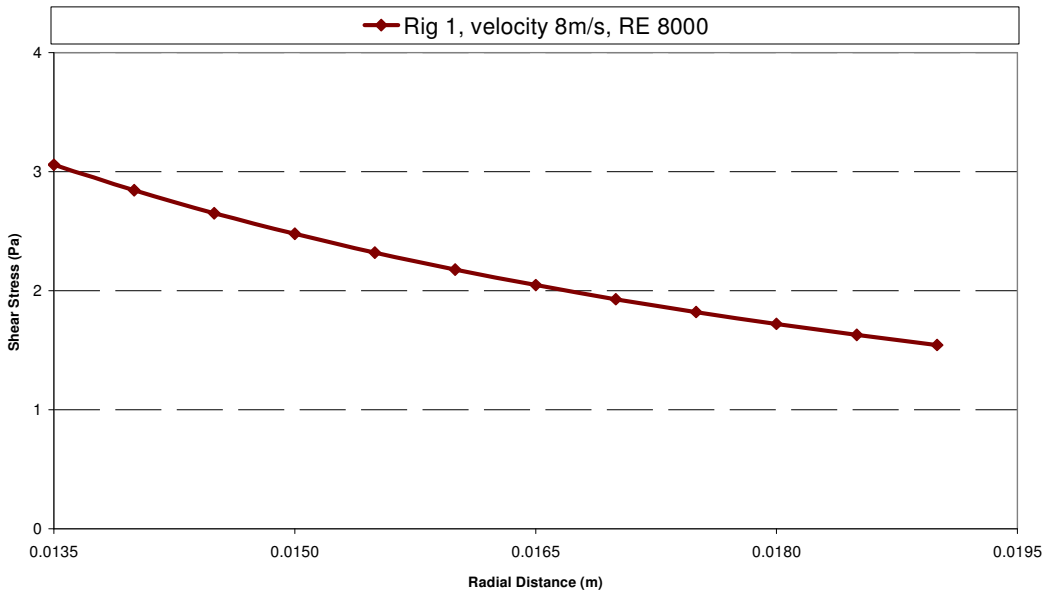

Figure 4-5. Shear stress distribution for the outer zone specimen at 8 m/s. Calculated from the Efird (2000) equation.

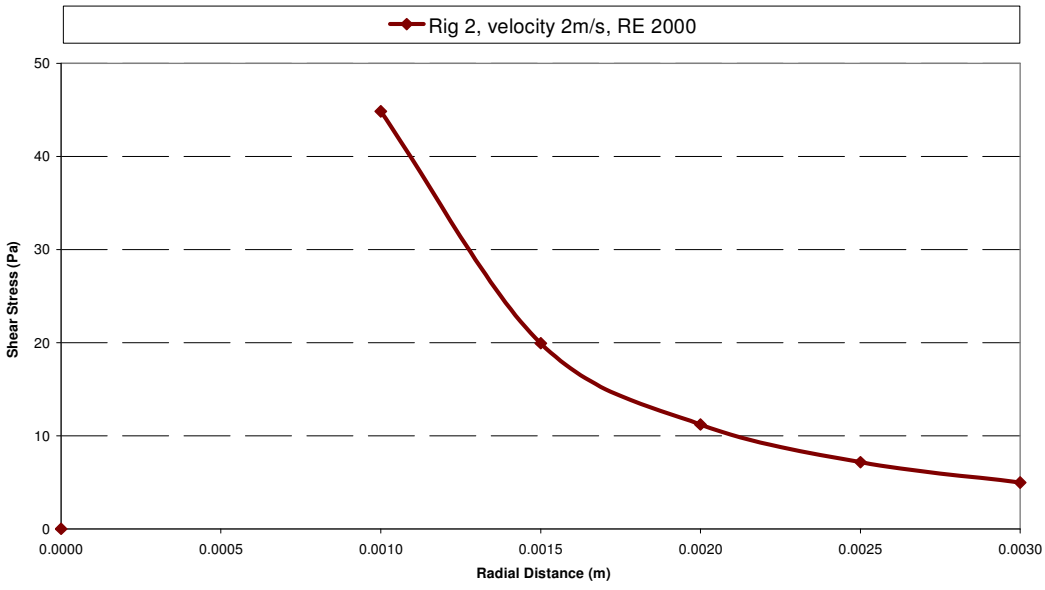

Figure 4-6. Shear stress distribution for the impingement zone specimen at 2 m/s. Calculated from Efird (2000) equation.

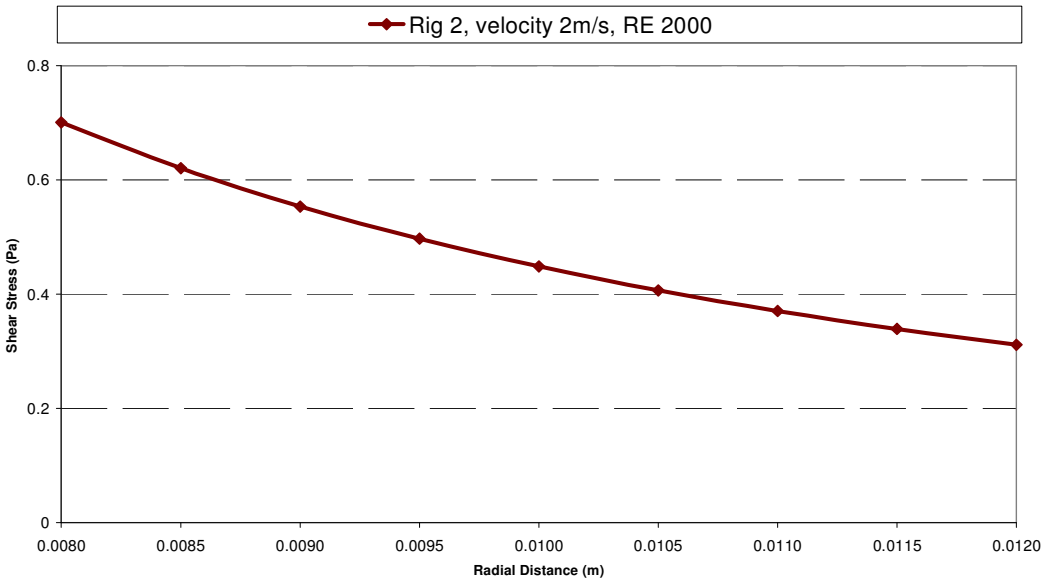

Figure 4-7. Shear stress distribution for the intermediate zone specimen at 2 m/s. Calculated from Efird (2000) equation.

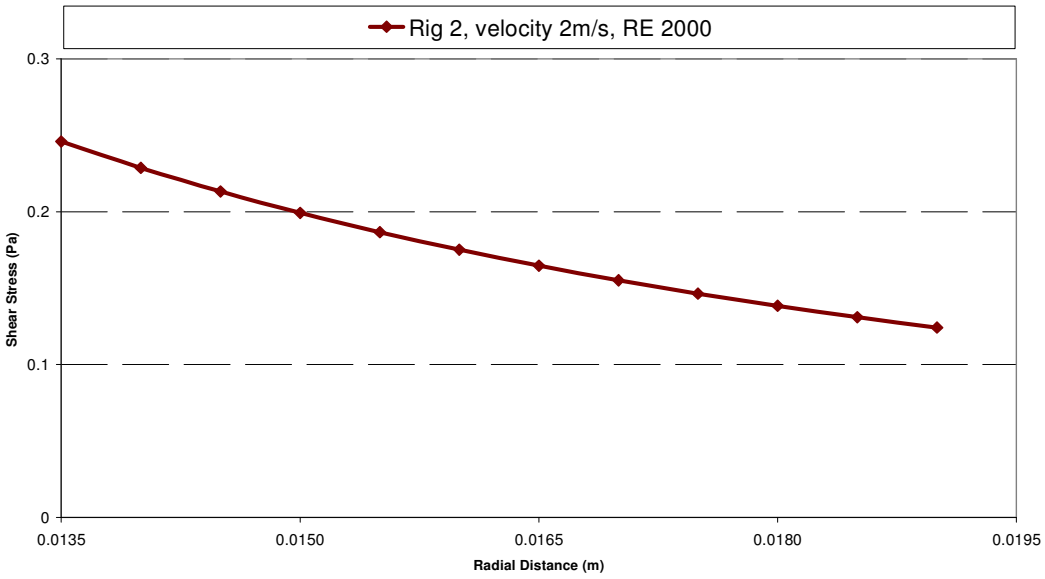

Figure 4-8. Shear stress distribution for the outer zone specimen at 2 m/s. Calculated from Efird (2000) equation.

4.4.2 Gravimetric

Figure 4-9 shows the gravimetric coupons for the weight loss tests. The specimens are identical to the specimens used in the electrochemistry specimen and are machined from the same bar of material as the electrochemistry specimens. Similar to the electrochemistry specimen, the impingement zone is located in the impingement zone with the intermediate and outer zones located in the wall jet region of the flow.

Figure 4-9

Gravimetric test coupons

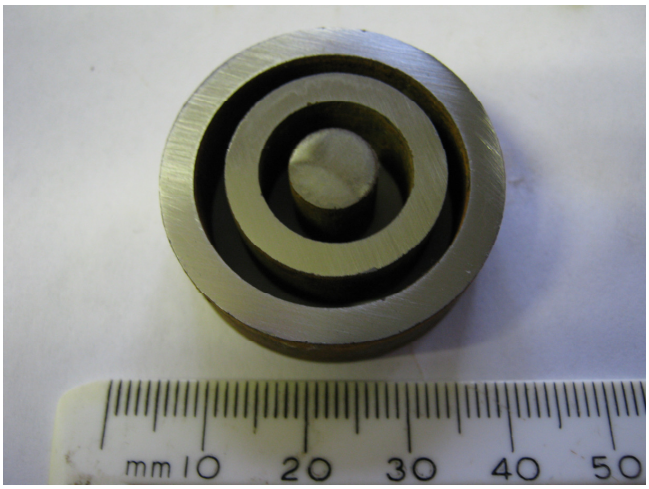

4.5 Gravimetric Tests

Corrosion rates are analysed by coupon mass loss using OHAUS AS120s electronic scales with a balance accuracy of 0.0001 g. Before each test, each coupon is polished down to 600 grit, degreased with methanol and dried using a METASERV specimen dryer. Post testing, the coupons are dipped in Clarke's solution for up to 5 minutes, rinsed with tap water and dried before reweighing. To ensure accurate mass loss determination, all coupons are weighed at least three times and an average value is taken as final. All tests are carried out for a duration of 24 hours and recorded by stopwatch. For the tests involving CO_2, the test solution is purged with

CO_2 for at least 1 hour before coupon insertion. For the inhibitor tests, the coupons lie in static conditions for an hour.

4.5.1 Post Test Procedures for Corrosion Product Removal

Post testing, the coupons are prepared for reweighing in accordance with ASTM G1-03. The coupons are cleaned and corrosion products are removed using the Clarke's solution method as detailed in the standard. The coupons are dipped in the solution for at least 1 min in order to remove all corrosion products on the surface. If required, the coupons are dipped for longer periods. The Clarke's solution is prepared as follows:

To 1000 mL of hydrochloric acid (HCl) with a specific gravity of 1.19, 20 g of antimony trioxide (Sb_2O_3) is added then 50 g of stannous chloride ($SnCl_2$) is finally added. Once the solution is made, it is always kept at room temperature. Corrosion product removal is achieved by dipping the coupons in a beaker filled with the Clarke's solution.

Clarke's solution is highly acidic and Personal Protective Equipment (PPE) such as eye protection and gloves is worn when handling the solution.

4.5.2 Determination of Equivalent Corrosion Rates

Equivalent corrosion rates in mm/year are determined by means of the mass losses in each test. The procedure for achieving such values is set out below:

1) Initial mass in grams of each specimen is recorded. To ensure accuracy, each specimen is weighed three times and an average value is calculated;
2) Specimens are then placed in the test rigs and experiment is carried out for duration of 24 hours;
3) Post testing, the samples are removed and quickly rinsed under tap water. Samples are then dipped in Clarke's solution in order to remove any residual corrosion product;
4) Samples are then re-rinsed under tap water, and dried using a Metaserv specimen dryer;

5) Samples are then re-weighed to determine test mass loss. Each sample is again reweighed three times and an average value is taken.

The total mass loss during each test is then calculated by Equation 4-1.

$$M = M_1 - M_2 \qquad \textbf{Equation 4-1}$$

Where

M_1 is the average specimen mass before the test.

M_2 is the average specimen mass after the test.

The equivalent corrosion rate in mm/year is then determined using Equation 4-2.

$$CR = \frac{3650M}{\rho A} \qquad \textbf{Equation 4-2}$$

Where

CR is the equivalent corrosion rate (mm/year

M is the total mass loss after 24 hours (g/day)

P is the material density (7.8 g/cm^3)

A is the specimen or coupon exposed surface area (cm^2)

4.5.3 Microscopy and Surface Analysis

The specimen surfaces are also analysed using a TalySurf surface profiling machine and light optical microscopy.

4.6 Electrochemical Testing

Electrochemical tests are carried out for a duration of 24 hours. The samples are analysed by means of the LPR method at interim exposures of 4 hours,15 hours and a full anodic polarisation after 24 hours exposure. The 24 hour full polarisation data is also used to plot R_p values after 24 hours. The corrosion current density after 24 hours exposure is determined by Tafel extrapolation of full anodic E/Log i curves.

The electrodes used for the corrosion monitoring are a calomel reference electrode, a platinum counter electrode and the working electrodes being the carbon steel samples in the various hydrodynamic (shear conditions). Figure 4-10 is a schematic of the electrochemical corrosion monitoring system. The potentiostat / sweep

generator varies the potential of the specimen under study in either the positive or negative direction from $E_{corr.}$

Throughout all these tests the same specimen surface preparation is carried out. The specimens are polished down to 600 grit, rinsed with tap water then degreased with methanol.

Figure 4-10

Electrochemical corrosion rate monitoring system

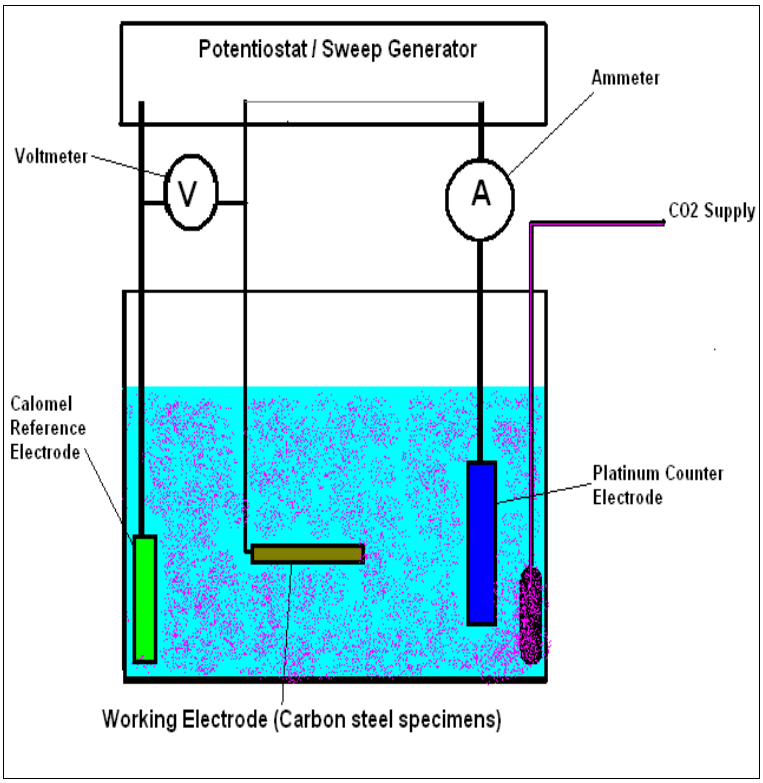

4.6.1 Linear Polarisation Resistance (LPR) Method

For the LPR method, the specimen potential is shifted by small perturbations, ΔE, of ±20 mV from E_{corr}. The resultant currents in response to the potential shift are measured by means of the ammeter. These measurements are then used to generate $\Delta E/I$ plots. The I part of the curve is the current density. The current

density is obtained by dividing the current with the specimen exposed surface area. A line of best fit of the $\Delta E/I$ plot is then used to ascertain the polarisation resistance, R_p, which is equivalent to the gradient of the plot. A detailed description of this method has already been presented in Chapter 2, section 2.6.1.3

4.6.2 Tafel Extrapolation

The Tafel extrapolation technique numerically estimates the corrosion current density. The specimen is shifted by larger perturbations of 200 mV away from E_{corr} and the current response is recorded. As the method imposes such large perturbations in potential, the method can only be used once as these shifts in potential may damage the surface of the specimen thus restricting any repetition of the scan within the same test. The Tafel method is only therefore applied once after the 24 hour exposure period. A detailed description of the method is already presented in Chapter 2, section 2.6.1.4

This project will only establish corrosion current densities by means of anodic polarisation curves. This is due to the large amount of time taken to scan 200 mV at a scan rate of 12 mV / min. At this scan rate, a total time of at least 30 mins per specimen would be required to carry out both anodic and cathodic polarisation scans. During each test, 6 scans would be required for each test rig as each test has 3 specimens. The time taken to complete such scans has been considered as too long and may introduce inconsistency through specimens developing time related variations in surface characteristics due in between scans. These variations would also be crucial in tests containing inhibitor.

Figure 4-3 shows an example of such an extrapolation. The extrapolation has been done in the Tafel region (linear region next to E_{corr}) and extrapolated back to E_{corr}. The corresponding current on the E/log I curve can then be converted to equivalent corrosion rates using Faraday's Law. A calculation for the sample extrapolation is performed below.

From Equation 2-9,

$$\frac{dm}{dt} = \frac{90x10^{-6} * 1 * 55.85}{2 * 96500} = 2.6x10^{-8}\, g/s$$

The value in g/s is then converted to g/year by multiplication with 31536000 which represents a conversion from seconds to years (60*60*24*365). In this case, this conversion would yield a loss of 0.8 g/year. This loss in g/year is L in Equation 2-10. Using Equation 2-10, the equivalent penetration rate (mm/year) is calculated as follows:

$$mm/\ year = 10\frac{0.8}{(7.8*1)} = \underline{1.0mm/\ year}$$

The density for carbon steel is 7.8 g/cm^3.

Figure 4-11

Tafel extrapolation from anodic polarisation curve

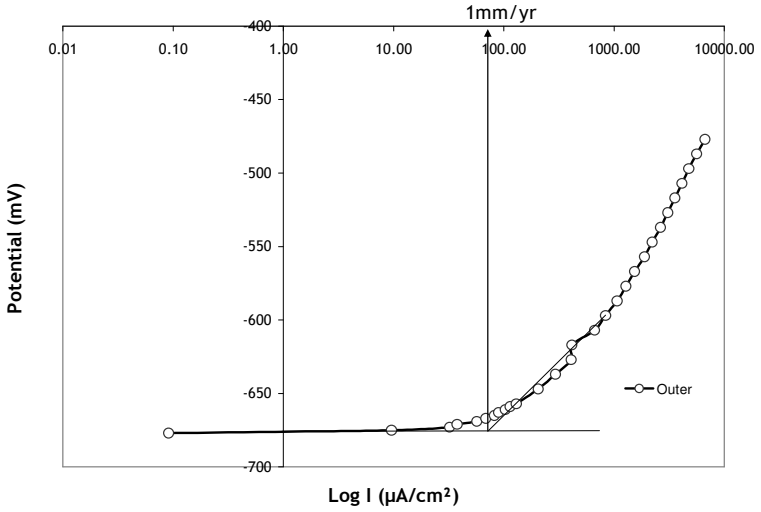

4.7 Galvanic Interactions

The galvanic interactions between hydrodynamic zones in each test are measured by a zero resistance ammeter connection (series) establishing a couple between the two specimens. The ammeter then reads the amount of negative current flowing from the more electro-negative specimen (higher Ecorr in the negative direction) to the lesser negative specimen. A connection system has also been established in order to identify

the direction in which the current flows. This connection sequence involves polarity and is shown in Figure 4-4. If the recorded current is negative then the specimen connected to the negative terminal of the ammeter is identified as the anode. If the current is positive then the specimen connected to the positive terminal of the ammeter is identified as the anode. The last schematic shows the arrangement where the outer and intermediate specimens are coupled to establish a mutual potential between the zones. This coupling is then connected to the ammeter as one connection with the galvanic current measured against the impingement specimen.

Figure 4-12

Schematics of polarity connection between hydrodynamic zones

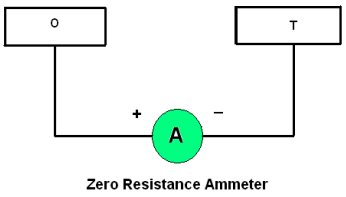

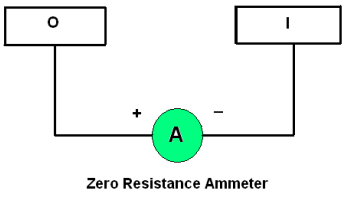

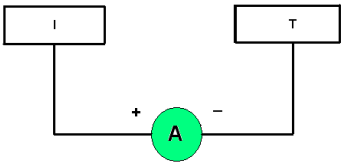

Zero Resistance Ammeter

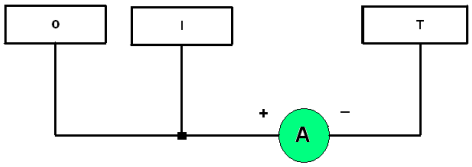

Zero Resistance Ammeter

5.0 GRAVIMETRIC INVESTIGATIONS

5.1 Introduction

Gravimetric assessments are carried out to investigate the influence of variable shear on erosion-corrosion of carbon steel in simulated oilfield environments. The conditions investigated are aerated 3.5% NaCl, CO_2 saturated NaCl, CO_2 saturated NaCl with 100 ppm, 150 ppm, 200 ppm, 1000 ppm and 1500 ppm Corr Treat 727 corrosion inhibitor. All tests are carried out in glass cells at 50^{o}C and the fluid impingement velocities are 8 m/s and 2 m/s. Corrosion rates are analysed by coupon mass loss using OHAUS AS120s electronic scales with a balance accuracy of 0.0001 g. Before each test, each coupon is polished down to 600 grit, degreased with methanol and dried using a METASERV specimen dryer. Post testing, the coupons are dipped in Clarke's solution for up to 5 minutes, rinsed with tap water and dried before reweighing. To ensure accurate mass loss determination, all coupons are weighed at least three times and an average value is taken as final. All tests are carried out for a duration of 24 hours and recording is by stopwatch. For the tests involving CO_2, the test solution is purged with CO_2 for at least 1 hour before coupon insertion. For the inhibitor tests, the coupons lie in static conditions for an hour.

The results obtained are presented in the following manner:

- Tests in aerated brines;
- Tests in CO_2 saturated brines;
- Tests in CO_2 saturated brines with 100 ppm inhibitor;
- Tests in CO_2 saturated brines with 150 ppm inhibitor;
- Tests in CO_2 saturated brines with 200 ppm inhibitor.

The equivalent mass loss is converted to a corrosion rate in mm/year through Equation 5-1

$$CR = \frac{3650W}{\rho A} \qquad \textbf{Equation 5-1}$$

Where

CR = Corrosion rate in mm/year

W = Mass loss in grams after 24 hours exposure (g/day)

ρ = Density of carbon steel (7.8 g/cm^3)

A = Coupon surface area in cm^2

Impingement Coupon (0.6249cm^2)
Intermediate Coupon (1.971cm^2)
Outer Coupon (3.4262cm^2)

5.2 Tests in Aerated 3.5% NaCl

In total, 6 tests were carried out for both rigs running at 8 m/s and 2 m/s. The mass loss is converted to a corrosion rate in mm/year through Equation 5-1. Tests in aerated conditions showed characteristically high corrosion rates with the impingement (higher shear) zones having the highest corrosion rate at both velocities.

5.2.1 Tests at 8 m/s

Table 5-1 represents the mass loss results for aerated tests done at 8 m/s flow. The results are converted to equivalent yearly loss and displayed in Figure 5-1.

Table 5-1

Results for 8 m/s flow in aerated conditions. Results show hydrodynamic zone mass losses in grams for tests at 50°C and 24 hrs.

	Impingement	Intermediate	Outer
Test 1	0.0355	0.0245	0.0448
Test 2	0.0346	0.0380	0.0507
Test 3	0.0307	0.0299	0.0413
Test 4	0.0281	0.0412	0.0494
Test 5	0.0312	0.0353	0.0498
Test 6	0.0327	0.0318	0.0454

From Figure 5-1, the impingement (higher shear) zone has the highest value of corrosion rate compared to the intermediate and outer zones respectively. The equivalent corrosion rate in the impingement zone is at least twice the value of the other two shear zones and this result indicates the influence of impinging flow in aerated conditions.

Figure 5-1

Hydrodynamic zone equivalent corrosion rates (mm/year) at 8 m/s flow in aerated 3.5 wt% brine. Test duration 24 hrs at 50°C. Zone regions indicate average shear stress values in Pascal's.

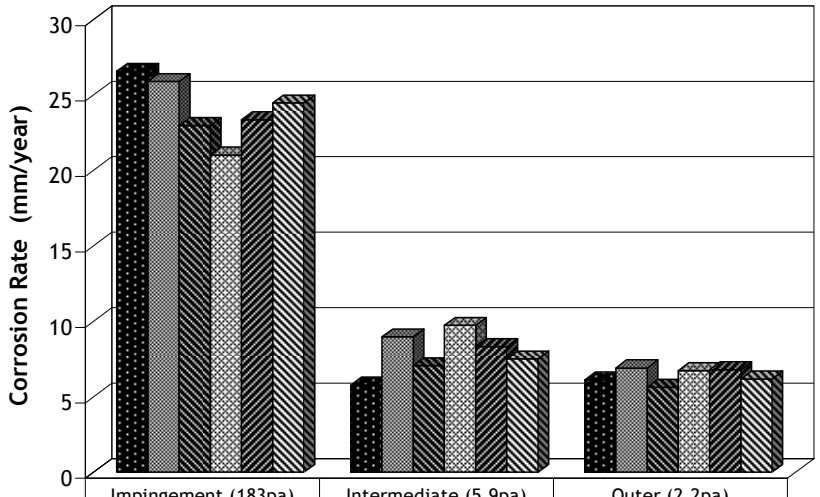

	Impingement (183pa)	Intermediate (5.9pa)	Outer (2.2pa)
Test 1	26.5832	5.7929	6.1188
Test 2	25.9092	8.9850	6.9247
Test 3	22.9888	7.0697	5.6408
Test 4	21.0419	9.7416	6.7471
Test 5	23.3633	8.3371	6.8017
Test 6	24.4865	7.5190	6.2008

Photography, microscopy and surface profiling provided additional information on corrosion damage in all three hydrodynamic zones. Figure 5-2 is a photograph of the three corroded coupons after 24 hrs at 8 m/s flow. The impingement zone specimen seems the worst affected with large pits clearly visible over the entire surface of the specimen. The intermediate and outer specimens appear to have no pitting present. Further investigation through microscopy and surface profiling indicated the severity and nature of the pits. Figure 5-3 is a microscopic image of a pit located in the impingement zone at position r≈2d. Pit depth, measured by

microscopy is 105 µm. Figure 5-4 is a microscopic image of another pit located at r≈2.5d and of depth 163 µm.

The intermediate specimens had significantly less pitting and both microscopy and surface profiling established these pits to be of less than 20 µm in depth. Figure 5-5 is a microscopic image of a pit in the intermediate specimen whose depth is 14 µm. Figure 5-6 is a similar image for the outer specimen. The recorded depth of all pits in the outer specimen is less than 10 microns.

Figures 5-7, 5-8 and 5-9 are surface profile images of the three hydrodynamic zones. The impingement specimen profile, Figure 5-7 clearly shows pitting activity of depths over 100 µm. Figures 5-8 and 5-9 for the intermediate and outer specimen show significantly less pitting activity. From Figure 5-9, it is clear the outer specimen experiences the least pitting activity with pits less than 10 µm in depth.

This result is consistent with the weight loss results and clearly signifies the amount of corrosion damage occurring mainly on the impingement specimen.

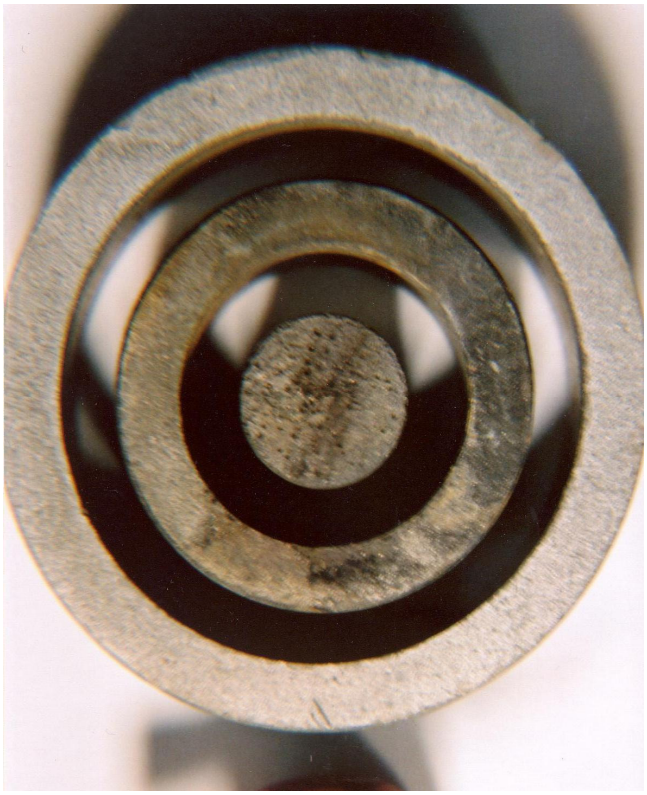

Figure 5-2. Photograph showing hydrodynamic zone specimens after 24 hrs in aerated 3.5 wt% brine at 8 m/s. Photograph shows visible pits in impingement zone (centre) specimen.

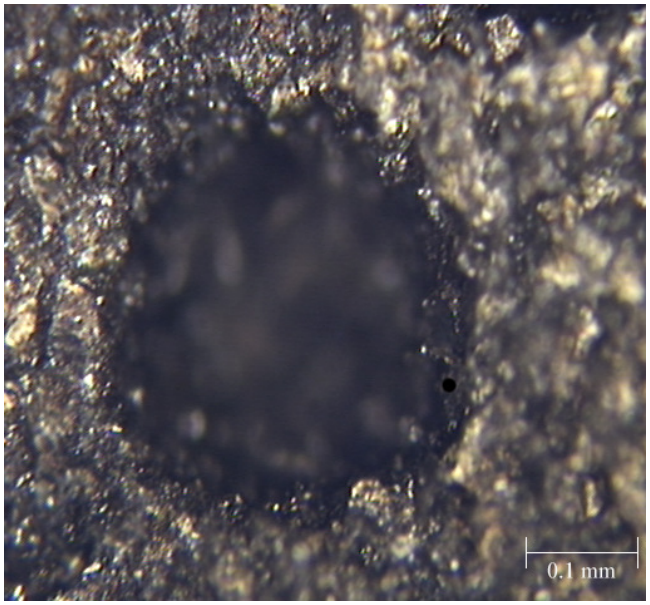

Figure 5-3. Microscopic image of pit located in impingement zone at position r≈2d. Pit depth measured as 105 µm after 24 hrs in flow at 8 m/s.

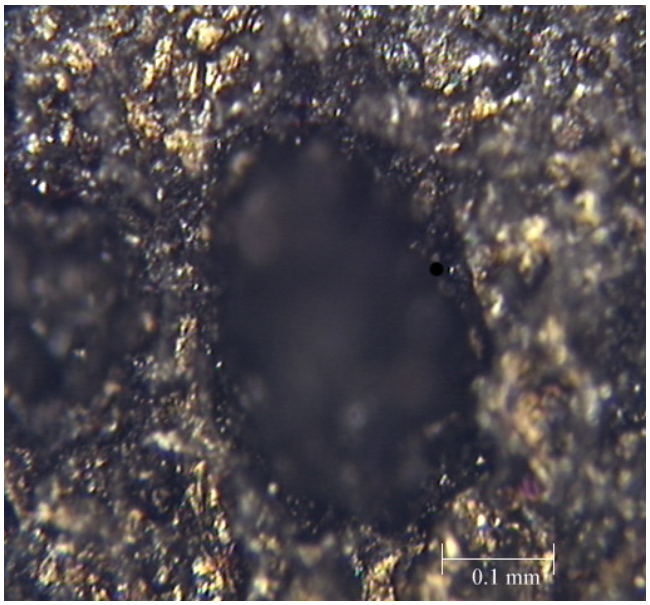

Figure 5-4. Microscopic image of pit located in impingement zone at position r≈2.5d. Pit depth measured as 163 µm after 24 hrs in flow at 8 m/s.

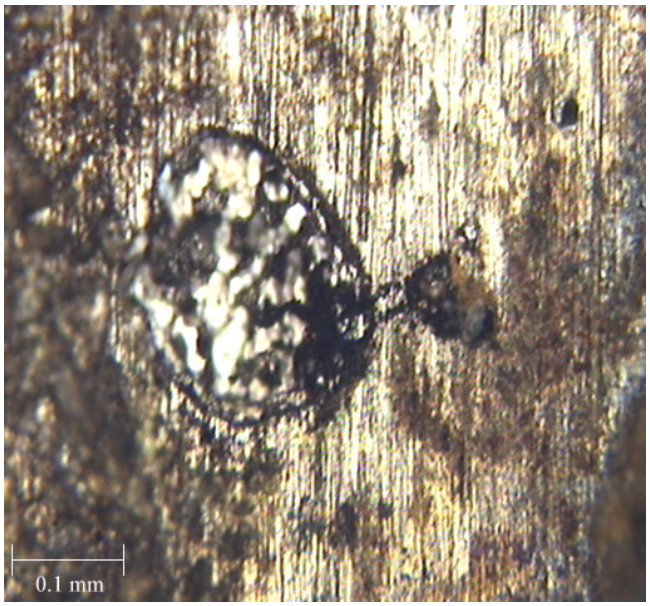

Figure 5-5. Microscopic image of pit located in intermediate zone. Pit depth measured as 14 µm after 24 hrs in flow at 8 m/s.

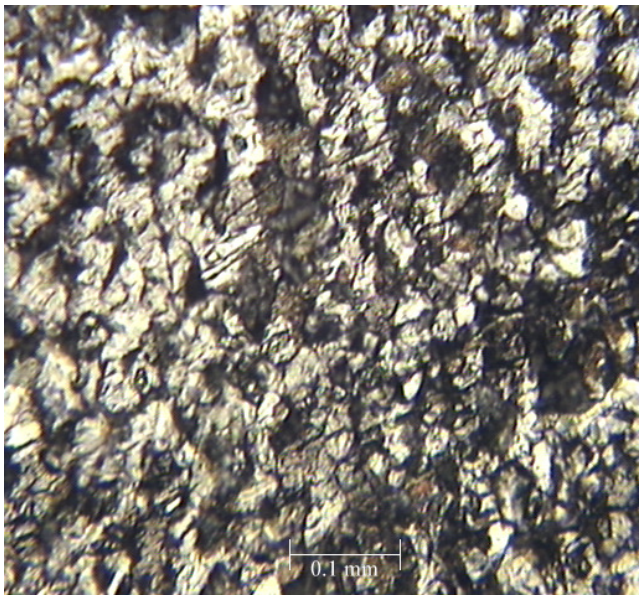

Figure 5-6. Microscopic image of small pits located in outer zone. Pit depths are measured as less than 10 µm after 24 hrs in flow at 8 m/s.

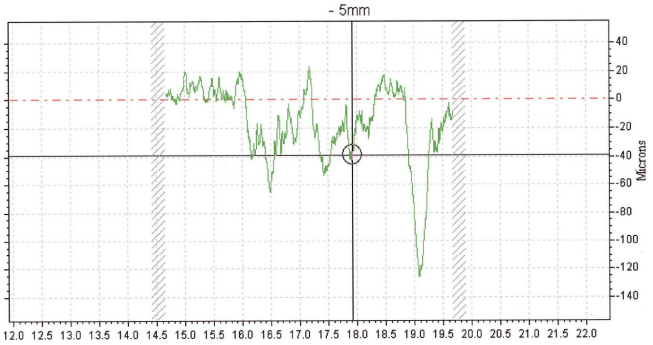

Figure 5-7. Surface profile image of impingement specimen after 24 hrs in aerated flow impinging at 8 m/s. Image shows deep Pitting along the surface. X-axis in mm and Y-axis in µm.

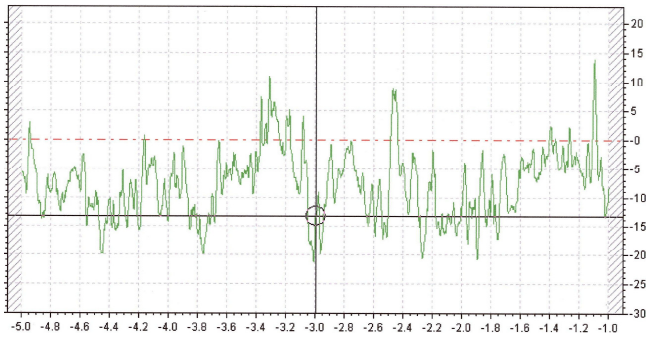

Figure 5-8. Surface profile image of intermediate specimen after 24 hrs in aerated flow at 8 m/s. X-axis in mm and Y-axis in µm.

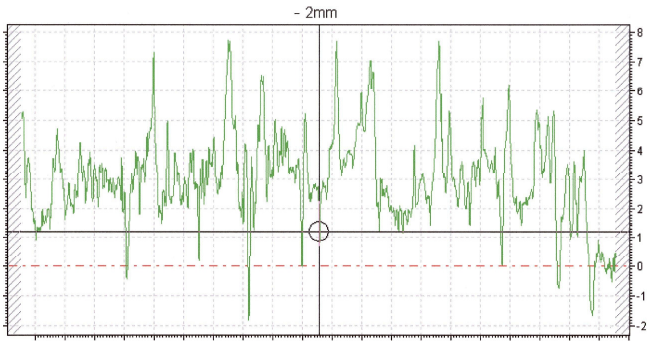

Figure 5-9. Surface profile image of outer specimen after 24 hrs in aerated flow at 8 m/s. X-axis in mm and Y-axis in µm.

5.2.2 Tests at 2 m/s

Table 5-2 represents the mass loss results for aerated tests done at 2 m/s. The results are converted to equivalent yearly loss and displayed in Figure 5-10.

Table 5-2

Results for 2 m/s flow in aerated conditions. Results show hydrodynamic zone mass losses in grams for tests at 50°C and 24 hrs.

	Impingement	Intermediate	Outer
Test 1	0.0148	0.0161	0.0272
Test 2	0.0257	0.0325	0.0437
Test 3	0.0161	0.0160	0.0255
Test 4	0.0177	0.0216	0.0267
Test 5	0.0154	0.0199	0.0256
Test 6	0.0127	0.0205	0.0305

From Figure 5-10, the impingement (higher shear) zone again has the highest value of corrosion rate compared to the intermediate and outer zones respectively. It is also worth noting that the corrosion rate in the three hydrodynamic zones is less than the respective values at 8 m/s. Although test 2 shows some scatter, the reproducibility of the other tests is good.

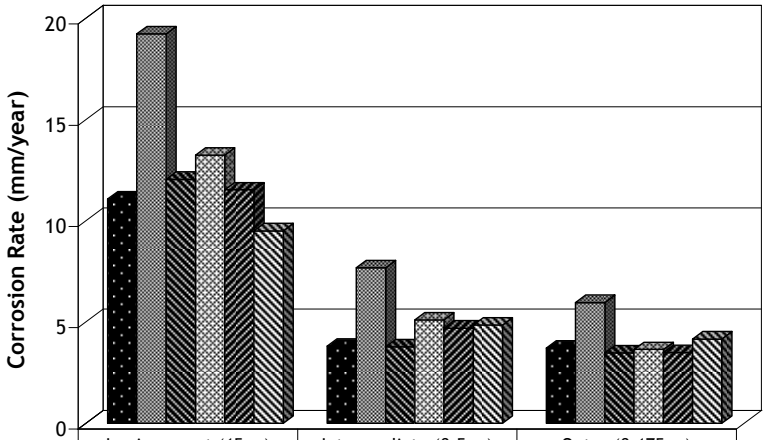

	Impingement (15pa)	Intermediate (0.5pa)	Outer (0.175pa)
Test 1	11.083	3.807	3.715
Test 2	19.245	7.685	5.969
Test 3	12.056	3.783	3.483
Test 4	13.254	5.107	3.647
Test 5	11.532	4.705	3.496
Test 6	9.510	4.847	4.166

Figure 5-10. Hydrodynamic zone equivalent corrosion rates (mm/year) at 2 m/s flow in aerated 3.5 wt% brine. Test duration 24 hrs at 50°C. Zone regions indicate average shear stress values in Pascals.

Photography, microscopy and surface profiling of specimens from the 2m/s rig (Figures 5-11 to 5-17) show less damage in comparison to specimens from the 8m/s rig.

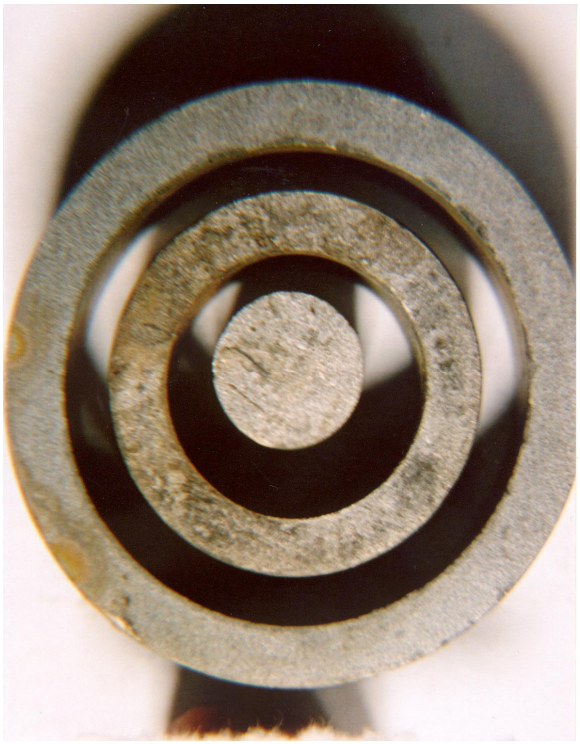

Figure 5-11. Photograph showing hydrodynamic zone specimens after 24 hrs in aerated 3.5 wt% brine at 2 m/s. Photograph shows impingement zone (centre), intermediate and outer specimen.

From Figure 5-11, the damage at 2 m/s is not visible with the naked eye. The lack of pitting damage in comparison to the experiments done at 8 m/s is again evident. Microscopy and surface profiling established the amount of pitting in the impingement (central) zone as significantly less than the damage observed at 8 m/s. Figure 5-12 is a microscopic image of a pit located in the impingement zone. The pit depth was measured as 17 μm which is less than the damage of over 100 μm for the experiments at 8 m/s. The pits observed in the 2 m/s experiments are also less wide than those at 8 m/s. From Figure 5-12, the pit is clearly less than 0.1 mm in diameter whereas the pit in the same zone in experiments at 8 m/s is nearly 0.2 mm in diameter.

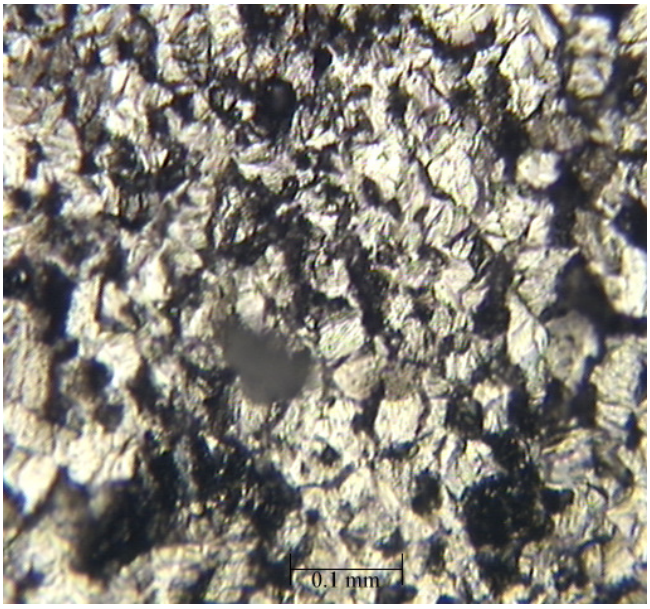

Figure 5-12. Microscopic image of pit located in impingement zone at position r≈2d. Pit depth measured as 17 µm after 24 hrs in flow at 2 m/s.

Figures 5-13 and 5-14 are microscopic images for the intermediate and outer specimens for the 2 m/s experiments. The diameter of the pits is smaller and they are of shallower depths compared to those observed in the same regions at 8 m/s. The surface profiles of all three specimens at 2 m/s are shown by Figures 5-15, 5-16 and 5-17. The surface profiles of these specimens indicate shallower and narrower pits in comparison to the experiments done at 8 m/s.

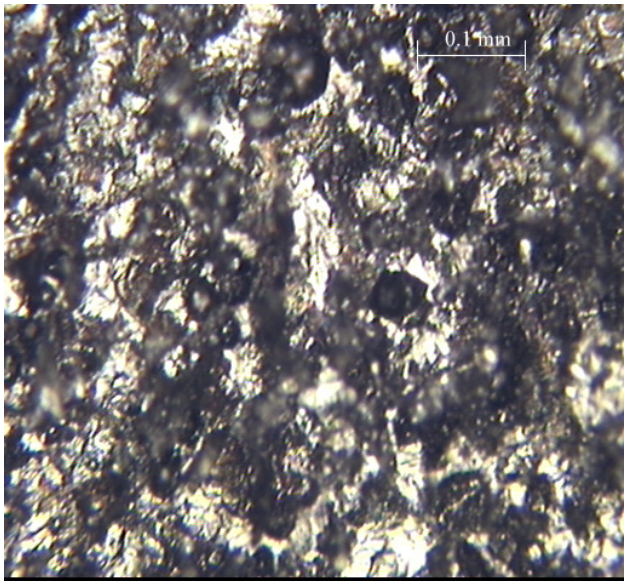

Figure 5-13. Microscopic image of pits located in intermediate zone. Average pit depths measured as 7 µm after 24 hrs in flow at 2 m/s.

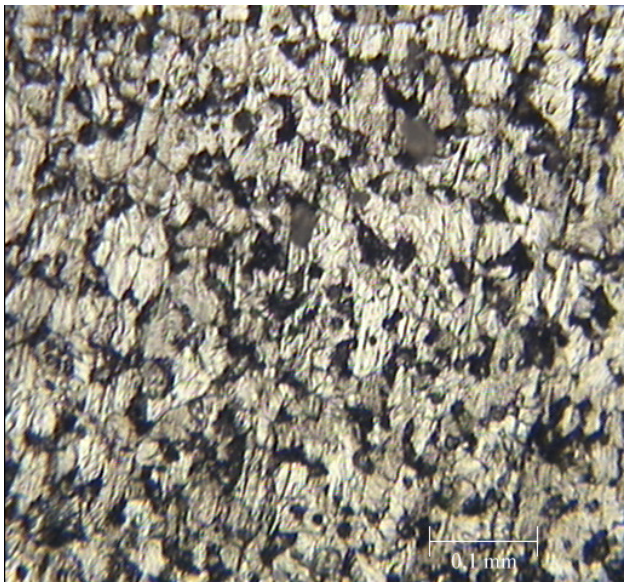

Figure 5-14. Microscopic image of pits located in outer zone. Pit depths measured as below 9 µm after 24 hrs in flow at 2 m/s.

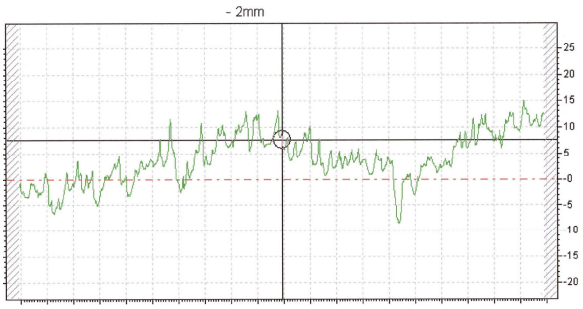

Figure 5-15. Surface profile image of impingement specimen after 24 hrs in aerated flow at 2 m/s. X-axis in mm and Y-axis in µm.

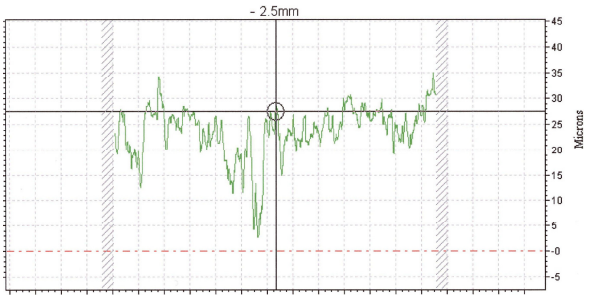

Figure 5-16. Surface profile image of intermediate specimen after 24 hrs in aerated flow at 2 m/s. X-axis in mm and Y-axis in µm.

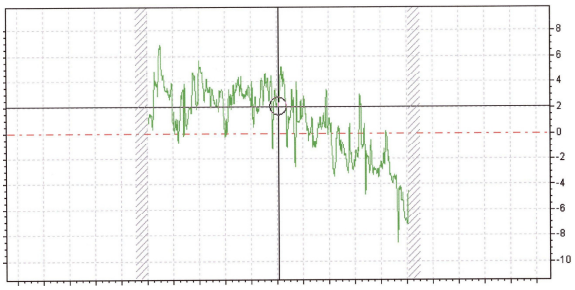

Figure 5-17. Surface profile image of outer specimen after 24 hrs in aerated flow at 2 m/s. X-axis in mm and Y-axis in µm.

From Figure 5-18, the gravimetric tests in aerated conditions show that in all three hydrodynamic zones, the average corrosion rate calculated from all 6 tests is always higher for the 8 m/s tests compared to the 2m/s. At both velocities, the impingement conditions produce the highest corrosion rate. The intermediate and outer conditions follow with the later conditions producing the lowest corrosion rate.

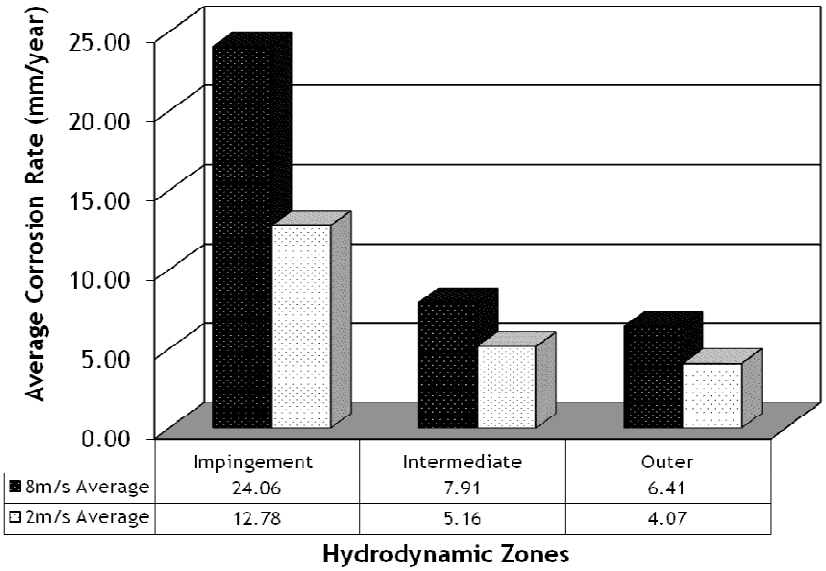

Figure 5-18. Average corrosion rates for experiments at 8m/s and 2m/s. Figure shows the corresponding average corrosion rates obtained in the three hydrodynamic conditions.

Figure 5-18 also indicates the high influence of the impingement conditions. The corrosion rate in the impingement conditions is substantially higher than the intermediate and outer respectively. Microscopy and surface profiling has indicated pitting activity in aerated flow with the impingement zones experiencing the worst pitting. The pitting activity also appears to be velocity dependent with larger and deeper pits occurring mainly in specimens at the higher velocity (8m/s).

5.3 Tests in CO_2 saturated 3.5% NaCl

The results of tests in CO_2 saturated 3.5 wt% brine are presented below. The tests are carried out at 50°C for a period of 24 hours. To facilitate reliable comparisons between hydrodynamic zones, numerous tests have been carried out to establish reproducibility at 8 m/s and 2 m/s. Measured mass losses are converted to a corrosion rate in mm/year using Equation 5-1. Before the flow is started, the specimens are left in static conditions while the fluid is purged with CO_2. For all tests, the specimens were left in static conditions for an hour. This allowed sufficient de-aeration of the test brines and also allowed any films to form evenly across all three specimens.

5.3.1 Tests at 8 m/s

Table 5-3 shows the mass loss readings for all three zones and in total, 7 tests were carried out to facilitate reliable comparisons between the three hydrodynamic zones.

Table 5-3

Results for 8 m/s flow in CO_2 saturated conditions. Results show hydrodynamic zone weight losses in grams and pH for tests at 50°C and 24 hrs.

	Impingement	Intermediate	Outer	pH
Test 1	0.0105	0.0600	0.0227	5.2
Test 2	0.0123	0.0523	0.0285	5.5
Test 3	0.0145	0.0638	0.0367	5.3
Test 4	0.0112	0.0567	0.0271	5.6
Test 5	0.0126	0.0587	0.0229	5.2
Test 6	0.0098	0.0450	0.0225	5.4
Test 7	0.0121	0.0460	0.0285	5.7

Figure 5-19 shows the weight loss values converted into equivalent yearly corrosion rates using Equation 5-1. From Figure 5-19, the impingement zone no longer has the highest corrosion rate. The intermediate zone surprisingly has the highest corrosion rate followed by the impingement and outer specimens respectively. In all 7 experiments, the outer specimen has the lowest corrosion rate with the intermediate the highest. It is also worth noting that the corrosion rate in the intermediate zone is higher than in aerated conditions but in the other two regions (impingement and outer), the rate is lower than in aerated water.

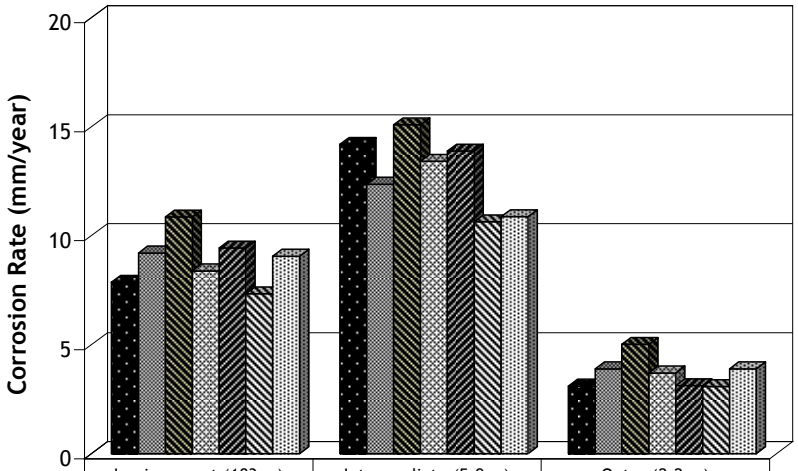

	Impingement (183pa)	Intermediate (5.9pa)	Outer (2.2pa)
Test 1	7.8626	14.1868	3.1004
Test 2	9.2105	12.3661	3.8926
Test 3	10.8579	15.0853	5.0125
Test 4	8.3868	13.4065	3.7013
Test 5	9.4352	13.8794	3.1277
Test 6	7.339	10.640	3.073
Test 7	9.061	10.877	3.893

Figure 5-19. Hydrodynamic zone equivalent corrosion rates (mm/year) at 8 m/s flow in CO_2 saturated 3.5 wt% brine. Test duration 24 hrs at 50°C. Zone regions indicate average shear stress values in Pascal's.

Figure 5-20 is a photograph of all three specimens after 24 hours in CO_2 saturated flow at 8 m/s. The photograph is taken before the specimens are dipped in Clarke's solution and reweighed. The photo shows a film formation on the surface of all three specimens and no initial pits are present as observed in the aerated tests (Figure 5-2) at similar velocity and shear.

Figure 5-20. Photograph showing hydrodynamic zone specimens after 24 hrs in CO_2 saturated 3.5 wt% brine at 8 m/s. Photograph shows film formation in all three zones.

On closer microscopic investigation of the central specimen, a thick film was observed just outside the stagnation zone (r/d≈1.2) of the jet. The film thickness was consistent and covered the entire remainder of the specimen surface. Figure 5-21 shows the film formed just outside the stagnation zone of the jet and Figure 5-22 shows this film further located from the stagnation zone but with a pit formed on the surface. The pit depth was measured as 32 μm.

The surface profile of the impingement specimen, Figure 5-23 shows a flat surface with spaced out pits.

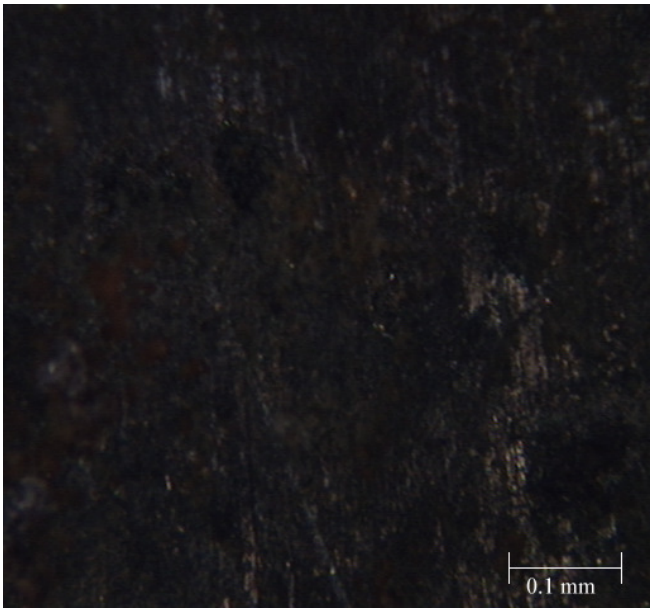

Figure 5-21. Microscopic image of impingement zone heavy film located just outside the stagnation zone. Film extended throughout the remainder of the specimen. Test conditions are 8m/s CO_2 saturated brine.

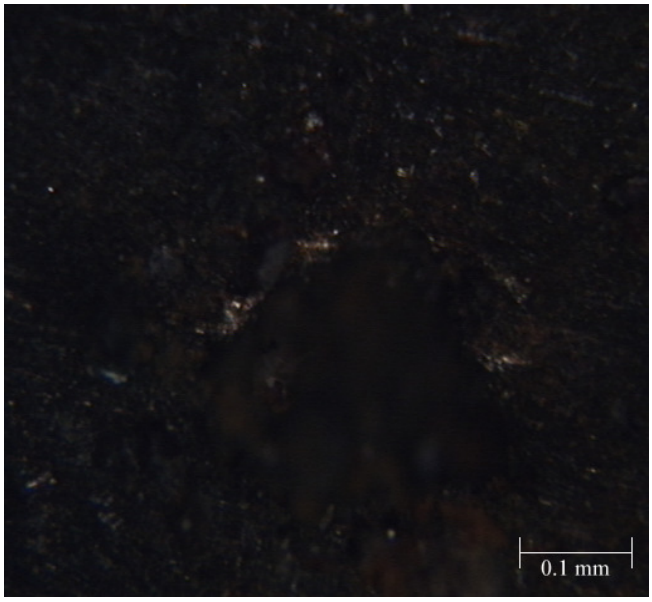

Figure 5-22. Microscopic image of heavy film and pit located further outside the stagnation zone of the impingement specimen. Test conditions are 8m/s CO_2 saturated brine.

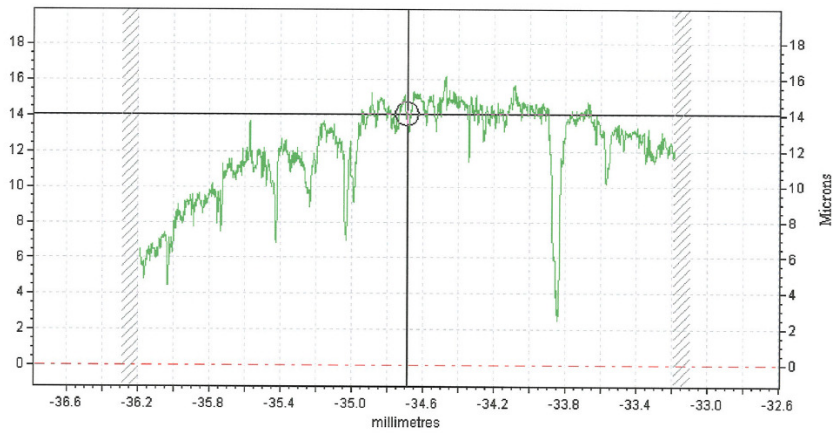

Figure 5-23. Surface profile image of impingement specimen after 24 hrs in CO_2 saturated flow impinging at 8 m/s. X-axis in mm and Y-axis in µm.

The Intermediate specimen microscopy showed a patchy film towards the inner diameter (left of picture) of the specimen. Figure 5-24 shows the exposed metal (to the left) and a film forming away from the internal diameter. The further distance moved away from the internal diameter the thicker the film became as shown in Figure 5-25.

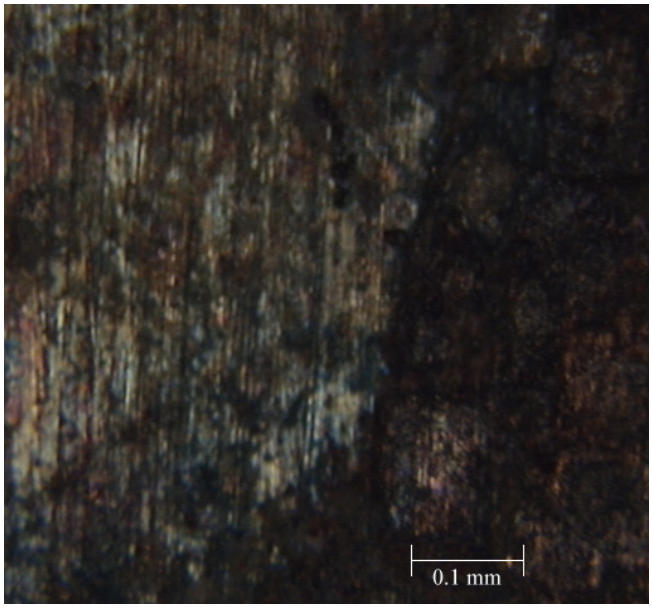

Figure 5-24. Microscopic image of patchy film in the intermediate zone. Test conditions are 8m/s CO_2 saturated brine.

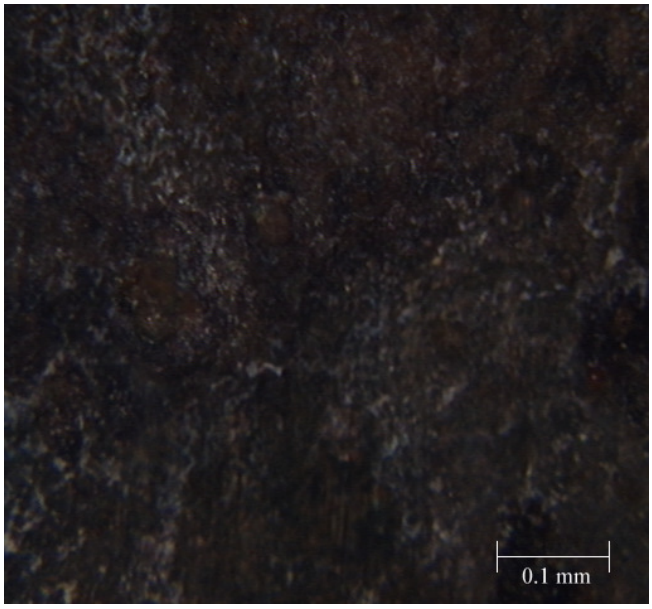

Figure 5-25. Microscopic image of dense thick film in the intermediate zone. Test conditions are 8m/s CO_2 saturated brine. Film thickened with radial distance away from specimen internal diameter (left of picture)

The outer specimen predominantly showed a heavy intense film as shown in Figure 5-26 although some smaller regions, Figure 5-27 indicated zones of bare metal and small shallow pits surrounding the bare metal islands.

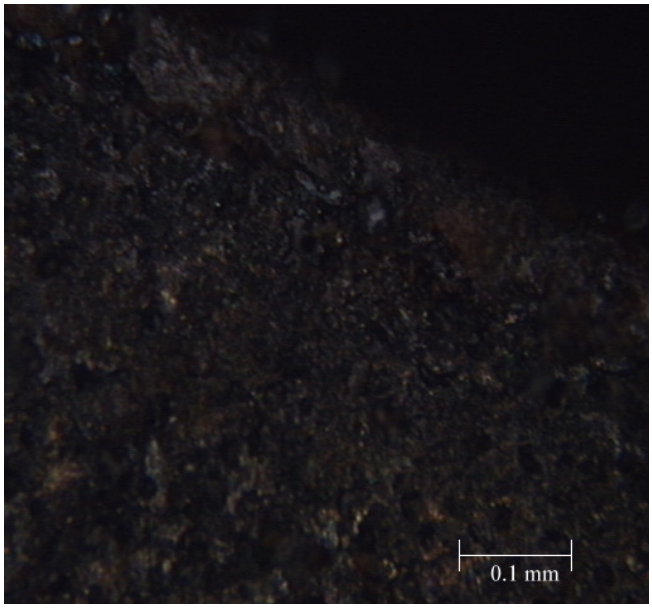

Figure 5-26. Microscopic image of dense thick film in the outer zone. Test conditions are 8m/s CO_2 saturated brine. Film thickness was mainly consistent with radial distance from internal diameter

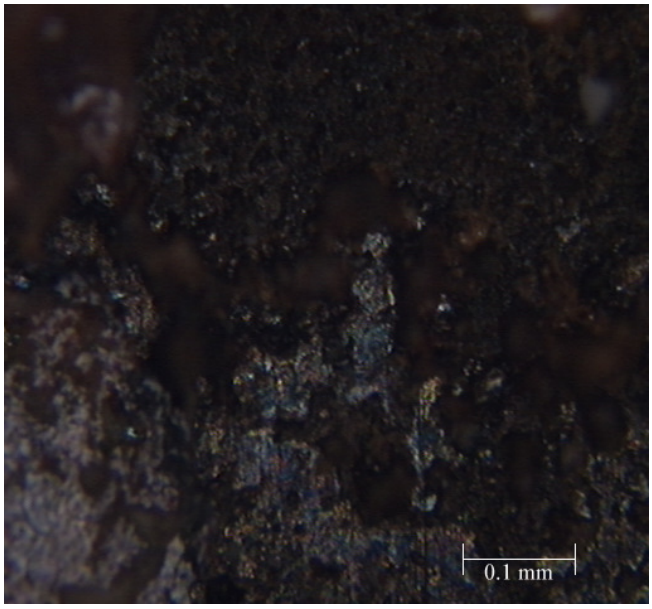

Figure 5-27. Microscopic image of patchy film with islands of bare metal and pits in the outer zone. Test conditions are 8m/s CO_2 saturated brine.

The surface profiles for the intermediate and outer specimens are presented below by Figures 5-28 and 5-29. The profiles display a rough surface possibly reflecting the presence of a patchy film and pits.

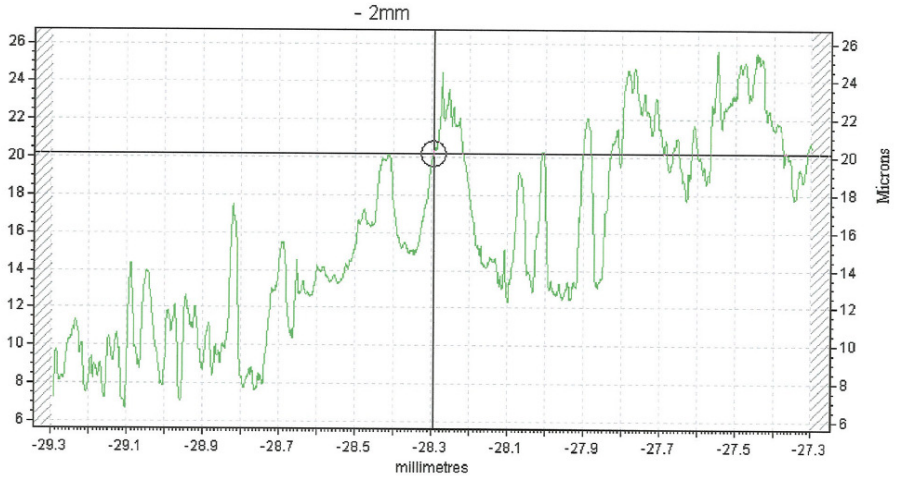

Figure 5-28. Surface profile image of intermediate specimen after 24 hrs in CO_2 saturated flow at 8 m/s. X-axis in mm and Y-axis in µm.

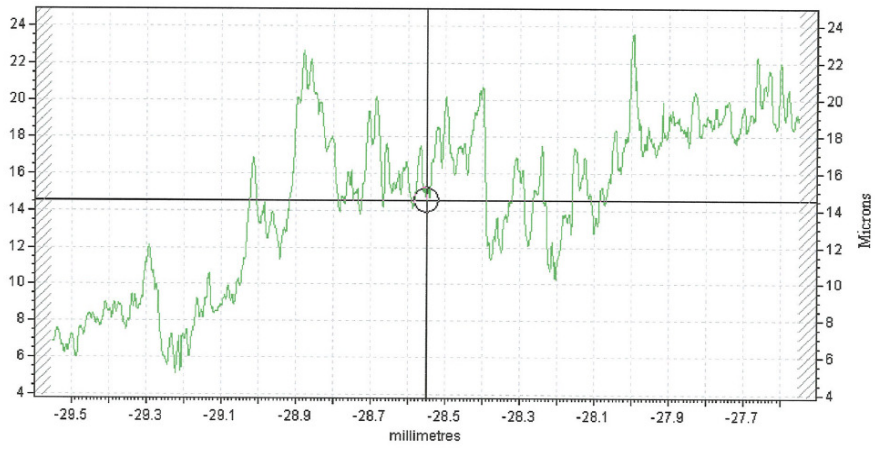

Figure 5-29. Surface profile image of outer specimen after 24 hrs in CO_2 saturated flow at 8 m/s. X-axis in mm and Y-axis in µm.

5.3.2 Tests at 2m/s

The scatter between experiments at the lower velocity was such as to make distinctions between the three hydrodynamic zones not clear cut. The CO_2 experiments carried out at 2m/s show reproducibility with a large scatter. In total, 8 tests were carried out and in the majority of experiments, the intermediate specimen showed the highest corrosion rate as shown in Figure 5-30. The last two experiments however show the impingement specimen as having higher corrosion rates than the intermediate and outer. In all tests except test 4, the outer zone has the lowest corrosion rate.

Table 5-4

Results for 2 m/s flow in CO_2 saturated conditions. Results show hydrodynamic zone mass losses in grams for tests at 50°C and 24 hrs.

	Impingement	Intermediate	Outer	pH
Test 1	0.0070	0.0310	0.0387	5.8
Test 2	0.0082	0.0326	0.0345	5.1
Test 3	0.0092	0.0380	0.0362	5.3
Test 4	0.0086	0.0415	0.0474	5.4
Test 5	0.0087	0.0315	0.0430	5.2
Test 6	0.0075	0.0255	0.0327	5.6
Test 7	0.0096	0.0190	0.0360	5.5
Test 8	0.0104	0.0230	0.0266	5.3

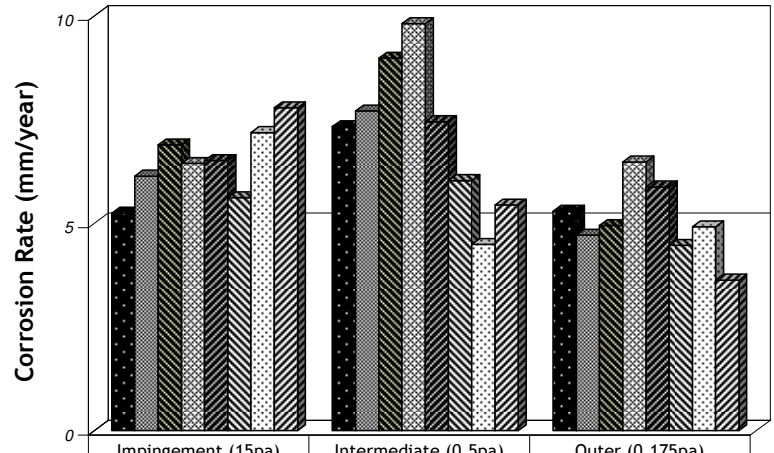

	Impingement (15pa)	Intermediate (0.5pa)	Outer (0.175pa)
Test 1	5.242	7.330	5.286
Test 2	6.140	7.708	4.712
Test 3	6.889	8.985	4.944
Test 4	6.440	9.813	6.474
Test 5	6.515	7.448	5.873
Test 6	5.616	6.029	4.466
Test 7	7.189	4.493	4.917
Test 8	7.788	5.438	3.633

Figure 5-30. Hydrodynamic zone equivalent corrosion rates (mm/year) at 2 m/s flow in CO_2 saturated 3.5 wt% brine. Test duration 24 hrs at 50°C. Zone regions indicate average shear stress values in Pascal's.

Figure 5-31 is a photograph of all three specimens after 24 hours in CO_2 saturated flow at 2 m/s. The photograph is taken before the specimens are dipped in Clarke's solution and reweighed. From the picture, it is clear that heavy films have formed on the surfaces of all three specimens and there is no indication of any pit formation. The film in the impingement (centre) specimen seems to have two distinct regions, one surrounding the stagnation zone and forming a figure eight-like figure and another region surrounding the figure eight-like figure.

The intermediate and outer specimens seem to have thicker films but closer inspection reveals a patchy nature. The outer specimen especially has large amounts of material surface that seems to have patchy films.

Figure 5-31. Photograph of impingement (centre), intermediate and outer specimens after 24 hours impingement with CO_2 saturated brine at 2m/s. Photograph also shows patchy film in intermediate and outer specimens.

The microscopic investigation of the impingement specimen shows a thick consistent film formed outside the stagnation zone. Although small pits are regularly visible, the film generally has no patches. Figure 5-32 shows the thick film just

outside the stagnation zone and Figure 5-33 shows the continued thickness and consistency of the film with distance increasing away from the stagnation zone.

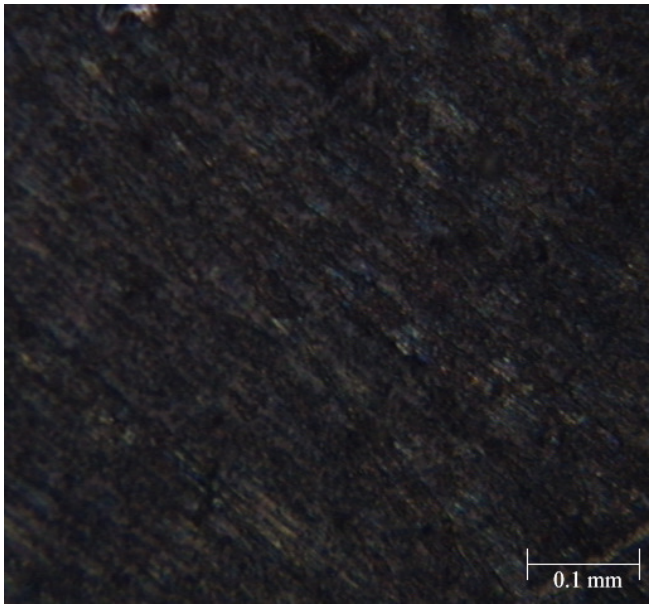

Figure 5-32. Microscopic image of thick film outside the stagnation zone of the impingement specimen. Test conditions are 2m/s CO_2 saturated brine.

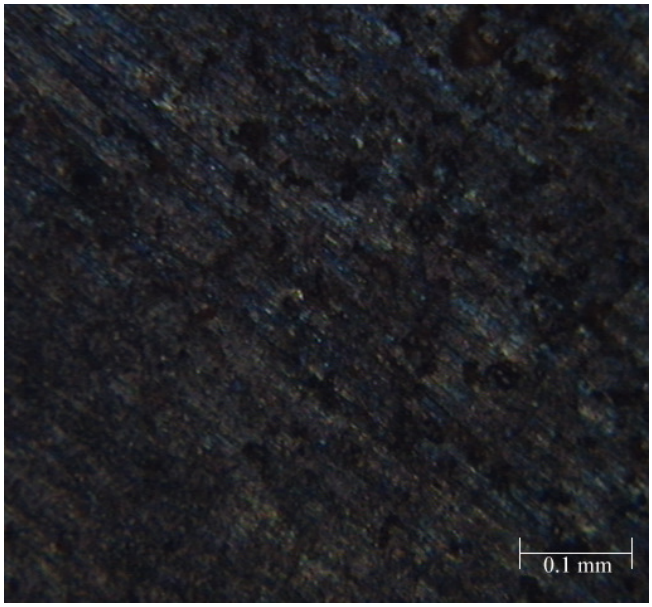

Figure 5-33. Microscopic image of continued thick film outside the stagnation zone of the impingement specimen. Test conditions are 2m/s CO_2 saturated brine.

The surface profile of the impingement specimen is shown by Figure 5-34. There appears to be lots of small pits on the specimen surface but the depth seems to be no more than 10 µm.

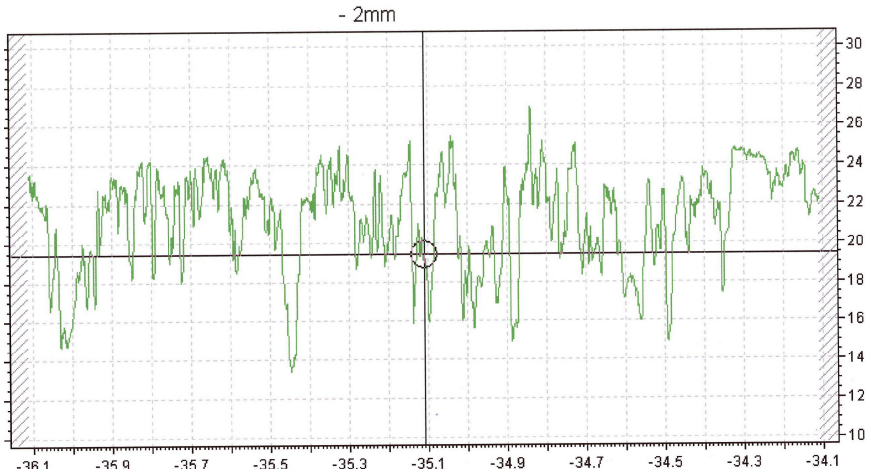

Figure 5-34. Surface profile image of impingement specimen after 24 hrs in CO_2 saturated flow at 2 m/s. X-axis in mm and Y-axis in µm.

The intermediate and outer specimen microscopy, Figure 5-35 and Figure 5-36 show a film with a streaky patch (Figure 5-35) and a very thin film with patches of exposed metal (Figure 5-36).

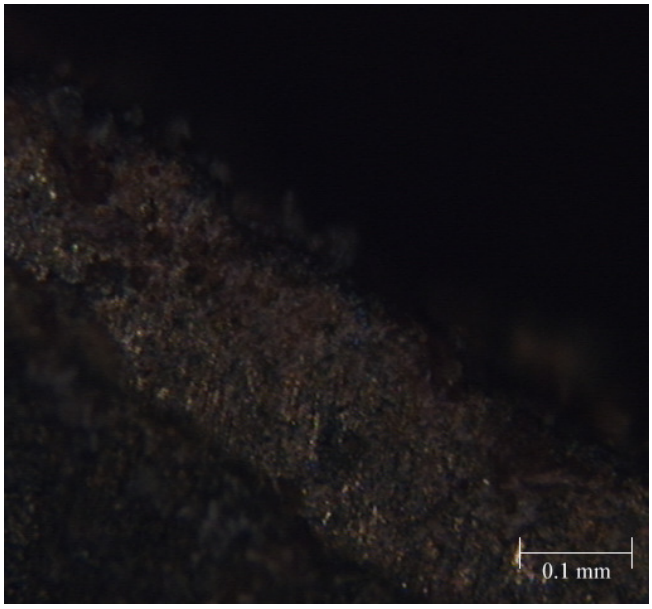

Figure 5-35. Microscopic image of film with large streaky patch away from the internal edge of the intermediate specimen. Test conditions are 2m/s CO_2 saturated brine.

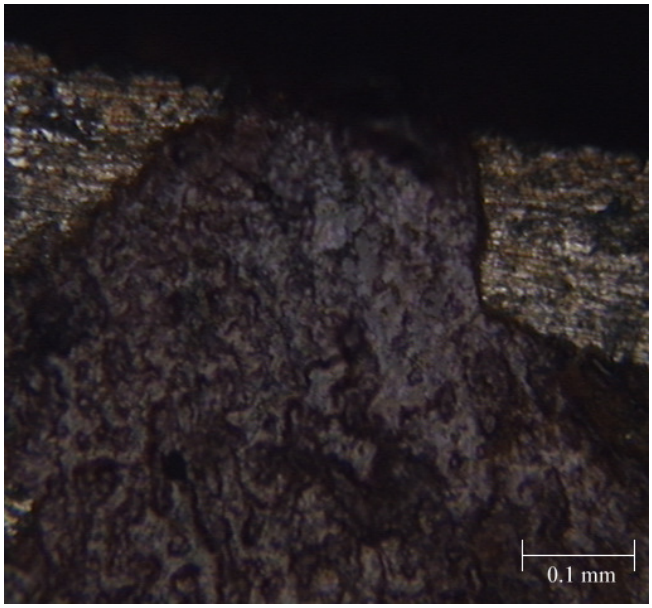

Figure 5-36. Microscopic image of thin film with patches of bare metal away from the internal edge of the outer specimen. Test conditions are 2m/s CO_2 saturated brine.

The surface profiles of the intermediate and outer specimens show a significant reduction in pitting. The intermediate surface profile (Figure 5-37), appears to indicate a film on the surface and the only possible pit is of depth less than 10 µm.

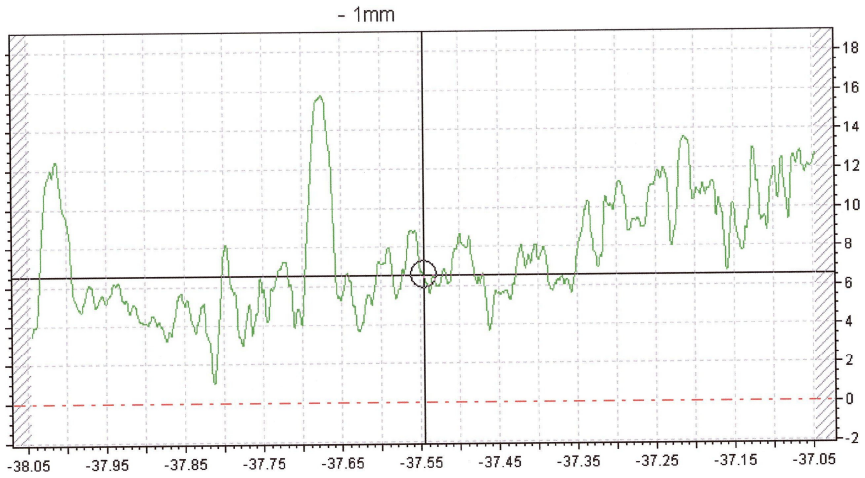

Figure 5-37. Surface profile image of intermediate specimen after 24 hrs in CO_2 saturated flow at 2 m/s. X-axis in mm and Y-axis in µm.

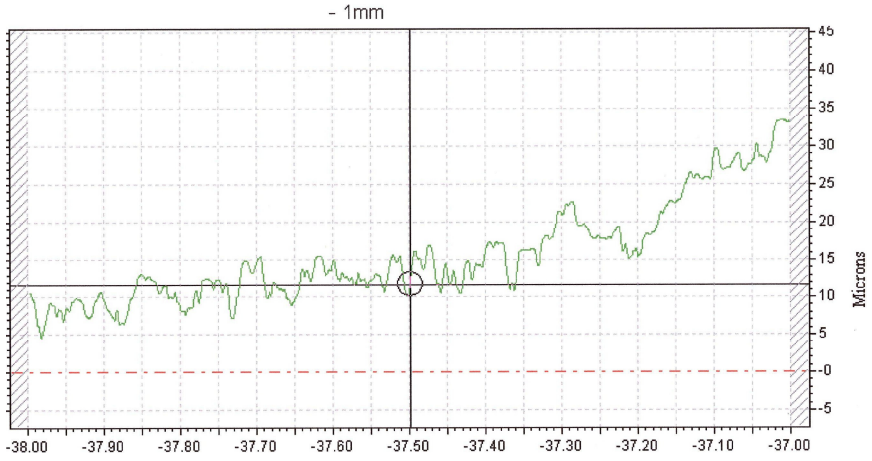

Figure 5-38. Surface profile image of outer specimen after 24 hrs in CO_2 saturated flow at 2 m/s. X-axis in mm and Y-axis in µm.

Figure 5-38 represents the surface profile for the outer specimen. From the image it is clear that the surface has no significant pitting.

To summarise, the hydrodynamic zones studied are impingement zone, intermediate (wall jet zone) and outer (wall jet zone). The average mass loss results for the two velocities in CO_2 saturated water, expressed as equivalent corrosion rates are presented in Figure 5-39.

From Figure 5-39, the intermediate zone experiences the highest average corrosion rate at both velocities. Again, the outer specimen experiences the lowest average corrosion rates although the average result for the 2 m/s outer zone is higher than the 8 m/s outer zone. This is an unexpected result and could be linked to the formation of protective corrosion product films. The presence of films in CO_2 has also been confirmed by microscopy.

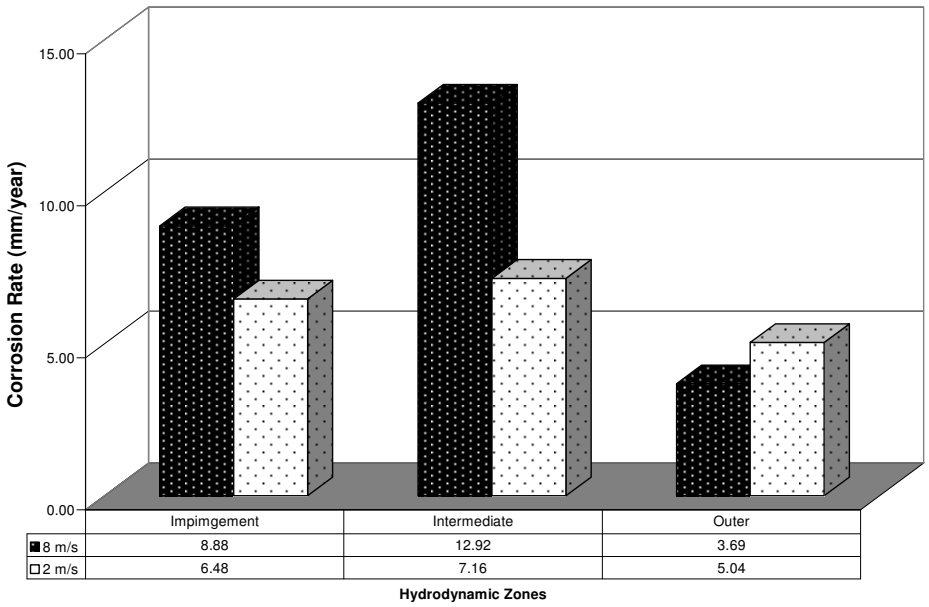

Figure 5-39 Average corrosion rates for 8m/s and 2m/s tests in CO_2 saturated brine at 50°C.

5.4 Tests with 100 ppm inhibitor

The previous section of this chapter established the corrosion behaviour of carbon steel in CO_2 containing environments and established corrosion data for specimens under different hydrodynamic conditions signified by shear stress.

This section of the chapter investigates the effect of the inhibitor addition on corrosion rates and assesses the inhibitor effectiveness in the different hydrodynamic zones and shear stresses.

5.4.1 Tests at 8 m/s

A concentration of 100 ppm inhibitor is used to establish the corrosion rate and corrosion behaviour of the three hydrodynamic zones. Table 5-5 shows the weight loss results of the tests.

Table 5.5

Results for 8 m/s flow in CO_2 saturated conditions with 100ppm inhibitor. Results show hydrodynamic zone weight losses in grams for tests at 50°C and 24 hrs.

	Impingement	Intermediate	Outer	pH
Test 1	0.0061	0.0053	0.0070	5.7
Test 2	0.0082	0.0058	0.0085	5.8
Test 3	0.0050	0.0053	0.0086	5.5
Test 4	0.0060	0.0049	0.0075	5.9

Figure 5-40 shows the results converted to equivalent corrosion rates. Firstly, the corrosion rate of all three hydrodynamic zones has decreased in comparison to the results in CO_2 saturated brine. The impingement (higher shear) zone still experiences the highest amount of corrosion followed by the intermediate and outer zone respectively. The next point to note is that the intermediate zone, which had the highest corrosion rate in CO_2 saturated brines, without inhibitor, seems to have benefited best from inhibitor addition. The intermediate and outer zones seem to have similar corrosion rates though the value of average shear stress in each zone is different. The higher shear conditions in the impingement zone seem to be restricting somewhat the rate at which the inhibitor protective layer

forms as the average corrosion rate is 3 times larger than the corrosion rate of the other two zones. It is however noted that though the average shear value in the impingement zone is much larger than the other two zones, the difference in corrosion rates is less than 5.

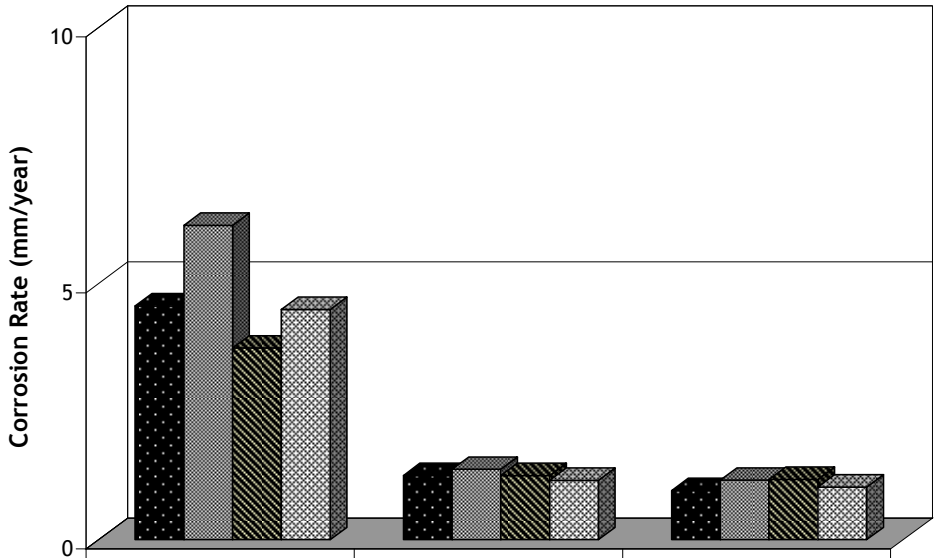

	Impingement (183pa)	Intermediate (5.9pa)	Outer (2.2pa)
Test 1	4.568	1.253	0.956
Test 2	6.140	1.371	1.161
Test 3	3.744	1.253	1.175
Test 4	4.493	1.159	1.024

Figure 5-40. Hydrodynamic zone equivalent yearly corrosion rates at 8 m/s flow in CO_2 saturated 3.5 wt% brine with 100 ppm inhibitor. Test duration 24 hrs at 50°C. Zone regions indicate average shear values in Pascal's.

Microscopic examination gives an insight into the inhibitor film characteristics. The observations in the impingement zone (Figure 5-41) show a thick pink inhibitor film with very small voids of exposed metal. Intermediate zone observations (Figure 5-42) also confirm this inhibitor film over the entire surface. The image is at a lower magnification but clearly shows over the majority of the metal surface covered by the inhibitor film. Outer zone observations (Figure 5-43) reveal patchy inhibitor coverage with small shallow pits present over the specimen surface.

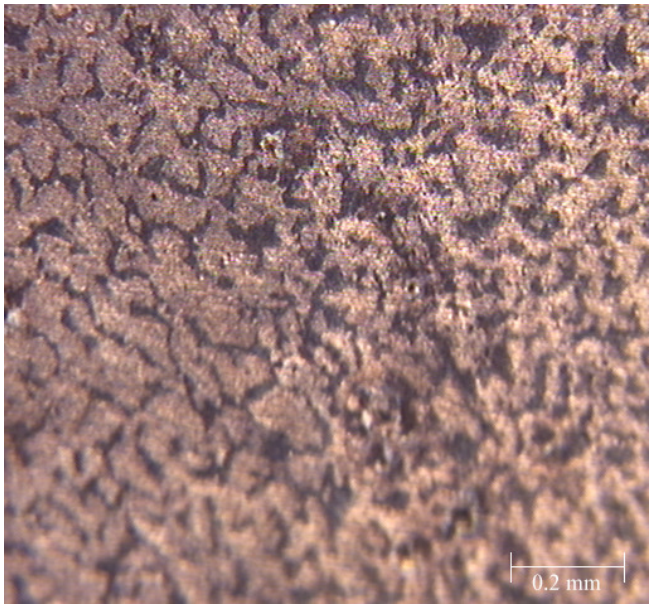

Figure 5-41 Microscopic image of impingement specimen after 24 hours in experiments with 100 ppm inhibitor and 8m/s flow.

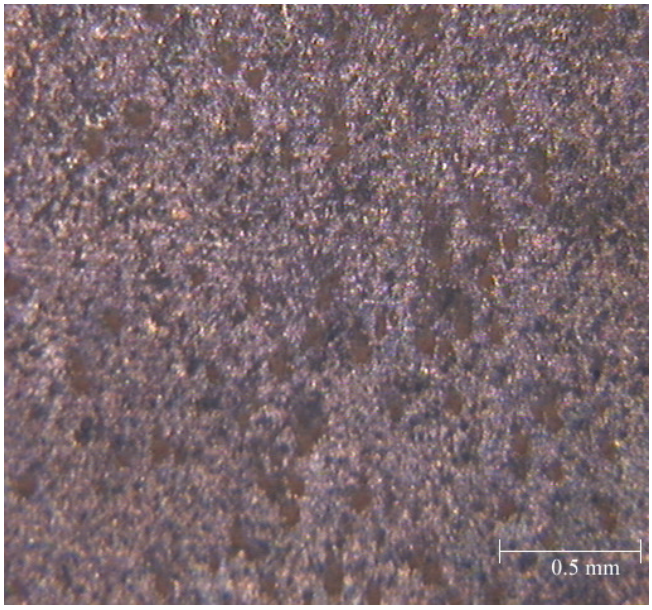

Figure 5-42. Microscopic image of intermediate specimen after 24 hours in experiments with 100 ppm inhibitor.

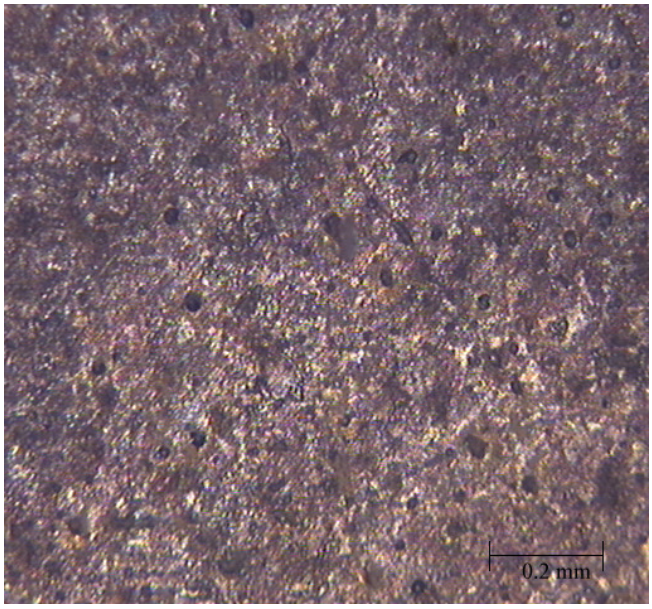

Figure 5-43. Microscopic image of outer specimen after 24 hours in experiments with 100 ppm inhibitor.

5.4.2 Tests at 2 m/s

Table 5-5 shows the respective weight losses in each hydrodynamic zone at the lower velocity of 2 m/s. Figure 5-44 shows the equivalent corrosion rates in each hydrodynamic zone. On comparison with results at 8 m/s, the impingement and outer zones have lower corrosion rates at 2 m/s compared to 8 m/s. The intermediate zone seems somewhat unchanged compared to results at 8 m/s. Considering the large reduction in shear stress, the reduction in corrosion rate seems modest and may suggest a complex relation between shear stress and inhibitor effectiveness. Further discussion and analysis of this subject will be made in Chapter 8.

Table 5-5

Results for 2 m/s flow in CO_2 saturated conditions with 100 ppm. Results show hydrodynamic zone weight losses in grams at 50°C and 24 hrs

	Impingement	Intermediate	Outer	pH
Test 1	0.0053	0.0068	0.0050	5.6
Test 2	0.0065	0.0063	0.0054	5.8
Test 3	0.0027	0.0047	0.0046	5.4
Test 4	0.0042	0.0057	0.0058	5.6

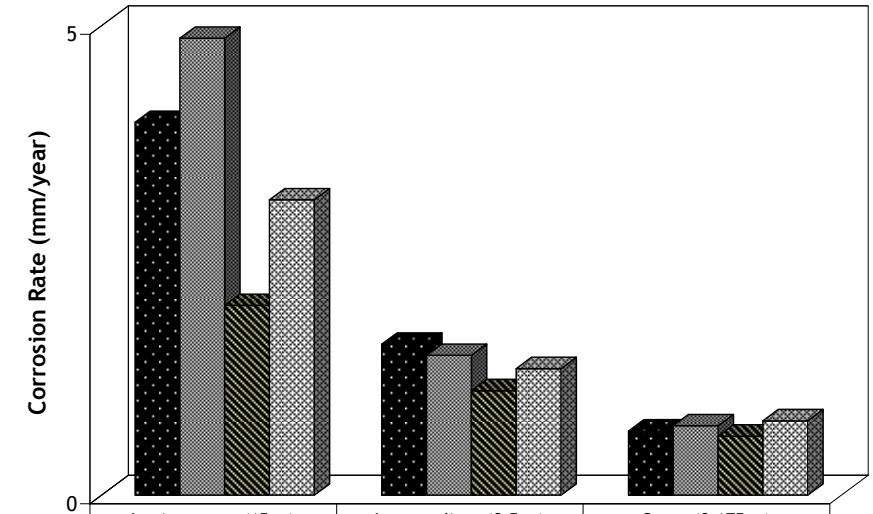

	Impingement (15pa)	Intermediate (0.5pa)	Outer (0.175pa)
Test 1	3.969	1.608	0.683
Test 2	4.867	1.490	0.738
Test 3	2.022	1.111	0.628
Test 4	3.145	1.348	0.792

Figure 5-44. Hydrodynamic zone equivalent yearly corrosion rates at 2 m/s flow in CO_2 saturated 3.5 wt% brine with 100 ppm inhibitor. Test duration 24 hrs at 50°C. Zone regions indicate average shear values in Pascal's.

Microscopic investigation revealed similar observations to the tests at 8 m/s. Figure 5-45 shows the pink appearing inhibitor film in the impingement zone. Figure 5-46 shows the outer zone specimen with again pits visible on the surface. The pits however seem shallower compared to those seen at 8 m/s

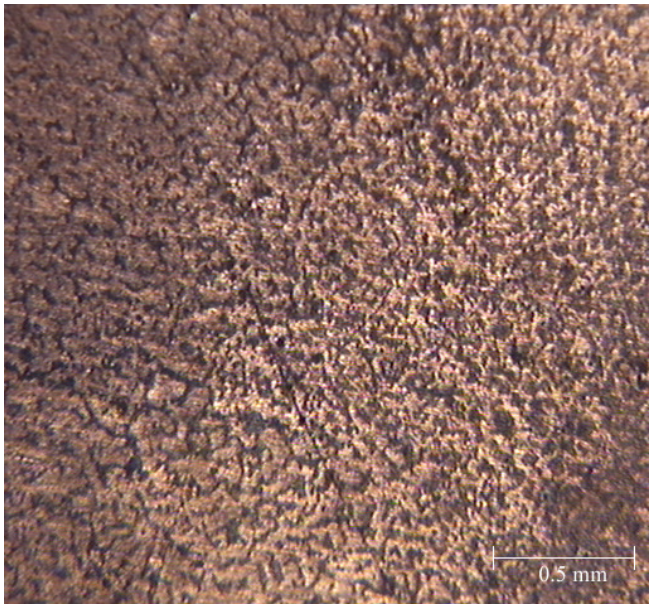

Figure 5-45. Microscopic image of impingement specimen after 24 hours in experiments with 100 ppm inhibitor and 2m/s flow

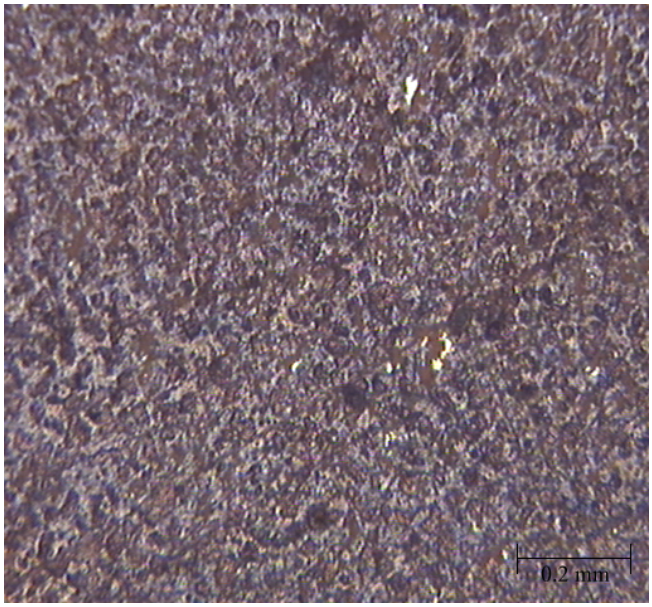

Figure 5-46. Microscopic image of outer specimen after 24 hours in experiments with 100 ppm inhibitor and 2m/s flow

5.5 Tests with 150 ppm inhibitor

With tests completed at 100 ppm inhibitor concentration, the concentration was increased to 150 ppm. The aim of the increment is to establish any concentration related effects in the three zones. The results of the 8 m/s and 2 m/s flow with 150 ppm are presented below.

5.5.1 Tests at 8 m/s

Table 5-6 details the weight loss values and in total, 5 tests were performed. Increasing the inhibitor concentration to 150 ppm resulted in a corrosion rate reduction in the impingement specimen with the intermediate specimen increasing its corrosion rate and the outer remaining largely unchanged.

Table 5-6

Results for 8 m/s flow in CO_2 saturated conditions with 100ppm inhibitor. Results show hydrodynamic zone weight losses in grams for tests at 50°C and 24 hrs.

	Impingement	Intermediate	Outer	pH
Test 1	0.0028	0.0155	0.0181	5.6
Test 2	0.0018	0.0033	0.0042	5.9
Test 3	0.0014	0.0068	0.0091	6.1
Test 4	0.0012	0.0084	0.0071	5.4
Test 5	0.0012	0.0104	0.0034	5.8

Figure 5-47 shows the equivalent corrosion rates of all three zones. As observed by the mass loss results above, the corrosion rate in the impingement zone reduces with the concentration increment. Considering the values of shear in the respective zones, the impingement specimen performs best and the inhibitor effectiveness seems to be working at optimum.

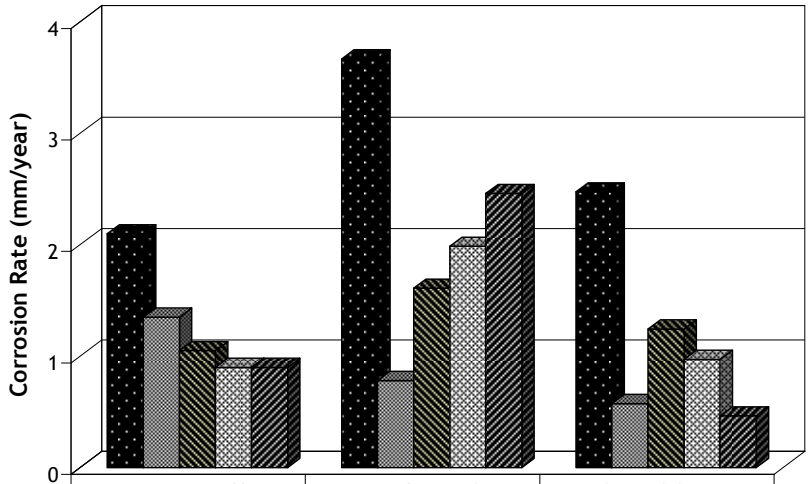

	Impingement (183pa)	Intermediate (5.9pa)	Outer (2.2pa)
Test 1	2.097	3.665	2.472
Test 2	1.348	0.780	0.574
Test 3	1.048	1.608	1.243
Test 4	0.899	1.986	0.970
Test 5	0.899	2.459	0.464

Figure 5-47. Hydrodynamic zone equivalent yearly corrosion rates at 8 m/s flow in CO_2 saturated 3.5 wt% brine with 150 ppm inhibitor. Test duration 24 hrs at 50°C. Zone regions indicate average shear values in Pascal's.

The microscopic image for the impingement specimen, Figure 5-48 shows a different inhibitor film structure to that observed at 100 ppm inhibitor concentration. The outer zone microscopy, Figure 5-49 shows no pitting activity on the metal surface compared to observations at 100 ppm.

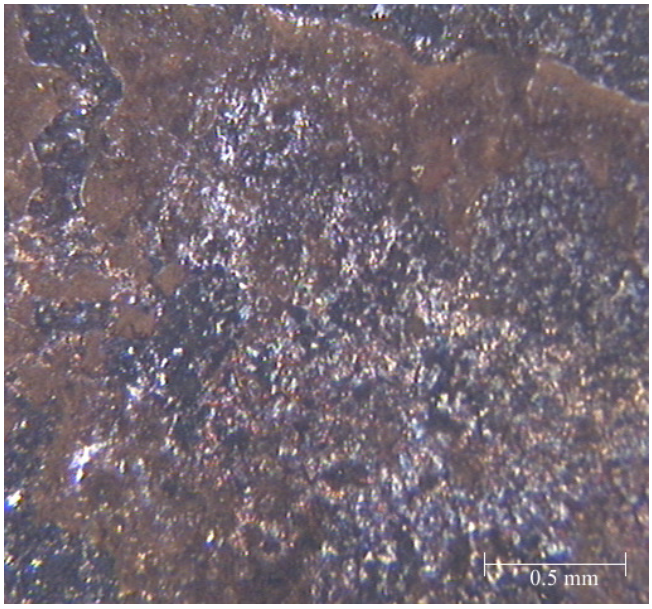

Figure 5-48. Microscopic image of impingement specimen after 24 hours in experiments with 150 ppm inhibitor and 8 m/s flow

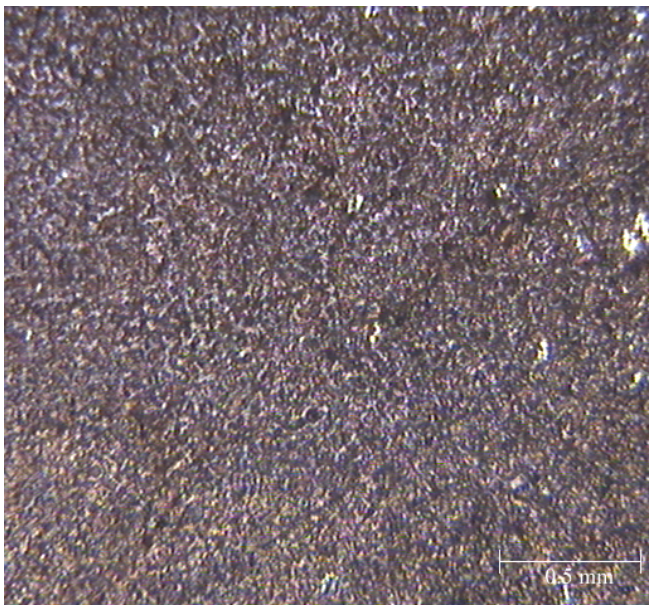

Figure 5-49. Microscopic image of outer specimen after 24 hours in experiments with 150ppm inhibitor and 8m/s flow

5.5.2 Tests at 2 m/s

Tests at 2 m/s show a concentration related reduction in corrosion rate for the impingement specimen only. The intermediate and outer specimens showed an increase in corrosion rate compared to the tests at 100 ppm. Table 5-7 shows the weight loss values of 6 tests performed at 150 ppm.

Table 5-7

Results for 2 m/s flow in CO_2 saturated conditions with 150 ppm inhibitor. Results show hydrodynamic zone weight losses in grams for tests at 50°C and 24 hrs

	Impingement	Intermediate	Outer	pH
Test 1	0.0039	0.0167	0.0163	5.6
Test 2	0.0008	0.0078	0.0066	5.8
Test 3	0.0015	0.0092	0.0125	5.6
Test 4	0.0009	0.0110	0.0060	6.0
Test 5	0.0015	0.0107	0.0098	5.4

Figure 5-50 shows the equivalent corrosion rates for all three zones. The impingement zone has the smallest average corrosion rate followed by the outer and the intermediate respectively. The higher shear conditions in the impingement zone seem to create optimum conditions for better inhibitor film formation at 150 ppm inhibitor concentration. The intermediate and outer specimens actually see an average increase in corrosion rate compared to the 100 ppm concentration. This may indicate less effective film formation compared to films formed at 100 ppm inhibitor concentration.

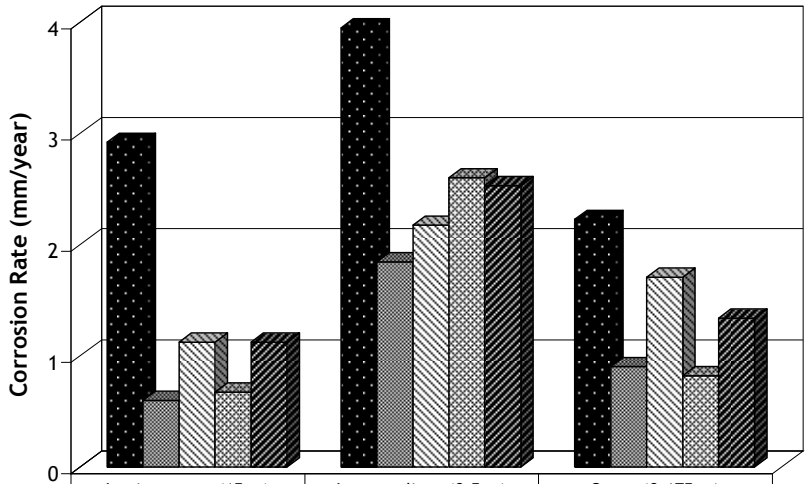

	Impingement (15pa)	Intermediate (0.5pa)	Outer (0.175pa)
Test 1	2.920	3.949	2.226
Test 2	0.599	1.844	0.901
Test 3	1.123	2.175	1.707
Test 4	0.674	2.601	0.819
Test 5	1.123	2.530	1.338

Figure 5-50. Hydrodynamic zone equivalent yearly corrosion rates at 2 m/s flow in CO_2 saturated 3.5 wt% brine with 150 ppm inhibitor. Test duration 24 hrs at 50°C. Zone regions indicate average shear values in Pascal's.

Microscopy showed interesting features in the impingement and intermediate zones. Figure 5-51 represents the impingement zone microscopy and shows the inhibitor film on the specimen surface. Very small shallow pits are observed on the image. Figure 5-52 represents the intermediate zone microscopy where large deep pits are observed and the surface structure is observed to be different compared to the impingement zone surface structure. This observation could also agree with the equivalent corrosion rates as the intermediate zone is shown to have the highest corrosion rate in all 5 tests compared to the impingement and outer zones. The impingement zone is also observed to have the lowest corrosion rate 4 of the 5 tests.

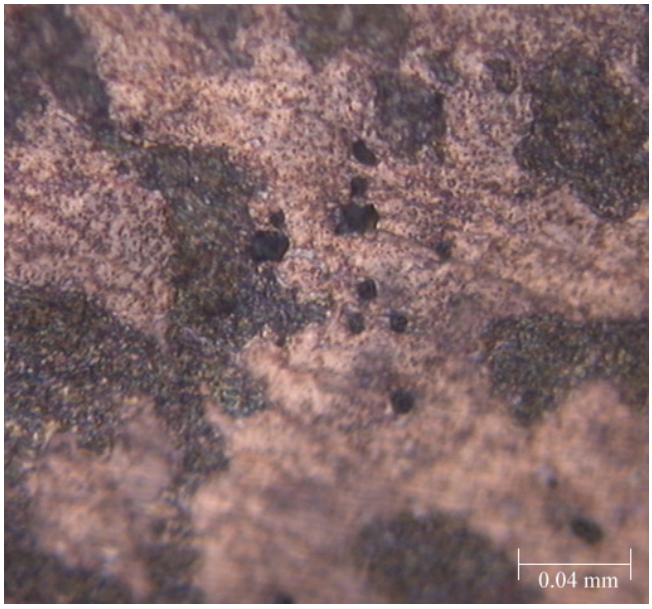

Figure 5-51. Microscopic image of impingement specimen after 24 hours in experiments with 150 ppm inhibitor and 2 m/s flow

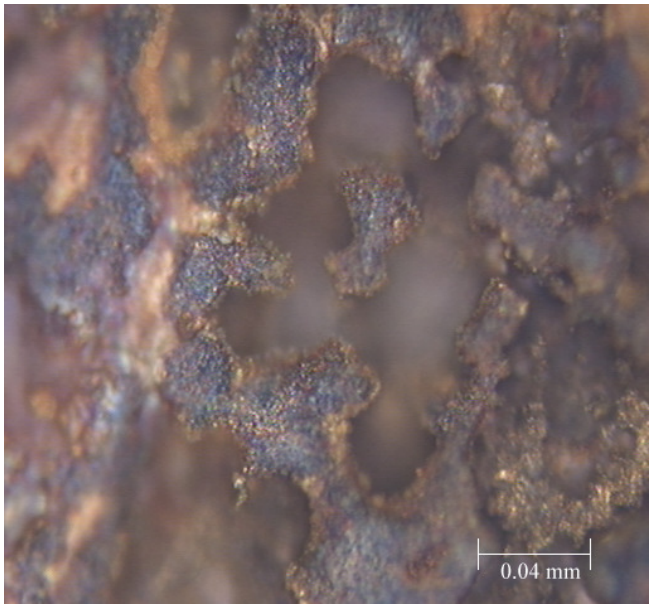

Figure 5-52. Microscopic image of intermediate specimen after 24 hours in experiments with 150 ppm inhibitor and 2 m/s flow

5.6 Tests with 200 ppm inhibitor

Tests at a higher inhibitor concentration of 200 ppm indicated an adverse inhibitor effect with the corrosion rates in all three hydrodynamic zones showing an increase compared to lower concentrations of 100 ppm and 150 ppm. The results do however contribute the need to evaluate optimum inhibitor concentrations and are evidence that increasing inhibitor concentration above optimum levels may actually increase corrosion rates. The results presented indicate the increase in corrosion rates.

5.6.1 Tests at 8 m/s

As shown in Figure 5-53, increasing the inhibitor concentration to 200 ppm did not yield any reduction in corrosion rate for all three hydrodynamic zones. In fact, increasing the concentration actually increases the corrosion rates of all three hydrodynamic zones.

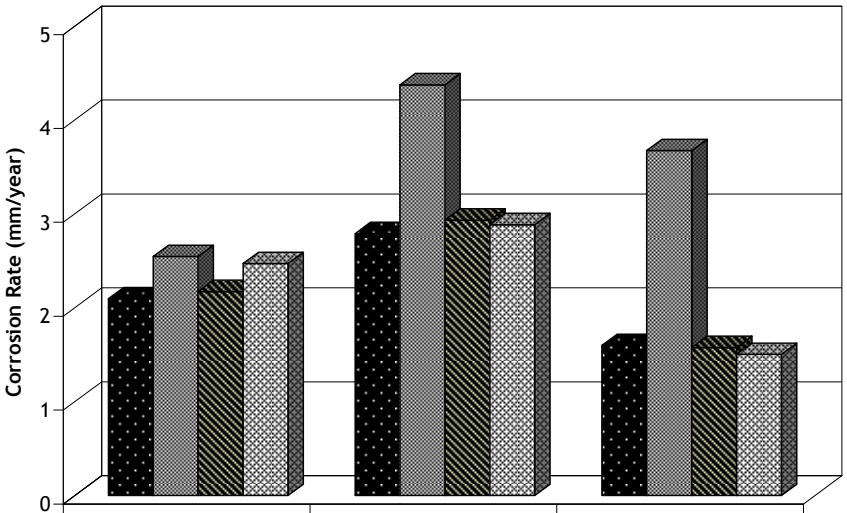

	Impingement (183pa)	Intermediate (5.9pa)	Outer (2.2pa)
Test 1	2.097	2.790	1.598
Test 2	2.546	4.374	3.674
Test 3	2.172	2.932	1.576
Test 4	2.471	2.885	1.502

Figure 5-53. Hydrodynamic zone equivalent yearly corrosion rates at 8 m/s flow in CO_2 saturated 3.5 wt% brine with 200 ppm inhibitor. Test duration 24 hrs at 50°C. Zone regions indicate average shear values in Pascal's.

5.6.2 Tests at 2 m/s

Tests done at 2 m/s again showed no benefit in increasing the concentration to 200 pm. The corrosion rates of all three hydrodynamic zones are higher than those at 100 ppm and 150 ppm as shown in Figure 5-54.

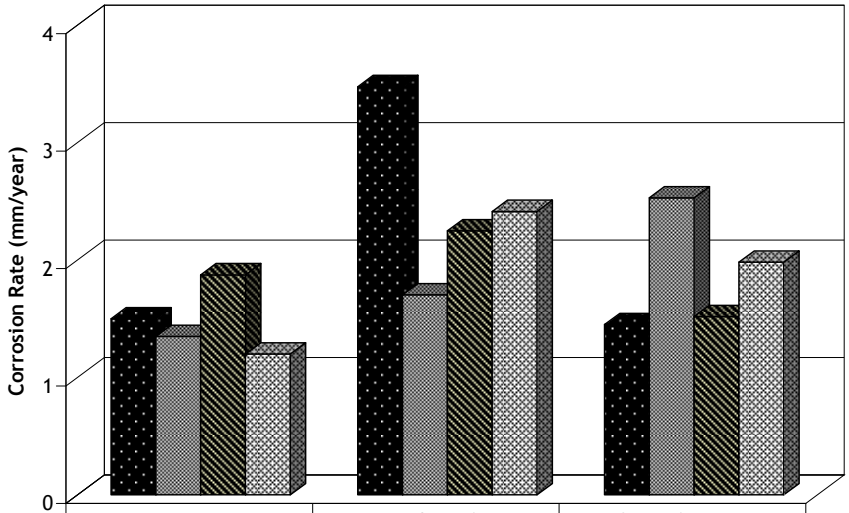

	Impingement (15pa)	Intermediate (0.5pa)	Outer (0.175pa)
Test 1	1.498	3.476	1.448
Test 2	1.348	1.702	2.527
Test 3	1.872	2.246	1.516
Test 4	1.198	2.412	1.980

Figure 5-54. Hydrodynamic zone equivalent yearly corrosion rates at 2 m/s flow in CO_2 saturated 3.5 wt% brine with 200 ppm inhibitor. Test duration 24 hrs at 50°C. Zone regions indicate average shear values in Pascal's.

5.7 Tests at 1000 ppm and 1500 ppm

Tests at 1000 ppm and 1500 ppm were considered in order to try and establish whether a significant increase in concentration would have any effect in reducing corrosion rates. The test at these concentrations showed higher corrosion rates compared to tests done at lower concentration and yielded no benefits with regard to corrosion rates. The results are therefore only presented in the summary of this chapter as emphasis on possible inhibitor adverse effects at concentrations higher than optimum.

5.8 Summary

This chapter has analysed the corrosion behaviour of carbon steel in environments that closely simulate oilfield conditions. Internal CO_2 corrosion of hydrocarbon transportation pipelines is principally mitigated by the use of chemical inhibitors. One current industrial issue with chemical inhibitors is their effectiveness in high shear conditions. The chapter has established the corrosion behaviour of carbon steel in aerated and CO_2 saturated brines with consideration of three hydrodynamic zones of variable shear. A commercial corrosion inhibitor (Corr Treat 727) has been assessed in these hydrodynamic zones with focus on its ability to reduce hydrodynamically related corrosion mechanisms.

Aerated tests indicated a strong corrosion enhancing influence in the impingement zone at both velocities. Corrosion rates in this zone are much higher than the intermediate and outer zones. Average corrosion rates in the impingement zone for the 8 m/s and 2 m/s experiments are 24.06 mm/year and 12.78 mm/year respectively. Severe pitting has also been documented in these conditions as demonstrated by microscopy and specimen surface profiling.

The main observations in CO_2 saturated brines include a reduction in regional corrosion rates presumably due to formation of protective carbonate films. Formation of these films is however dependant on hydrodynamic conditions as some conditions such as 8 m/s intermediate, 2 m/s intermediate and 2 m/s outer show an increase in corrosion rate. Microscopic observation in the two intermediate zones has indicated a strong tendency for localised pitting. This form of pitting seems related to the patchy and uneven nature of protective carbonate films forming on specimen surfaces.

Addition of the Corr Treat 727 inhibitor reduced the corrosion rates in all three hydrodynamic zones and at both velocities. The optimum inhibitor efficiency in each zone, or shear condition, depends on concentration with the impingement zone requiring higher inhibitor concentrations of 150ppm for optimum efficiency at both velocities. The intermediate and outer zones required a lower concentration at 100 ppm at both velocities. Increasing inhibitor concentration above these optimum levels does not reduce the corrosion rate but is actually observed to

increase corrosion rates above the optimum values. The corrosion rates are nevertheless lower than in CO_2 saturated environments. Figures 5-55 to 5-60 give a full numerical summary of the results discussed in this chapter.

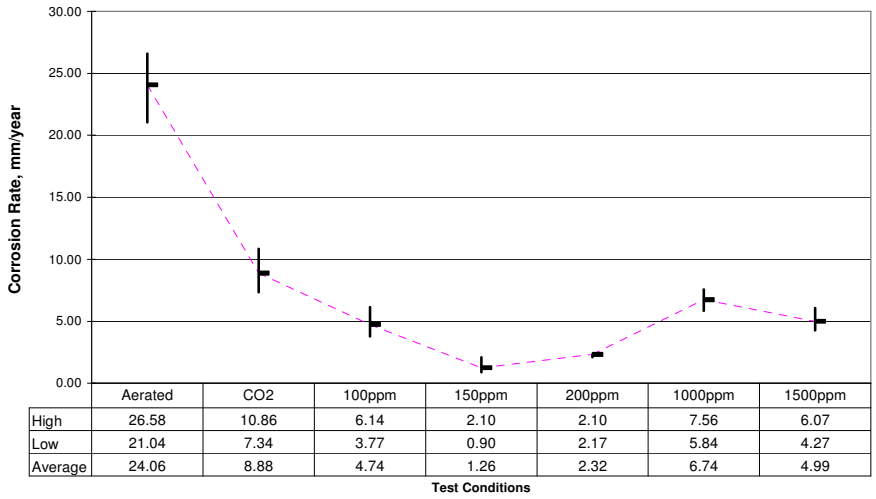

	Aerated	CO2	100ppm	150ppm	200ppm	1000ppm	1500ppm
High	26.58	10.86	6.14	2.10	2.10	7.56	6.07
Low	21.04	7.34	3.77	0.90	2.17	5.84	4.27
Average	24.06	8.88	4.74	1.26	2.32	6.74	4.99

Figure 5-55. Average equivalent corrosion rates for the impingement zone at 8m/s flow. Average shear stress value in region is 183 Pa.

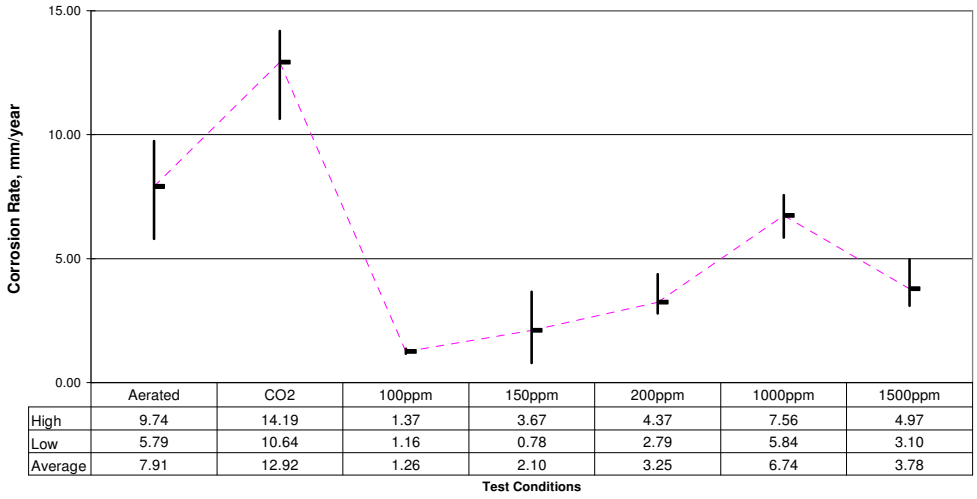

	Aerated	CO2	100ppm	150ppm	200ppm	1000ppm	1500ppm
High	9.74	14.19	1.37	3.67	4.37	7.56	4.97
Low	5.79	10.64	1.16	0.78	2.79	5.84	3.10
Average	7.91	12.92	1.26	2.10	3.25	6.74	3.78

Figure 5-56. Average equivalent corrosion rates for the intermediate zone at 8m/s flow. Average shear stress value in region is 5.9 Pa

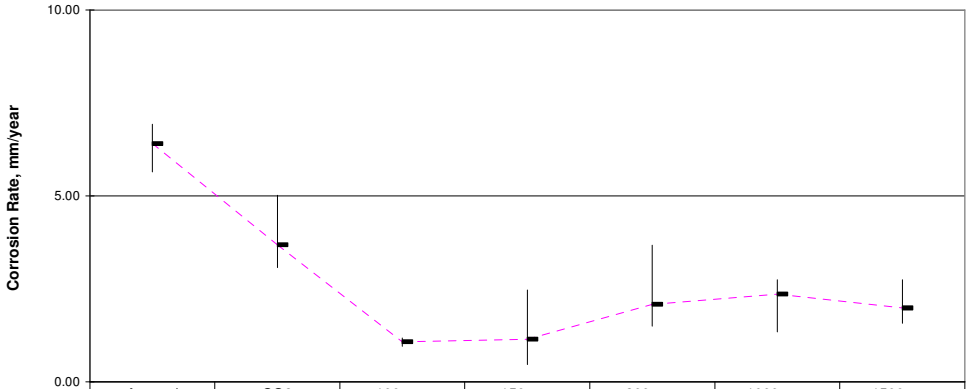

	Aerated	CO2	100ppm	150ppm	200ppm	1000ppm	1500ppm
High	6.92	5.01	1.18	2.47	3.67	2.75	2.75
Low	5.64	3.07	0.96	0.46	1.50	1.34	1.57
Average	6.41	3.69	1.08	1.14	2.09	2.36	1.99

Test Conditions

Figure 5-57. Average equivalent corrosion rates for the outer zone at 8m/s flow. Average shear stress value in region is 2.2 Pa

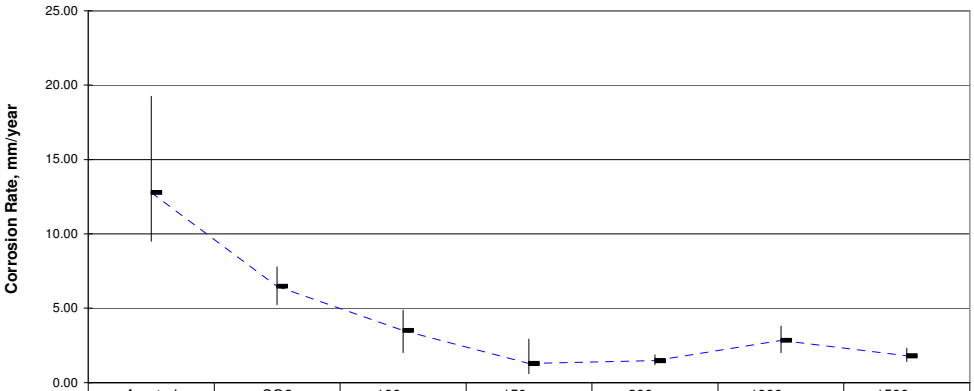

	Aerated	CO2	100ppm	150ppm	200ppm	1000ppm	1500ppm
High	19.25	7.79	4.87	2.92	1.87	3.82	2.32
Low	9.51	5.24	2.02	0.60	1.20	2.02	1.42
Average	12.78	6.48	3.50	1.28	1.48	2.85	1.80

Test Conditions

Figure 5-58. Average equivalent corrosion rates for the impingement zone at 2m/s flow. Average shear stress value in region is 15 Pa

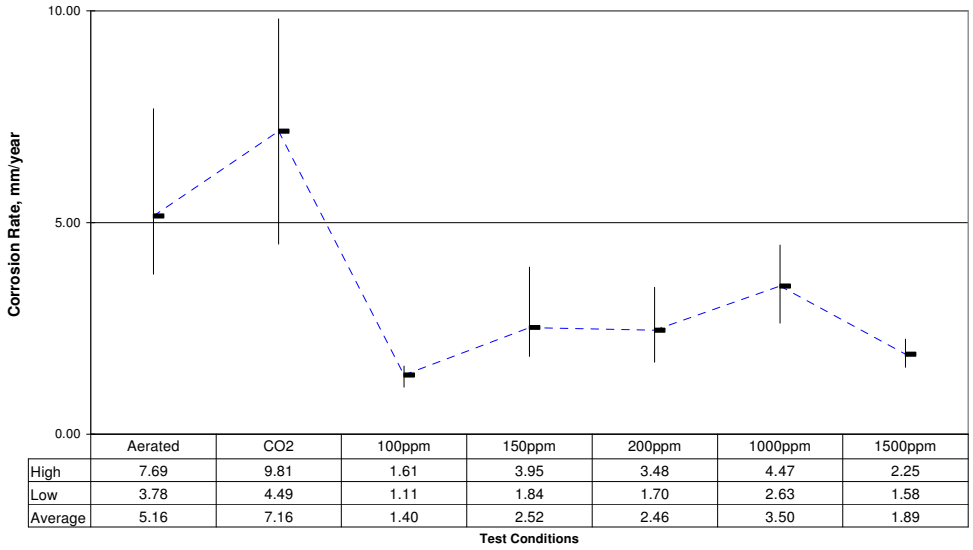

	Aerated	CO2	100ppm	150ppm	200ppm	1000ppm	1500ppm
High	7.69	9.81	1.61	3.95	3.48	4.47	2.25
Low	3.78	4.49	1.11	1.84	1.70	2.63	1.58
Average	5.16	7.16	1.40	2.52	2.46	3.50	1.89

Test Conditions

Figure 5-59. Average equivalent corrosion rates for the intermediate zone at 2 m/s flow. Average shear stress value in region is 0.5 Pa

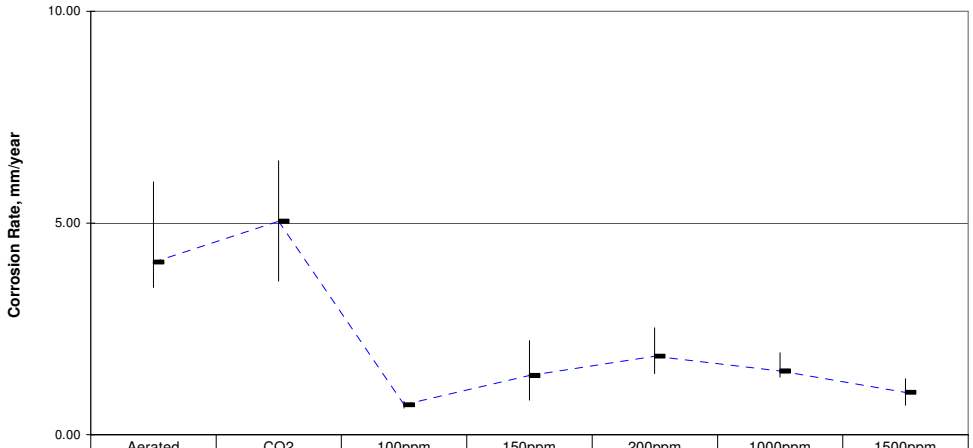

	Aerated	CO2	100ppm	150ppm	200ppm	1000ppm	1500ppm
High	5.97	6.47	0.79	2.23	2.53	1.37	1.33
Low	3.48	3.63	0.63	0.82	1.45	1.94	0.70
Average	4.08	5.04	0.71	1.40	1.86	1.51	1.00

Test Conditions

Figure 5-60. Average equivalent corrosion rates for the outer zone at 2m/s flow. Average shear stress value in region is 0.175 Pa

As discussed in the literature review of this thesis, one broader issue with monitoring flow-induced corrosion is the possibility of non-Faraday material loss. Weight loss experiments as performed above are capable of monitoring the total material weight loss attributed to Faraday and non-Faraday mechanisms.

The next chapter takes this issue forward and addresses the possibility of material losses by mechanical and interactive processes in solid-free flow. The tests conducted are evaluated by electrochemical monitoring and represent material loses attributed to electrochemical processes. Analysis of results from the two methods enables further discussion on the possibility of synergy and mechanical damage in solid-free flow.

6.0 ELECTROCHEMICAL STUDIES

6.1 Introduction

Chapter 5 of this thesis established the corrosion behaviour of carbon steel specimens in three variable hydrodynamic zones of high shear, intermediate shear and low shear. The values of shear in each zone are varied by changing the velocity of the flow from a peak velocity of 8 m/s down to 2 m/s. Tests were done in flow at 50^{o}C. The erosion-corrosion behaviour in the previous chapter is analysed through weight loss techniques and to further address the issue of non-Faraday material loss in solid-free flow, this chapter presents results obtained from electrochemical monitoring exercises.

The key concept of this chapter is to reproduce all the tests done previously and analyse the corrosion behaviour using a Faraday related monitoring technique. As weight loss methods are capable of measuring total material loss attributed to corrosion, erosion and synergy, the purpose of reproducing the tests done in chapter 5 is to establish the pure electrochemical corrosion component. This type of assessment will facilitate discussion in later sections on whether sold-free flow involves chemical as well as mechanical damage and establish mechanical and synergistic contributions to overall material loss. The inhibitor is also assessed to establish any effects related to reducing corrosion and consequently synergy.

Finally, a later chapter will investigate possible hydrodynamically influenced galvanic activity and in addition establish any inhibitor influence on such interactions. All results in this chapter are analysed through full anodic polarisation of 200 mV from E_{corr} complemented by anodic and cathodic linear polarisation of 20 mV from E_{corr}.

6.2 Tests in Aerated Flow

The results of the electrochemical monitoring are presented below in the following format. Full E/log i polarisation curves from all three hydrodynamic zones are initially presented to establish regional differences followed by extrapolation exercises of the linear segments for each zone displaying equivalent corrosion rates.

Anodic and cathodic linear polarisation curves are finally presented to establish any time related effects and scans are done at 4 hour, 15 hour and 24 hour timescales. This process is repeated for both velocities in order to reproduce variable shear. effects.

6.2.1 Tests at 8 m/s

Results of tests carried out at 8 m/s flow are presented. Figure 6-1 shows the full anodic polarisation curves after 24 hours in aerated conditions. Figures 6-2, 6-3 and 6-4 display the results separately for the Impingement, intermediate and outer specimens respectively. The impingement zone has a higher corrosion rate compared to the intermediate and outer zones. The corrosion potentials of the three zones are different with the higher shear zones having more positive potentials. The natural corrosion potential, E_{corr} of the impingement, intermediate and outer specimens are -615mV, -657mV and -677mV respectively.

The corrosion current densities from Figures 6-2 to 6-4 were converted to corrosion rates in mm/year using Faraday's law. For example, for the impingement specimen this iteration is carried out in the two steps described in Chapter 4 and demonstrated below. The extrapolated current taken from the plot is 550 μA/cm^2:

$$\frac{dm}{dt} = \frac{iAM}{nF} = \frac{550x10^{-6} * 1 * 55.85}{193000} = 1.6x10^{-7}\, g/s = \underline{5.02\, g/year}$$

$$mm/year = 10\frac{\frac{dm}{dt}}{\rho A} = 10\frac{5.02}{(7.8*1)} = \underline{\underline{6.435 mm/year}}$$

Figure 6-5 and 6-6 indicate the linear polarisation resistance values for the three zones with Figure 6-5 being the anodic scans and Figure 6-6 the cathodic scans.

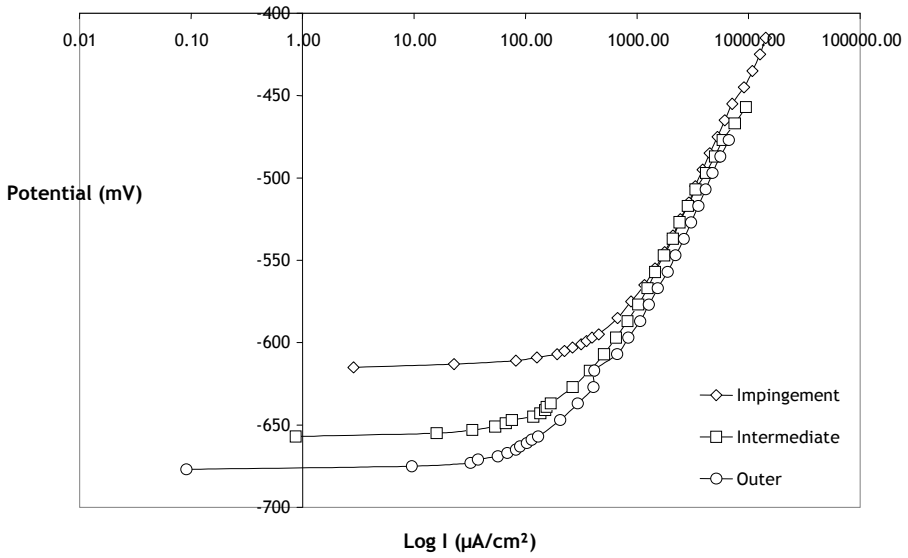

Figure 6-1. Full anodic polarisation curves for experiments in aerated 3.5 wt% NaCl at 50°C. Fluid impingement velocity is 8 m/s.

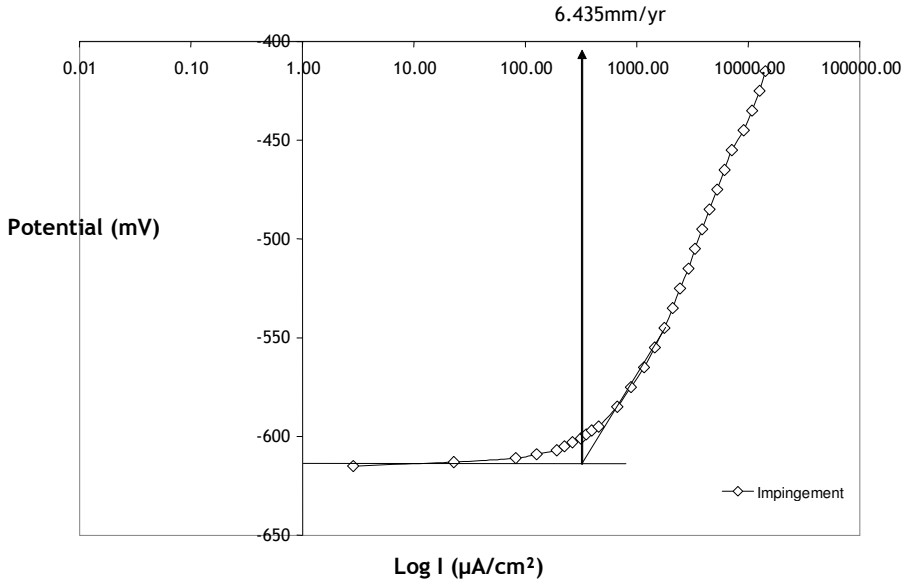

Figure 6-2. Extrapolated corrosion rate for 8 m/s full anodic polarisation for the impingement zone at 50°C in aerated flow.

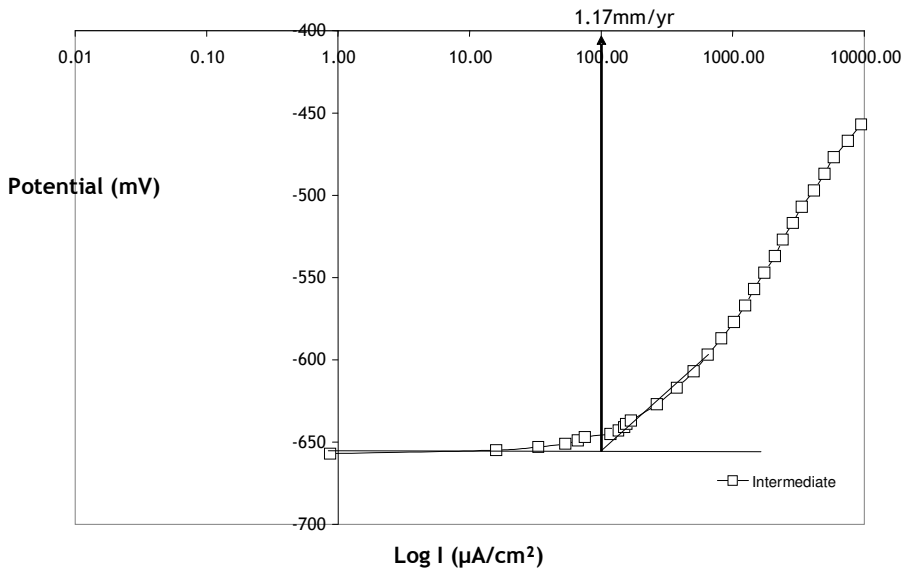

Figure 6-3. Extrapolated corrosion rate for 8 m/s full anodic polarisation for the intermediate zone at 50°C in aerated flow.

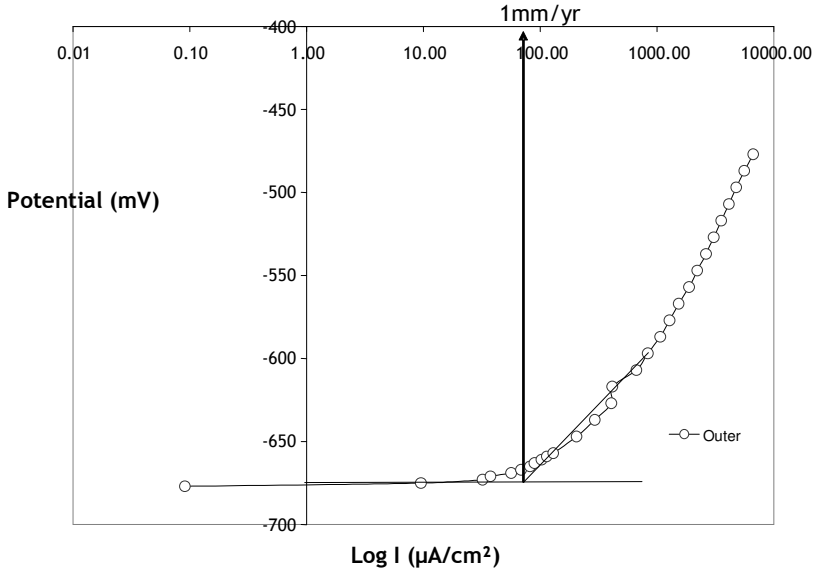

Figure 6-4. Extrapolated corrosion rate for 8 m/s full anodic polarisation for the outer zone at 50°C in aerated flow.

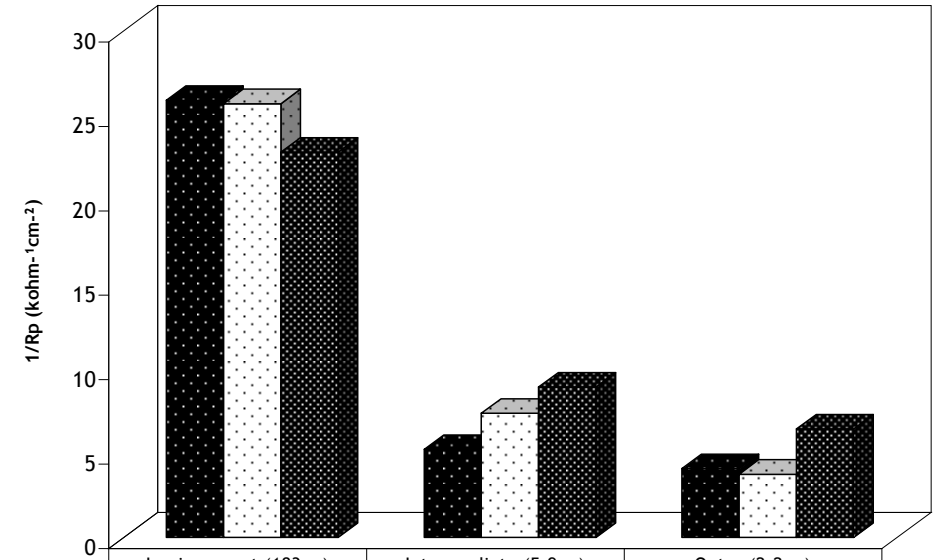

	Impingement (183pa)	Intermediate (5.9pa)	Outer (2.2pa)
4 Hours	25.9	5.2	4.1
15 Hours	25.7	7.4	3.8
24 Hours	22.8	8.9	6.4

Figure 6-5. Anodic linear polarisation results for tests in 8 m/s aerated flow at 50°C.

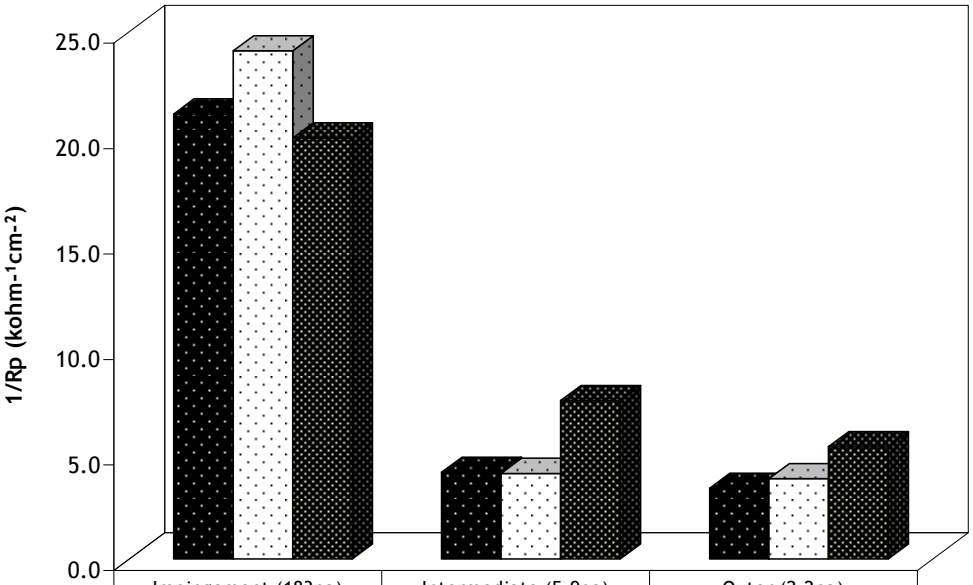

	Impingement (183pa)	Intermediate (5.9pa)	Outer (2.2pa)
4 Hours	21.1	4.1	3.4
15 Hours	24.1	4.1	3.8
24 Hours	20.0	7.5	5.3

Figure 6-6. Cathodic linear polarisation results for tests in 8 m/s aerated flow at 50°C.

The electrochemical results above indicate the impingement region as the worst affected with a corrosion rate of 6 times more than the intermediate and the outer zones. The linear polarisation scans verify this and do not indicate any significant time related effects on the corrosion rates. Although the anodic scans indicate slightly higher corrosion rates, there is good agreement between the anodic and cathodic scans.

While the electrochemistry results show a similar trend in corrosion behaviour between the three hydrodynamic zones as observed in the gravimetric tests in Chapter 5, the electrochemically determined corrosion rates are much lower and therefore suggest possible erosion and synergy mechanisms.

6.2.2 Tests at 2 m/s

Tests at 2 m/s also show the impingement zone as having the highest corrosion rate. The impingement zone again has the more positive electrode potential in comparison the intermediate and outer respectively. Figure 6-7 shows the full anodic polarisation curves for all three zones. The extrapolated values of corrosion rate in the three zones are shown in Figures 6-8, 6-9 and 6-10 respectively. From Figure 6-8, the corrosion rate and E_{corr} values in the impingement zone are 4.68 mm/year and -701 mV respectively. The intermediate values are presented by Figure 6-9 and are 1.29 mm/year and -712 mV. The outer values as shown by Figure 6-10 are 1.05 mm/year and -733 mV.

Figures 6-11 and 6-12 show the linear polarisation (1/Rp) values for both anodic and cathodic polarisation respectively. Again, from the linear polarisation results, the impingement zone has the biggest influence on the corrosion rate. The corrosion rate in this zone is also shown to decrease with time for both anodic and cathodic scans.

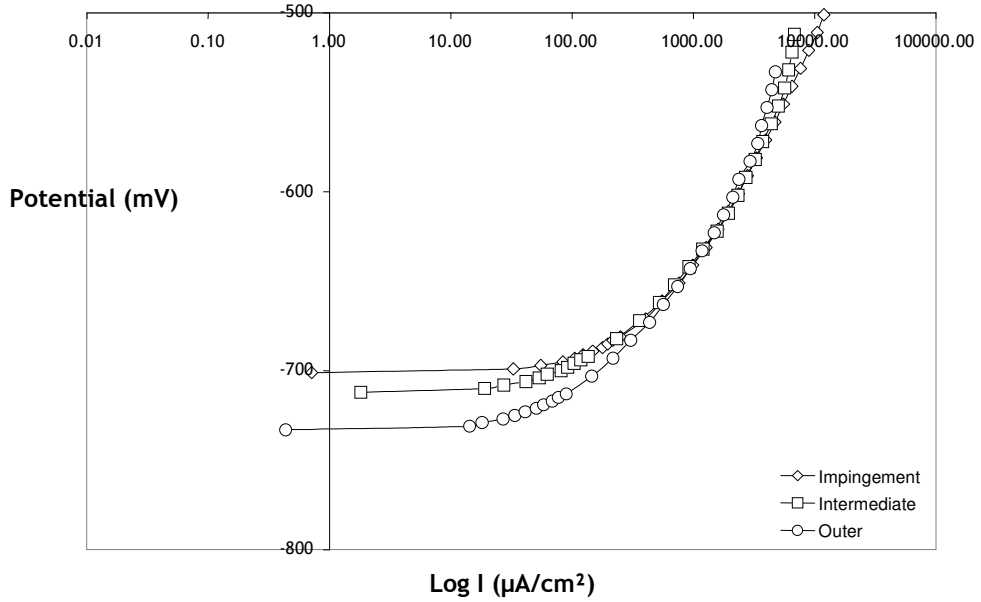

Figure 6-7. Full anodic polarisation curves for experiments in aerated 3.5 wt% NaCl at 50°C. Fluid impingement velocity is 2 m/s.

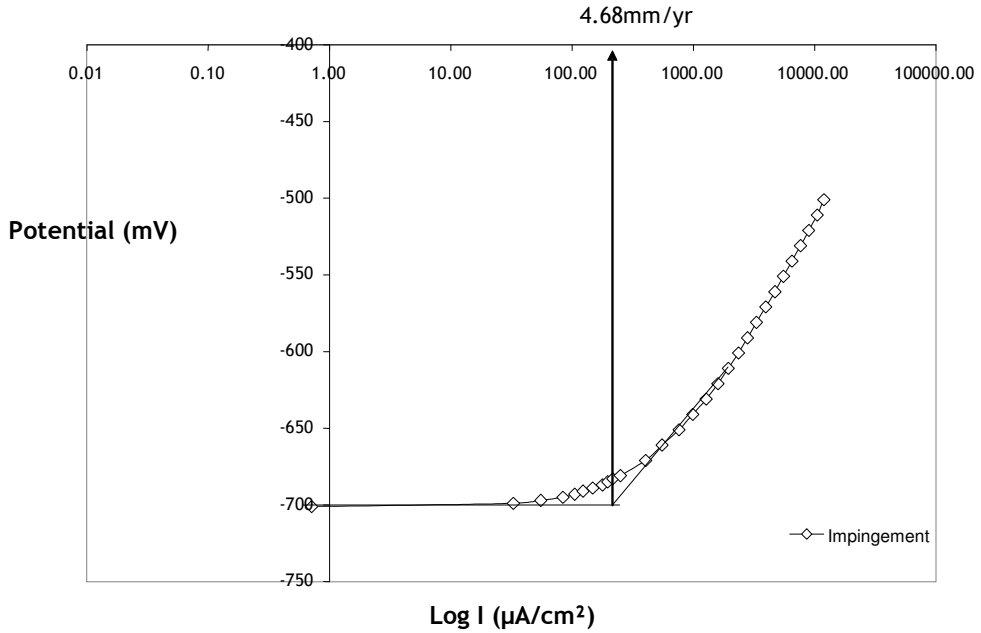

Figure 6-8. Extrapolated corrosion rate for 2 m/s full anodic polarisation for the impingement zone in 50°C aerated flow.

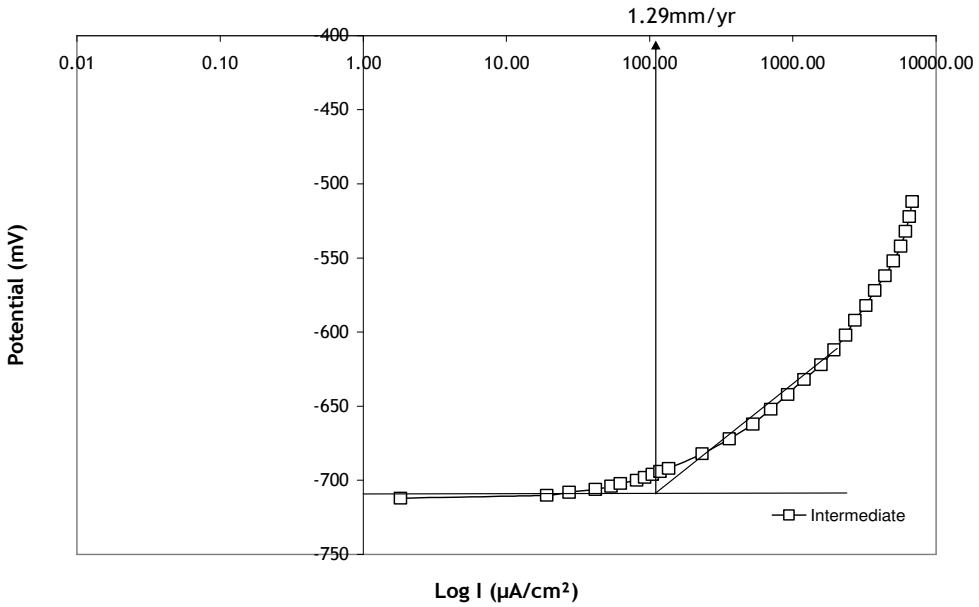

Figure 6-9. Extrapolated corrosion rate for 2 m/s full anodic polarisation for the intermediate zone in 50°C aerated flow.

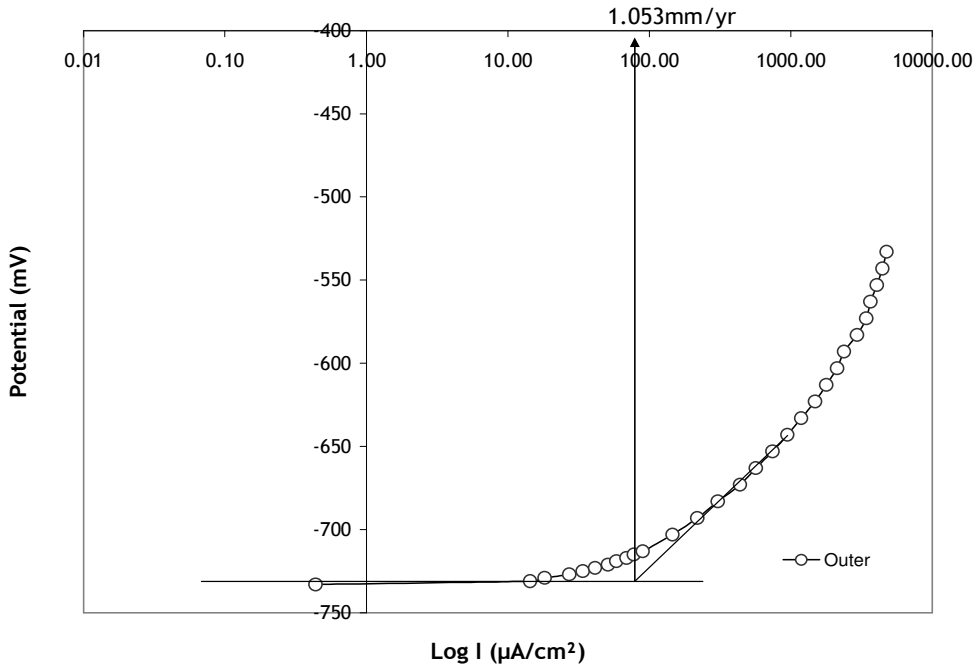

Figure 6-10. Extrapolated corrosion rate for 2 m/s full anodic polarisation for the outer zone in 50°C aerated flow.

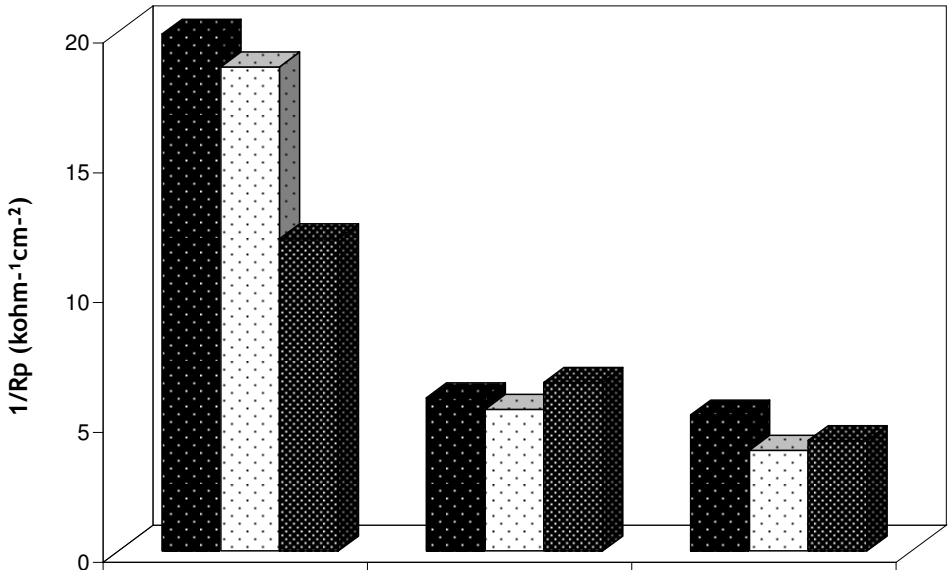

	Impingement (15pa)	Intermediate (0.5pa)	Outer (0.175pa)
4 Hours	19.9	5.9	5.3
15 Hours	18.7	5.5	3.9
24 Hours	12.0	6.5	4.3

Figure 6-11. Anodic linear polarisation results for tests in 2 m/s aerated flow at 50°C.

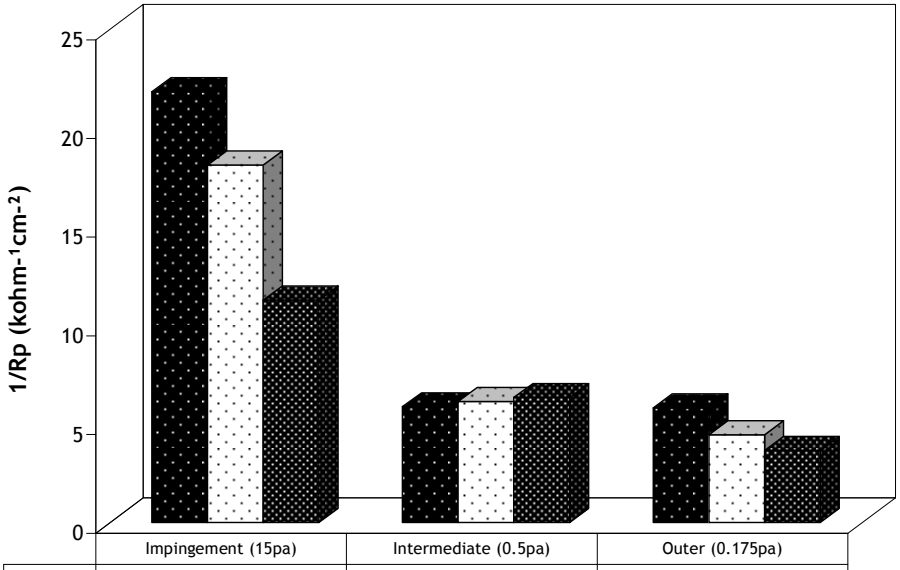

	Impingement (15pa)	Intermediate (0.5pa)	Outer (0.175pa)
4 Hours	21.8	5.9	5.8
15 Hours	18.1	6.1	4.4
24 Hours	11.3	6.3	3.7

Figure 6-12. Cathodic linear polarisation results for tests in 2 m/s aerated flow at 50°C.

Table 6-1

E_{corr} values for tests at 8 m/s and 2m/s. Table shows values of E_{corr} in each hydrodynamic zone. Values are in mV

	Impingement	Intermediate	Outer
8 m/s	-615	-657	-677
2 m/s	-701	-712	-733

Table 6-2

Corrosion rates extrapolated from full polarisation curves after 24 hours aerated flow. Extrapolated values are in mm/year.

	Impingement	Intermediate	Outer
8 m/s	6.44	1.17	1.00
2 m/s	4.68	1.29	1.05

Table 6-3

Linear polarisation resistance data (1/Rp) after 24 hours for tests in aerated flow at 8 m/s. Values are in $kohm^{-1}cm^{-2}$

	Impingement	Intermediate	Outer
Anodic	22.8	8.9	6.4
Cathodic	20.0	7.5	5.3

Table 6-4

Linear polarisation resistance values after 24 hours for tests in aerated flow at 2 m/s. Values are in $kohm^{-1}cm^{-2}$

	Impingement	Intermediate	Outer
Anodic	12.03	6.5	4.3
Cathodic	11.27	6.3	3.6

Tables 6-1 to 6-4 summarise the behaviour in aerated conditions. From Table 6-1, the more impingement conditions show a more positive value of $E_{corr.}$ From the tables, both the tafel extrapolation and linear polarisation demonstrate large differences between the impingement zone and the intermediate and outer zones.

6.3 Tests in CO_2 saturated brine

Tests in CO_2 involved the same procedure as the aerated tests but with CO_2 bubbled in the recirculating fluids.

6.3.1 Tests at 8 m/s

Figure 6-13 below shows the full anodic polarisation curves after 24 hours in CO_2 saturated brine. The natural corrosion potential, E_{corr}, of all three hydrodynamic zones is more within the same region as compared to the results in aerated conditions. It is also noted below that the E_{corr} values are more negative as compared to the values in aerated conditions. The values of E_{corr} for the impingement, intermediate and outer specimens are -731 mV, -729 mV and -727 mV respectively. Again from the curves below, the impingement zone has the highest extrapolated corrosion rate followed by the outer and the intermediate has the lowest value.

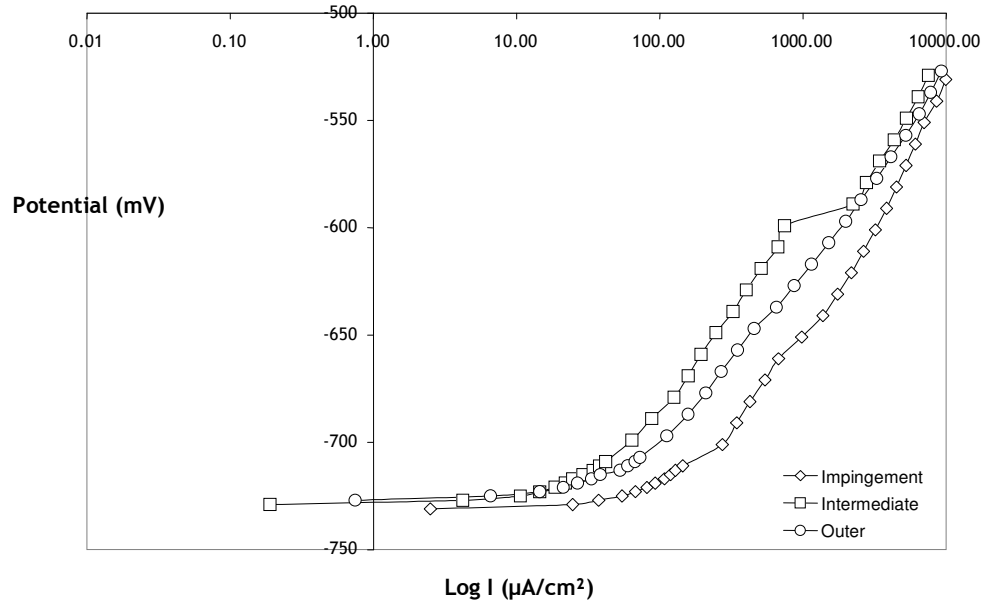

Figure 6-13. Full anodic polarisation curves for experiments in CO_2 saturated 3.5 wt% NaCl at 50°C. Fluid impingement velocity is 8 m/s.

Figures 6-14, 6-15 and 6-16 show the individual extrapolated corrosion rates for the three zones. From Figure 6-14 and 6-15, the extrapolated corrosions rate in the impingement and intermediate zones are 1.755 mm/year and 0.585 mm/year respectively which are less than the extrapolated values in aerated conditions, 6.435 mm/year and 1.17 mm/year respectively. This reduction in corrosion rate is possibly due to formation of protective carbonate films as observed in the previous chapter. As mentioned above, the value of E_{corr} is more negative in these regions compared to E_{corr} values in aerated conditions.

Figure 6-16 shows the extrapolated value for the outer zone. The extrapolated corrosion rate of 1.053 mm/yr is almost similar to the extrapolated value in aerated conditions which is 1.000 mm/year.

Figures 6-17 and 6-18 are the calculated values of 1/Rp derived from the anodic and cathodic linear polarisation resistance curves. Both the anodic and cathodic tests indicate a reduction in corrosion rate as a function of time, which is indicative of the gradual establishment of surface films. After 24 hours the

intermediate zone has the lowest corrosion rate as indicated by both the anodic and cathodic scans. The impingement zone has the highest corrosion rate followed by the outer. The results of the linear polarisation scans therefore agree with the full polarisation curves done after 24 hours.

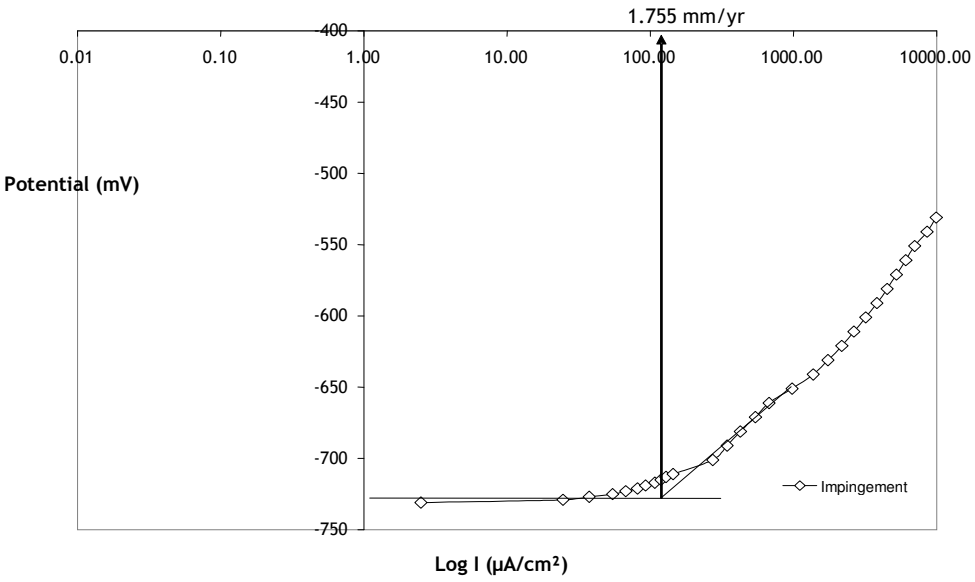

Figure 6-14. Extrapolated corrosion rate for 8 m/s full anodic polarisation for the impingement zone at 50°C in CO_2 saturated brine, pH 5.2

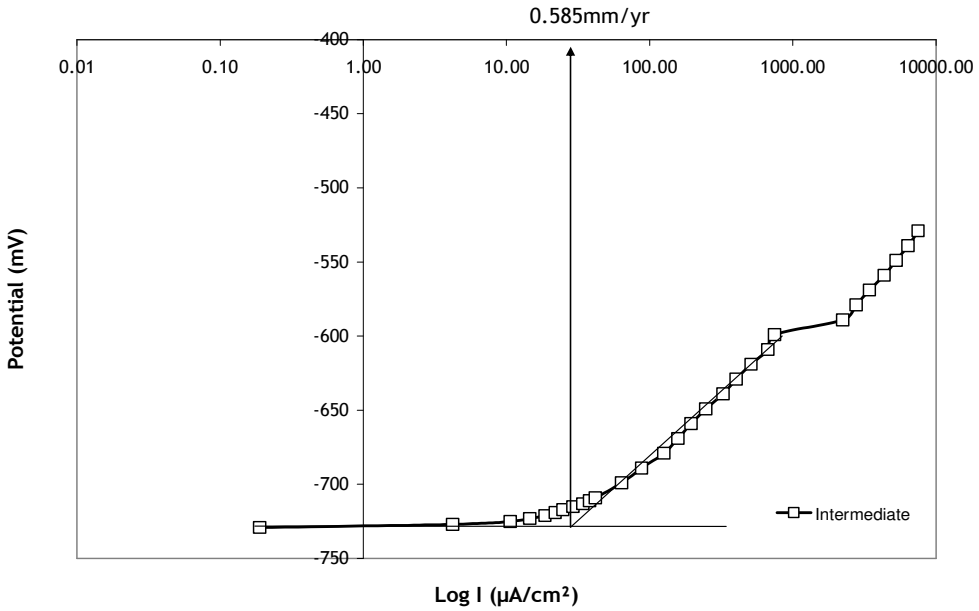

Figure 6-15. Extrapolated corrosion rate for 8 m/s full anodic polarisation for the intermediate zone at 50°C in CO_2 saturated brine, pH 5.2.

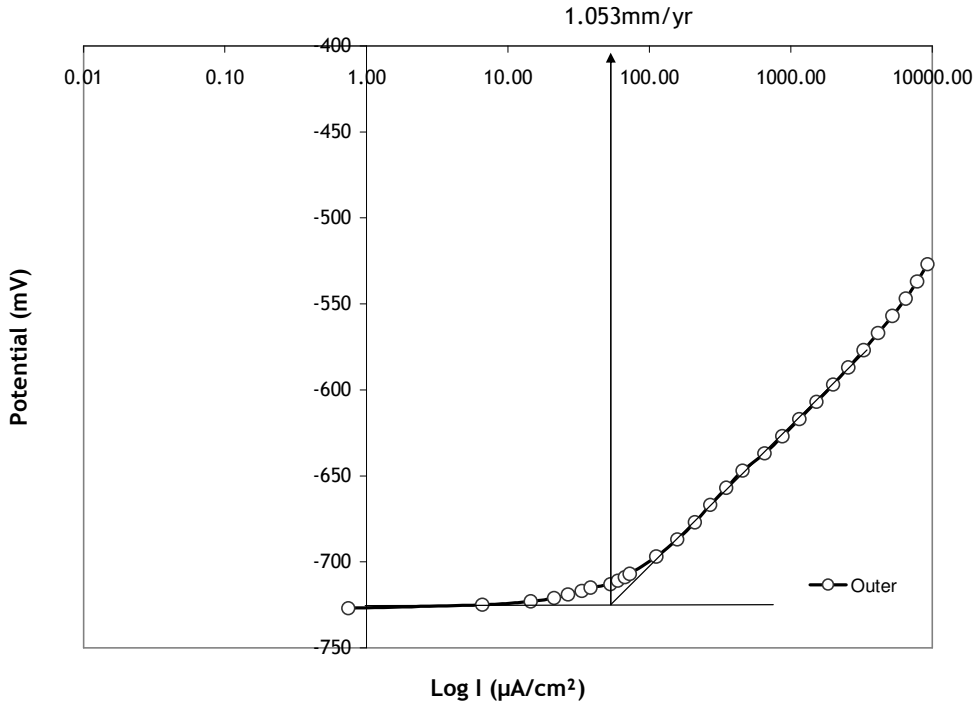

Figure 6-16. Extrapolated corrosion rate for 8 m/s full anodic polarisation for the outer zone at 50°C in CO_2 saturated brine, pH 5.2.

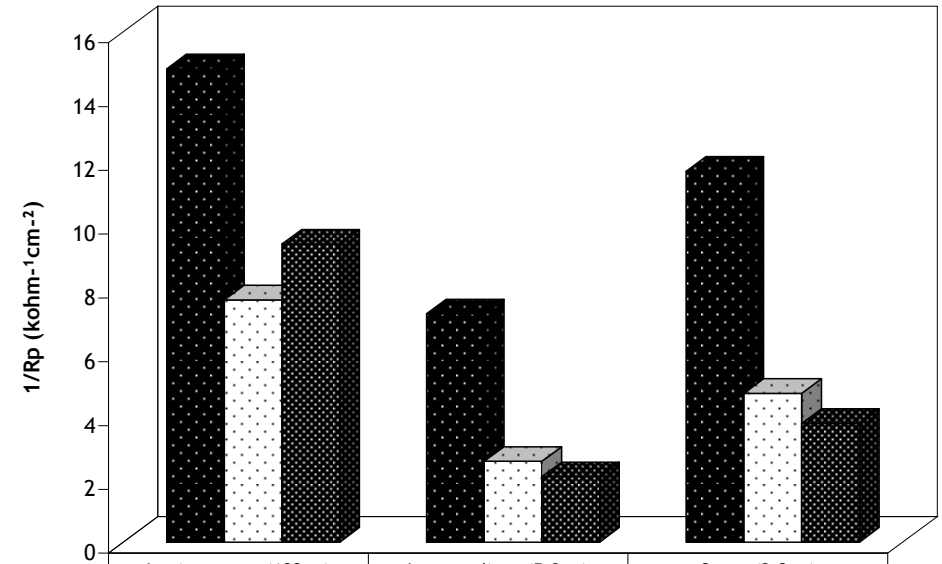

	Impingement (183pa)	Intermediate (5.9pa)	Outer (2.2pa)
4 Hours	14.8	7.2	11.6
15 Hours	7.6	2.5	4.7
24 Hours	9.3	2.1	3.7

Figure 6-17. Anodic linear polarisation results for tests at 8m/s in CO_2 saturated flow at 50^{o}C.

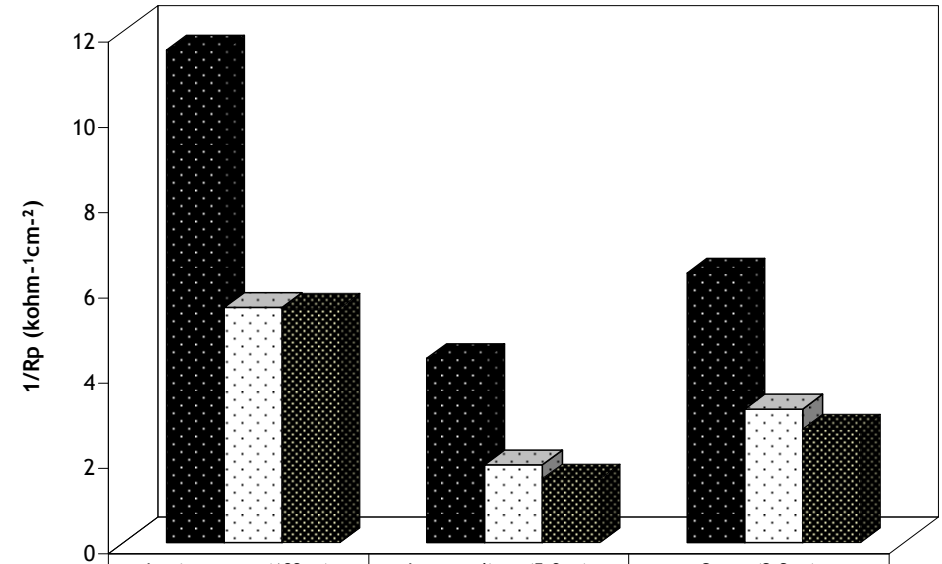

	Impingement (183pa)	Intermediate (5.9pa)	Outer (2.2pa)
4 Hours	11.6	4.3	6.3
15 Hours	5.5	1.8	3.1
24 Hours	5.5	1.5	2.7

Figure 6-18 Cathodic linear polarisation results for tests at 8 m/s in CO_2 saturated flow at 50^{o}C.

6.3.2 Tests at 2 m/s

Figure 6-19 shows the full anodic polarisation curves for tests at 2m/s. The behaviour of the three zones is almost similar and the values of E_{corr} for the impingement, intermediate and outer zones are -758 mV, -762 mV and -761 mV respectively indicating near similar behaviour.

Figures 6-20, 6-21 and 6-22 show the extrapolated values of corrosion rate for the impingement, intermediate and outer zones. The extrapolated values of corrosion rate are 3.5 mm/year, 4.1 mm/ year and 4.68 mm/year. A very interesting feature is that these corrosion rates are greater than the values at 8 m/s suggesting higher flow conditions are more favourable to what is presumed protective film formation.

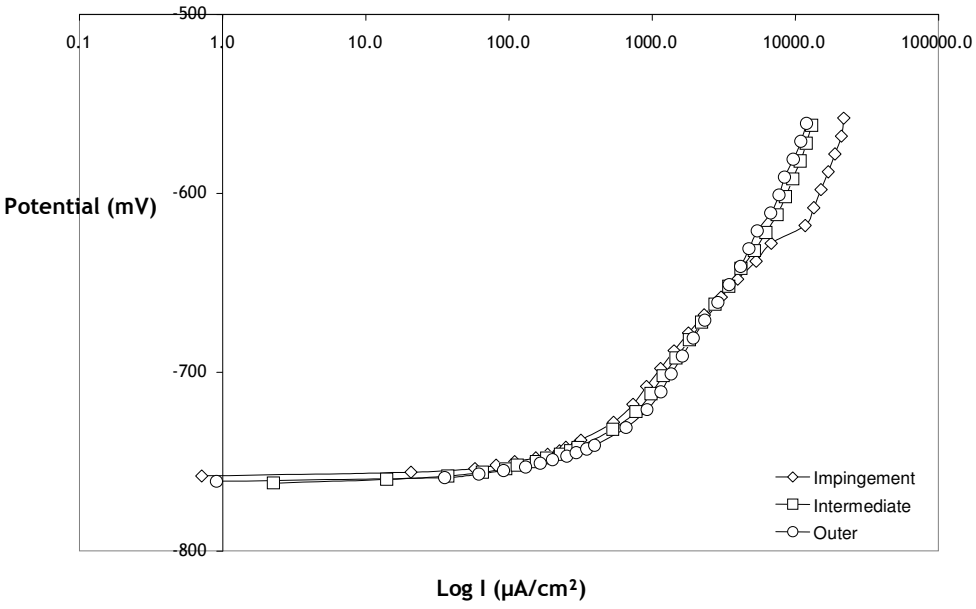

Figure 6-19. Full anodic polarisation curves for experiments in CO_2 saturated 3.5 wt% NaCl at 50°C. Fluid impingement velocity is 2 m/s.

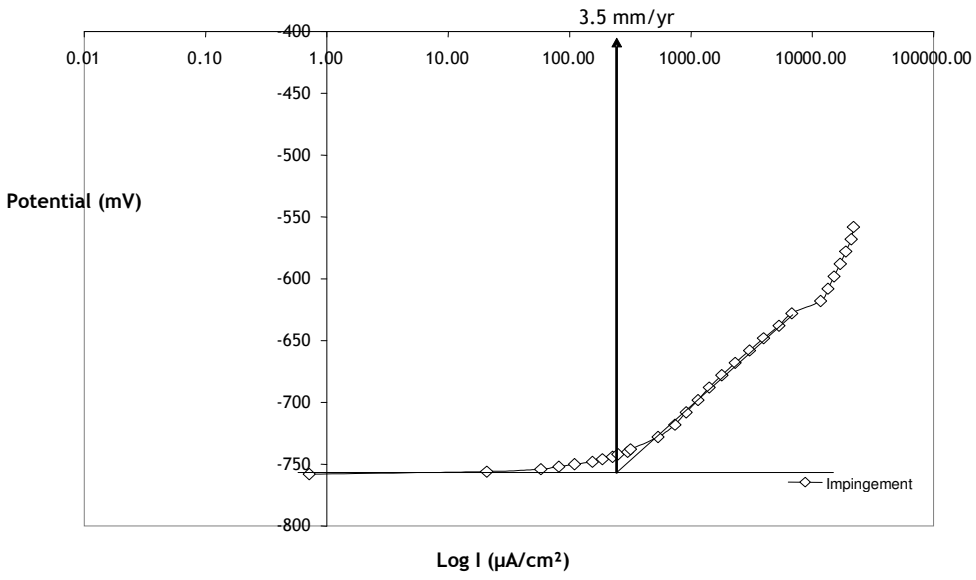

Figure 6-20. Extrapolated corrosion rate for 2 m/s full anodic polarisation for the impingement zone at 50°C in CO_2 saturated brine, pH 5.5.

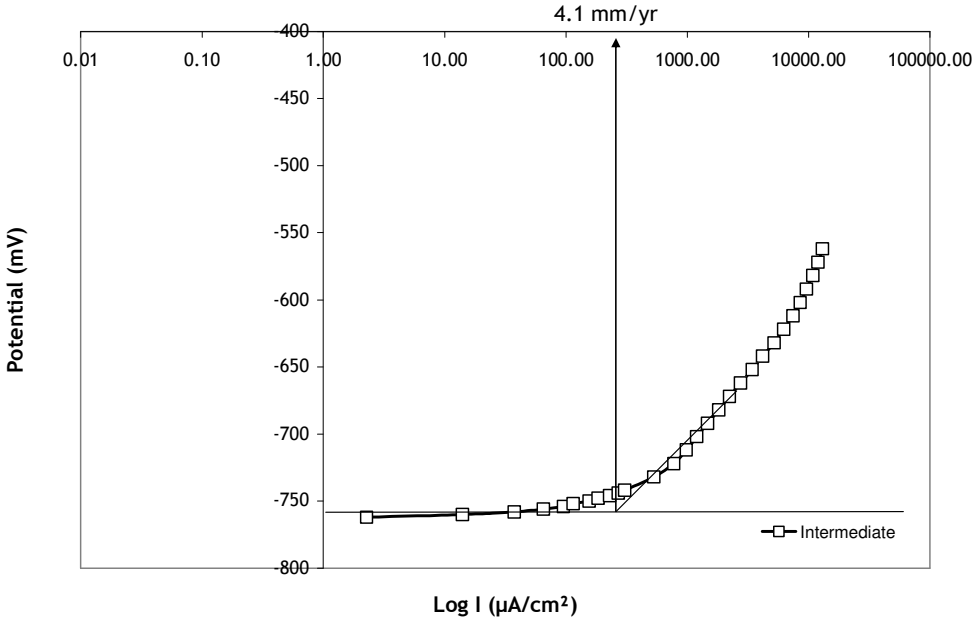

Figure 6-21. Extrapolated corrosion rate for 2 m/s full anodic polarisation for the intermediate zone at 50°C in CO_2 saturated brine, pH 5.5.

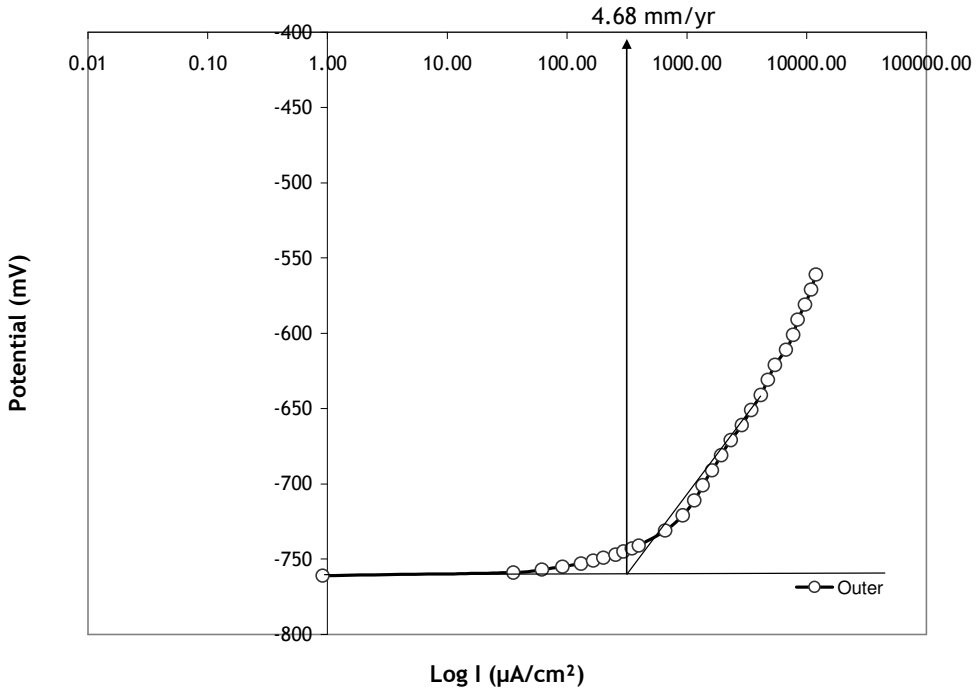

Figure 6-22. Extrapolated corrosion rate for 2 m/s full anodic polarisation for the outer zone at 50°C in CO_2 saturated brine, pH 5.5.

Comparing the CO_2 corrosion rate to the aerated corrosion rate at the lower velocity, the impingement zone is the only zone where the protective film seems to be forming. The intermediate and outer zones at 2 m/s actually show higher corrosion rates than in aerated water suggesting lack of effective protection from likely carbonate films and possibly a higher corrosion rate relate to the acidity of the carbonic acid conditions. Without sufficient protection from films, it is possible the higher corrosion rates could also be driven by the hydrogen evolution reaction in the acidic conditions.

Figures 6-23 and 6-24 show the 1/Rp values from the anodic and cathodic linear polarisation resistance curves for the tests at 2 m/s. As observed by the full polarisation scans, the corrosion rate at 2 m/s is higher than observed in tests at 8m/s and there are no systematic reductions in 1/Rp with time. Again this implies films in CO_2 saturated water form better at higher velocities or impingement conditions.

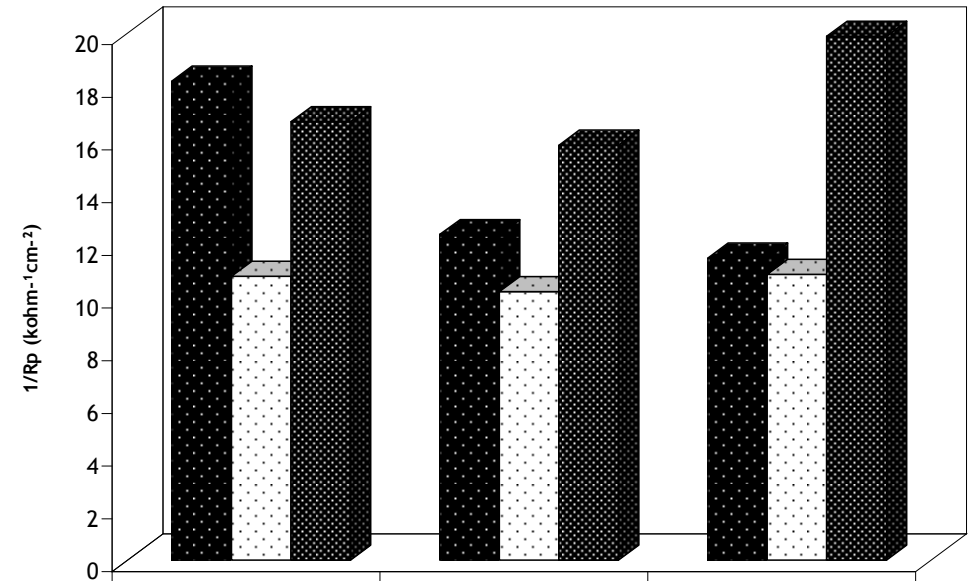

	Impingement (15pa)	Intermediate (0.5pa)	Outer (0.175pa)
4 Hours	18.2	12.4	11.5
15 Hours	10.8	10.2	10.8
24 Hours	16.6	15.7	19.9

Figure 6-23. Anodic linear polarisation results for tests at 2 m/s in CO_2 saturated flow at 50°C.

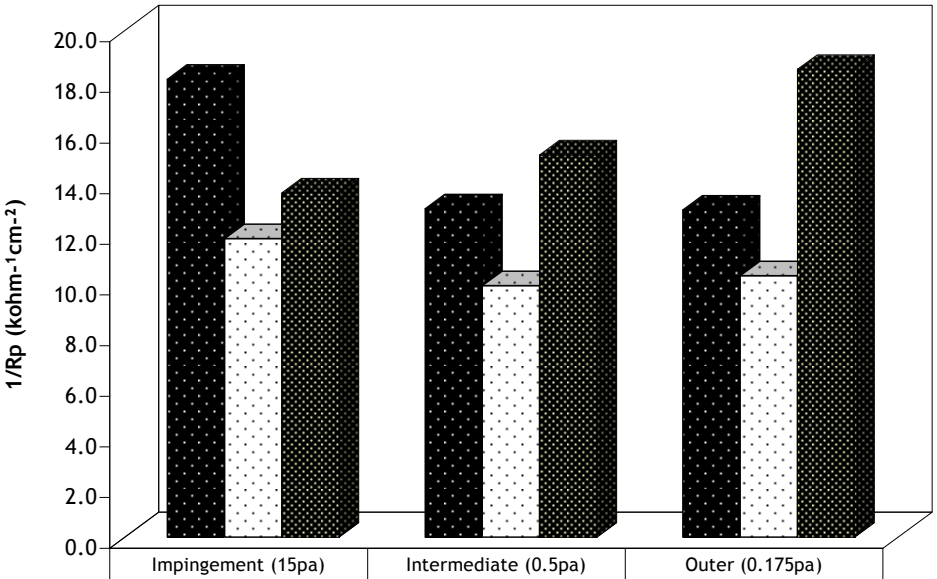

	Impingement (15pa)	Intermediate (0.5pa)	Outer (0.175pa)
4 Hours	18.1	13.0	12.9
15 Hours	11.8	9.9	10.3
24 Hours	13.6	15.1	18.5

Figure 6-24. Cathodic linear polarisation results for tests at 2 m/s in CO_2 saturated flow at 50°C

Tables 6-5 to 6-8 summarise the behaviour noticed in CO_2 saturated brines. Table 6-5 shows that although the E_{corr} values in each hydrodynamic zone are nearly the same, the values for the 8 m/s tests are still more positive in relation to those at 2 m/s. Table 6-6 indicates that the corrosion rates in CO_2 saturated conditions are higher for 2m/s flow compared to 8m/s flow. This result again implies protective films form better in conditions that are more aggresive. Tables 6-6, 6-7 and 6-8 show the 2m/s result as having higher corrosion rates for both Tafel extrapolation and linear polarisation.

Table 6-5

Ecorr values for tests at 8 m/s and 2 m/s. Table shows values of Ecorr in each hydrodynamic zone. Values are in mV.

	Impingement	Intermediate	Outer
8 m/s	-731	-729	-727
2 m/s	-758	-762	-761

Table 6-6

Corrosion rates extrapolated from full polarisation curves after 24 hours in CO_2 saturated flow. Extrapolated values are in mm/year.

	Impingement	Intermediate	Outer
8 m/s	1.8	0.6	1.0
2 m/s	3.5	4.1	4.7

Table 6-7

Linear polarisation resistance values (1/Rp) after 24 hours for tests in CO_2 saturated flow at 8 m/s. Values are in $kohm^{-1}cm^{-2}$.

	Impingement	Intermediate	Outer
Anodic	9.3	2.1	3.7
Cathodic	5.5	1.5	2.7

Table 6-8

Linear polarisation resistance values (1/Rp) after 24 hours for tests in CO_2 saturated flow at 2 m/s. Values are in kohm^{-1}cm^{-2}.

	Impingement	Intermediate	Outer
Anodic	16.6	15.7	19.9
Cathodic	13.6	15.1	18.5

6.4 Tests in CO_2 saturated brine with 100 ppm corrosion inhibitor

Following an establishment of the corrosion behaviour in CO_2 saturated brines, this and the following sections of this chapter present the results of tests in CO_2 saturated brines containing Corr Treat 727 corrosion inhibitor. As expected, the corrosion rate in the various hydrodynamic zones decreases in the presence of the inhibitor and a benefit of using corrosion inhibition is demonstrated. The results presented below are obtained at both velocities and hence variable shear.

6.4.1 Tests at 8 m/s

Figure 6-25 shows the full anodic polarisation curves for tests in water containing 100 ppm inhibitor and saturated with CO_2. The impingement zone clearly has the highest corrosion rate and the intermediate zone has the lowest corrosion rate. The values of E_{corr} for all three zones are within 10 mV of each other and are recorded as -689 mV, -686 mV and -684 mV for the impingement, intermediate and outer zones respectively. In this circumstance, the impingement zone has a value more negative compared to the intermediate and outer zones.

Figures 6-26, 6-27 and 6-28 show the extrapolated corrosion rates for the three hydrodynamic zones. The corrosion rates are 0.7 mm/yr, 0.1 mm/yr and 0.3 mm/yr for the impingement, intermediate and outer zones respectively.

Figures 6-29 and 6-30 are the anodic and cathodic linear polarisation resistance (1/Rp) curves and clearly show a beneficial reduction in corrosion rate with time in all three zones at both velocities. Again, the intermediate zone has the lowest corrosion rate.

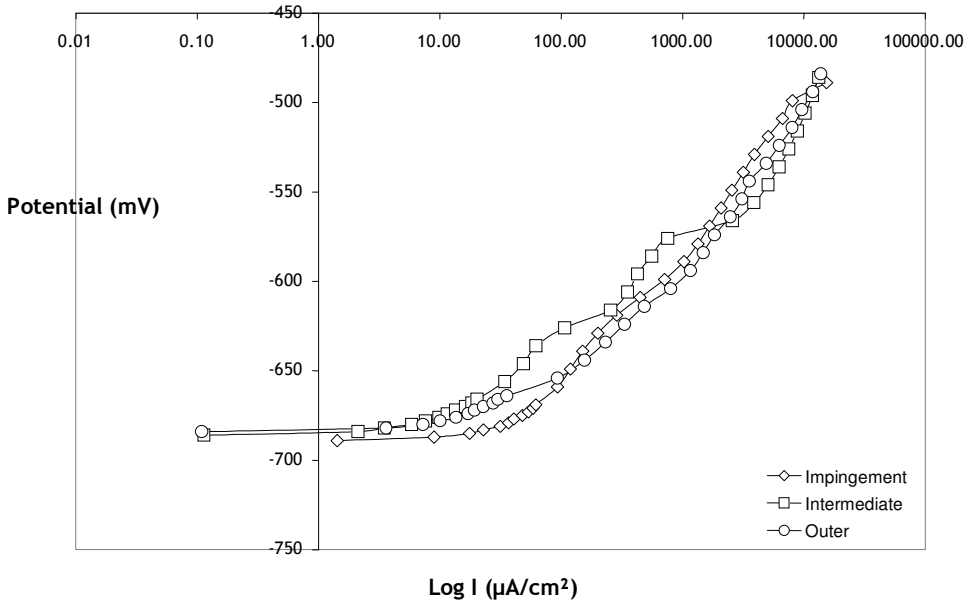

Figure 6-25. Full anodic polarisation curves for experiments in CO_2 saturated brine containing 100 ppm corrosion inhibitor. Fluid impingement velocity is 8 m/s.

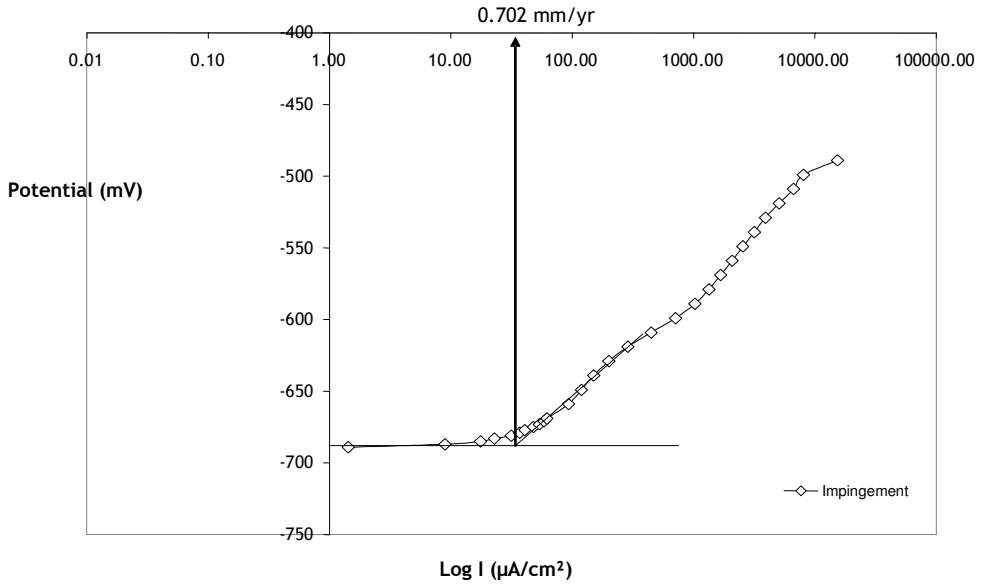

Figure 6-26. Extrapolated corrosion rate for 8 m/s full anodic polarisation curve for the impingement zone in CO_2 saturated brine with 100ppm inhibitor, pH 5.7.

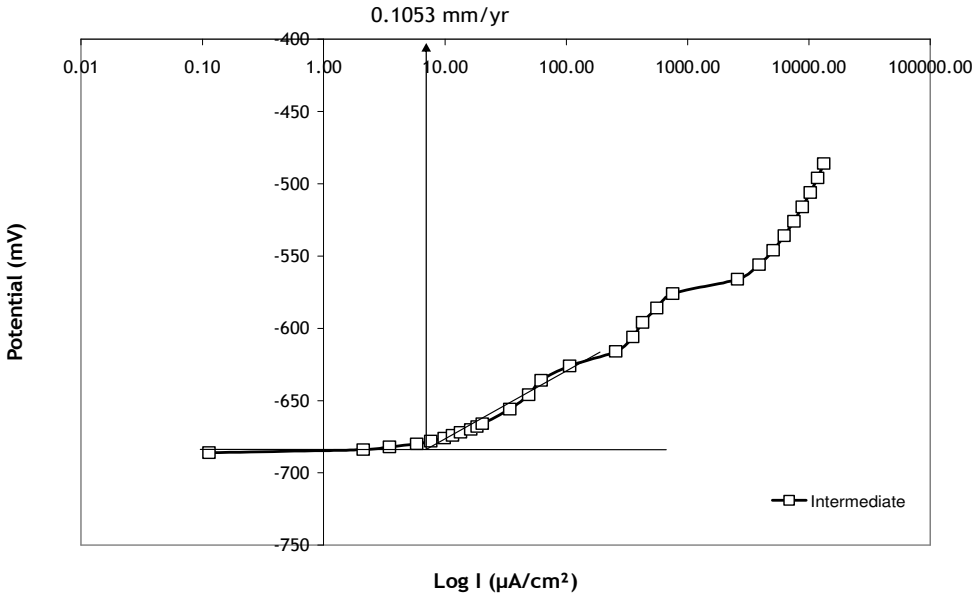

Figure 6-27. Extrapolated corrosion rate for 8 m/s full anodic polarisation curve for the intermediate zone in CO_2 saturated brine with 100ppm inhibitor, pH 5.7.

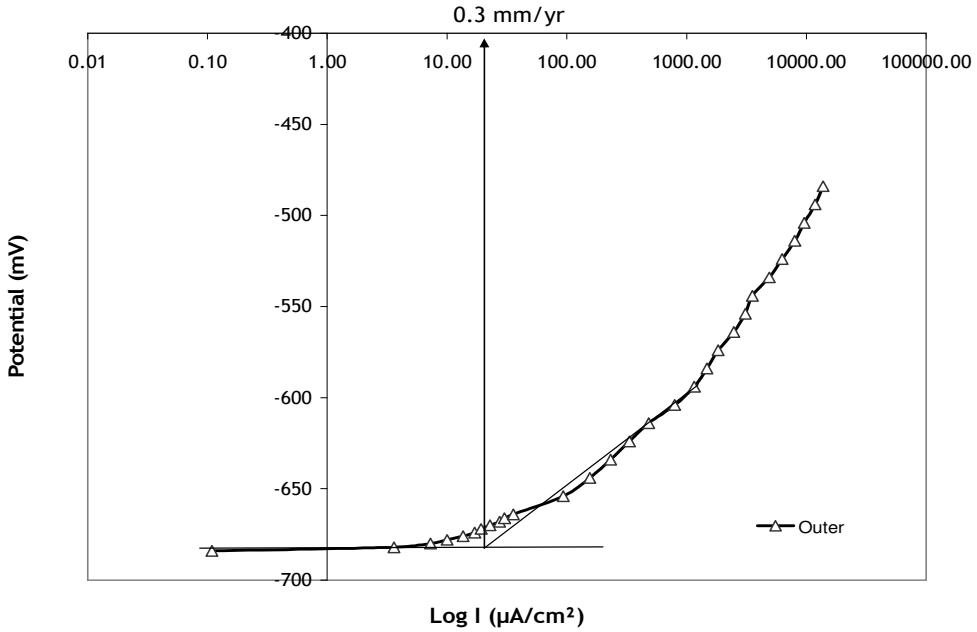

Figure 6-28. Extrapolated corrosion rate for 8 m/s full anodic polarisation curve for the intermediate zone in CO_2 saturated brine with 100ppm inhibitor, pH 5.7.

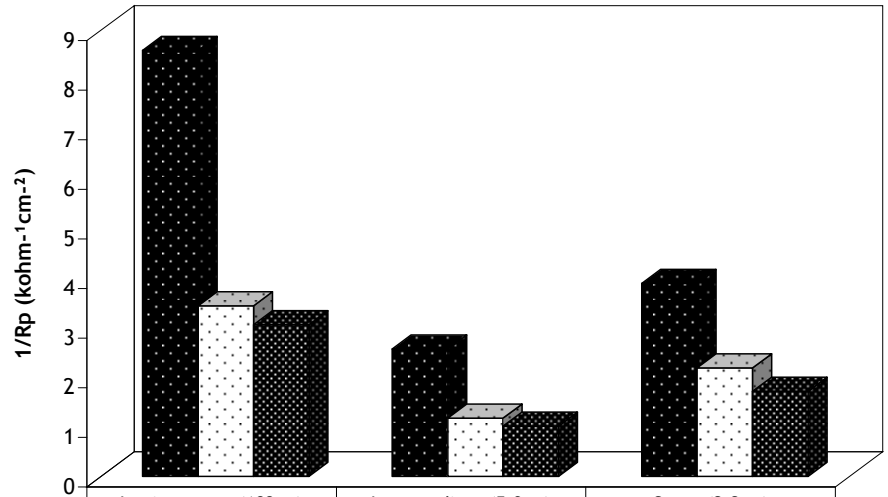

	Impingement (183pa)	Intermediate (5.9pa)	Outer (2.2pa)
4 Hours	8.6	2.6	3.9
15 Hours	3.4	1.2	2.2
24 Hours	3.1	1.0	1.7

Figure 6-29. Anodic linear polarisation results for tests in 8 m/s CO_2 saturated flow with 100 ppm inhibitor.

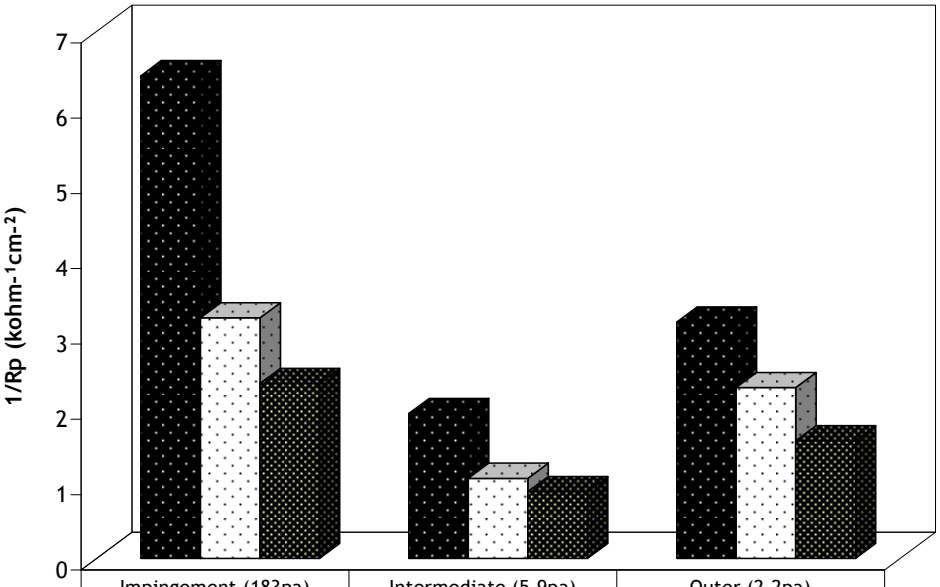

	Impingement (183pa)	Intermediate (5.9pa)	Outer (2.2pa)
4 Hours	6.4	1.9	3.1
15 Hours	3.2	1.1	2.3
24 Hours	2.3	0.9	1.6

Figure 6-30. Cathodic linear polarisation results for tests in 8 m/s CO_2 saturated flow with 100 ppm inhibitor.

6.4.2 Tests at 2 m/s

Figure 6-31 shows the 2m/s full anodic polarisation curves for CO_2 saturated tests containing 100 ppm corrosion inhibitor. The values of E_{corr} for all three zones are within 1 mV of each other and are observed to be -719 mV, -720 mV and -720 mV for the impingement, intermediate and outer zones respectively.

The extrapolated corrosion rates as observed by Figures 6-32, 6-33 and 6-34 show corrosion rates of 1.0 mm/year and 0.7 mm/year for the impingement and outer zones. The intermediate zone however shows a significantly lower corrosion rate compared to the impingement and outer zones with the rate extrapolated as 0.1 mm/year.

Figures 6-35 and 6-36 show the anodic and cathodic linear polarisation resistance plots for the tests at 2 m/s. The intermediate zone is shown to have the lowest corrosion rate on both plots, which is in agreement with the full polarisation results.

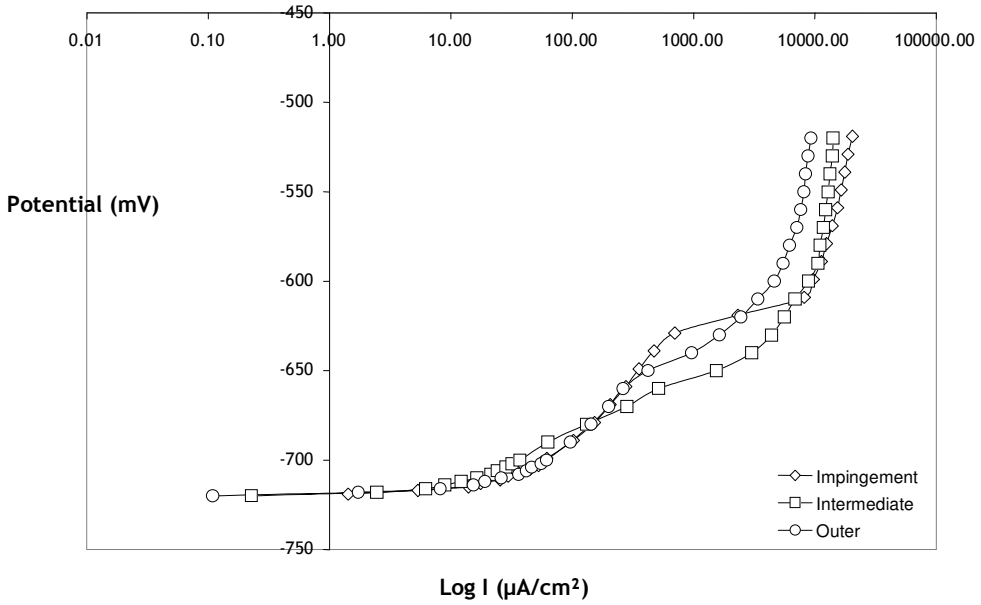

Figure 6-31. Full anodic polarisation curves for tests in CO_2 saturated brine containing 100 ppm inhibitor. Fluid impingement velocity is 2 m/s.

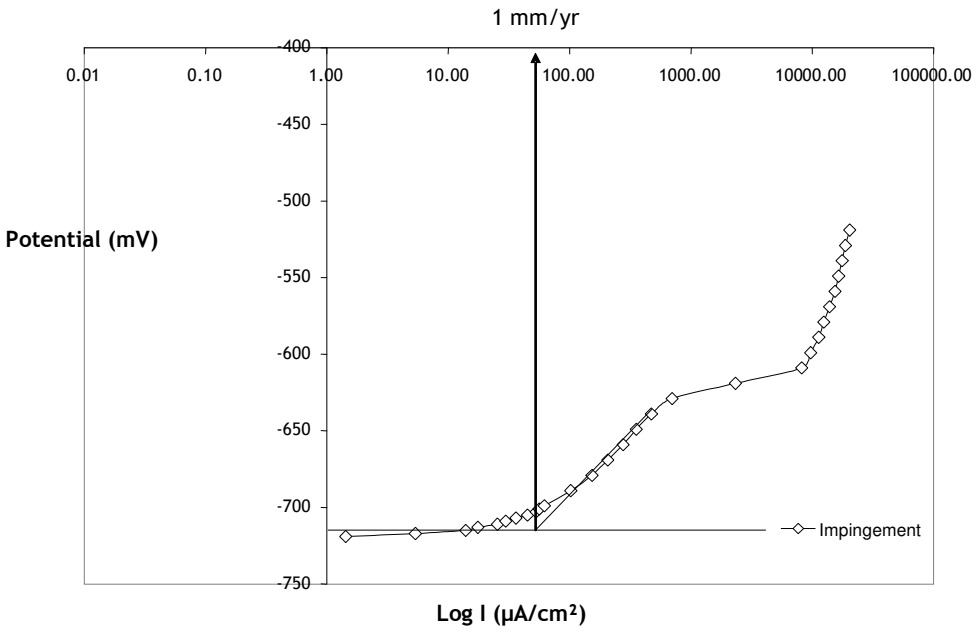

Figure 6-32. Extrapolated corrosion rate for 2 m/s full anodic polarisation curve for the impingement zone in CO_2 saturated brine with 100ppm inhibitor, pH 5.5

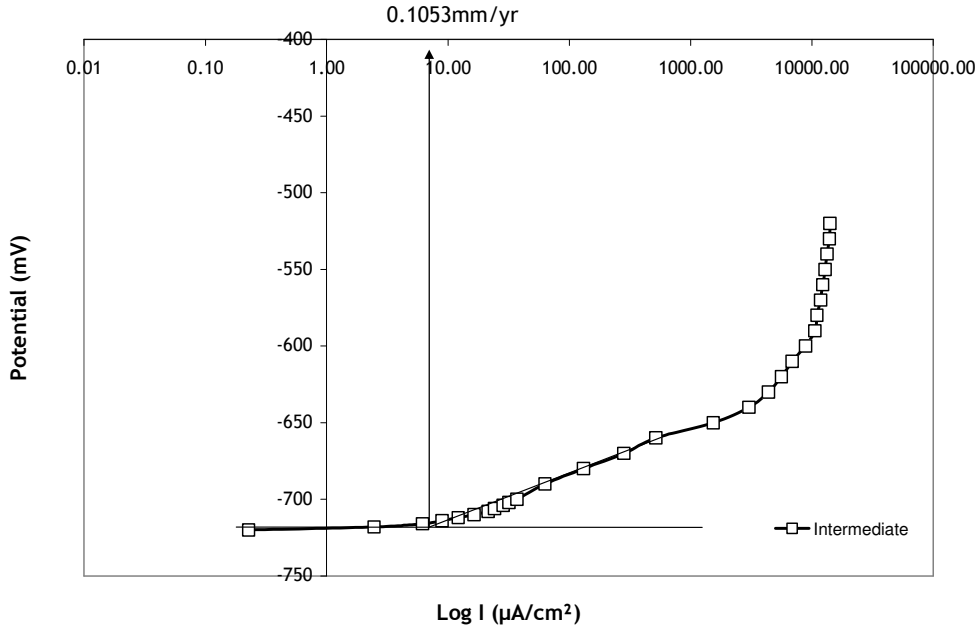

Figure 6-33. Extrapolated corrosion rate for 2 m/s full anodic polarisation curve for the intermediate zone in CO_2 saturated brine with 100ppm inhibitor, pH 5.5

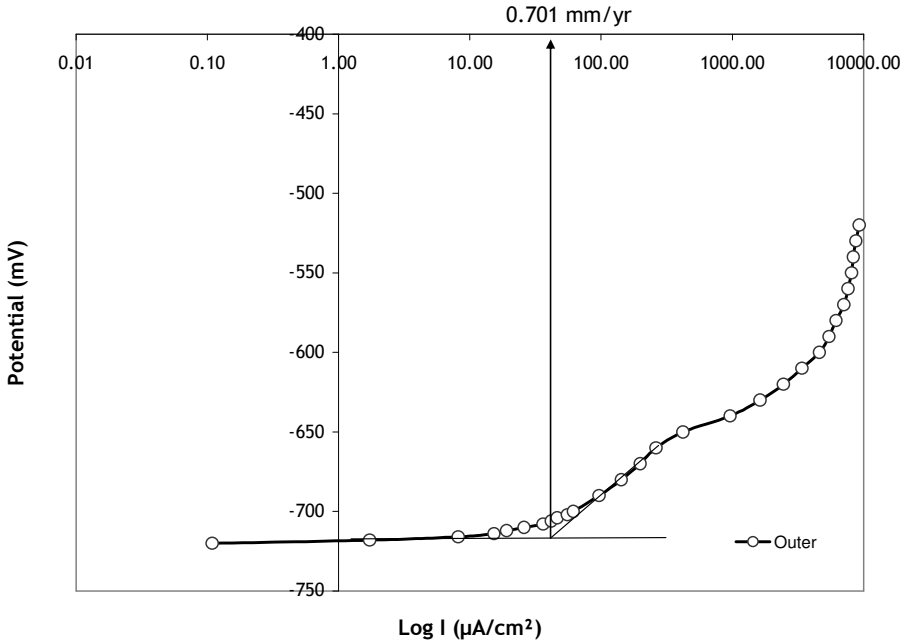

Figure 6-34. Extrapolated corrosion rate for 2 m/s full anodic polarisation curve for the outer zone in CO_2 saturated brine with 100ppm inhibitor, pH 5.5

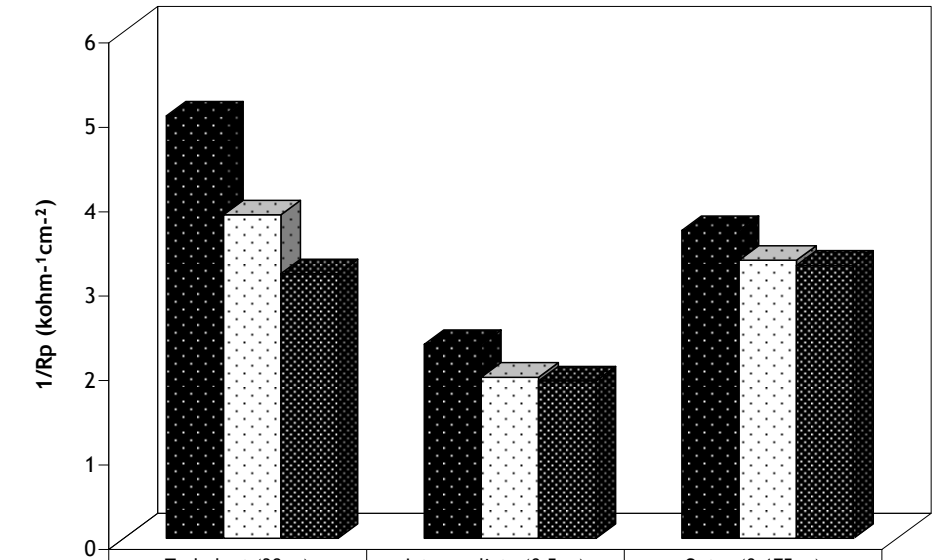

	Turbulent (38pa)	Intermediate (0.5pa)	Outer (0.175pa)
4 Hours	5.0	2.3	3.6
15 Hours	3.8	1.9	3.3
24 Hours	3.1	1.9	3.2

Figure 6-35. Anodic linear polarisation results for tests in 2 m/s CO_2 saturated flow with 100 ppm inhibitor.

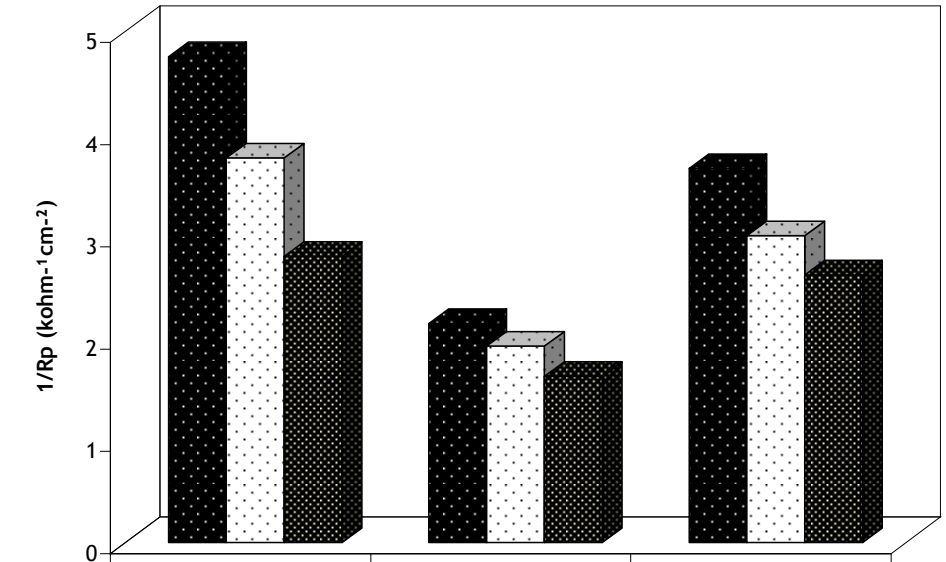

	Turbulent (38pa)	Intermediate (0.5pa)	Outer (0.175pa)
4 Hours	4.8	2.1	3.7
15 Hours	3.8	1.9	3.0
24 Hours	2.8	1.6	2.6

Figure 6-36. Cathodic linear polarisation results for tests in 2 m/s CO_2 saturated flow with 100 ppm inhibitor.

In summary, the benefit of using a corrosion inhibitor has been established. The corrosion rates of all three hydrodynamic zones at both velocities have shown reductions in comparison to results in CO_2 saturated conditions. At both velocities, the intermediate zone benefits the most and has the lowest corrosion rate. A time effect is also noted as the linear polarisation resistance scans show a continual reduction in corrosion rate with the passage of time.

Table 6-9 shows a comparison of the electrode potential values, E_{corr}, at both velocities. The 8 m/s conditions have a more positive value of E_{corr} in all three hydrodynamic zones compared to the 2 m/s.

Table 6-10 compares the extrapolated corrosion rates obtained from full polarisation after 24 hours and suggest better inhibitor film formation in the intermediate zone at both velocities. The corrosion rate in the intermediate zone at both velocities is extrapolated as 0.1 mm/year. The impingement zone has the highest corrosion rate as expected but surprisingly, both the impingement and

outer zones exhibit higher corrosion rates at 2 m/s than at 8 m/s with the intermediate zone having the same corrosion rate at both velocities. The linear polarisation resistance scans confirm the above trends and add confirmation of the above observations noted through Tables 6-11 and 6-12.

Table 6-9

E_{corr} values for tests at 8 m/s and 2 m/s. Table shows values of E_{corr} in each hydrodynamic zone. Values are in mV

	Impingement	Intermediate	Outer
8 m/s	-689	-686	-684
2 m/s	-719	-720	-720

Table 6-10

Corrosion rates extrapolated from full polarisation curves after 24 hours in CO_2 saturated brine with 100 ppm inhibitor. Extrapolated values are in mm/year

	Impingement	Intermediate	Outer
8 m/s	0.7	0.1	0.3
2 m/s	1.0	0.1	0.7

Table 6-11

Linear polarisation resistance values (1/Rp) after 24 hours in CO_2 saturated flow at 8 m/s with 100 ppm inhibitor. Values are in $kohm^{-1}cm^{-2}$

	Impingement	Intermediate	Outer
Anodic	3.1	1.0	1.7
Cathodic	2.3	0.9	1.6

Table 6-12

Linear polarisation resistance values after 24 hours in CO_2 saturated flow at 2 m/s with 100 ppm inhibitor. Values are in $kohm^{-1}cm^{-2}$

	Impingement	Intermediate	Outer
Anodic	3.1	1.9	3.2
Cathodic	2.8	1.6	2.6

6.5 Tests in CO_2 saturated brine with 150 ppm corrosion inhibitor

6.5.1 Tests at 8 m/s

Figure 6-37 illustrates the full anodic polarisation curves for the 8 m/s tests containing 150 ppm inhibitor. From Figure 6-37, the impingement and outer zones are observed to have higher corrosion rates compared to the intermediate.

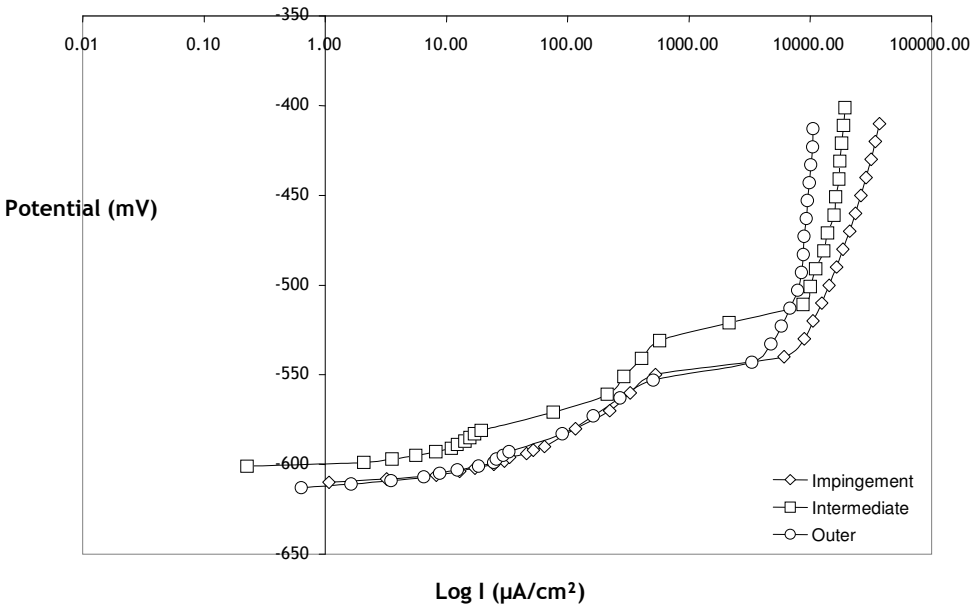

Figure 6-37. Anodic full polarisation curves for 8 m/s flow saturated with CO_2 and containing 150 ppm inhibitor.

Figures 6-38 to 6-40 show extrapolated corrosion rates for the impingement, intermediate and outer zones. The extrapolated values of corrosion rates are 0.5 mm/year, 0.1 mm/year and 0.2 mm/year respectively. The impingement zone has the highest corrosion rate but has seen a reduction from 0.7 mm/year at 100 ppm to 0.5 mm/year at 150 ppm. The outer zone also has a concentration reduction from 0.3 mm/year at 100 ppm to 0.2 mm/year at 150 ppm. The intermediate zone could be considered as having no major reduction related to the increase in concentration.

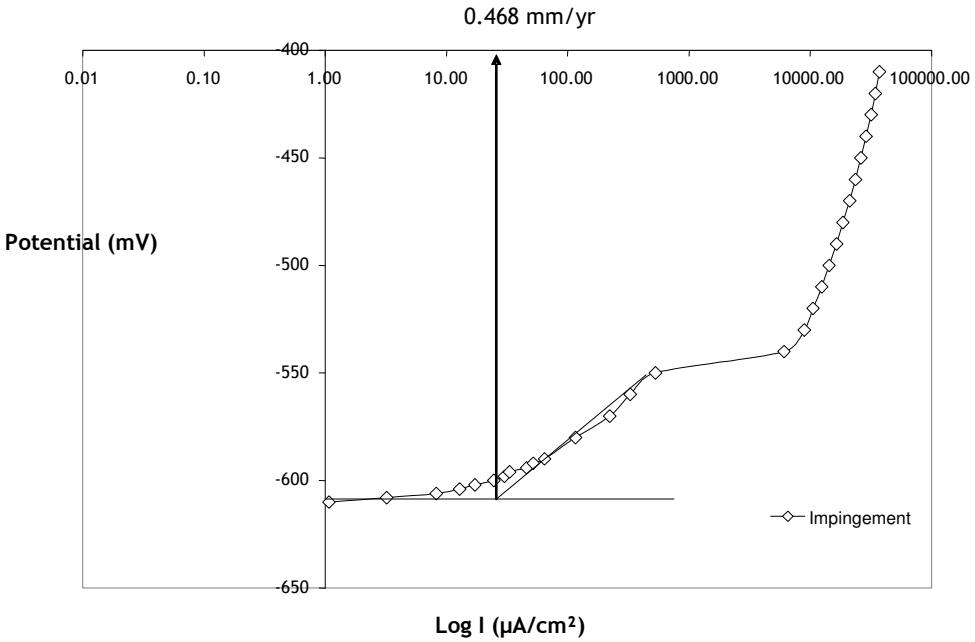

Figure 6-38. Extrapolated corrosion rate for the impingement zone at 8 m/s flow saturated with CO_2 and containing 150 ppm inhibitor, pH 6

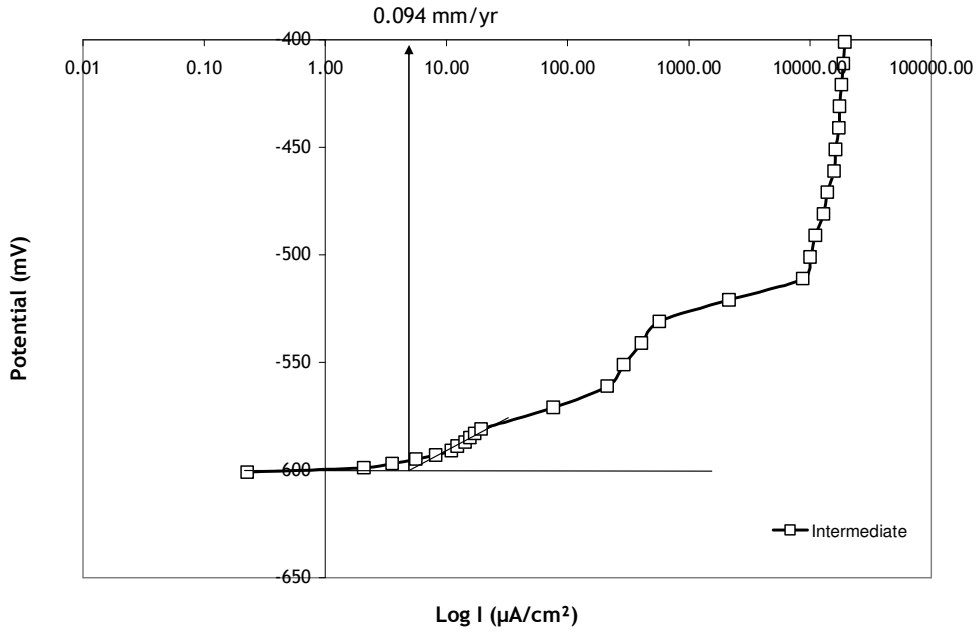

Figure 6-39. Extrapolated corrosion rate for the intermediate zone at 8 m/s flow saturated with CO_2 and containing 150 ppm inhibitor, pH 6

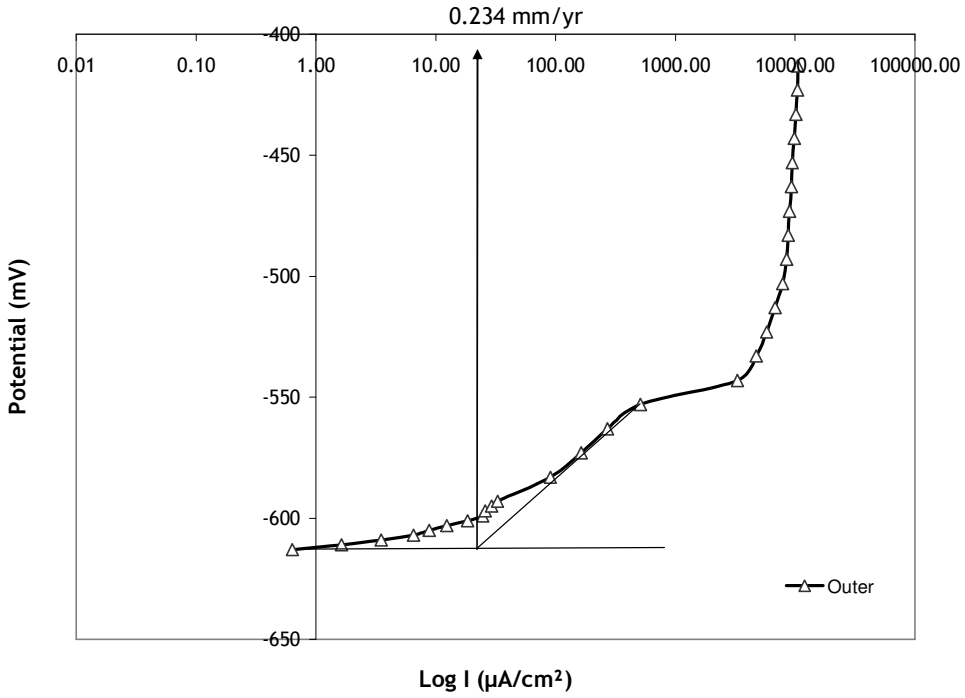

Figure 6-40. Extrapolated corrosion rate for the outer zone at 8 m/s flow saturated with CO_2 and containing 150 ppm inhibitor, pH 6

Figures 6-41 and 6-42 show the anodic and cathodic linear polarisation 1/Rp values for tests with 150 ppm inhibitor. The anodic scans show a time related reduction in corrosion rate indicating the inhibitor is working more effectively with the passage of time. This observation is not as consistent for the cathodic scans but a reduction in corrosion rate is still observed in the intermediate and outer zones. For both the anodic and cathodic scans, the intermediate zone has the lowest corrosion rate while the impingement zone the highest.

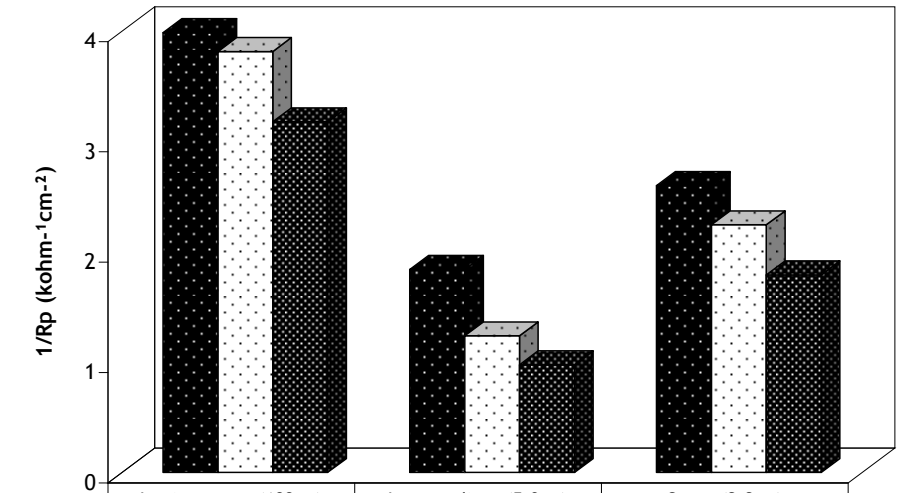

	Impingement (183pa)	Intermediate (5.9pa)	Outer (2.2pa)
4 Hours	4.0	1.8	2.6
15 Hours	3.8	1.2	2.2
24 Hours	3.2	1.0	1.8

Figure 6-41. Anodic linear polarisation results for tests in 8 m/s CO_2 saturated flow with 150 ppm inhibitor.

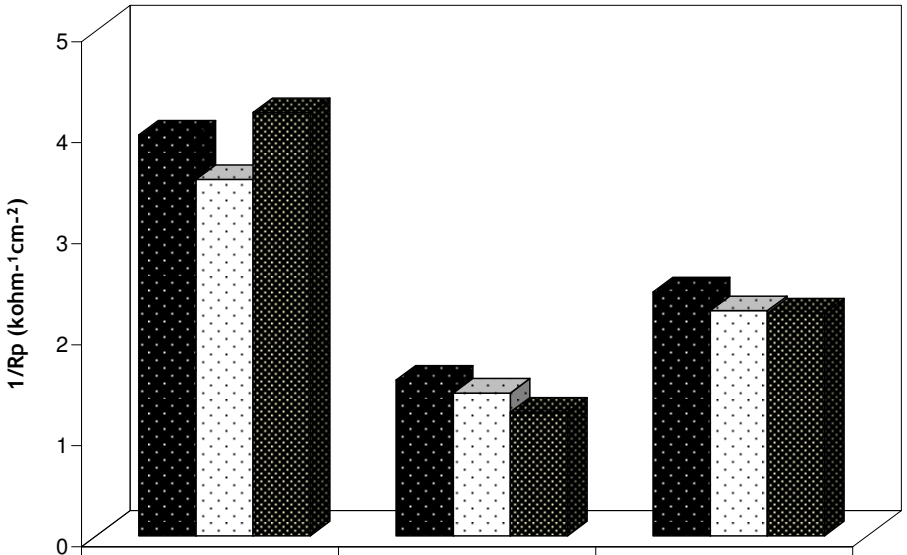

	Impingement (183pa)	Intermediate (5.9pa)	Outer (2.2pa)
4 Hours	4.0	1.5	2.4
15 Hours	3.5	1.4	2.2
24 Hours	4.2	1.2	2.2

Figure 6-42. Cathodic linear polarisation results for tests in 8 m/s CO_2 saturated flow with 150 ppm inhibitor.

6.5.2 Tests at 2 m/s

Tests at 2 m/s with 150 ppm inhibitor again show reduced corrosion rates in comparison to tests without inhibitor. The intermediate zone has the lowest corrosion rate while the impingement zone has the highest followed by the outer zone. Figure 6-43 shows the full anodic polarisation curves with the values of E_{corr} for the impingement and the intermediate zones being -690 mV and -692 mV respectively. The outer zone has a more positive value of -682 mV. Figures 6-44 to 6-46 show the extrapolated corrosion rates for the impingement, intermediate and outer zones. The respective extrapolated corrosion rates are 0.6 mm/year, 0.2 mm/year and 0.5 mm/year respectively.

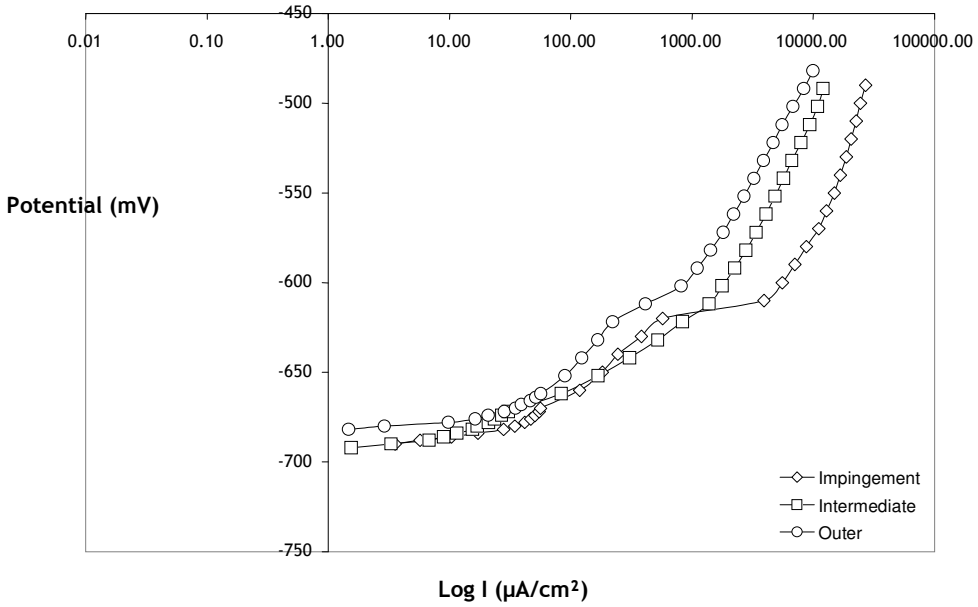

Figure 6-43. Anodic full polarisation curves for tests at 2 m/s flow saturated with CO_2 and containing 150 ppm inhibitor.

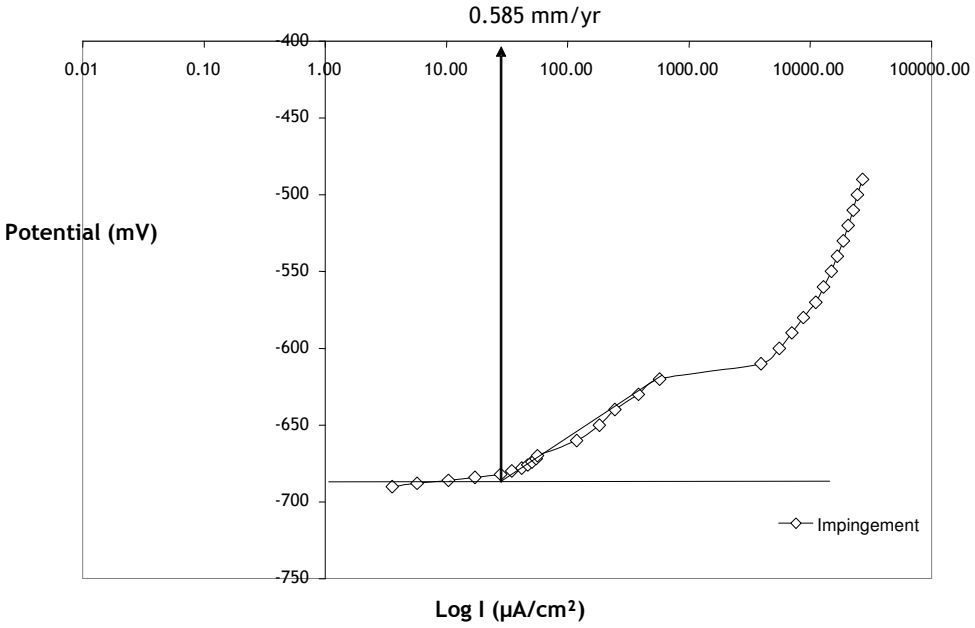

Figure 6-44. Extrapolated corrosion rate for 2 m/s full anodic polarisation curve for the impingement zone in CO_2 saturated brine with 150ppm inhibitor, pH 5.4

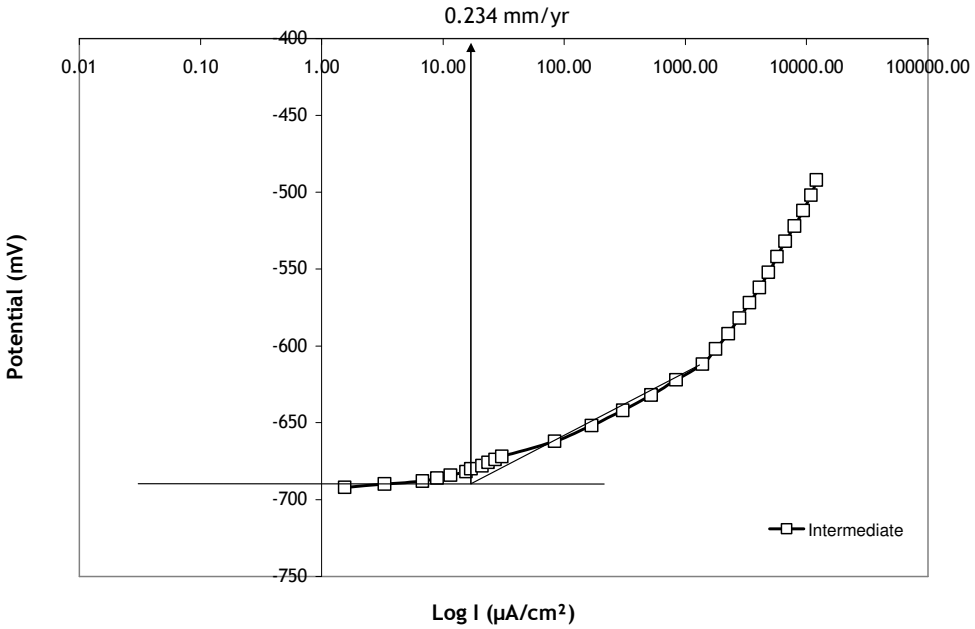

Figure 6-45 Extrapolated corrosion rate for 2 m/s full anodic polarisation curve for the intermediate zone in CO_2 saturated brine with 150ppm inhibitor, pH 5.4

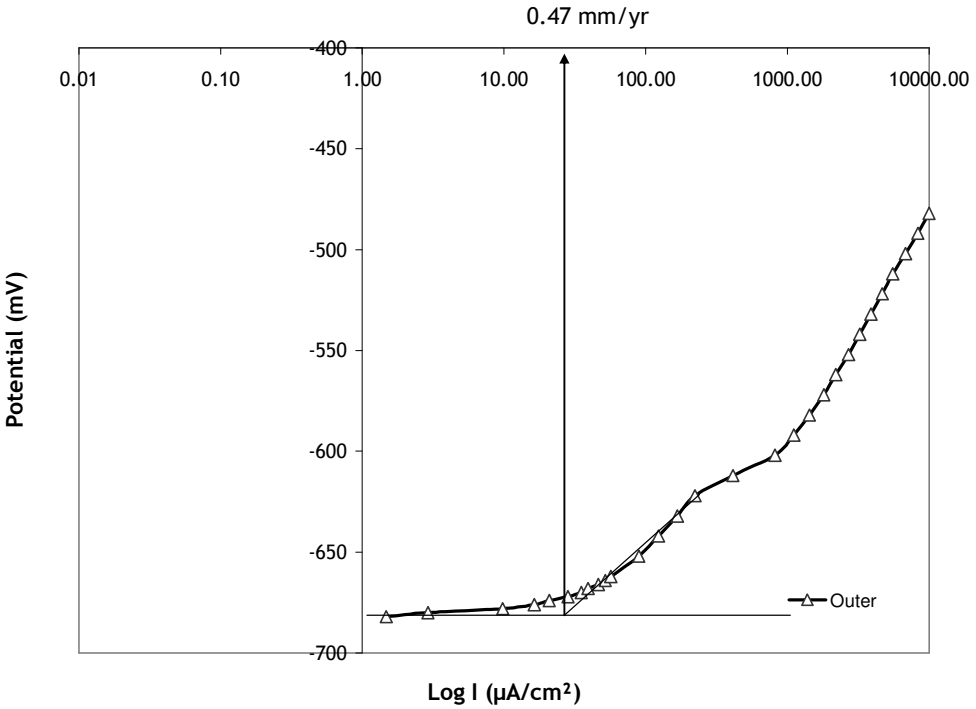

Figure 6-46. Extrapolated corrosion rate for 2 m/s full anodic polarisation curve for the outer zone in CO_2 saturated brine with 150ppm inhibitor pH 5.4

Figures 6-47 and 6-48 show the anodic and cathodic linear polarisation resistance scans for the 150 ppm inhibitor concentration. Figure 6-47 shows the anodic scan results and after 24 hours, the intermediate zone has the lowest corrosion rate at all times with the impingement and outer zones having almost similar rates. The cathodic scans are represented by Figure 6-48 and also confirm the intermediate zone as having the lowest corrosion rate. The impingement and outer zones follow respectively. It is however noted that the difference in corrosion rate between the outer and impingement zones is negligible but would favour the impingement zone if shear stress values are taken into account. Considering the values of shear in each zone, the impingement zone could arguably be presented as benefiting from the 150 ppm concentration of inhibitor.

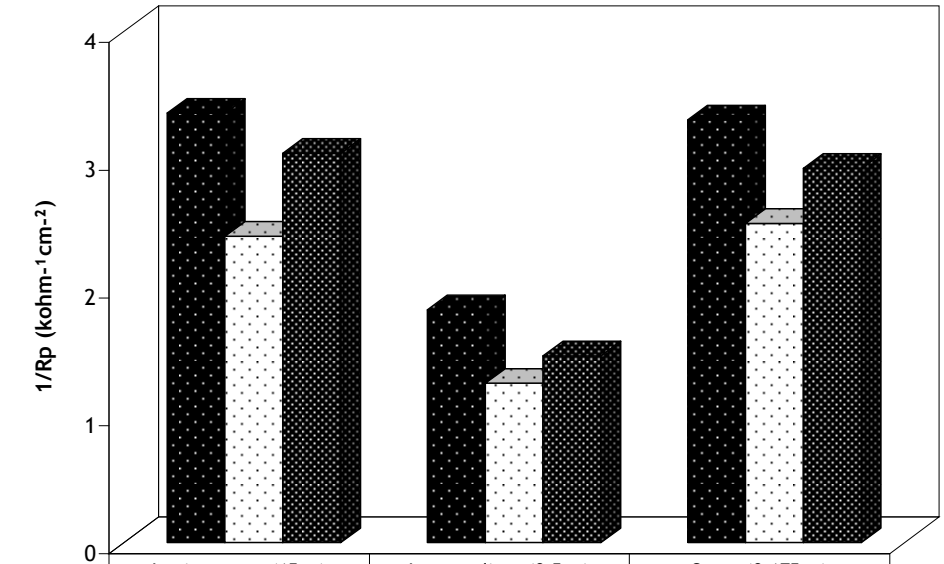

	Impingement (15pa)	Intermediate (0.5pa)	Outer (0.175pa)
4 Hours	3.4	1.8	3.3
15 Hours	2.4	1.2	2.5
24 Hours	3.0	1.5	2.9

Figure 6-47. Anodic linear polarisation resistances for 2 m/s flow saturated with CO_2 and containing 150 ppm inhibitor.

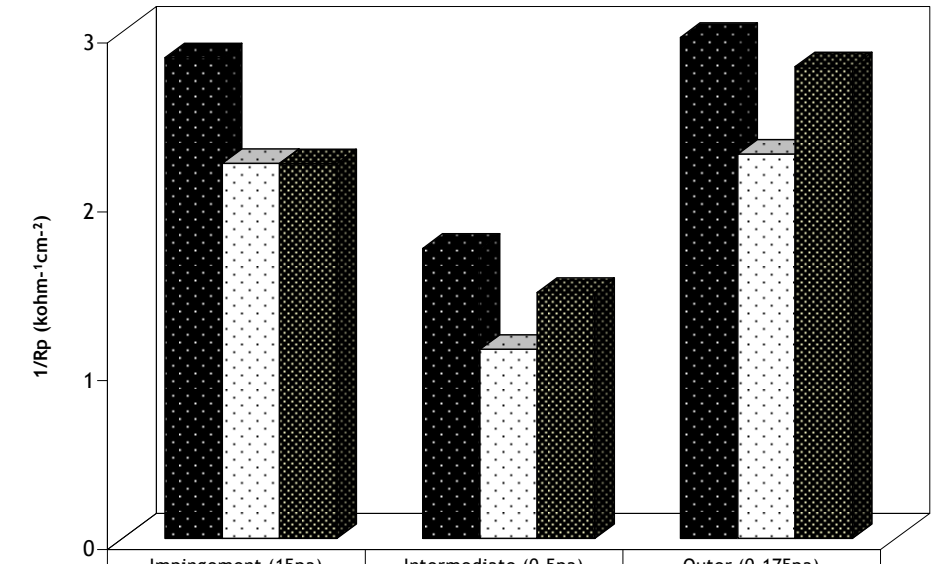

	Impingement (15pa)	Intermediate (0.5pa)	Outer (0.175pa)
4 Hours	2.8	1.7	3.0
15 Hours	2.2	1.1	2.3
24 Hours	2.2	1.5	2.8

Figure 6-48. Cathodic linear polarisation resistances for 2 m/s flow saturated with CO_2 and containing 150 ppm inhibitor.

The opening section of this chapter reported a significant reduction in corrosion rates when 100 ppm of the corrosion inhibitor is used. Results in this section have been established by using 150 ppm of inhibitor in order to ascertain if increased concentrations further reduce corrosion rates. The tables below summarise the results obtained in this section.

Table 6-13 shows the values of electrode potential, E_{corr} for the 8 m/s and 2 m/s velocities with the high velocity conditions having more positive values of E_{corr} compared to their corresponding zones at low velocity. Table 6-14 shows the extrapolated corrosion rates after 24 hours and surprisingly, in all three hydrodynamic zones, the high velocity conditions (8 m/s) have lower corrosion rates compared to 2 m/s velocity.

Therefore, increasing the concentration of the inhibitor seems to benefit the 8 m/s flow conditions with these regions not only having better corrosion rates than the 2 m/s conditions but also showing some improvement in corrosion rates compared to results obtained with 100 ppm inhibitor.

Table 6-13

E_{corr} values for tests at 8 m/s and 2 m/s. Table shows values of E_{corr} in each hydrodynamic zone. Values are in mV

	Impingement	Intermediate	Outer
8 m/s	-610	-601	-613
2 m/s	-690	-692	-682

Table 6-14

Corrosion rates extrapolated from full polarisation curves after 24 hours in CO_2 saturated brine with 100 ppm inhibitor. Extrapolated values are in mm/year

	Impingement	Intermediate	Outer
8 m/s	0.468	0.094	0.234
2 m/s	0.585	0.234	0.47

Table 6-15

Linear polarisation resistance values (1/Rp) after 24 hours in CO_2 saturated flow at 8 m/s with 150 ppm inhibitor. Values are in $kohm^{-1}cm^{-2}$

	Impingement	Intermediate	Outer
Anodic	3.2	1.0	1.8
Cathodic	4.2	1.2	2.2

Table 6-16

Linear polarisation resistance values(1/Rp) after 24 hours in CO_2 saturated flow at 2 m/s with 150 ppm inhibitor. Values are in $kohm^{-1}cm^{-2}$

	Impingement	Intermediate	Outer
Anodic	3.0	1.5	2.9
Cathodic	2.2	1.5	2.8

6.6 Tests with CO_2 saturated brine with 200 ppm inhibitor

6.6.1 Tests at 8 m/s

Figure 6-49 shows the full anodic polarisation curves for all three zones at 8 m/s flow. The values of E_{corr} for the impingement, intermediate and outer zones are observed to be -674 mV, -685 mV and -675 mV.

The extrapolated corrosion rates are presented by Figures 6-50 to 6-52. From the extrapolated corrosion rates, the intermediate zone has the lowest corrosion rate at 0.2 mm/year with the impingement having the highest at 0.7 mm/year. The extrapolated rate for the outer is 0.5 mm/year.

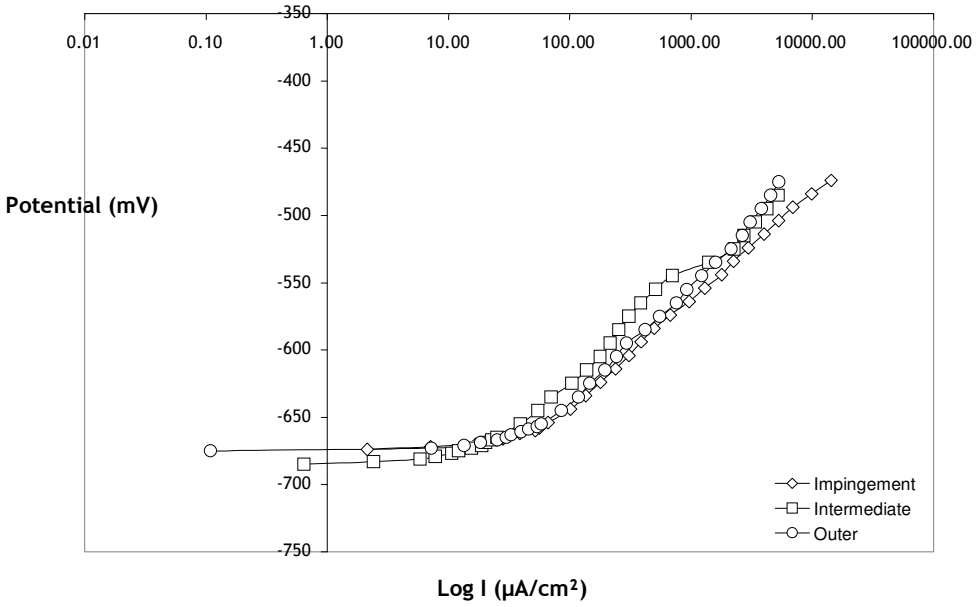

Figure 6-49. Anodic full polarisation curves for 8 m/s flow with 200 ppm inhibitor.

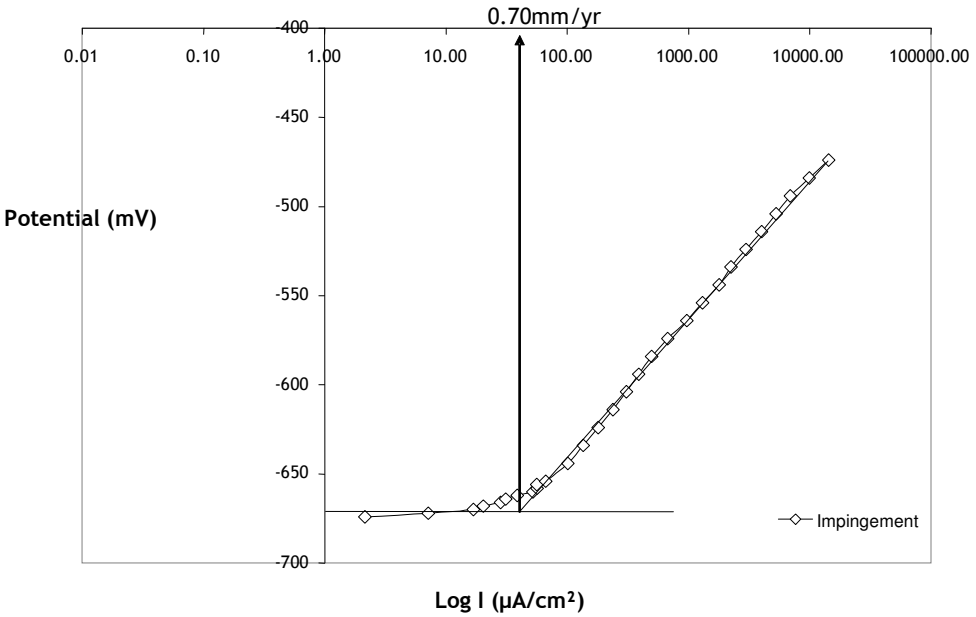

Figure 6-50. Extrapolated corrosion rate for the impingement zone at 8 m/s flow with 200 ppm inhibitor, pH 5.5

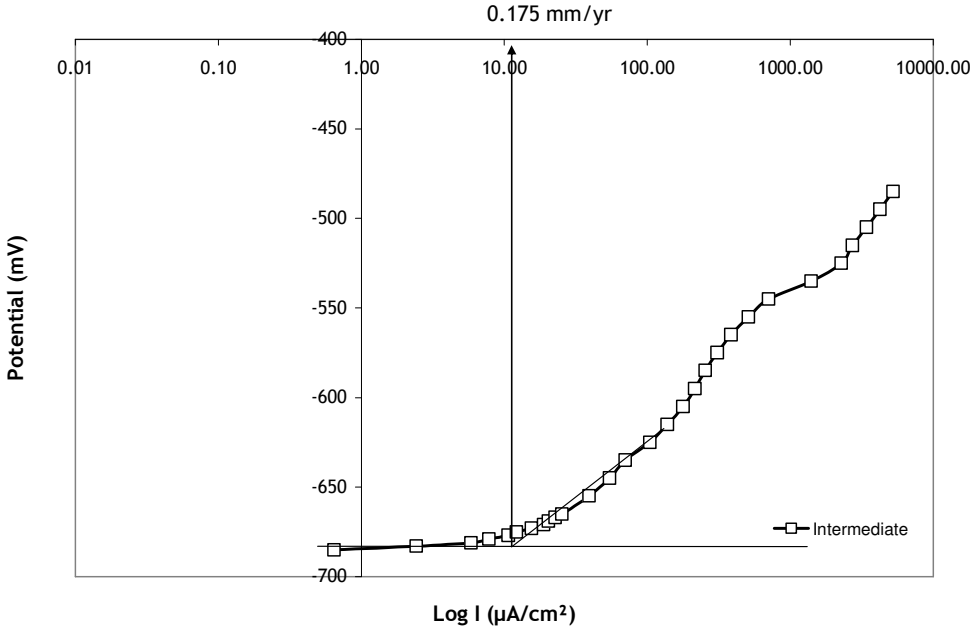

Figure 6-51. Extrapolated corrosion rate for the intermediate zone at 8 m/s flow with 200 ppm inhibitor, pH 5.5

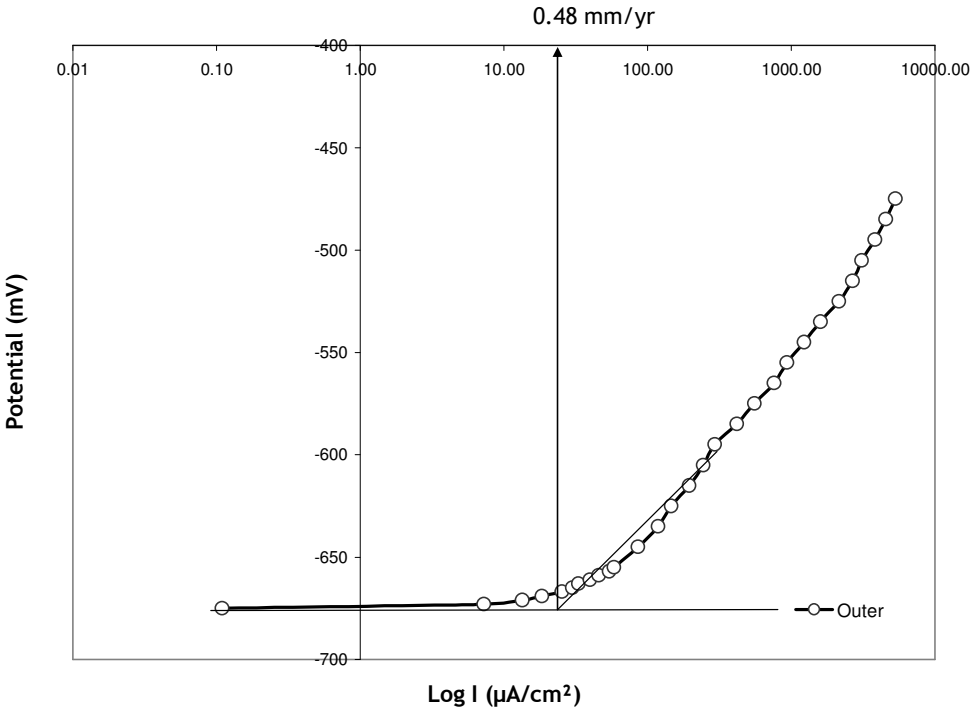

Figure 6-52. Extrapolated corrosion rate for the outer zone at 8 m/s with 200 ppm inhibitor.

Figures 6-53 and 6-54 show the linear polarisation values (1/Rp) for the anodic and cathodic scans respectively. Both the anodic and cathodic results confirm the intermediate zone as having the lowest corrosion rate with the impingement having the highest corrosion rate followed by the outer zone although the difference between the impingement and outer zones is marginal. The anodic and cathodic scans are in good agreement. For both the cathodic and anodic scans, a time related reduction in corrosion rate is noticed after 4 hours with a drop in 1/Rp in the impingement and outer zones.

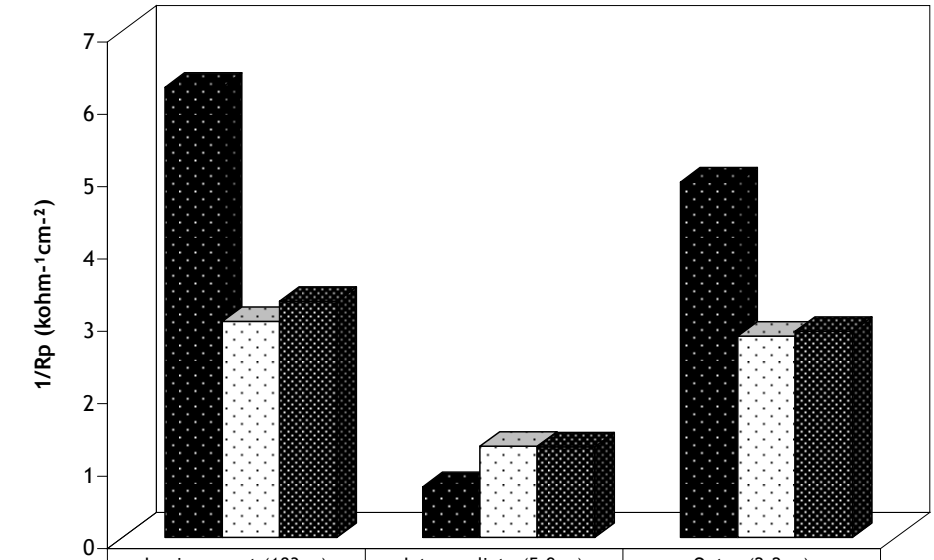

	Impingement (183pa)	Intermediate (5.9pa)	Outer (2.2pa)
4 Hours	6.2	0.7	4.9
15 Hours	3.0	1.3	2.8
24 Hours	3.3	1.3	2.9

Figure 6-53. Anodic polarisation resistances for 8 m/s flow with 200 ppm corrosion inhibitor. Values of average zone shear are indicated in Pascal's.

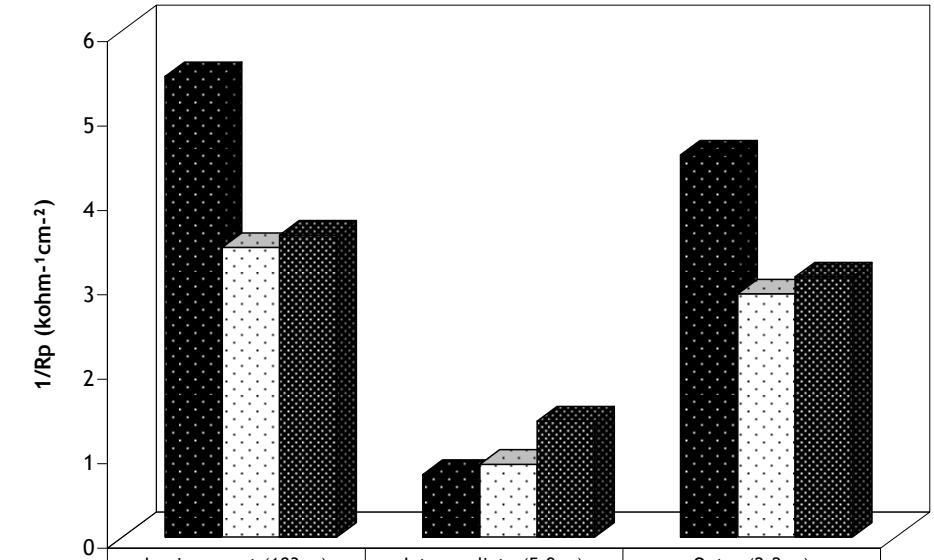

	Impingement (183pa)	Intermediate (5.9pa)	Outer (2.2pa)
4 Hours	5.5	0.7	4.5
15 Hours	3.4	0.9	2.9
24 Hours	3.6	1.4	3.1

Figure 6-54. Cathodic polarisation resistances for 8 m/s flow with 200 ppm corrosion inhibitor. Values of average zone shear are indicated in Pascal's.

6.6.2 Tests at 2 m/s

From Figure 6-55, the electrode potential values, E_{corr} in each hydrodynamic zone are spread out with the impingement zone being the most positive. The values of E_{corr} for the impingement, intermediate and outer zone are -679 mV, -696 mV and -704 mV respectively. The extrapolated corrosion rates are shown on Figures 6-56 to 6-58. The respective corrosion rates for the impingement, intermediate and outer zones are 0.35 mm/year, 0.10 mm/year and 0.58 mm/year. The intermediate zone again has the lowest value of corrosion rate and surprisingly the outer zone has the highest value.

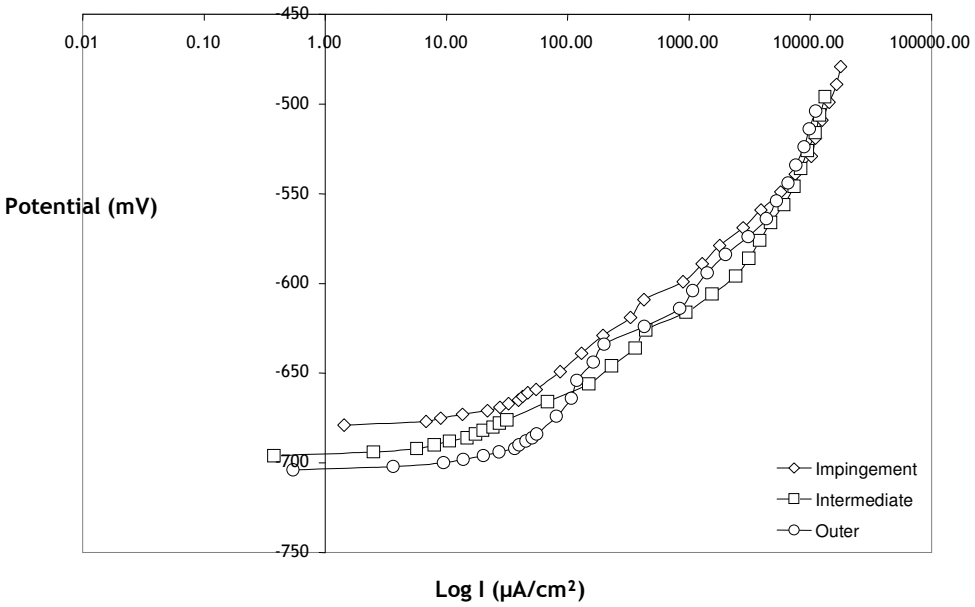

Figure 6-55. Anodic full polarisation curves after 24 hours for 2 m/s flow with 200 ppm corrosion inhibitor.

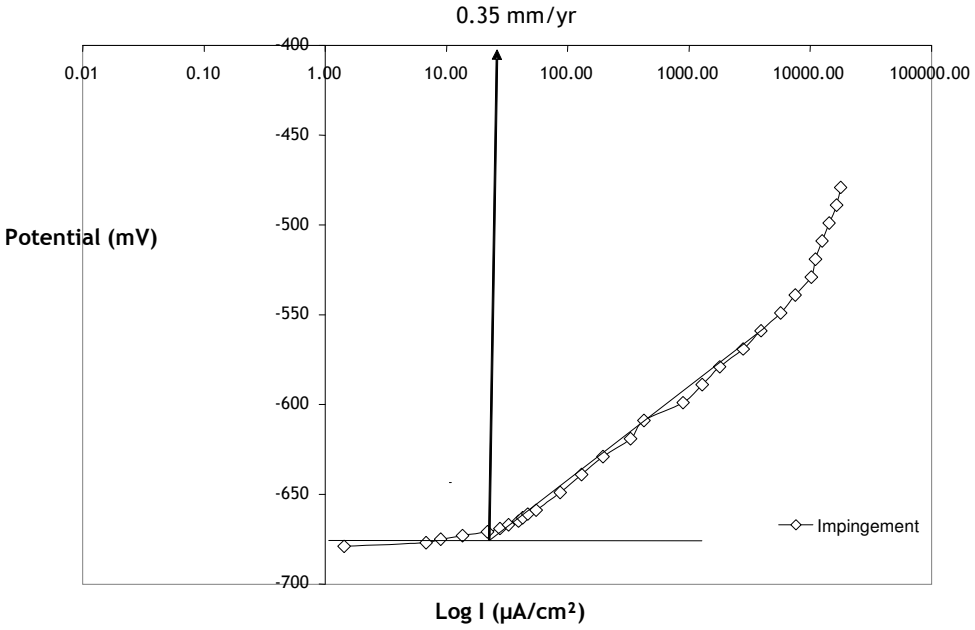

Figure 6-56. Extrapolated corrosion rate for the impingement zone at 2 m/s flow with 200 ppm inhibitor, pH 5.7

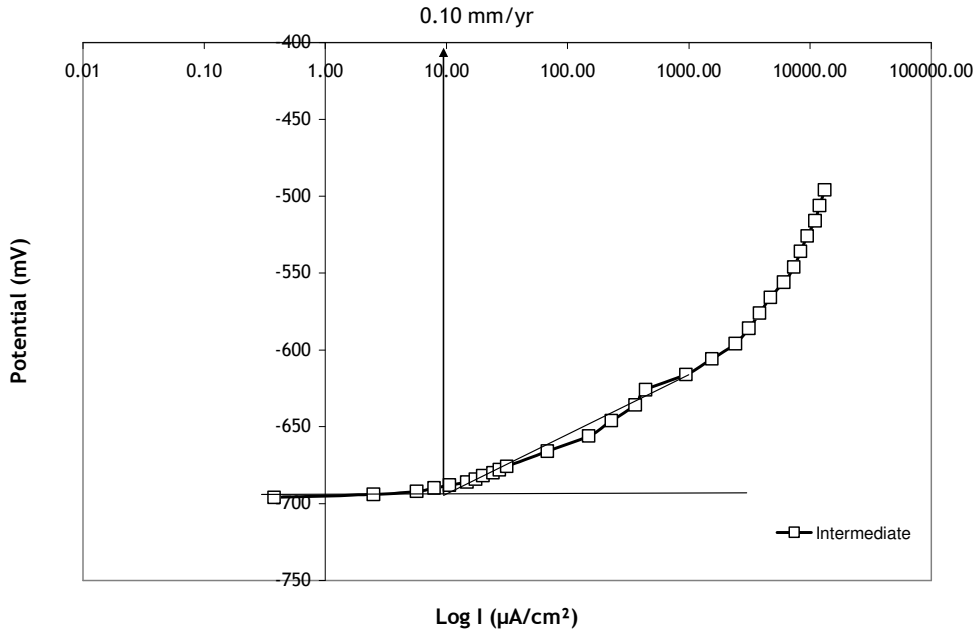

Figure 6-57. Extrapolated corrosion rate for the intermediate zone at 2 m/s flow with 200 ppm inhibitor, pH 5.7

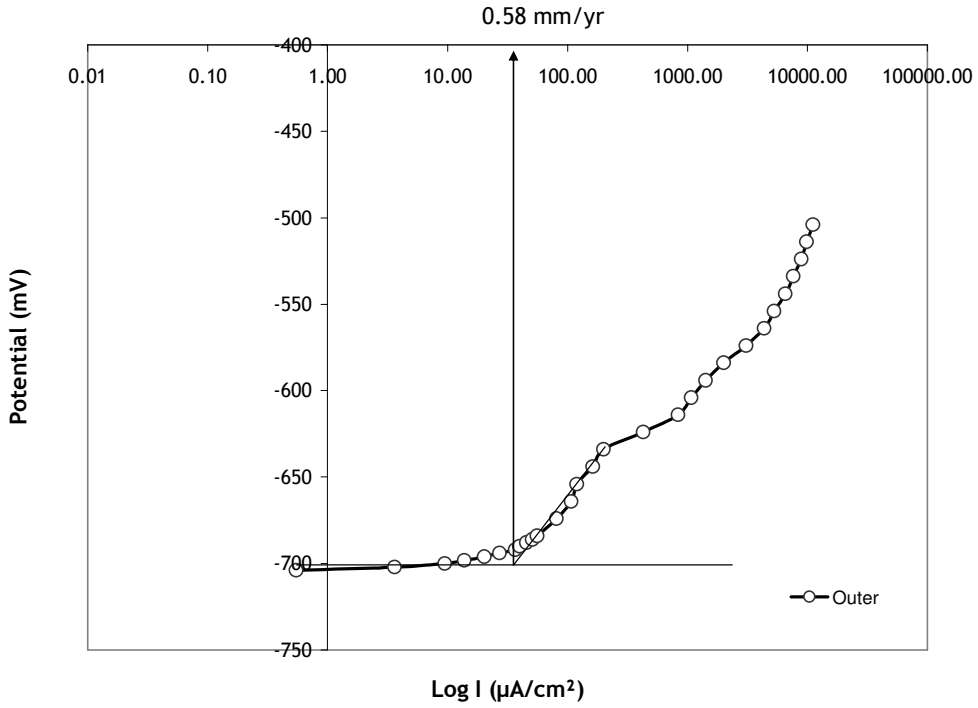

Figure 6-58 **Extrapolated corrosion rate for the outer zone at 2 m/s flow with 200 ppm inhibitor, pH 5.7**

Figures 6-59 and 6-60 show the anodic and cathodic values of (1/Rp). The intermediate zone is once more confirmed as having the lowest corrosion rate with the impingement and outer zones having rather similar values after 24 hours.

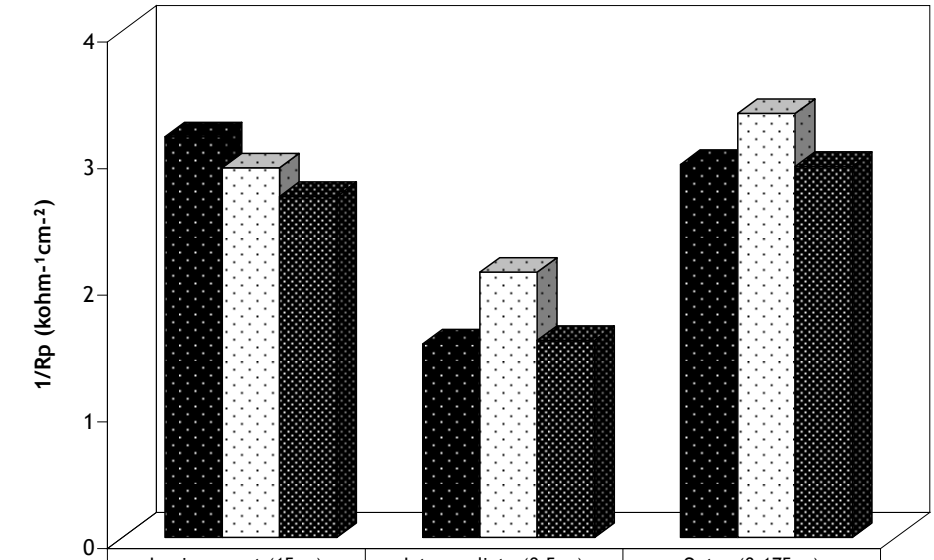

	Impingement (15pa)	Intermediate (0.5pa)	Outer (0.175pa)
4 Hours	3.2	1.5	2.9
15 Hours	2.9	2.1	3.4
24 Hours	2.7	1.6	2.9

Figure 6-59. Anodic polarisation resistances for 2 m/s flow with 200 ppm corrosion inhibitor. Values of average zone shear are indicated in Pascal's.

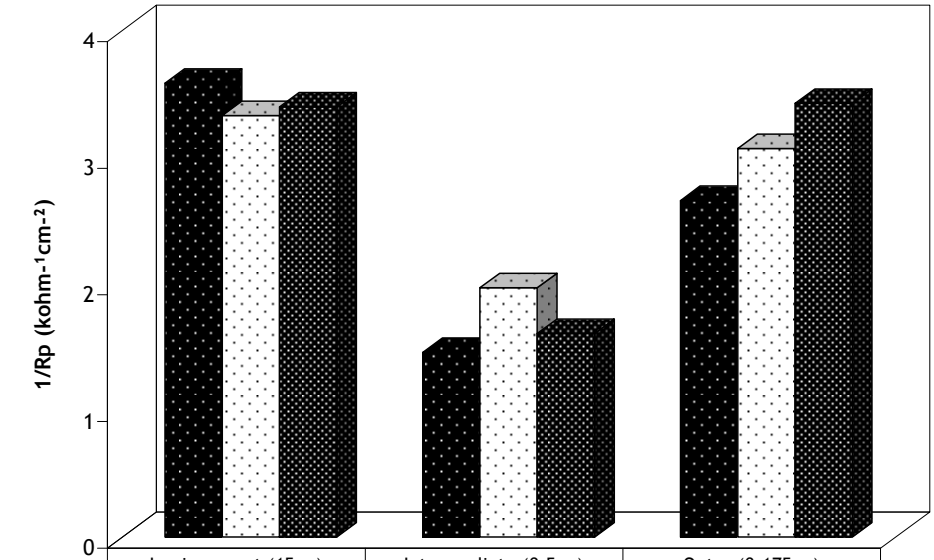

	Impingement (15pa)	Intermediate (0.5pa)	Outer (0.175pa)
4 Hours	3.6	1.5	2.7
15 Hours	3.3	2.0	3.1
24 Hours	3.4	1.6	3.4

Figure 6-60. Anodic polarisation resistances for 8 m/s flow with 200 ppm corrosion inhibitor. Values of average zone shear are indicated in Pascal's.

Table 6-17

E_{corr} values for tests at 8 m/s and 2 m/s. Table shows values of E_{corr} in each hydrodynamic zone at 200 ppm inhibitor concentration. Values are in mV

	Impingement	Intermediate	Outer
8 m/s	-674	-685	-675
2 m/s	-679	-696	-704

Table 6-18

Corrosion rates extrapolated from full polarisation curves after 24 hours in CO_2 saturated brine with 200 ppm inhibitor. Extrapolated values are in mm/year.

	Impingement	Intermediate	Outer
8 m/s	0.70	0.175	0.48
2 m/s	0.35	0.10	0.58

Table 6-19

Linear polarisation values (1/Rp) after 24 hours in CO_2 saturated flow at 8 m/s with 200 ppm inhibitor. Values are in $kohm^{-1}cm^{-2}$

	Impingement	Intermediate	Outer
Anodic	3.3	1.3	2.9
Cathodic	3.6	1.4	3.1

Table 6-20

Linear polarisation values (1/Rp) after 24 hours in CO_2 saturated flow at 2 m/s with 200 ppm inhibitor. Values are in $kohm^{-1}cm^{-2}$

	Impingement	Intermediate	Outer
Anodic	2.7	1.6	2.9
Cathodic	3.4	1.6	3.4

Tables 6-17 to 6-20 summarise this section of the chapter. Table 6-17 compares the values of E_{corr} between the two flow velocities and the E_{corr} values of all hydrodynamic zones at 8 m/s are observed to be more positive than values at 2 m/s. Table 6-18 shows the extrapolated corrosion rates and the corrosion rates at 2

m/s are observed to be lower in the impingement and intermediate zones with the outer zone value being higher than the 8 m/s rate.

Tables 6-19 and 6-20 show both the anodic and cathodic linear polarisation values (1/Rp) for the 8 m/s and 2 m/s velocities. At both velocities, the intermediate zone has the lowest corrosion rate with the impingement and outer zones having almost similar values of 1/Rp. The differences between the 8 m/s and 2 m/s corrosion rates are relatively small.

6.7 Summary

To summarise this chapter, Figures 6-61 to 6-64 show a summary of all conditions considered within this chapter and monitored by electrochemical techniques.

Figure 6-61 shows the E_{corr} values after 24 hours and it is clear that the more severe hydrodynamic conditions are associated with a more positive value of E_{corr} in all conditions with this characterised by the more positive E_{corr} values of tests at 8 m/s compared to 2 m/s. In aerated conditions, this observation is also the case at both velocities where the impingement zone is more positive than the intermediate and outer zones respectively. This large distribution of E_{corr} is likely to have significance on galvanic activity between hydrodynamic zones and this will be discussed in the next chapter. Introducing CO_2 shifts E_{corr} negative and reduces the E_{corr} difference between hydrodynamic zones. The inhibitor shifts the E_{corr} values of all zones positive whilst reducing the corrosion rate as shown earlier. This reduction in corrosion rate is confirmed both by full polarisation and by linear polarisation with a concentration of 150 ppm being more effective at reducing corrosion rates in all three hydrodynamic zones and at both velocities.

Figure 6-62 shows the extrapolated corrosion rates for both the 8 m/s and 2 m/s velocities. From Figure 6-62, the CO_2 extrapolated corrosion rates at 2 m/s are observed to be higher than the CO_2 corrosion rates at 8 m/s. This observation is in all three hydrodynamic zones.

Figures 6-63 and 6-64 show the anodic and cathodic values of 1/Rp. From the figures, it is observed that both the anodic and cathodic scan show a similar observation to the extrapolated corrosion rates where the 2 m/s velocity has higher

corrosion rates compared to the 8 m/s velocity. A significant reduction in 1/Rp is also observed in the tests containing inhibitor.

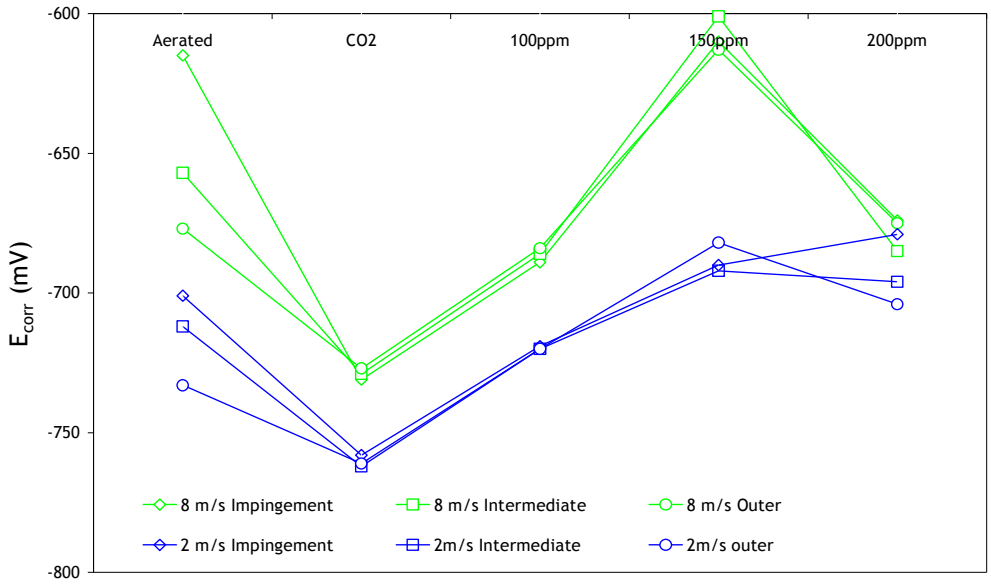

Figure 6-61. E_{corr} values after 24 hours flow for both 8 m/s (green) and 2 m/s (blue)

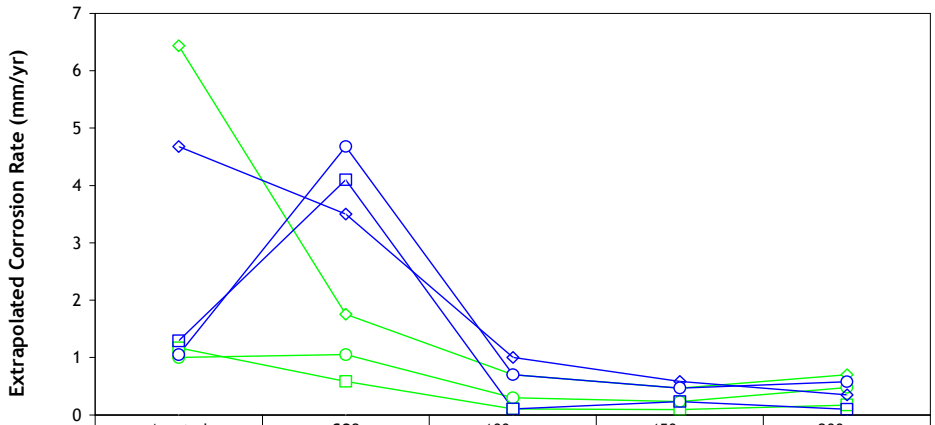

	Aerated	CO2	100ppm	150ppm	200ppm
8 m/s Impingement	6.44	1.76	0.70	0.47	0.70
8 m/s Intermediate	1.17	0.59	0.11	0.09	0.18
8 m/s Outer	1.00	1.05	0.30	0.23	0.48
2 m/s Impingement	4.68	3.50	1.00	0.59	0.35
2m/s Intermediate	1.29	4.10	0.11	0.23	0.10
2m/s outer	1.05	4.68	0.70	0.47	0.58

Figure 6-62. Extrapolated corrosion rates after 24 hours flow for 8 m/s (green) and 2 m/s (blue).

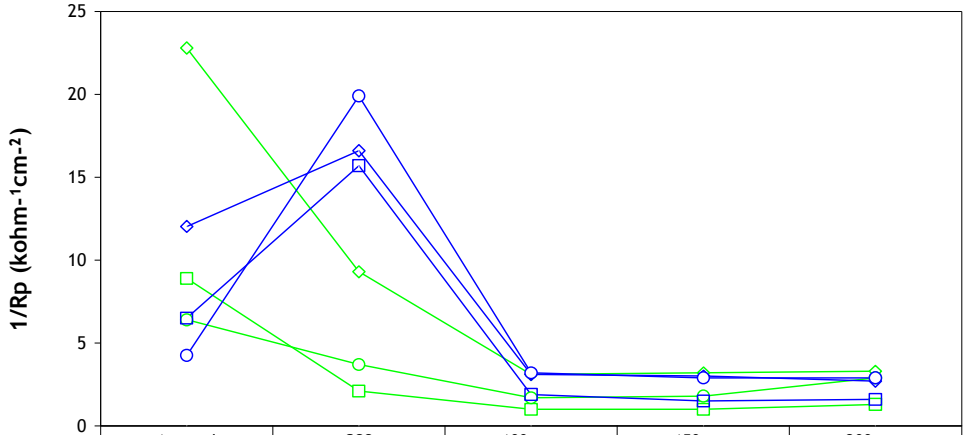

	Aerated	CO2	100ppm	150ppm	200ppm
8 m/s Impingement	22.8	9.3	3.1	3.2	3.3
8 m/s Intermediate	8.9	2.1	1.0	1.0	1.3
8 m/s Outer	6.4	3.7	1.7	1.8	2.9
2 m/s Impingement	12.0	16.6	3.1	3.0	2.7
2m/s Intermediate	6.5	15.7	1.9	1.5	1.6
2m/s outer	4.3	19.9	3.2	2.9	2.9

Figure 6-63. Anodic polarisation resistances for 8 m/s (green) and 2 m/s (blue) after 24 hours flow.

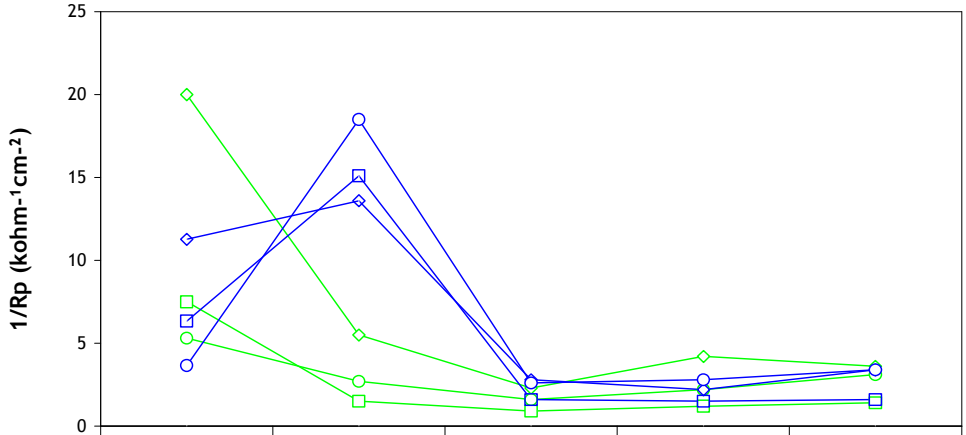

	Aerated	CO2	100ppm	150ppm	200ppm
8 m/s Impingement	20.0	5.5	2.3	4.2	3.6
8 m/s Intermediate	7.5	1.5	0.9	1.2	1.4
8 m/s Outer	5.3	2.7	1.6	2.2	3.1
2 m/s Impingement	11.3	13.6	2.8	2.2	3.4
2m/s Intermediate	6.3	15.1	1.6	1.5	1.6
2m/s outer	3.7	18.5	2.6	2.8	3.4

Figure 6-64. Cathodic polarisation resistances for 8 m/s (green) and 2 m/s (blue) after 24 hours flow.

7.0 GALVANIC INTERACTIONS

7.1 Introduction

This chapter presents results of the galvanic-interaction monitoring carried out between the various hydrodynamic zones presented in this thesis. As discussed earlier in Chapter 3, galvanically-induced corrosion can play a significant role in enhancing overall corrosion and hence overall metal loss.

Tests presented in this chapter are carried out at 50°C and at velocities of 8 m/s and 2 m/s representing both high and low shear flow. Conditions presented are aerated flow, CO_2 saturated flow and CO_2 saturated flow with inhibitor concentrations of 100 ppm, 150 ppm and 200 ppm. Discussion of results addresses any inhibitor capabilities to reduce galvanic activity between zones. The methodology used to assess such galvanic activity is a series connection between the hydrodynamic zones by means of a zero resistance ammeter. The values of E_{corr} in each zone are measured by a voltmeter and the ammeter measures the galvanic current flowing between zones. A positive/negative sign convention identifies the anode and cathode in the connection. Should the current be negative then the zone connected to the negative terminal of the ammeter is the cathode. The anode is then the zone connected to the positive terminal.

7.2 Aerated Tests

7.2.1 Tests at 8 m/s

Figure 7-1 below shows the E_{corr} behaviour as a function of time. The impingement zone is more positive compared to the intermediate and outer zones respectively. All three zones coupled have E_{corr} values closer to the intermediate and outer zones. From the graph it is also clear that any galvanic activity between any zones would see the impingement zone as the cathode on all occasions.

Figure 7-2 shows the galvanic currents flowing between zones when connected. From Figure 7-2, it is clear that in 8 m/s aerated flow, the galvanic activity favours the impingement zone as the zone is observed to be the cathode in all connections considered.

Table 7-1 details the galvanic connections and nature of their activity. The table shows the trend of lesser hydrodynamic zones to suffer galvanic corrosion in favour of more hydrodynamic zones. This has been characterised by the outer and intermediate zones categorically being the anode when in connection to the impingement zone. Again the outer and intermediate zones coupled act as an anode when connected to the impingement zone. The outer and intermediate zone connection also establishes the outer zone as the anode. This observation is further marked by the size of the galvanic currents. The biggest currents after 24 hours are between the impingement and outer zones with a current of 90 μA and the impingement and intermediate-outer couple with a current of 70 μA. This is due to the extent of the difference in hydrodynamic conditions. In general, more severe hydrodynamic conditions are observed to have more positive values of E_{corr} with respect to the lesser hydrodynamic zones. This situation is also characterised with the more positive zones having higher corrosion rates as observed in earlier chapters.

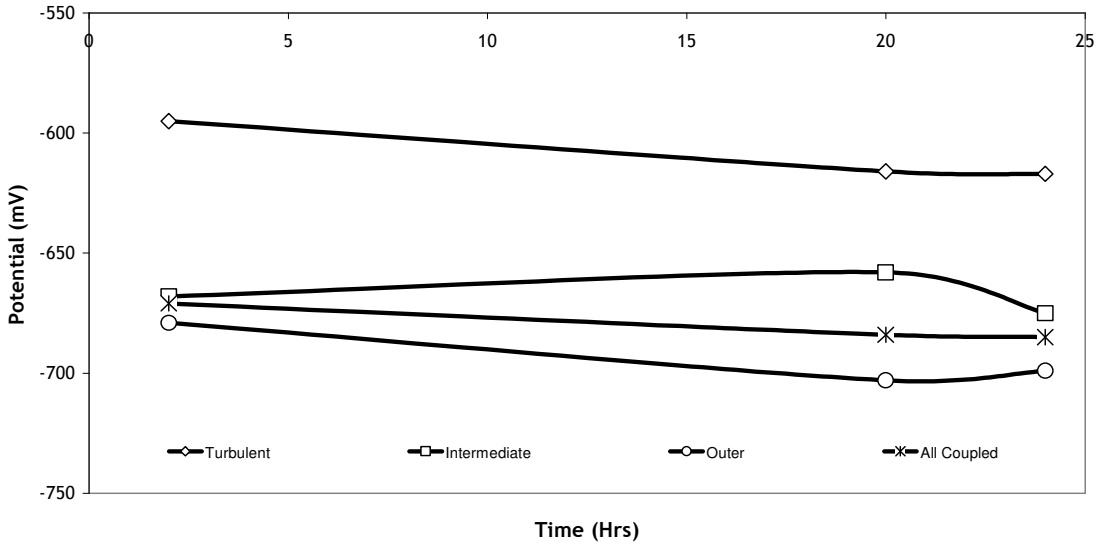

Figure 7-1. E_{corr} values for 8m/s aerated flow. Figure shows time related E_{corr} variation in each hydrodynamic zone and all the zones coupled.

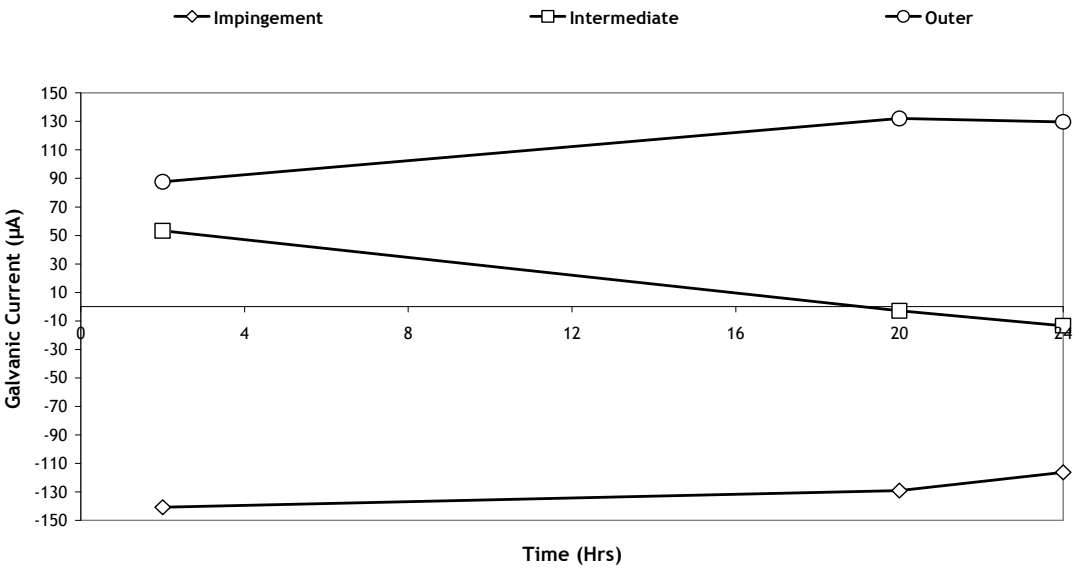

Figure 7-2. Galvanic currents for 8m/s aerated flow. Figure shows time related galvanic currents for connections between hydrodynamic zones.

Table 7-1

Galvanic activity in aerated flow at 8m/s

Anode	Galvanic Current (µA)	Galvanic Current Density (µA/cm^2)	Cathode
Outer	80.9	14.7	Impingement
Outer	48.8	8.9	Intermediate
Intermediate	35.4	13.4	Impingement
Intermediate Outer	66.9	-	Impingement

7.2.2 Tests at 2 m/s

Tests at 2 m/s show a smaller range in E_{corr} compared to tests done at 8 m/s. Figure 7-3 shows the E_{corr} values within each zone and again, the impingement zone is yet again more positive. The trend observed in tests at 8 m/s is again demonstrated with the outer zone being the most negative in comparison to the other zones. The respective Ecorr values for the impingement, intermediate and outer zone after 24 hours are -627 mV, -685 mV and -697 mV. All three zones coupled have an Ecorr value of -688 mV.

Figure 7-4 shows the galvanic currents measured. Again the currents are dominated by the potential difference between zones with the impingement zone benefiting as the cathode during all pairings. Table 7-2 shows the galvanic currents after 24 hrs and also details the anode and cathode.

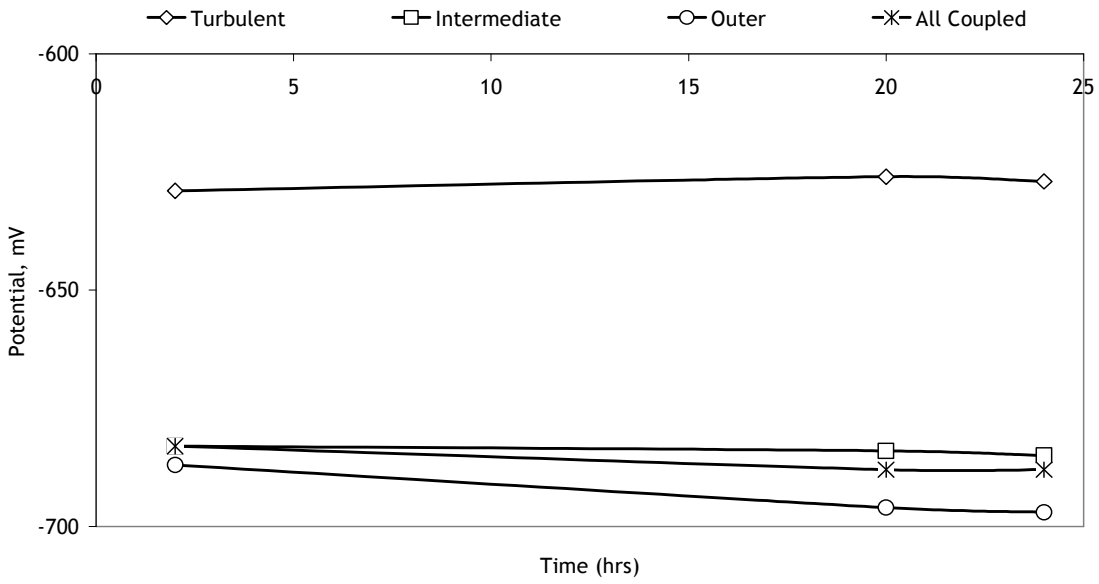

Figure 7-3. E_{corr} values for 2 m/s aerated flow. Figure shows time related E_{corr} variation in each hydrodynamic zone and all the zones coupled

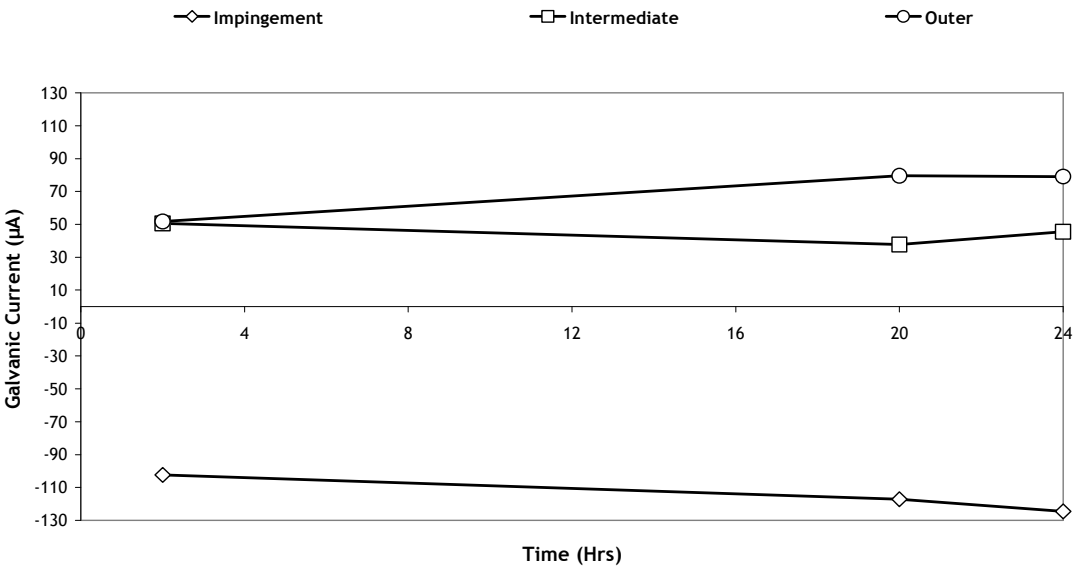

Figure 7-4. Galvanic currents for 2 m/s aerated flow. Figure shows time related galvanic currents for connections between hydrodynamic zones.

Table 7-2

Galvanic activity in aerated flow at 2m/s

Anode	Galvanic Current (µA)	Galvanic Current Density (µA/cm^2)	Cathode
Outer	64.9	11.8	Impingement
Outer	14.2	2.6	Intermediate
Intermediate	51.4	19.5	Impingement
Intermediate Outer	59.7	-	Impingement

To summarise the galvanic activity in aerated conditions, both velocities have similar trends with the more hydrodynamic zones benefiting from the galvanic

activity. The currents at 8 m/s are larger than those at 2 m/s except for the connection between the intermediate and impingement zone where the 2 m/s connection has a higher current at 51.4 μA compared to 35.4 μA for 8 m/s. Both velocities also have no exchange of anodes and cathode for the full 24 hour duration considered.

7.3 Test in CO_2

7.3.1 Tests at 8 m/s

Figure 7-5 shows the E_{corr} behaviour for tests done at 8 m/s and in CO_2 saturated brine. For all three hydrodynamic zones, E_{corr} drifts more negative with the passage of time and the values of Ecorr are also observed to be more negative compared to tests in similar aerated conditions. The impingement zone is again more positive in comparison to the intermediate and outer.

From Figure 7-6, the galvanic currents in CO_2 saturated brine are observed to be less than currents in aerated conditions. Again, in all pairings, the impingement zone is observed to benefit as the cathode. Table 7-3 details the current exchanges at 24 hrs.

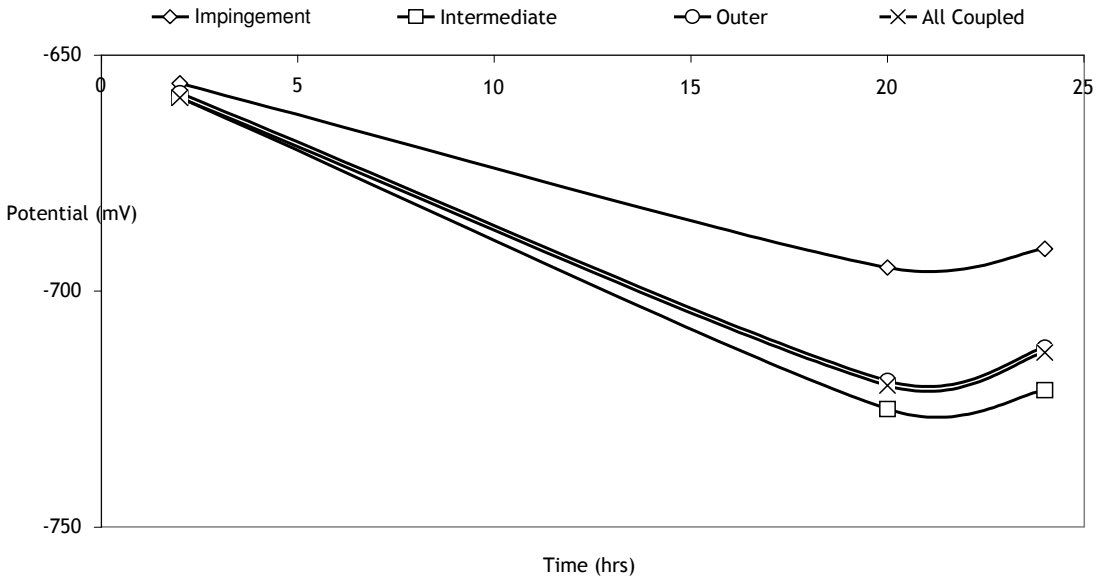

Figure 7-5. E_{corr} values for 8m/s CO_2 saturated flow. Figure shows time related E_{corr} variation in each hydrodynamic zone and all the zones coupled.

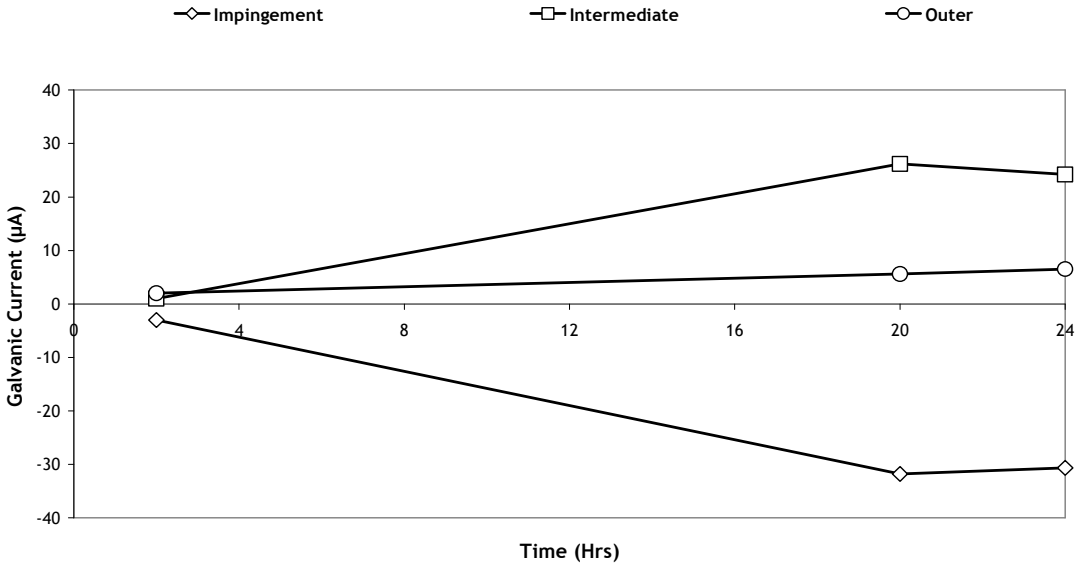

Figure 7-6. Galvanic currents for 8 m/s CO_2 saturated flow. Figure shows time related galvanic currents for connections between hydrodynamic zones.

Table 7-3

Galvanic activity in CO_2 saturated flow at 8 m/s

Anode	Galvanic Current (μA)	Galvanic Current Density (μA/cm^2)	Cathode
Outer	13.5	2.5	Impingement
Intermediate	7	2.7	Outer
Intermediate	17.2	6.5	Impingement
Intermediate Outer	14.6	-	Impingement

7.3.2 Tests at 2 m/s

Figure 7-7 below shows the E_{corr} values for tests at 2 m/s. The E_{corr} values are closer and all drift more negative with the passage of time. Figure 7-8 shows the galvanic currents and again, the magnitude of the currents is smaller than observed in CO_2 tests at 8 m/s. It is also worth noting that the intermediate zone benefits as a cathode whilst the impingement is a cathode at the start of the test but then switches to be an anode.

Table 7-4 shows the magnitude of the galvanic currents with the highest current being between the intermediate and outer zones. The currents are again much lower than currents in aerated conditions.

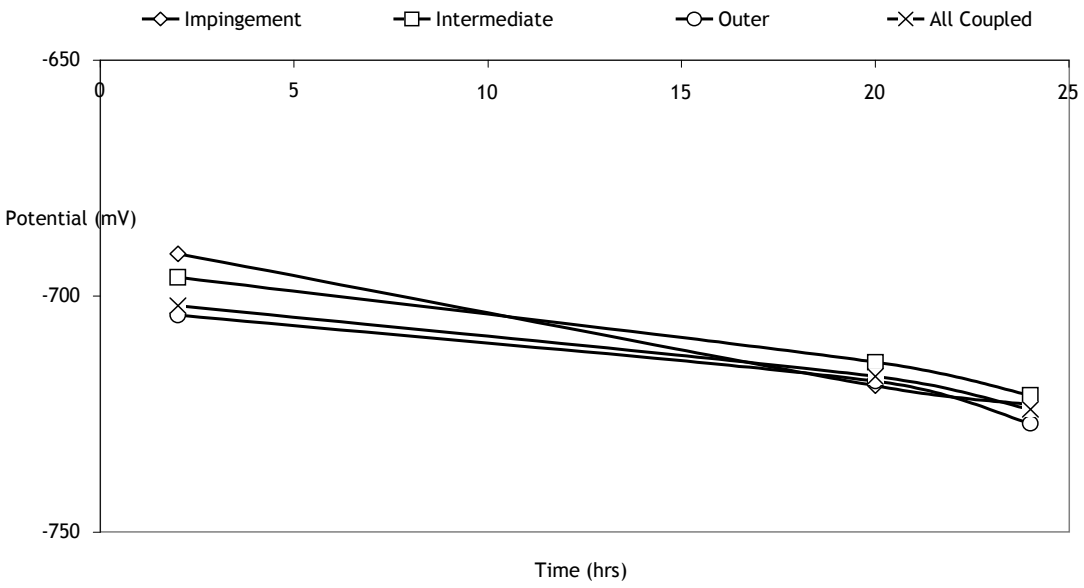

Figure 7-7. E_{corr} values for 2 m/s CO_2 saturated flow. Figure shows time related E_{corr} variation in each hydrodynamic zone and all the zones coupled.

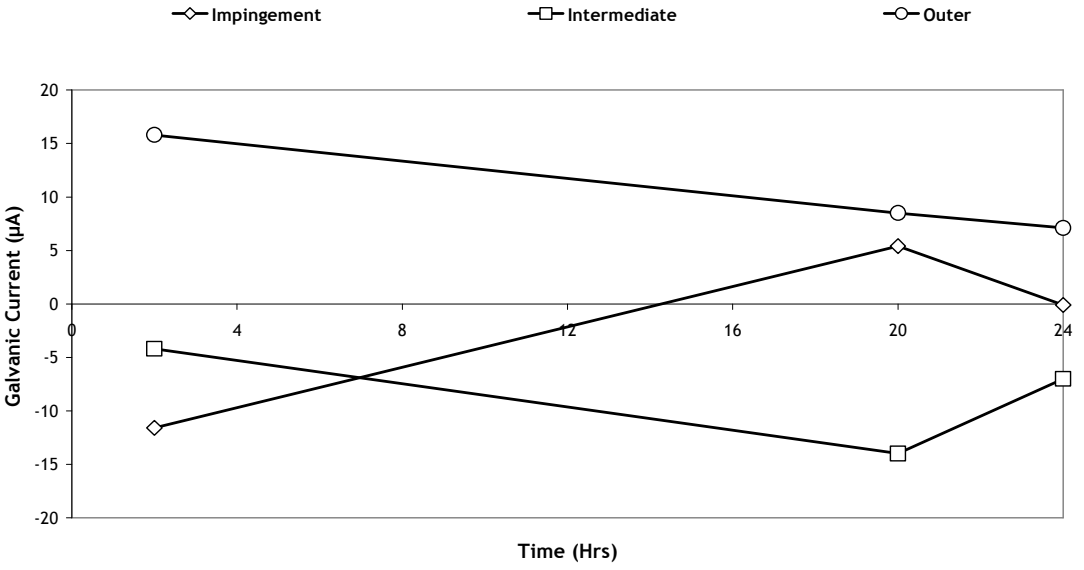

Figure 7-8. Galvanic currents for 2 m/s CO_2 saturated flow. Figure shows time related galvanic currents for connections between hydrodynamic zones.

Table 7-4

Galvanic activity in CO_2 saturated flow at 2 m/s

Anode	Galvanic Current (μA)	Galvanic Current Density (μA/cm^2)	Cathode
Outer	1.9	0.3	Impingement
Intermediate	5.2	2.0	Outer
Impingement	1.8	6.4	Intermediate
Intermediate Outer	0.5	-	Impingement

To summarise, in CO_2 saturated conditions, the E_{corr} values of each hydrodynamic zone are much closer and drift negative with the passage of time. The galvanic currents are much lower compared to aerated conditions and there is frequent exchange of anode and cathode. The currents at 2 m/s are very small and indicate consistently similar behaviour in hydrodynamic zones. This is likely due to carbonate film formation.

7.4 Tests in CO_2 with 100ppm inhibitor

7.4.1 Tests at 8 m/s

Figure 7-9 below shows the E_{corr} behaviour for the 8 m/s tests in 100 ppm inhibitor. From Figure 7-9, the E_{corr} values at 4 hours are almost similar for the impingement intermediate and outer zones. The respective values of E_{corr} are -686 mV, -688 mV and -686 mV. At 24 hours, a slight difference appears, nevertheless the difference in E_{corr} between zones is only 4 mV between the impingement and outer zones. Figure 7-10 shows the galvanic interaction currents. As expected, with such similar

behaviour in E_{corr} between all three zones, the galvanic currents are small.

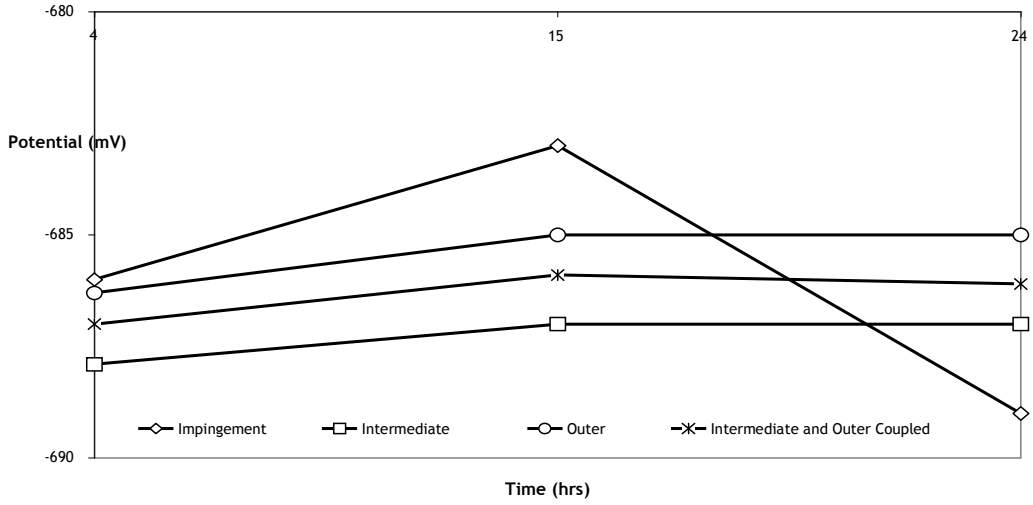

Figure 7-9. E_{corr} values for 8 m/s CO_2 saturated flow with 100ppm inhibitor. Figure shows time related E_{corr} variation in each hydrodynamic zone and the intermediate and outer coupled.

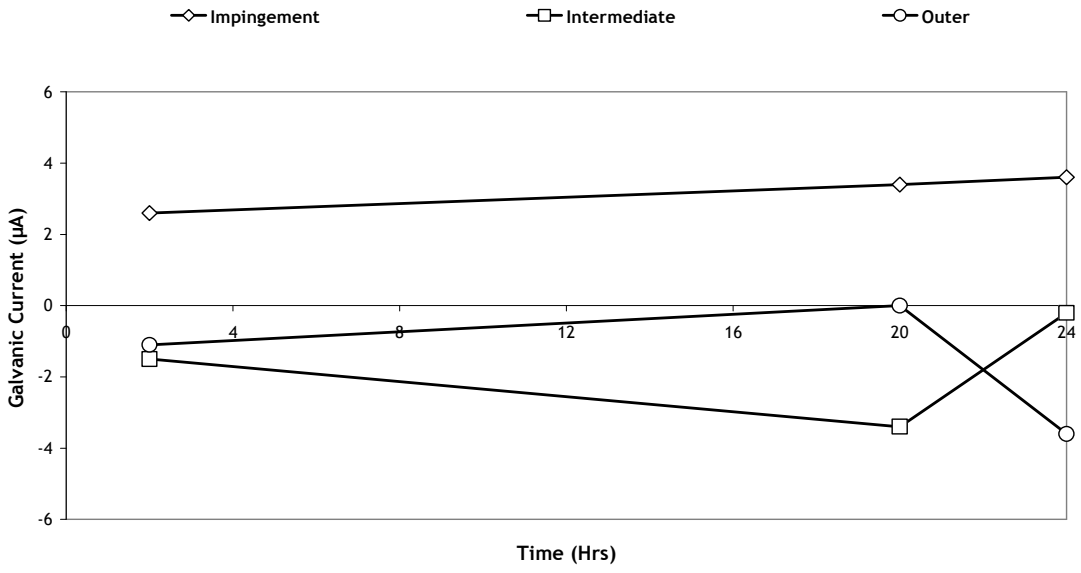

Figure 7-10. Galvanic currents for 8 m/s CO_2 saturated flow with 100 ppm inhibitor. Figure shows time related galvanic currents for connections between hydrodynamic zones.

Table 7-5

Galvanic activity in CO_2 saturated flow at 8 m/s with 100 ppm inhibitor

Anode	Galvanic Current (μA)	Galvanic Current Density (μA/cm^2)	Cathode
Impingement	2.3	8.2	Outer
Intermediate	1.1	0.4	Outer
Impingement	1.4	5.0	Intermediate
Impingement	1.6	-	Intermediate Outer

Table 7-5 summarises the galvanic activity after 24 hours in 8 m/s flow with 100 ppm inhibitor. The currents are low and the inhibitor seems to benefit the less aggressive conditions although the difference can also be considered to be negligible.

7.4.2 Tests at 2 m/s

Tests at 2 m/s show the best inhibitor effect in reducing the galvanic interactions between zones. Figure 7-11 shows the E_{corr} behaviour and after 24 hours the behaviour in all three hydrodynamic zones is almost similar with the biggest difference in E_{corr} being only 1.5 mV. Figure 7-12 shows the galvanic interactions and indicates the inhibitor effectiveness at reducing the galvanic activity. After 24 hours (Table 7-6 and Figure 7-12), all galvanic activity is near 0 μA and the inhibitor switches the anode and cathode behaviour.

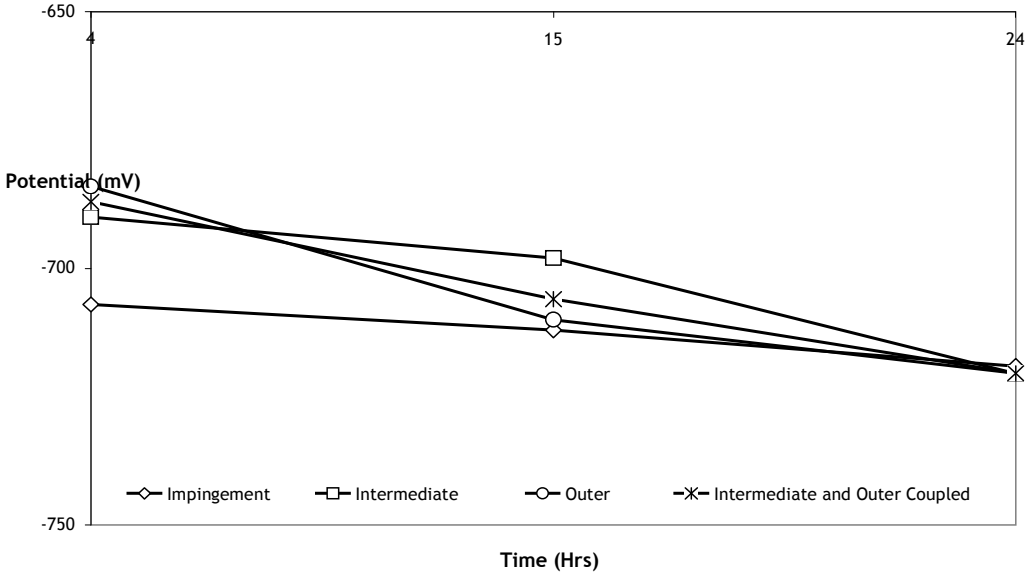

Figure 7-11. E_{corr} values for 2 m/s CO_2 saturated flow with 100ppm inhibitor. Figure shows time related E_{corr} variation in each hydrodynamic zone and the intermediate and outer coupled.

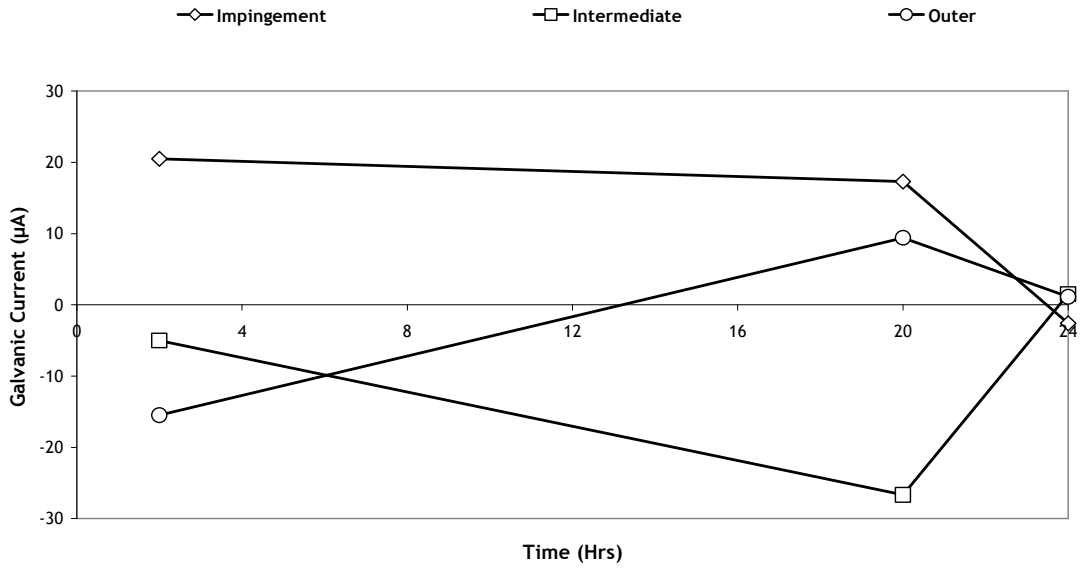

Figure 7-12. Galvanic currents for 2 m/s CO_2 saturated flow with 100 ppm inhibitor. Figure shows time related galvanic currents for connections between hydrodynamic zones.

Table 7-6

Galvanic activity in CO_2 saturated flow at 2 m/s with 100 ppm inhibitor

Anode	Galvanic Current (μA)	Galvanic Current Density (μA/cm^2)	Cathode
Impingement	1.2	4.3	Outer
Intermediate	0.1	0.0	Outer
Intermediate	1.4	0.5	Impingement
Intermediate Outer	1.3	-	Impingement

7.5 Tests in CO_2 with 150 ppm inhibitor

7.5.1 Tests at 8 m/s

Figure 7-13 shows the E_{corr} behaviour for tests at 8 m/s with 150 ppm inhibitor. The value of E_{corr} for the impingement zone is more negative than any other zone at 4 hours. As time passes by, the E_{corr} values of the intermediate, outer and intermediate-outer coupled drift negative and after 24 hours, the respective values for the impingement, intermediate, outer and intermediate-outer coupled are -651 mV, -670 mV, -677 mV and -679 mV. Figure 7-14 shows the galvanic currents indicating an exchange of anode and cathode for the impingement and outer zones. Table 7-7 shows the galvanic currents after 24 hours and shows that the galvanic activity tends to favour more aggresive conditions. This is demonstrated by the impingement zone being the cathode on all pairings and the intermediate also being the cathode when paired with the outer. This observation is slightly different to the CO_2 tests as the intermediate zone was the anode when paired with the outer specimen.

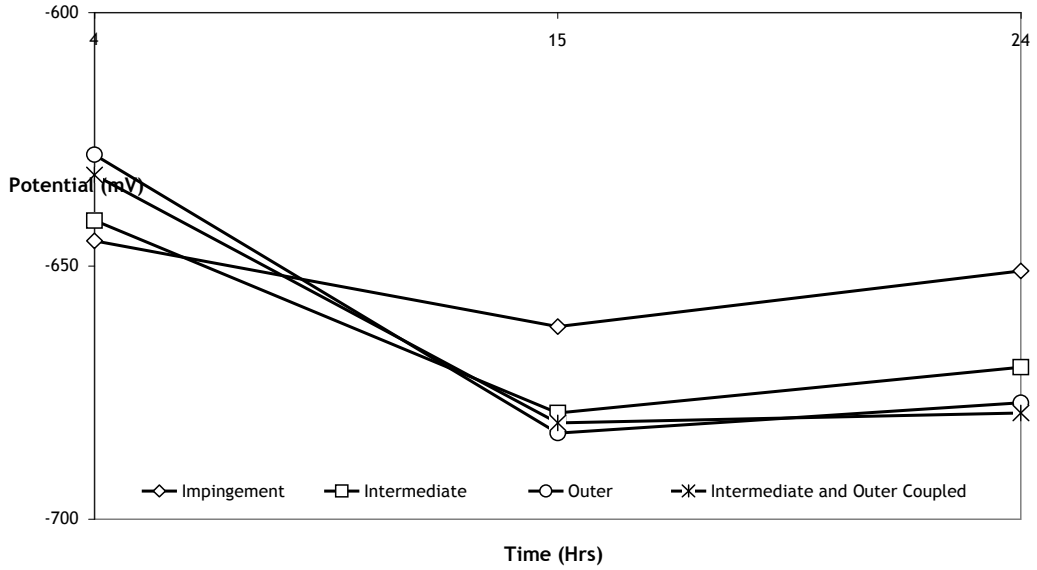

Figure 7-13. E_{corr} values for 8 m/s CO_2 saturated flow with 150 ppm inhibitor. Figure shows time related E_{corr} variation in each hydrodynamic zone and all the zones coupled.

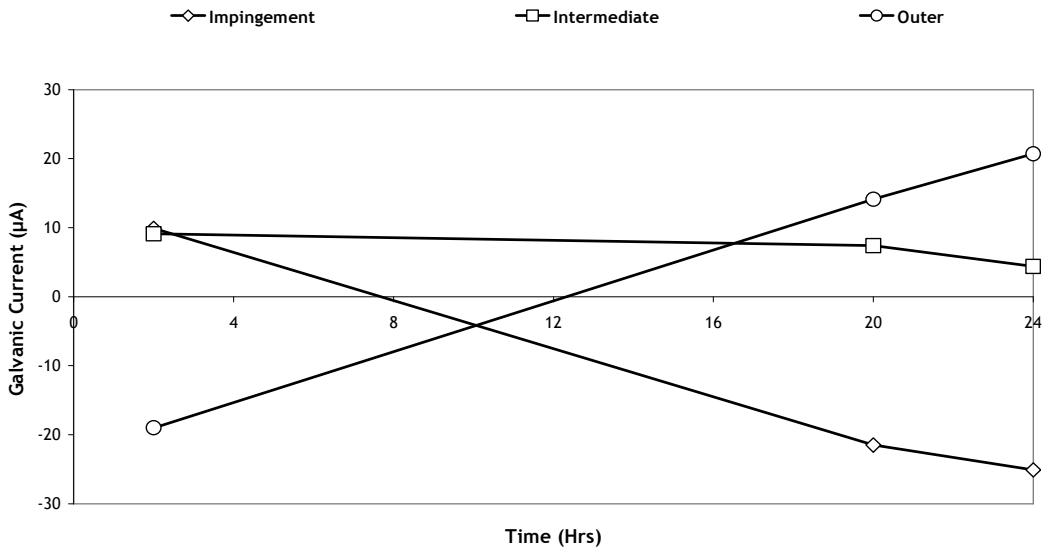

Figure 7-14. Galvanic currents for 8 m/s CO_2 saturated flow with 150 ppm inhibitor. Figure shows time related galvanic currents for connections between hydrodynamic zones.

Table 7-7

Galvanic activity in CO_2 saturated flow at 8 m/s with 150ppm inhibitor

Anode	Galvanic Current (μA)	Galvanic Current Density (μA/cm^2)	Cathode
Outer	15.5	2.8	Impingement
Outer	5.2	0.9	Intermediate
Intermediate	9.6	3.6	Impingement
Intermediate Outer	12.3	-	Impingement

7.5.2 Tests at 2 m/s

Figure 7-15 shows the E_{corr} behaviour for tests done at 2 m/s with 150 ppm inhibitor. After 24 hours in such conditions, the variance in E_{corr} between all three hydrodynamic zones is less than 1.5 mV and all three zones show a time related drift in potential. The galvanic currents, represented by Figure 7-16 agree with the above observation. From Figure 7-16, the currents all start positive with this indicating the galvanic activity is of advantage to the least aggresive zones such as the outer and the intermediate with the intermediate also acting as anode when connected to the outer.

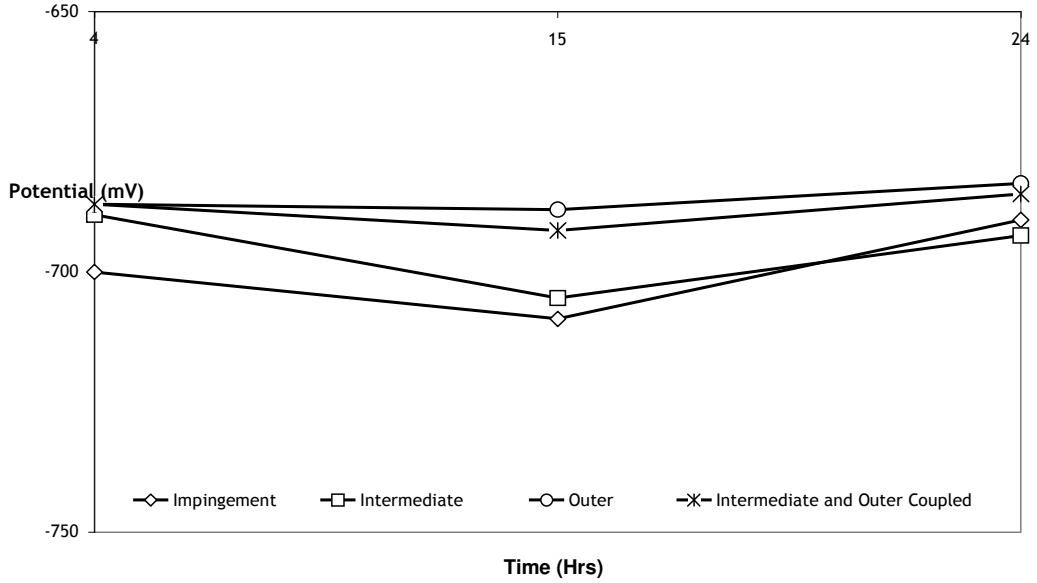

Figure 7-15. E_{corr} values for 2 m/s CO_2 saturated flow with 150 ppm inhibitor. Figure shows time related E_{corr} variation in each hydrodynamic zone and all the zones coupled.

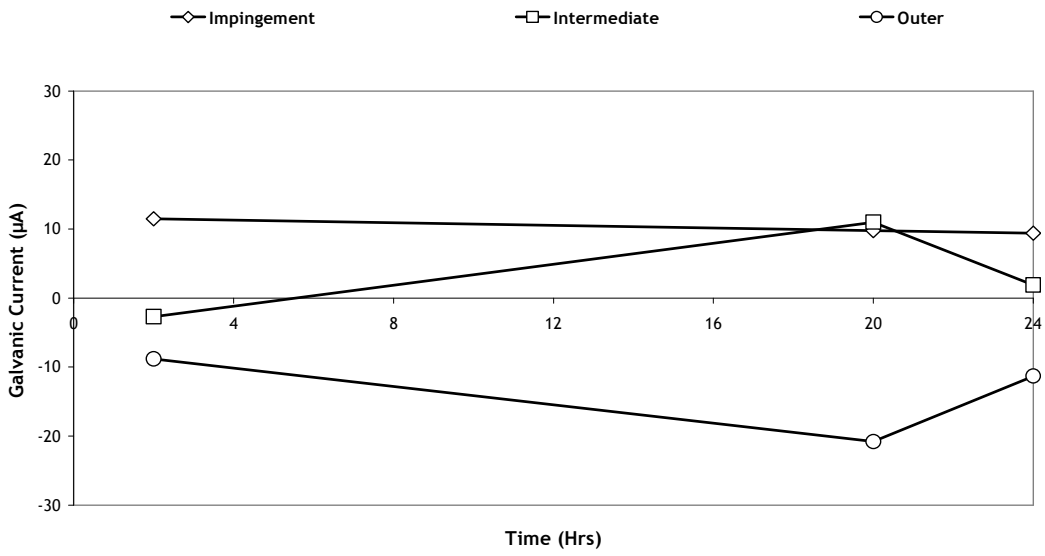

Figure 7-16. Galvanic currents for 2 m/s CO_2 saturated flow with 150 ppm inhibitor. Figure shows time related galvanic currents for connections between hydrodynamic zones.

Table 7-8

Galvanic activity in CO_2 saturated flow at 2 m/s with 150 ppm inhibitor

Anode	Galvanic Current (μA)	Galvanic Current Density (μA/cm^2)	Cathode
Impingement	3.4	12.1	Outer
Intermediate	7.9	3.0	Outer
Intermediate	1.5	0.6	Impingement
Impingement	2.1	-	Intermediate Outer

7.6 Tests in CO_2 with 200 ppm inhibitor

7.6.1 Tests at 8 m/s

Figure 7-17 shows the E_{corr} behaviour for tests done with 200 ppm inhibitor. Initially, the E_{corr} values in each zone are near similar with largest difference being 4 mV and after 24 hours. This variation is much larger with the impingement zone being the most positive at -673 mV and the intermediate the most negative at -685 mV. Figure 7-18 shows the galvanic current activity between zones and indicates a switch of anode/cathode in all zones during the 24 hour test duration. Table 7-7 details the galvanic activity after 24 hours.

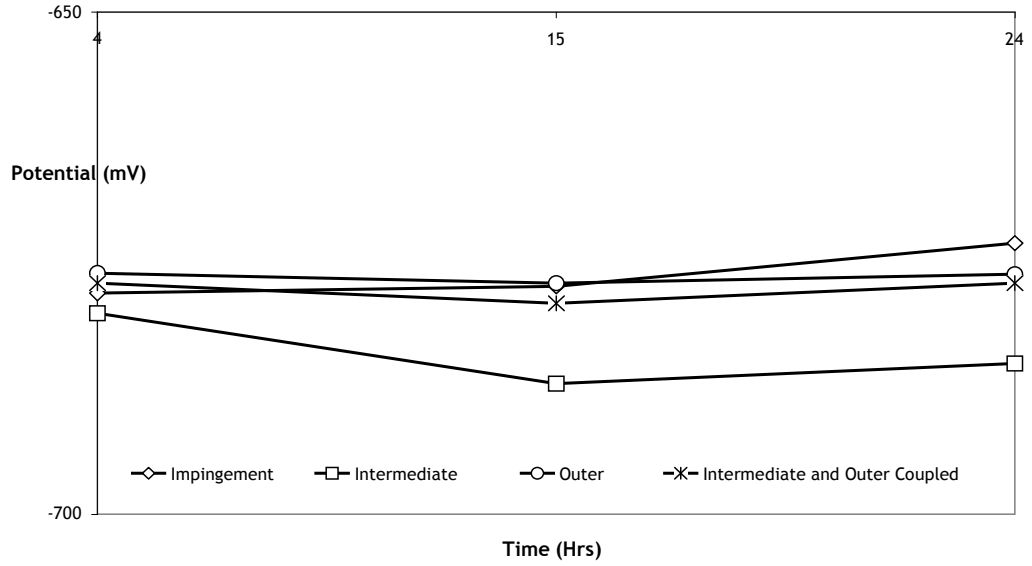

Figure 7-17. E_{corr} values for 8 m/s CO_2 saturated flow with 200 ppm inhibitor. Figure shows time related E_{corr} variation in each hydrodynamic zone and the intermediate and outer coupled.

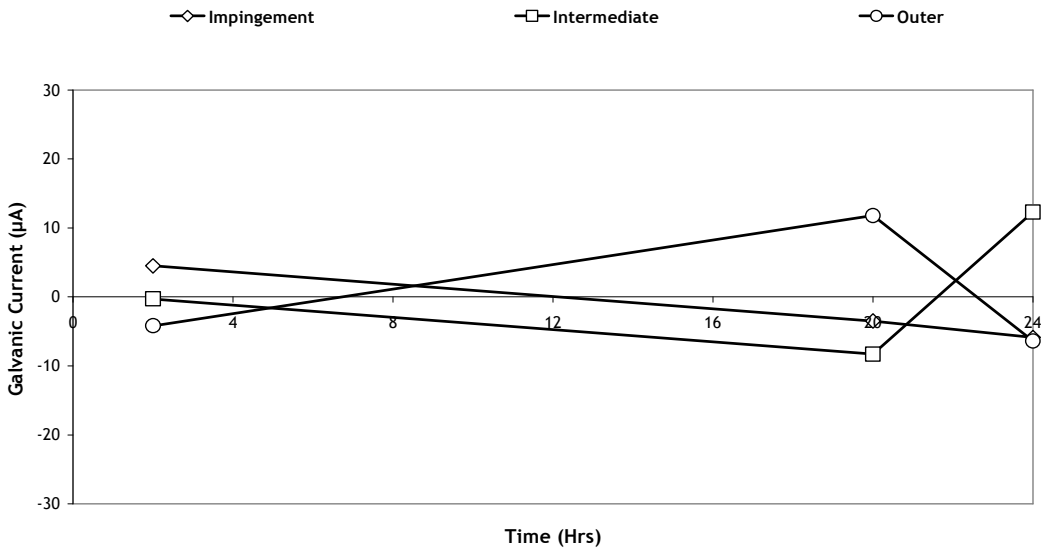

Figure 7-18. Galvanic currents for 8 m/s CO_2 saturated flow with 200 ppm inhibitor. Figure shows time related galvanic currents for connections between hydrodynamic zones.

Table 7-9

Galvanic activity in CO_2 saturated flow at 8 m/s with 200ppm inhibitor

Anode	Galvanic Current (μA)	Galvanic Current Density (μA/cm^2)	Cathode
Outer	1	0.2	Impingement
Intermediate	7.4	2.8	Outer
Intermediate	4.9	1.9	Impingement
Intermediate Outer	1.3	-	Impingement

From Table 7-9, the biggest galvanic current value is between the intermediate and outer zone. The current after 24 hours is 7.4 μA with the intermediate zone being the anode. The least value is 1 μA between the impingement and outer zone. The presence of the inhibitor favours the impingement zone and least favours the intermediate zone.

7.6.2 Tests at 2 m/s

Tests at 2 m/s show a consistent switch in polarity for all hydrodynamic zones. Figure 7-19 shows the E_{corr} behaviour with the impingement zone initially being more negative and becoming more positive with the passage of time. At 15 hours, the impingement zone is the most positive and continues to drift positive throughout the 24 hour period. After 24 hours, the respective potentials for the impingement, intermediate, outer and intermediate-outer are -676 mV, -696 mV, -704 mV and -703 mV.

The galvanic activity is detailed in Figure 7-20 and shows a polarity switch in all zones. Table 7-8 details the galvanic activity after 24 hours.

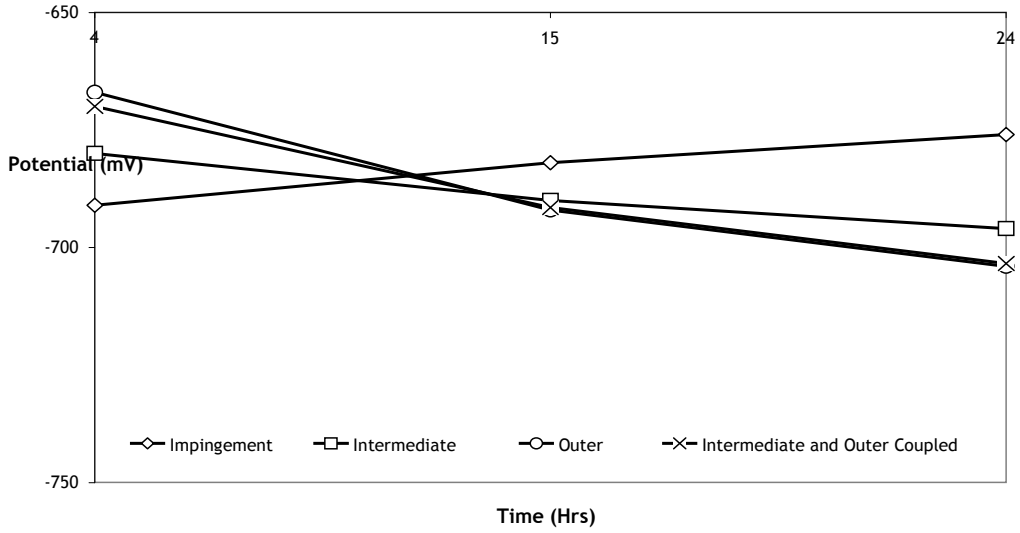

Figure 7-19. E_{corr} values for 2 m/s CO_2 saturated flow with 200 ppm inhibitor. Figure shows time related E_{corr} variation in each hydrodynamic zone and the intermediate and outer coupled.

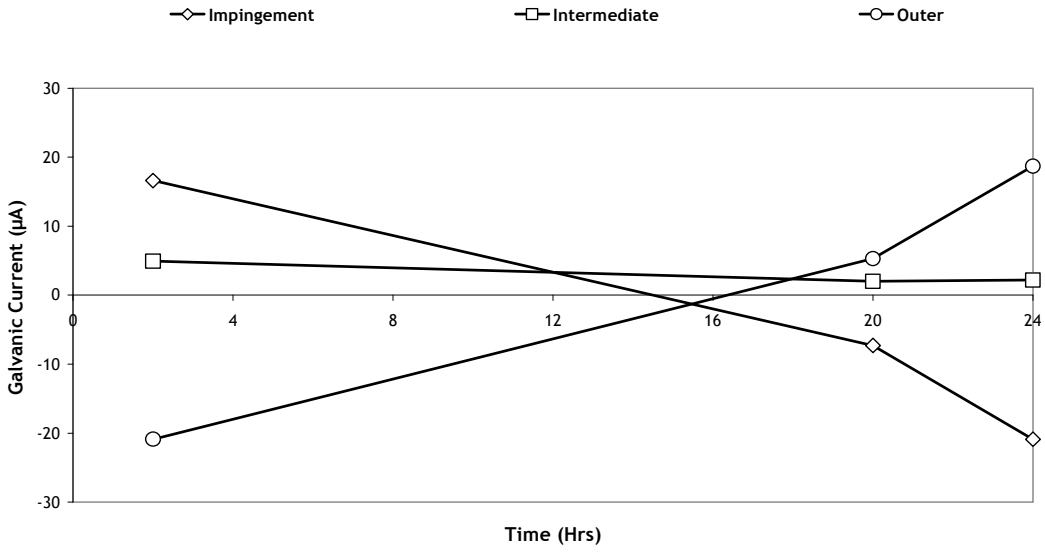

Figure 7-20. Galvanic currents for 2 m/s CO_2 saturated flow with 200 ppm inhibitor. Figure shows time related galvanic currents for connections between hydrodynamic zones.

Table 7-10

Galvanic activity in CO_2 saturated flow at 2 m/s with 200 ppm inhibitor

Anode	Galvanic Current (μA)	Galvanic Current Density (μA/cm^2)	Cathode
Outer	12.3	2.2	Impingement
Outer	6.4	1.2	Intermediate
Intermediate	8.6	3.3	Impingement
Intermediate Outer	11.8	-	Impingement

From Table 7-10, the inhibitor favours the more hydrodynamic conditions as the outer is the majority anode. The magnitude of the currents has increased compared to tests at 8 m/s again indicating stronger inhibitor effectiveness in more hydrodynamic conditions.

7.7 Summary

To summarise, galvanic interactions between hydrodynamic zones at 8 m/s and 2 m/s have been assessed. The test conditions considered are aerated, CO_2 saturated and CO_2 saturated with inhibitor concentrations of 100 ppm, 150 ppm and 200 ppm. Figure 7-21 summarises the galvanic activity in various conditions. The aerated conditions have the highest galvanic currents followed by CO_2 and as expected, the inhibitor reduces the galvanic activity with an optimum concentration of 100 ppm.

Figures 7-22 to 7-25 show the galvanic interactions between zones and at both velocities. For all tests, the 2 m/s galvanic interactions are smaller compared to those at 8 m/s. The lowest galvanic currents are observed with 100 ppm inhibitor. Increasing inhibitor concentration above this peak has no major benefit on decreasing galvanic activity any further and essentially increases the galvanic

currents as demonstrated. With the passage of time, the inhibitor has also been observed to switch the anode and cathode.

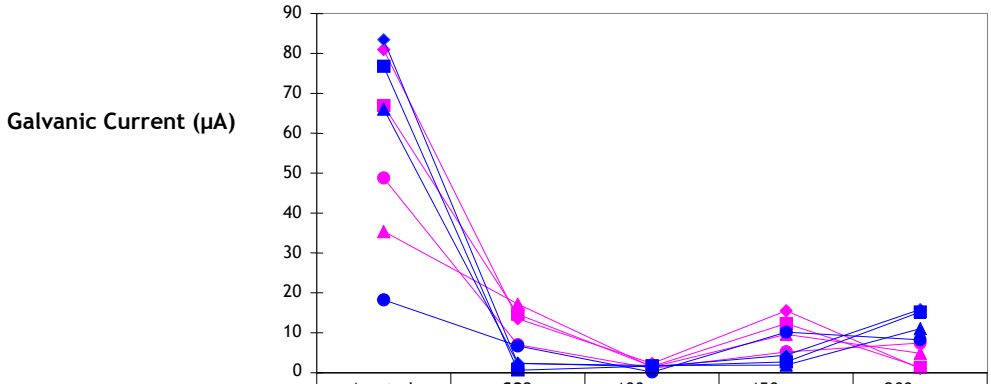

	Aerated	CO2	100 ppm	150 ppm	200 ppm
Impingement-Outer 8 m/s	80.9	13.5	2.3	15.5	1
Impingement-Intermediate 8 m/s	35.4	17.2	1.4	9.6	4.9
Intermediate-Outer 8 m/s	48.8	7	1.1	5.2	7.4
IntermediateOuter-Impingement 8 m/s	66.9	14.6	1.6	12.3	1.3
Impingement-Outer 2 m/s	64.9	1.9	1.2	3.4	12.3
Impingement-Intermediate 2 m/s	51.4	1.8	1.4	1.5	8.6
Intermediate-Outer 2 m/s	14.2	5.2	0.1	7.9	6.4
IntermediateOuter-Impingement 2 m/s	59.7	0.5	1.3	2.1	11.8

Figure 7-21. Galvanic activities for all three zones at 8 m/s and 2 m/s. Figure shows galvanic currents in µA for tests in various conditions.

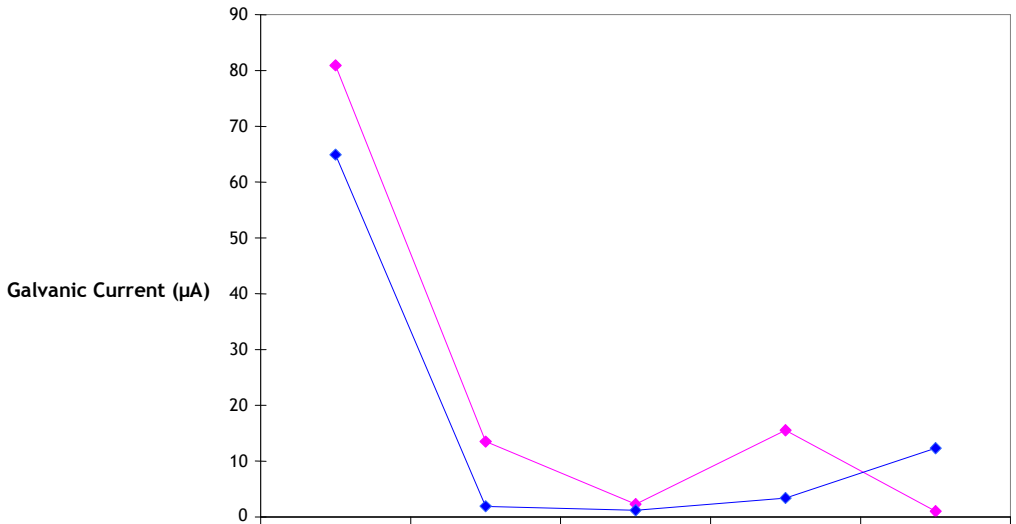

	Aerated	CO2	100 ppm	150 ppm	200 ppm
Impingement-Outer 8 m/s	80.9	13.5	2.3	15.5	1
Impingement-Outer 2 m/s	64.9	1.9	1.2	3.4	12.3

Figure 7-22. Galvanic activities between impingement and outer zones at 8 m/s and 2 m/s. Figure shows galvanic currents in µA for tests in various conditions.

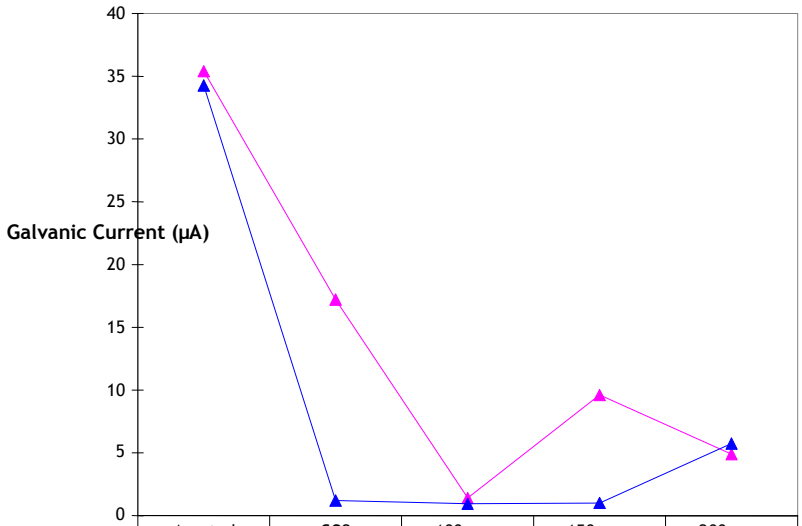

	Aerated	CO2	100 ppm	150 ppm	200 ppm
Impingement-Intermediate 8 m/s	35.4	17.2	1.4	9.6	4.9
Impingement-Intermediate 2 m/s	51.4	1.8	1.4	1.5	8.6

Figure 7-23. Galvanic activities between impingement and intermediate zones at 8 m/s and 2 m/s. Figure shows galvanic currents in µA for tests in various conditions.

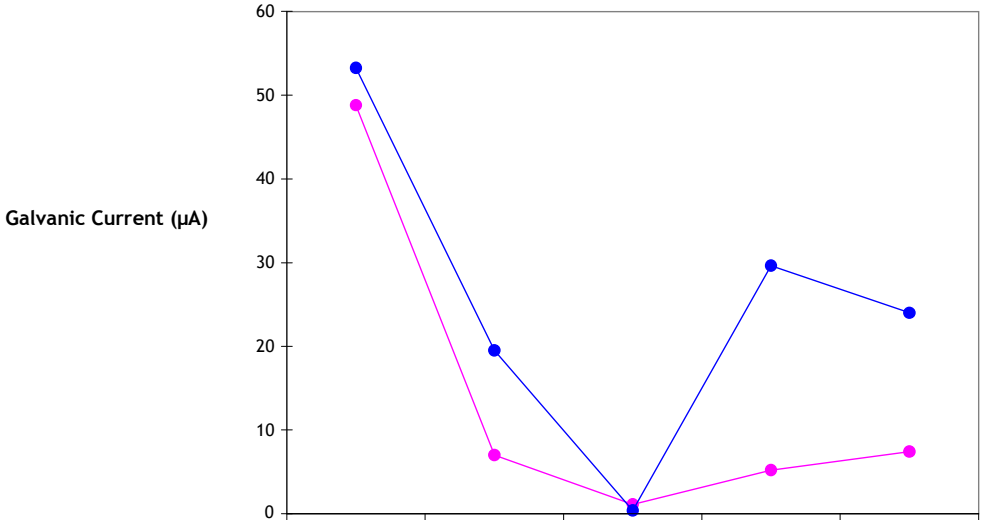

	Aerated	CO2	100 ppm	150 ppm	200 ppm
Intermediate-Outer 8 m/s	48.8	7	1.1	5.2	7.4
Intermediate-Outer 2 m/s	14.2	5.2	0.1	7.9	6.4

Figure 7-24. Galvanic activities between intermediate and outer zones at 8 m/s and 2 m/s. Figure shows galvanic currents in µA for tests in various conditions

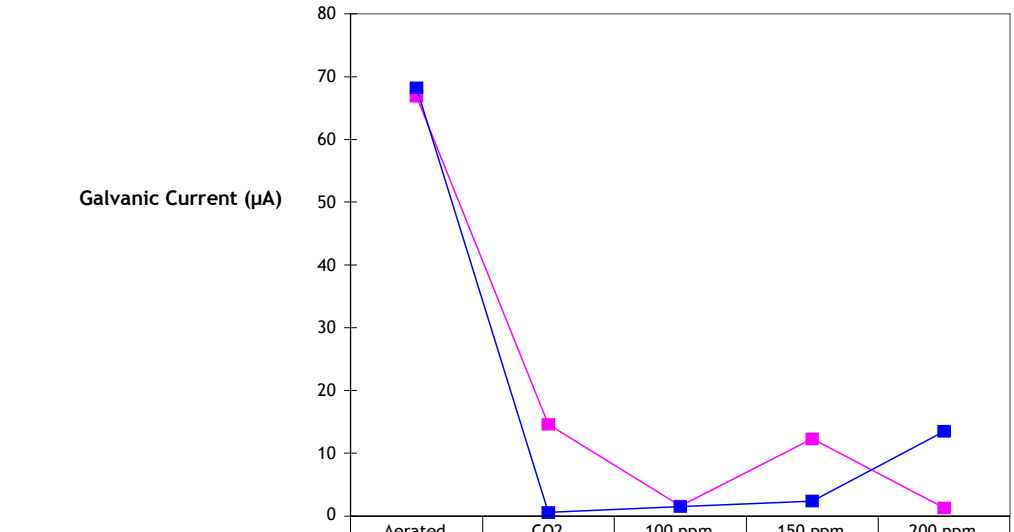

	Aerated	CO2	100 ppm	150 ppm	200 ppm
IntermediateOuter-Impingement 8 m/s	66.9	14.6	1.6	12.3	1.3
IntermediateOuter-Impingement 2 m/s	59.7	0.5	1.3	2.1	11.8

Figure 7-25. Galvanic activities between intermediate and outer coupled and impingement zone at 8 m/s and 2 m/s. Figure shows galvanic currents in µA for tests in various conditions

8.0 DISCUSSION

8.1 Introduction

This thesis examines the influence of hydrodynamics on the efficiency of a corrosion inhibitor in simulated oil field environments. The main themes presented are corrosion assessments by mass loss techniques, corrosion assessments by electrochemical techniques and galvanic activity between various hydrodynamic zones.

Chapters 5 presented results of corrosion monitoring by mass loss (Gravimetric analysis) and Chapter 6 presented results in similar conditions but monitored by electrochemistry. Results by both monitoring techniques have shown likely similarities in corrosion behaviour which is expected as the exact test environments are replicated.

In light of current literature reviewed in Chapter 3, one issue identified was large synergistic components observed in studies involving flowing corrosive fluids. Although this may be an expected observation in conditions containing solids, attention is drawn to the possibility of synergy in solid-free flow. Work by Neville, et al., (2003) and Wang, et al., (2004) has shown that the combined effect of erosion and corrosion (often referred to as synergy) may possibly result in material losses larger than the sum of their individual components. Guidelines for assessing this amount of increased material loss due to synergy have been given in ASTM standard G119-09.

In agreement with the above observations, Hodgkiess, et al., (2005), amongst others, identified an indirect method of establishing the amount of synergy by the following eqaution, as defined earlier in Chapter 3:

$$T = E + C + S$$

This Equation may be used or rearranged in any order to determine “E”, the pure erosion component, “C” the pure corrosion component or “S”, the synergy component of the total material loss “T”. Chapter 5 presents results by mass loss and these results can therefore be substituted in for “T”, Chapter 6 presents results by

electrochemistry and those results can therefore be substituted in for “C”, the pure corrosion component. From the two chapters and using the following rearranged expression, the component of non-Faraday related material loss can be established as follows:

$$T - C = E + S$$

The above numerical calculation will be used as a basis for this discussion.

8.2 Aerated Tests

Tests in aerated conditions have shown a significant hydrodynamic influence on both the total metal loss “T” and the electrochemical-corrosion metal loss “C”. Both the mass loss and electrochemical methods of assessment have shown the impingement zone as having significantly higher metal loss rates than the intermediate and outer zones respectively, and at both velocities of 8 m/s and 2 m/s. Figure B 1 (appendices) shows the metal loss rates determined by mass loss “T” and electrochemistry “C” and also indicates a large difference between the two assessment methods.

The impingement zone higher metal losses by both “T” and “C” may indicate a cathodic driven corrosion process influenced by the supply or availability of oxygen molecules at the metal surface. An analysis of this concept is given below.

Given that the cathodic reaction in aerated environments is the reduction of oxygen, the impingement zone is likely to be receiving a continuous supply of oxygen molecules from the bulk solution as the jet impinges on this specimen. If we assume the amount of oxygen available for the cathodic reactions of the intermediate and outer zone is delivered by the impinging solution only and not directly from the bulk then the intermediate and outer zones would have retarded oxygen levels at their surfaces as oxygen is initially consumed in the impingement zone. Should this be the case, this mechanism would have a concentration polarisation effect where the impingement zone would undergo activation polarisation due to sufficient levels of oxygen available at the metal surface with the intermediate and outer zones presumably undergoing concentration polarisation.

The behaviour in both potential and the equivalent corrosion rates determined by both electrochemistry and mass loss supports the idea that the cathodic reactions in aerated environments may be driven by activation or concentration polarisation with the later situation applying to the intermediate and outer zones. This would fit with the impingement zones at both velocities having higher corrosion rates and more positive values of electrode potential, E_{corr}, compared to the intermediate and outer zones. With the impingement zone having an E_{corr} value of -615 mV as observed in chapter 5 at 8 m/s, the intermediate zone would follow with an E_{corr} of -657 mV and a corrosion rate lower than the impingement but higher than the outer. Finally, the outer zone would follow with an E_{corr} of -677 mV and the lowest corrosion rate.

However, to substantiate this argument, a calculation of the amount of oxygen consumed in the impingement zone exposes a situation where the metal loss rates in the impingement zone do not correlate to large consumptions of oxygen sufficient to create an oxygen molecule deficiency in the ensuing cathodic reactions of the intermediate and outer zones.

This calculation is carried out as below:

From balanced anodic and cathodic reactions in aerated water,

$2Fe \rightarrow 2Fe^{2+} + 4e^{-}$ and

$$\underline{O_2 + H_2O + 4e^{-} \rightarrow 4(OH)^{-}}$$

$$2Fe + 2H_2O + O_2 \rightarrow 4(OH)^{-} + 2Fe^{2+}$$

2 moles of iron react with 1 mole of oxygen, therefore we can say
2 x 55.85g of iron reacts with 32g of oxygen
Therefore, 111.7g of iron react with 32g of oxygen.

Taking for example the mass loss rate for the aerated impingement zone at 8 m/s which is a mass loss of 0.035g after 24 hours, this amount of iron would equate to an oxygen consumption given as follows:

$\frac{0.035}{111.7} x32 = 0.010g$ of O_2 in 24 hours.

This equates to a rate of $1.16x10^{-7}$ g/sec or 1.16×10^{-4} mg/sec of O_2. Then from

Water supply in jet = velocity x Area of nozzle

$800x\pi(0.05^2) = 6.284cm^3/s = 6.28g/s$. Density of water is taken as 1g/cm^3 and the nozzle diameter is 1 mm.

Taking an average oxygen content of water as 1 litre water contains 5 mg of O_2. Therefore, 6.28 g/s of water contains:

$$\frac{5}{1000}x6.28 = 0.031mg \text{ of } O_2$$

Finally, from the above assessment, we have deduced that the oxygen supply from the nozzle of the jet is 0.031 mg/sec of O_2. The consumption rate from the corrosion process in the impingement zone is $1.16x10^{-4}$ mg/sec of O_2. The amount of oxygen consumed in the impingement zone is a very small fraction (1/267) of the amount available from the impinging jet. Since enough oxygen is readily available to the intermediate and outer zone specimens, the difference in corrosion rate cannot be attributed to polarisation effects. This leaves hydrodynamic mechanisms as the predominant source of the varying corrosion rate between the zones.

Turning to the numerical discrepancy but similar behaviour in the results obtained by "T" and "C", metal loss rates analysed by mass loss "T" are on all occasions larger than electrochemical rates "C". This observation is further indication of metal losses due to non-electrochemical mechanisms such as wear and synergy as follows:

Metal loss rates "T" obtained by mass loss assessments represent the total material loss by all mechanisms - in this case pure corrosion "C", pure erosion "E" and synergy "S". Rates calculated from electrochemical monitoring or Faraday related techniques represent the pure electrochemical corrosion component only and as already shown are denoted "C". From the summary in Figure B 1 (appendices) and utilising the relationship for synergy employed by many workers such as Hodgkiess, et al., (2005), the component "E+S" which represents the erosive and synergistic material loss can therefore be calculated and is presented in Figure 8-1.

From Figure 8-1, the combined amount of erosion and synergistic loss “E+S” is shown to be greater at 8 m/s compared to 2 m/s in all three regions. In all three regions and at both velocities, “E+S” is observed to be over 73 %. This result is somewhat a revelation on the amount of non-pure-electrochemical material loss occurring even in solid-free flow. As discussed by Heitz, (1996), the combined action of corrosion and flow may introduce additional mechanisms such as cavitation and erosion-corrosion. Reports by Postlethwaite, et al., (1994), suggest that cavitation damage occurs when variations in pressure resulting from sudden changes in velocity or flow geometry cause formation of bubbles in regions where the pressure is lower. It is therefore very much possible that given the flow changes direction from normal impingement to a radial velocity direction, bubble formation due to cavitation is occuring within the system.

Aerated environments have also shown deep pit formation (chapter 5 microscopy and surface profiling) which could be in line with suggestions again by Heitz, (1996) that cavitation damage causes deep sharp edged craters on the metal surface. Cavitation in aerated flow is also likely to originate from collapse of oxygen bubbles on the metal surface. Although simulation of such mechanisms was not intended in this project, the reality is that actual field conditions or pipelines are likely to contain cavitation due to the existance of flow variations in sections such as bends, tees, elbows and valves.

Impingement of fluid is also another mechanism present in field pipelines and may also be correlated to the impingement zone. This observation is therefore rather meaningfull as a picture representing large material losses originating from mechanisms other than pure electrochemical corrosion “C” is demonstrated in solid-free flow. Corrosion monitoring using methods reliant on electrochemical techniques need to be considered with care as such an approach may significantly underestimate the actual material losses involved in solid-free-flow corrosion.

From Figure 8-1, an interesting feature is that the value of “E+S” in the intermediate and outer zones is almost similar at both velocities. The “E+S” component at 8 m/s is however higher than the component at 2 m/s. This feature could be explained by the two regions existing in the wall jet region of the flow where the only variable is a difference in shear stress..

Figure 8-1

Components of erosion and synergy "E+S" in aerated tests

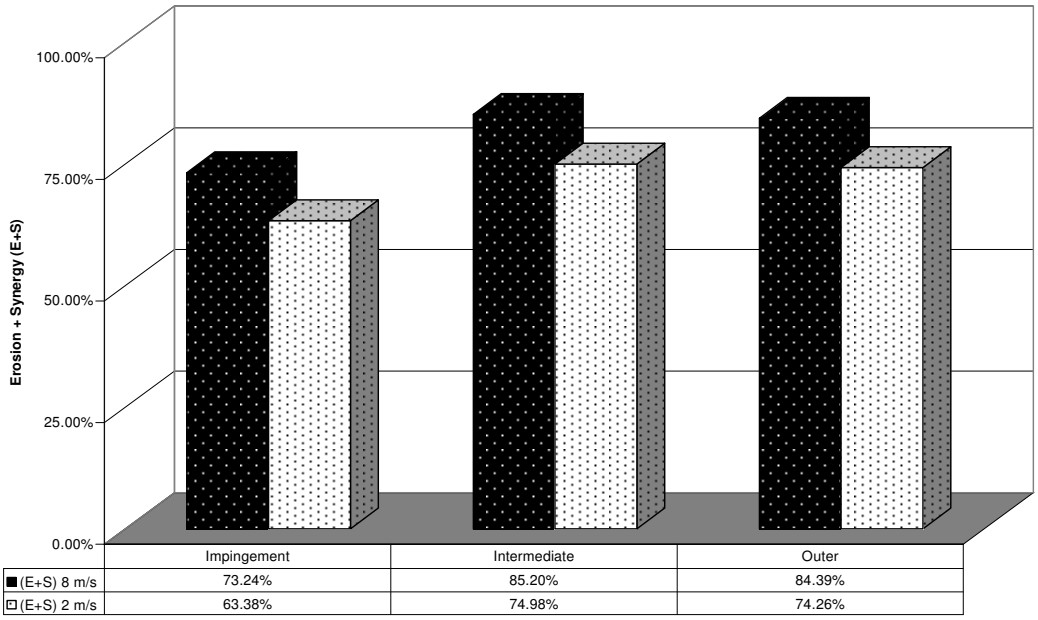

	Impingement	Intermediate	Outer
(E+S) 8 m/s	73.24%	85.20%	84.39%
(E+S) 2 m/s	63.38%	74.98%	74.26%

8.3 CO_2 Tests

Tests in CO_2 environments have shown a change in corrosion behaviour within the hydrodynamic zones compared to aerated environments (Figure B 1 and Figure B 2). In part, this may be due to a different cathodic reaction(s) compared to the oxygen reduction reaction in aerated environments. Tests in CO_2 environments within this project have shown pH values of about 5 and would point to reduction of either HCO_3^- or H_2CO_3 as remarked by Zhang, et al., (2006). Nesic, et al., (1996) also confirmed reduction of H_2CO_3 as the dominant cathodic reaction at pH values of around 5. These proposed cathodic reactions are discussed earlier in Chapter 3.

For the gravimetric testing at 8 m/s and 2 m/s, the intermediate zone has shown the highest material loss by all mechanisms "T". As shown in Figure B 2 (appendices) the "T" metal loss rates for the intermediate zone are 12.92 mm/year and 7.16 mm/year at 8 m/s and 2 m/s respectively. The impingement "T" metal loss rates are 8.88 mm/year and 6.48 mm/year with the outer metal loss rates being 3.69 mm/year and 5.04 mm/year.

Again, from Figure B 2, the electrochemistry or "C" tests show a different arrangement with the impingement zone having the highest metal loss rate at 8 m/s. The respective "C" metal losses are 1.76 mm/year, 0.59 mm/year and 1.05 mm/year for the impingement, intermediate and outer zones respectively. At 2 m/s, the outer zone surprisingly has the highest "C" metal loss rate of 4.68 mm/year. The impingement and intermediate zones have loss rates of 3.50 mm/year and 4.10 mm/year respectively. Although the above results indicate a complex mechanism occurring in CO_2 environments, the following statements can be clearly drawn from the observations:

1. The electrochemistry "C" results have shown higher CO_2 metal losses in all three zones at 2 m/s compared to "C" metal losses at 8 m/s (Figure B 2);
2. At both velocities of 8 m /s and 2 m /s, the impingement zone is the only zone that shows lower "T" and "C" metal losses in CO_2 compared to aerated environments (see Figure B 1 and Figure B 2).

These statements support a conclusion that in CO_2 environments, protective films may be forming better in more aggressive conditions. This is supported by the lower "C" metal losses which are observed at the higher velocity (8m/s) and also supported by the impingement zone at both velocities also showing lower "T" and "C" losses in CO_2 environments compared to aerated. A detailed justification is given in Section 8.3.1.

8.3.1 Pure Electrochemical Corrosion "C"

The results from electrochemical monitoring show a lower electrochemical corrosion component "C" at a velocity of 8 m/s compared to 2 m/s. This observation is noted in all three zones and suggests that films, which best act as a barrier to corrosive species may form better in conditions that are more aggresive.

Current literature reviewed in Chapter 3 recognises the formation of protective films in environments containing CO_2. Results presented in Chapter 5 and 6 largely show a reduction in corrosion rate in CO_2 environments compared to aerated environments. Post-test microscopic examination of specimens exposed to CO_2 containing tests have shown formation of a thick dark film formed on the surface of specimens (Chapter 5, Section 5.3). Given the species involved in CO_2 corrosion of

carbon steel are likely to be iron Fe^{2+} and carbonate CO_3^{2-} ions, it is conceivable that such films are in most cases films consisting of iron carbonate. Wang, et al., (2003), Sun, et al., (2006) and Fajardo, et al., (2008) define iron carbonate films as slowing down the corrosion process by formation of a diffusion barrier for species involved in corrosion. Results obtained from electrochemistry "C" may facilitate a good investigation of this idea as they only represent metal losses from pure electrochemical mechanisms to which such a barrier or film would have a greater effect.

Considering the electrochemical "C" results at 2 m/s and 8 m/s in all three hydrodynamic zones, this discussion focuses on mechanisms of protective film formation in CO_2 environments. The main issue to address is a possible explanation as to why such films seem to form better in more aggresive flow conditions. As recognised in a publication by Nesic, et al., (2002), porous and unprotective carbonate films can form in CO_2 environments particularly if the scaling tendency (ST) is less than 1. The scaling tendency depends on the precipitation and corrosion rates as shown previouosly by Equation 3-14. However, the precipitation rate depends on the supersaturation.

To aid an analysis of the film formation mechanisms in the various hydrodynamic zones, a consideration of a situation where porous unprotective films have formed is assumed and related to a scaling tendency (ST) of less than 1. From the equation of scaling tendency, Equation 3-14, the precipitation rate (PR) must be less than the corrosion rate (CR). The precipitation rate must therefore be the restraining factor. Going back to the definition of precipitation rate, Equation 3-15, it is observed that the values of K_r and K_{sp} are constants.

The area to volume ratio, A/V must also be negligible as the area of all the specimens is very small in comparison the the volume of the recirculating fluid. Therefore, the main variable factor from the precipitation rate must be the degree of supersaturation (SS) achieved locally in each hydrodynamic zone. The equations discussed are already presented in Chapter 3 but are included in this section as an aid to this discussion.

$$ST = \frac{PR}{CR}$$

$$PR = k_r \frac{A}{V} k_{sp} (SS - 1)(1 - SS^{-1})$$

$$SS = \frac{C_{Fe^{2+}} C_{CO_3^{2-}}}{K_{sp}}$$

Finally from the equation of supersaturation, Equation 3-13, the constant k_{sp} is the same for all three specimens. The amount of carbonate available in the bulk is also the same for all three zones and for the two test rigs. This has been assumed because the same amount of fluid is available in both rigs and both rigs are assumed to be fully saturated with CO_2. For that reason, the only variable factor in each hydrodynamic zone must be the concentration of Fe^{2+}. The bulk solution contains no iron and the only source of Fe^{2+} is from the specimen surfaces prior to film formation.

Zones such as the outer zone, where the corrosion rates are lowest in non CO_2 environments can inevitably end up having higher corrosion rates in CO_2 compared to the impingement and intermediate zone as already demonstrated by the electrochemistry "C" results at 2 m/s. This effect may be due to the degree of supersaturation achieved within the zone, driven by the rate at which the surface releases Fe^{2+} ions. The degree of supersaturation has already been shown to affect the corrosion rate. Chapter 3 presented experimental results by Chokshi, et al., (2005) showing that lower corrosion rates in CO_2 evironments are achieved if the degree of supersaturation is high. The effect of supersaturation is proposed in this project as a probable explanantion as to why the CO_2 electrochemistry "C" results at 2 m/s are higher than those at 8 m/s. As initial corrosion rates at 8 m/s are presumed to be higher than those at 2 m/s due to more aggresive flowing conditions, the concentration of Fe^{2+} in the 8 m/s zones must be higher than concentrations in similar zones at 2 m/s. Higher degrees of supersaturation are therefore assumed in zones at 8 m/s as the higher initial corrosion rates provide higher Fe^{2+} concentrations through higher dissolution rates. Again the work by Chokshi, et al., (2005) significantly supports this argument as the researchers also demonstrate that higher

degrees of supersaturation are achieved at higher Fe^{2+} concentrations (see Tables 3-1 and 3-2).

Further support on this argument is augmented by the linear polarisation activity presented independently in Chapter 6. The anodic and cathodic polarisation values (1/Rp) for tests at 8 m/s (Figure 6-17 and Figure 6-18) show a time related reduction in 1/Rp. A good example of this is the outer zone cathodic 1/Rp values which are 6.3 $kohm^{-1}cm^{-2}$, 3.1 $kohm^{-1}cm^{-2}$ and 2.7 $kohm^{-1}cm^{-2}$ at respective time intervals of 4 hours, 15 hours and 24 hours into the tests. Turning to the results of tests at 2 m/s (Figure 6-23 and Figure 6-24), it is first of all observed that the values of 1/Rp are higher than those at 8 m/s. Again a comparison is the outer zone cathodic 1/Rp values which are 12.9 $kohm^{-1}cm^{-2}$, 10.3 $kohm^{-1}cm^{-2}$ and 18.5 $kohm^{-1}cm^{-2}$. Importantly, no time related reduction in 1/Rp is clearly noticed which is indication that no significant protective film formation is occuring in these conditions. It is also noted that in some cases as the above, an increase in 1/Rp is actually observed after the 24 hour period. The exception to this is the impingement zone where a marginal reduction in 1/Rp is observed at completion of the tests. Again this exception is noticed in the more impingement conditions further emphasising that film formation in CO_2 environments is largely dependent on hydrodynamics with more aggresive flowing conditions favouring film formation. Taking note of this and the aerated results, it can also be concluded that hydrodynamics seem to have different effects in different systems with impingement zones experiencing higher metal losses in aerated flow and a reverse mechanism noticed in CO_2 envronments where the impingement zones experience lower metal losses.

8.3.2 Synergy and Erosion "E+S"

From Figure B 2 (appendices), the results from tests by the mass loss technique show significantly larger yearly penetration rates compared to results by electrochemistry. In both the 8 m/s and 2 m/s tests, the intermediate zone has the highest equivalent penetration rate as measured by gravimetric analysis "T". Comparing the mass loss results in the impingement and intermediate zones with those obtained by electrochemistry indicates the majority of the total mass loss in this zone is due to synergistic and erosive mechanisms. Figure 8-2 shows the calculated percentages of "E+S" at both velocities. From Figure 8-2, the percentages of "E+S"

are observed to make up the majority of the material loss at 8 m/s. The magnitude of these losses "E+S" as a percentage of the total "T" is much smaller at 2 m/s. The outer zone at 2 m/s shows a dissimilar result to the behaviour of the other zones. At 2 m/s, the majority of the material loss (92.89 %) is attributed to electrochemical mechanisms. This result is possibly due to the fact that the films in this zone are not as protective to pure corrosion "C" and thus allow higher corrosion rates attributed to "C". As a ratio, the percentage might then give the impression that there is lower "E+S" as the component "C" has increased significantly. Again from earlier remarks, the idea of less protective films can also be brought forward to this discussion as the absence of such films would leave the outer zone possibly exposed to the bulk solutions and may consequently drive the electrochemical corrosion process as the cathodic reaction could ultimately be dominated by the hydrogen evolution reaction due to the acidic environment signified by a pH of around 5.

Figure 8-2

Components of erosion and synergy in CO_2 tests

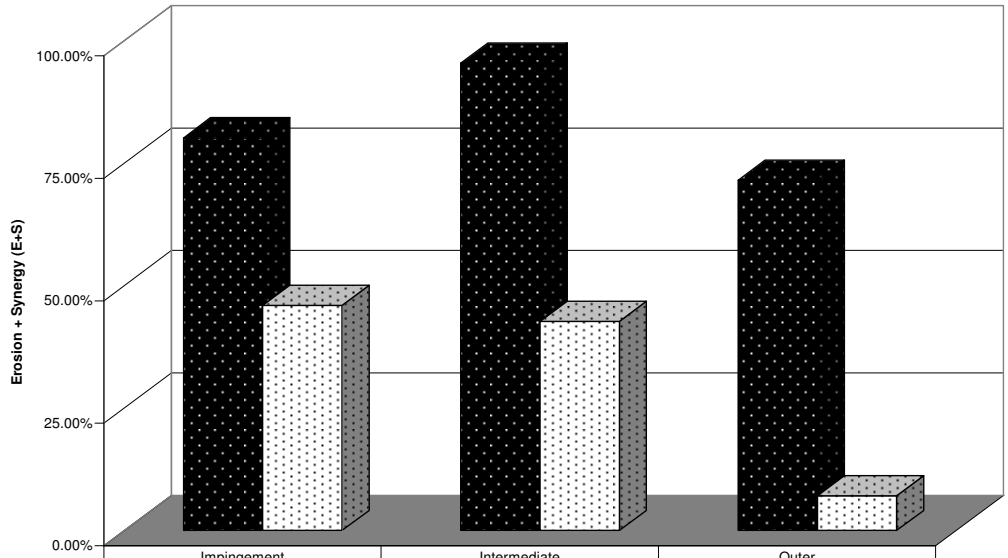

	Impingement	Intermediate	Outer
(E+S) 8 m/s	80.18%	95.43%	71.51%
(E+S) 2 m/s	45.97%	42.70%	7.11%

8.4 Inhibition

Tests involving the presence of the inhibitor in the CO_2 saturated brines have shown universal reductions in CO_2 corrosion rates at all concentrations considered. Tests at 8 m/s monitored by mass loss "T" show variable concentration effects with 150 ppm

being the optimum concentration for the impingement zone. The intermediate and outer zones showed optimum values at a lower concentration of 100 ppm. This observation was also noticed in the tests at 2 m/s. Increasing the inhibitor concentration above these optimum values has shown adverse effects, reducing the inhibitor efficiency and consequently increasing the corrosion rates.

Tests by electrochemistry show variable effects with peak efficiencies achieved at either 150 ppm or 200 ppm. In contrast to the mass loss "T" tests, the results by electrochemistry require significantly more inhibitor and in any case end up with higher amounts of "T", the total mass loss through all mechanisms. The peak efficiencies are therefore taken as those giving the lower value of "T" as the differences in electrochemistry are very small. This observation might however suggest that higher concentrations of inhibitor may act as a better barrier to electrochemical dissolution but in no way act better at preventing the total material loss through all mechanisms. This result calls attention to the importance of establishing optimum efficiencies especially targeting conditions closely simulating the actual field conditions. As already observed, increasing inhibitor concentration in order to reduce corrosion rates may in fact have detrimental effects with regard to corrosion rates. Other disadvantageous consequences are increased costs, environmental issues and possible separation/processing issues.

Again results by both techniques indicate presence of non-Faraday related material losses. The results at 8 m/s (Figure B 4) and at optimum efficiency of 150 ppm for the impingement zone reduce the "E+S" rate from 7.12 mm/year in CO_2 to 0.79 mm/year with the inhibitor. This amounts to a reduction in "E+S" of 80.9 %.

The 2 m/s impingement zone (Figure B 6) again requires 150 ppm for optimum efficiency and reduces the component "E+S" from 2.98 mm/year in CO_2 down to 0.69 mm/year at 150 ppm. This amounts to a reduction in "E+C" of 76.8 %.

The 8 m/s intermediate zone (Figure B 8) requires a lower concentration of inhibitor compared to the impingement zone. The intermediate zone at this velocity shows peak efficiency at 100 ppm and reduces "E+S" from 12.34 mm/year down to 1.15 mm/year. This indicates a reduction in "E+S" of 90.6 %. The lower velocity of 2 m/s

(Figure B 10) again requires 100 ppm for peak efficiency and reduces "E+S" from 3.06 mm/year down to 1.29 mm/year. This represents a reduction in "E+S" of 57.8 %.

Both outer zones require 100 ppm for optimum efficiency. The 8 m/s zone (Figure B 12) reduces the CO_2 "E+S" from 2.63 mm/year down to 0.78 mm/year. This indicates a reduction of 70.4 %. The 2m/s outer zone (Figure B 14) shows a reduction in CO_2 "E+S" from 0.36 mm/year down to about 0.01 mm/year. This represents a reduction in "E+S" of 97.2 %.

The inhibitor considered in this project has also demonstrated the capability to work well over a range of shear stresses if the optimum concentration is made available. The inhibitor has been more effective in the impingement zone at both velocities with final metal loss rates by mass loss "T" being 1.28 mm/year and 1.25 mm/year for the 2 m/s and 8 m/s velocities respectively at the optimum concentration of 150 ppm. The intermediate zone requires 100 ppm with final corrosion rates being 1.4 mm/year and 1.26 mm/year for the 2 m/s and 8 m/s respectively. The outer zone requires a similar concentration of 100 ppm for optimum efficiency with final corrosion rates being 0.7 mm/year and 1.1 mm/year for the 2 m/s and 8 m/s velocities respectively. The following tables summarise the overall findings of the inhibitor exercises.

Table 8-1 Summary of inhibitor effects at 8 m/s

	Impingement	Intermediate	Outer
Optimum Concentration (ppm)	150	100	100
Reduction in "T" (%)	85.7	90.3	70.7
Reduction in "E+S" (%)	80.9	90.7	70.5
Reduction in "C" (%)	73.3	81.34	71.4

Table 8-2 Summary of inhibitor effects at 2 m/s

	Impingement	Intermediate	Outer
Optimum Concentration (ppm)	150	100	100
Reduction in “T” (%)	80.3	80.4	85.9
Reduction in “E+S” (%)	76.9	57.8	97.2
Reduction in “C” (%)	83.1	97.3	90.0

Table 8-3 Summary of inhibitor effects at both velocities

	Impingement	Intermediate	Outer
Optimum Concentration (ppm)	150	100	100
Average corrosion rate at 8 m/s (mm/year)	1.25	1.26	1.1
Average corrosion rate at 2 m/s (mm/year)	1.28	1.4	0.7

From the summary tables, there is evidence that higher shear stresses require higher inhibitor concentrations in order to achieve peak efficiency. This result is supported by the two impingement zones requiring 150 ppm while the outer zones require 100 ppm. The two impingement zones have average shear stress values of 183 Pascal and 15 Pascal for the 8 m/s and 2 m/s flow respectively. The intermediate and outer zones at both velocities all have average shear stress values of less than 6 Pascal. In terms of corrosion rates in this project, it has been difficult to distinguish any shear related trends within the outer zones. However, a clear trend between the two impingement zones and outer zones (intermediate and outer) is shown as higher concentrations of inhibitor have been required in the impingement zones. This probably concludes that shear stresses below 6 Pa have no variable effect on inhibitor efficiency. Shear stress above 15 Pacals have been shown to require more inhibitor concentration suggesting that at higher shear stresses, higher concentrations are required. Electrochemistry in Chapter 6 has also shown the inhibitor to shift the electrode potential, E_{corr}, positive (Figure 6-61) whilst reducing the corrosion rates. This indicates this inhibitor principally works as an anodic inhibitor.

8.5 Impingement zones

Analysis of the average metal loss rates "T" by the mass loss technique shows a large difference between the 2 m/s and 8 m/s metal losses in aerated conditions. The 2 m/s impingement zone has a "T" metal loss rate of 12.78 mm/year compared to the 8 m/s impingement zone, which has a rate of 24.06 mm/year. Introducing CO_2 lowers the variation arising from the effect of velocity with the corresponding rates being 6.48 mm/year and 8.88 mm/year respectively. This is again indicative of probable film formation with the 8 m/s impingement zone seeming to benefit best from protective film formation in CO_2 environments.

When the inhibitor is introduced in the impingement zone, the optimum concentration at both velocities is 150 ppm. At this concentration, the 2 m/s impingement zone has a metal loss rate of 1.28 mm/year with the 8 m/s impingement zone having a metal loss rate of 1.25 mm/year. From this, there seems to be no shear related effect on inhibitor concentration as the inhibitor seems to be more effective in the 8 m/s shear conditions of about 183 Pa compared to the 2 m/s shear conditions of about 15 Pa. The inhibitor seems to be working best where it is needed most and this is evident with lower metal loss rates at the higher velocity compared to the lower velocity. It is however brought to attention that this effect is only at the optimum concentration and that other inhibitor concentrations such as 100 ppm and 200 ppm show different effects.

Figure 8-3 shows the difference between the two velocities in the conditions considered with the results monitored by mass loss "T" and Figure 8-4 shows the same comparison but with results monitored by electrochemistry "C". From Figure 8-4, it is noted that the electrochemistry "C" results at 8 m/s actually have lower electrochemical corrosion rates than the 2 m/s result in all conditions except aerated and 200 ppm inhibitor. The aerated behaviour shows good agreement in both "T" and "C" where 8 m/s zones have higher metal losses than those at 2 m/s.

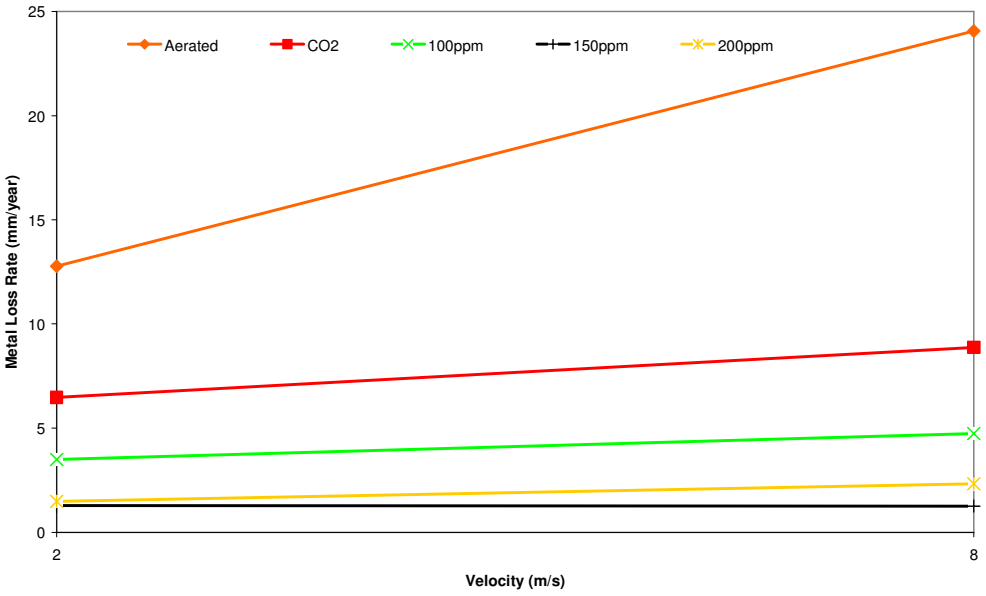

Figure 8-3. Comparison of total mass loss corrosion rates "T" at 8 m/s and 2 m/s in the impingement zone.

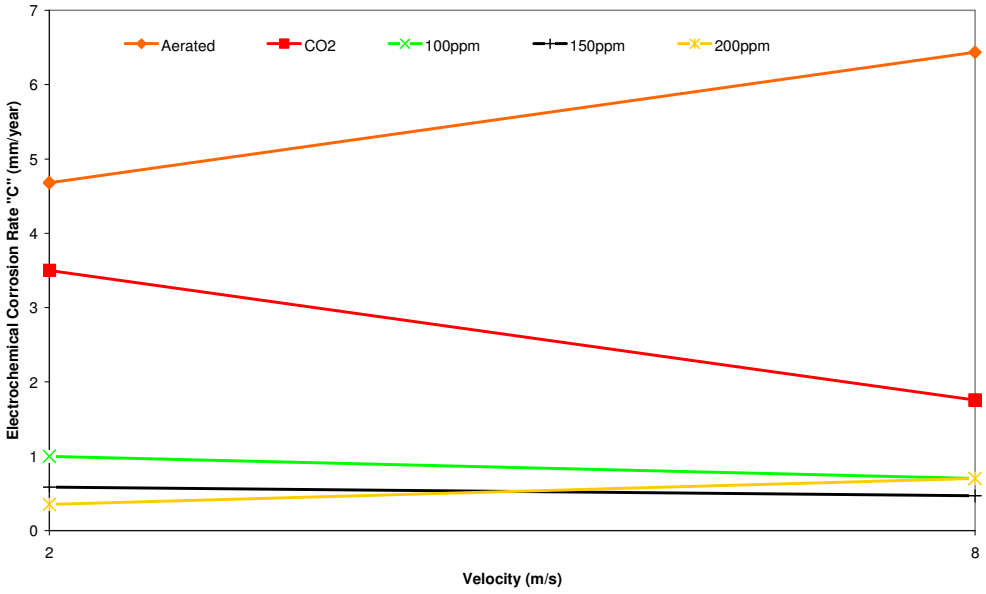

Figure 8-4. Comparison of electrochemistry "C" corrosion rates at 8 m/s and 2 m/s in the impingement zone.

8.5.1 8 m/s Impingement zone

As already demonstrated, there appears to be a significant amount of synergy and erosion effects in the conditions considered in this project. Comparisons of mass loss and electrochemistry results at both velocities are carried out for each hydrodynamic zone. Figure B 3 (appendices) shows the overall contrast between mass loss and electrochemistry metal loss rates across all environments tested in the 8 m/s impingement zone. Figure B 4 shows the combined erosion and synergy component "E+S" at 8 m/s in the impingement zone.

From Figure B 3, the component representing "T", the total material loss due to all mechanisms is represented by the gravimetric results whilst the component representing the material loss due to pure electrochemical corrosion "C" is the electrochemistry result. Both "T" and "C" are shown to be lower in CO_2 environments compared to aerated. As discussed earlier, the analogy of protective film formation in CO_2 environments has been observed in this project and is well reported by several authors identified in Chapter 3.

Figure B 4 shows the CO_2 reduction in "E+S" from an equivalent aerated value of 17.63 mm/year to a CO_2 equivalent "E+S" value lower at 7.12 mm/year. This represents a reduction in "E+S" from aerated to CO_2 brines of almost 60 % due to presumed iron carbonate protective film formation. As the electrochemistry result shows a reduction in electrochemical corrosion "C" (Figure B 3), it is also presumed that the film may be acting as a barrier to reactive species in CO_2 environments. In accordance with work by Nesic, et al., (2002), the scaling tendency in this zone is therefore supposed to be more than 1. This would indicate adequate supersaturation levels and consequently precipitaion.

Addition of the inhibitor reduces the CO_2 "T" metal loss rate with this observation accurate at all three concentrations considered (Figure B 3). Figure B 3 also shows the inhibitor reducing both "T" and "C" compared to CO_2 tests. Figure B 4 shows the inhibitor reducing the combined erosion and synergy component "E+C" at all concentrations compared to CO_2 values of "E+C".

From both Figures B 3 and B 4 (appendices), a concentration effect is noted with the best reduction of "T", "C" and "E+C" occurring at 150 ppm. The respective reductions

as percentages are 85.8 % for “T”, 73.3 % for “C” and 89 % for “E+C”. This observation agrees with work by Neville, et al., (2009) where inhibition was shown to reduce erosion-corrosion in brines representative of a typical gas condensate system at a temperature of 50^{o}C. Peak inhibitor efficiency was reliant on concentration with one inhbitor peaking at 50 ppm and another at 100 ppm. This effect is termed by Neville and Co as the “peak-value phenomenon”. Work by Neville, et al also shows that increasing the inhibitor concentration above this peak value actually decreases inhibitor efficiency and increases erosion-corrosion rates. This project has shown a similar result with Figures B 3 and B 4 showing an increase in “T”, “C” and “E+S” when a higher inhibitor concentration above the 150 ppm optimum is used.

8.5.2 2 m/s Impingement zone

Figure B 5 (appendices) shows the contrast between the mass loss and electrochemistry monitoring for the 2 m/s impingement zone. From Figure B 5, both components attributing to “T” and “C” are shown to be lower in CO_2 environments compared to aerated. The reduction in the “C” component is however lower than is noticed in the 8 m/s impingement zone, Figure B 3. The reduction in “C” at 2 m/s as a percentage is 25.2 % whereas the reduction at 8 m/s is 72.7%. This idea supports earlier remarks in section 8.3 of this chapter that lower velocities do not form effective protective films in CO_2 environments compared to higher velocity conditions as the local concentrations of Fe^{2+} supplied by the pre-film formation corrosion are lower and hence result in lower supersaturation levels compared to environments with high local concentrations of Fe^{2+} provided by higher pre-film formation corrosion. The 1/Rp results also support this as discussed in section 8.3 of this chapter.

Figure B 6 shows the combined erosion and synergy “E+S” component for the 2 m/s impingement zone. From Figure B 6, the reduction in “E+S” in CO_2 environments compared to aerated is determined to be 63.2 % which is almost similar to the reduction determined at 8 m/s. The effectiveness of films in both conditions is therefore initially considered to be a similar reduction in “E+S”.

The effect of the inhibitor has been to reduce “T”, “C” and “E+S” from the CO_2 environments and again the best efficiency is achieved at 150 ppm concentration. At this concentration, the respective reductions are 80.2 % for “T”, 83.3 % for “C” and

76.8 % for “E+C”. Compared to the percentage reductions at 8 m/s, the only component showing a higher percentage reduction at 2 m/s is “C”. The 150 ppm concentration is the most effective at reducing “T” and “E+C”. A better reduction in “C” is however noticed at 200 ppm although the overall beneficial and more important reduction in “T” is at 150 ppm.

8.6 Intermediate Zones

Figure 8-5 shows the metal loss behaviour between the 2 m/s and 8 m/s impingement zones. The metal loss rates “T” are obtained by the mass loss technique and show the CO_2 conditions as having the highest metal loss rates at both velocities. Compared to the behaviour in the impingement zone, the CO_2 metal loss at 8 m/s is much higher than that at 2 m/s. This signals some sort of lack of film formation in the intermediate zones at both velocities. The optimum inhibitor efficiency at both velocities is 100 ppm. At this concentration, the 2 m/s intermediate zone has a “T” metal loss rate of 1.28 mm/year with the 8 m/s “T” rate being 1.25 mm/year. Again, this shows that the inhibitor is working where it is most required and indicating better function at higher velocities.

Figure 8-6 shows a comparison of corrosion rates “C” obtained by electrochemistry. From Figure 8-6, the corrosion rates in CO_2 are observed to be higher at 2 m/s than at 8 m/s. Interestingly, the 2 m/s corrosion rate in CO_2 is higher than the 2 m/s aerated corrosion rate. At 8 m/s, a switch is observed where the corrosion rate in CO_2 is observed to be lower than in aerated conditions. The fact that in CO_2 conditions, the 8 m/s corrosion rate is lower than the 2 m/s corrosion rate supports ideas of selective film formation in CO_2 environments where the higher shear conditions seem to provide better environments for protective film formation. Introducing the inhibitor shows an optimum concentration of 200 ppm at both velocities.

Although the “C” results show an optimum inhibitor concentration of 200 ppm, the mass loss “T” results (Figure 8-5) show 150 ppm as the optimum concentration. This concentration is taken as the most effective optimum as the concentration of inhibitor required is lower and the total mass loss by all mechanisms “T” and not just electrochemical “C” is again observed to be lower at 150 ppm compared to 200 ppm.

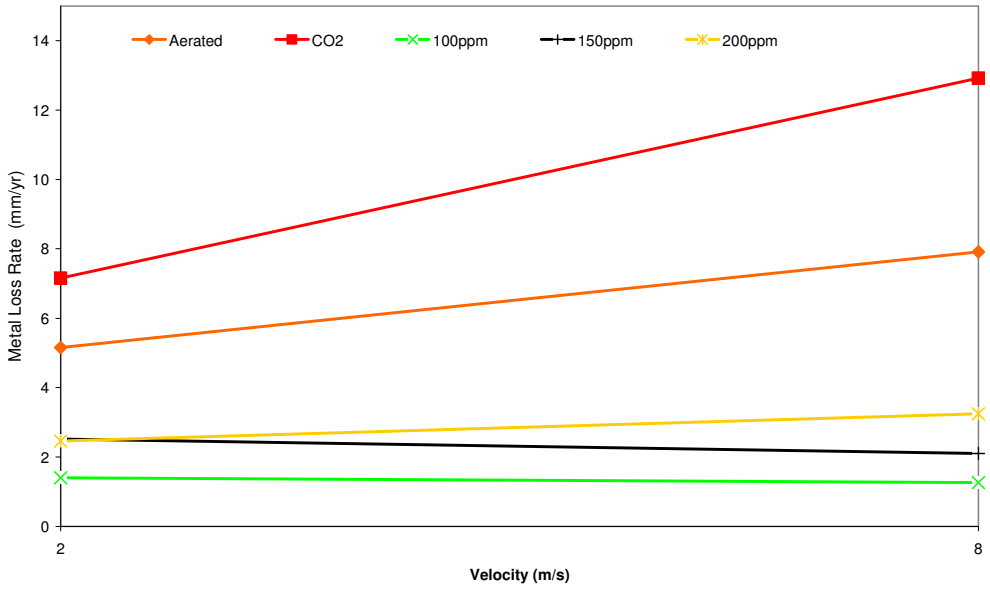

Figure 8-5. Comparison of total mass loss corrosion rates "T" at 8 m/s and 2 m/s in the intermediate zone.

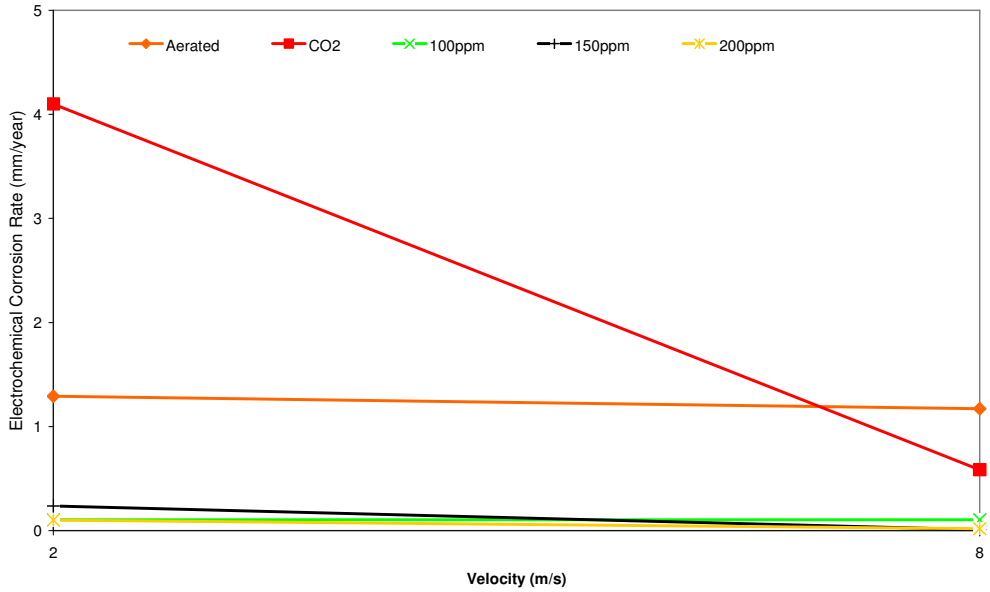

Figure 8-6. Comparison of electrochemistry "C" corrosion rates at 8 m/s and 2 m/s in the intermediate zone.

.

8.6.1 8 m/s Intermediate

Figure B 7 shows the contrast between the mass loss and electrochemistry results in the intermediate zone at 8 m/s. A surprising observation is the unexpected increase in "T" in CO_2 environments compared to aerated. A reduction in "C" is nevertheless observed with the percentage reduction being 49.6 %. This reduction is lower than results in the impingement zone suggesting the presumed carbonate film is acting as less of a barrier to corrosive species. Figure B 8 also shows an increase in "E+S" from aerated to CO_2 conditions suggesting larger metal losses as a result of wear mechanisms.

Addition of the inhibitor shows a reduction in all three components of "T", "C" and "E+S". The most effective concentration is however lower than levels required in the impingement zones with 100 ppm giving the lowest metal loss rates. The reduction rates at this concentration are 90.2 % for "T", 81.3 % for "C" and 91 % for "E+S". The percentage reductions are not only impressive but the final equivalent metal loss rates are lower than those experienced in the impingement zone. A clear increase in "E+S" is also noticed as the inhibitor concentration is increased from the optimum 100 ppm with the "E+S" component increasing at 150 ppm and increasing further at 200 ppm. The component "T" is also shown to increase with increasing concentration above the peak value of 100 ppm. This suggests an inhibitor mechanism where increasing the concentration above the peak concentration reduces the inhibitor film effectiveness to wear processes.

8.6.2 2 m/s Intermediate

Figure B 9 shows the contrast between the mass loss and electrochemical monitoring in the 2 m/s intermediate zone. A similar observation to that noticed in the 8 m/s intermediate zone is also observed where "T" and "C" are shown to increase in CO_2 environments compared to aerated environments. Introducing the inhibitor reduces the CO_2 rates with the most effective concentration similar to the 8 m/s intermediate zone and being 100 ppm. At this concentration, "T" is reduced by 80.4 % with the "C" component reduced by an impressive 97.3 % to a final value of 0.11 mm/year. Although the 200 ppm value of "C" is less at 0.10 mm/year, the value at 100 ppm has been chosen as best as 200 ppm gives a higher value of "T".

Figure B 10 shows the combined "E+S" component for the 2 m/s intermediate zone. In contrast to the "E+S" component at 8 m/s, no increase in "E+S" in CO_2 environments compared to aerated is noted. Again, the lowest "E+S" component is achieved at an inhibitor concentration of 100 ppm compared to the impingement concentration of 150 ppm. Increasing the inhibitor concentration above this peak value lessens the efficiency and increases the "E+S" component as the concentration is increased further suggesting higher inhibitor concentrations above this peak value lessen the inhibitor film efficiency at reducing wear related mechanisms. The peak concentration of 100 ppm reduces the CO_2 "E+C" component by 57.8 %.

8.7 Outer zones

Figures 8-7 and 8-8 show the "T" metal loss rates and "C" corrosion rates in the outer zone at 2 m/s and 8 m/s. Figure 8-7 shows the results by mass loss and Figure 8-8 shows the results by electrochemistry. From Figure 8-7, the metal loss rate at 2 m/s is observed to be higher in CO_2 compared to aerated conditions. The CO_2 "T" metal loss rate at 2 m/s is also observed to be higher than the CO_2 "T" rate at 8 m/s. Again this further supports the idea that protective films in CO_2 environments form better in higher flow conditions. This observation is also noted in Figure 8-8 where the corrosion rates are monitored by electrochemistry and show an even larger difference between the two velocities in CO_2. Addition of the inhibitor shows 100 ppm as the optimum concentration at 2 m/s and 8 m/s for reductions in "T". However, at this concentration, the 8 m/s velocity has the highest corrosion rate compared to the 2 m/s. The results by electrochemistry, Figure 8-8 show 150 ppm as the optimum inhibitor concentration. Nevertheless, as the 100 ppm is more effective at reducing the total material loss "T" by all mechanisms and requires 50 % less inhibitor, this concentration is chosen as optimum.

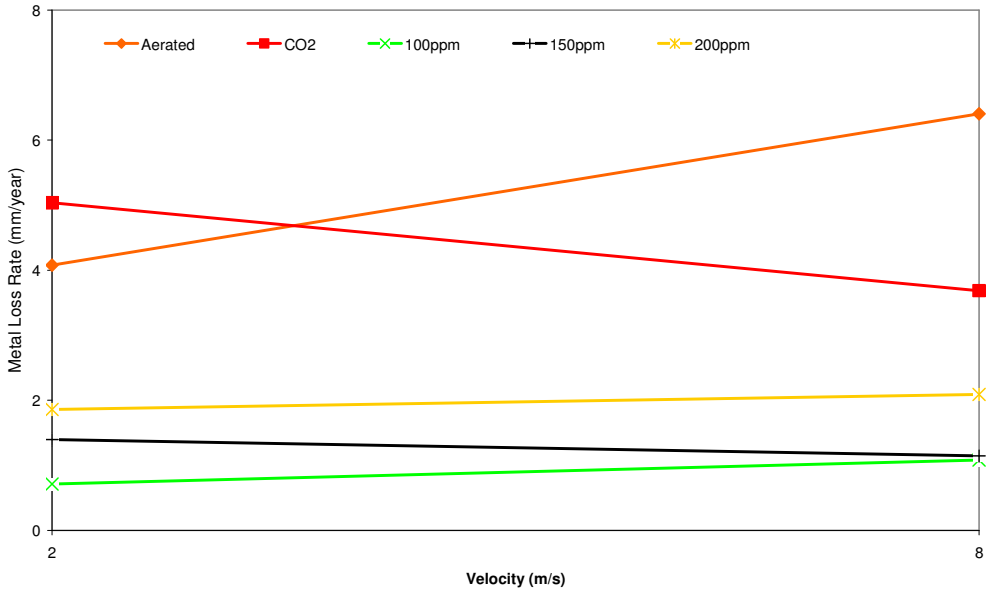

Figure 8-7. Comparison of total mass loss corrosion rates "T" at 8 m/s and 2 m/s in the outer zone

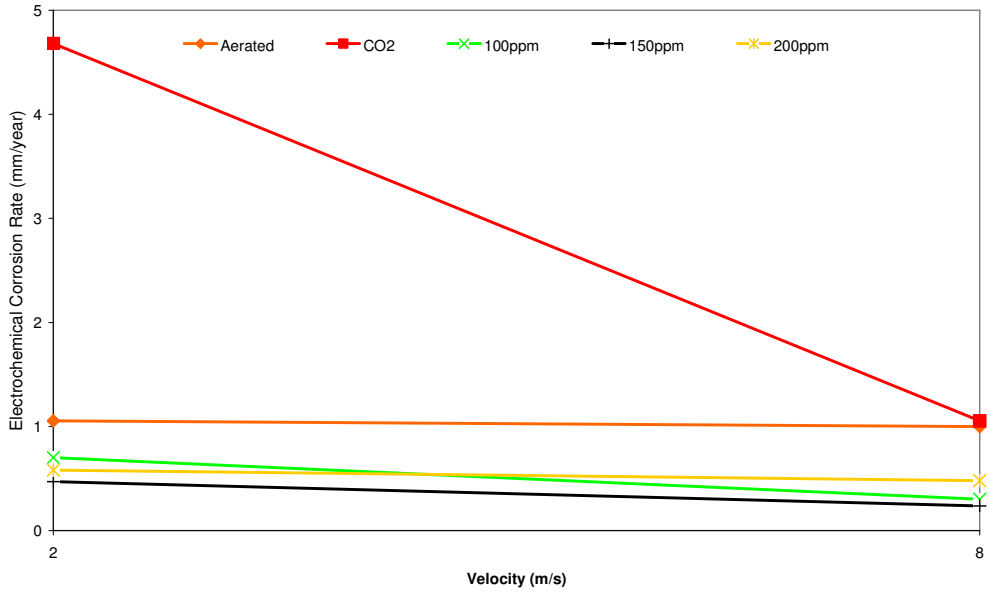

Figure 8-8. Comparison of electrochemistry "C" corrosion rates at 8 m/s and 2 m/s in the outer zone.

8.7.1 8 m/s Outer

Figure B 11 shows the contrast between mass loss and electrochemistry in the 8 m/s outer zone. A reduction is noticed in the mass loss tests in CO_2 environments compared to aerated. The electrochemistry "C" component shows no reduction but instead shows a small increase. The reduction in "T" from aerated to CO_2 environments equates to a percentage decrease of 42.4 %. Introducing the inhibitor shows a "T" and "C" reduction of CO_2 corrosion at all three concentrations with the 100 ppm being the most effective concentration for "T". Although 150 ppm shows a better "C" reduction, the difference is small. The increased concentration and higher "T" component at 150 ppm therefore makes 100 ppm the optimum concentration. Increasing the inhibitor concentration to 200 ppm increases both "T" and "C" again emphasising the concentration effect on inhibitor efficiency.

Figure B 12 shows the combined erosion and synergy component "E+S" at 8 m/s in the outer zone. The figure shows a reduction in "E+S" in CO_2 environments compared to aerated. This reduction as a percentage is 51.2 %. Introducing the inhibitor reduces the CO_2 "E+S" component at all three concentrations. The concentration at 100 ppm is again the most effective and has a percentage reduction in "E+S" of 70.5 %. Again increasing the inhibitor concentration above the 100 ppm optimum lessens the inhibitor efficiency and increases the "E+C" component as the concentration is increased further.

8.7.2 2 m/s Outer

Figure B 13 shows the contrast between the mass loss and electrochemistry in the 2 m/s outer zone. It is quickly noticeable that the contrast between the two methods especially in CO_2 and inhibitor environments has decreased in comparison to the other zones discussed. Both "T" and "C" also increase in CO_2 environments compared to aerated pointing to increased corrosion rates due to lack of film formation within the zone. Introducing the inhibitor shows a reduction in both "T" and "C" at all three concentrations with the best overall effect of reducing "T" achieved at 100 ppm. Reductions in "C" however show a dissimilar effect with increasing inhibitor concentrations showing lower corrosion rates compared to the optimum value effective for "T". The optimum concentration for "C" is 150 ppm, which shows a

percentage reduction of 90 %. However, 100 ppm shows the lowest value for “T” with the inhibitor efficiency at this concentration being 86 %.

Figure B 14 shows the combined erosion and synergy component “E+S”. The highest amount of “E+S” is in aerated conditions with the lowest in conditions with inhibitor concentration of 100 ppm. The “E+S” component reduces significantly in CO_2 environments compared to aerated. The effect of the inhibitor only reduces the CO_2 corrosion at a concentration of 100 ppm and a corresponding efficiency of 97.2 %. Increasing the inhibitor concentration above 100 ppm actually increases the “E+S” components above those in CO_2 environments. This could indicate some conflict in inhibitor and CO_2 films resulting in less effective protection from both.

8.8 Galvanic Interactions

The galvanic interaction results were presented in Chapter 7 of this thesis and have shown a large difference in galvanic currents between the hydrodynamic zones and conditions considered in this project. The aerated galvanic activity has shown the highest galvanic currents with the more impingement conditions benefiting from the galvanic currents and acting as the cathode in all pairings.

Figure 8-9 shows a summary of the galvanic activity presented in Chapter 7. The figure only shows the galvanic currrents of the CO_2 tests and CO_2 tests with inhibitor as the aerated currents have not been included in order to focus on the CO_2 and inhibitor tests only. From Figure 8-9, The optimum inhibitor concentration that gives the lowest current exchanges in most cases is 100 ppm. This concentration lowers the CO_2 galvanic currents in all cases except the 2 m/s Intermediate-outer to the Impingement pairing.

Again the “peak-value phenomenon” is noticed in the galvanic activity as the currents are observed to increase as the inhibitor concentration is increased above the optimum 100 ppm concentration. This is especially so at a concentration of 150 ppm as all currents observed at 100 ppm show an increase when 150 ppm inhibitor is used. At 200 ppm, an increase above the peak concentration is observed in all pairings except the Intermediate-outer to Impingement pairing.

Chapter 7 also demonstrated the switching of polarity in conditions containing inhibitor suggesting the inhibitor is also having an added effect of constraining the additional preferential corrosion between the zones by swithcing the anode and cathode. In practice this would ensure the preferrential galvanic activity is not contained in one zone and hence prevents excessive corrosion rates by reducing preferential attack within one zone.

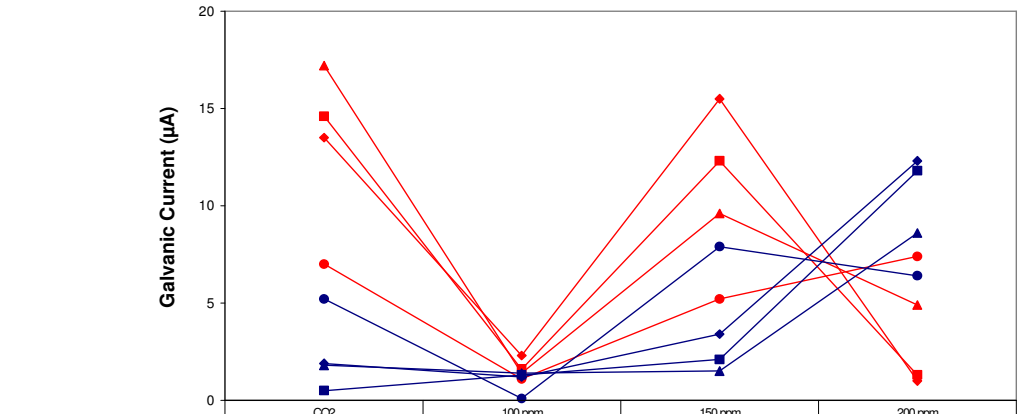

	CO2	100 ppm	150 ppm	200 ppm
Impingement-Outer 8 m/s	13.5	2.3	15.5	1.0
Impingement-Intermediate 8 m/s	17.2	1.4	9.6	4.9
Intermediate-Outer 8 m/s	7.0	1.1	5.2	7.4
IntermediateOuter-Impingement 8 m/s	14.6	1.6	12.3	1.3
Impingement-Outer 2 m/s	1.9	1.2	3.4	12.3
Impingement-Intermediate 2 m/s	1.8	1.4	1.5	8.6
Intermediate-Outer 2 m/s	5.2	0.1	7.9	6.4
IntermediateOuter-Turbulent 2 m/s	0.5	1.3	2.1	11.8

Figure 8-9 Galvanic activity for all three zones at 8 m/s (red) and 2 m/s (blue). Figure shows currents in µA for tests in various conditions.

9.0 CONCLUSIONS RECOMMENDATIONS AND FURTHER WORK

9.1 Conclusions

This project adds some valuable contributions to corrosion and has established issues that require further research. From the tests and issues considered in this project, the following conclusions are made:

- Solid-free flowing corrosive fluids may involve non-electrochemical material losses which contribute to the total material loss. This has been the case in both aerated and CO_2 environments. This component has been identified as the combined erosion and synergy component "E+S";
- The combined erosion and synergy component "E+S" has been found to make up the majority of the total material loss in the flowing corrosive fluids studied in this project. This questions whether electrochemical monitoring techniques **alone** are suitable for monitoring corrosion in such conditions as they are incapable of assessing non non-Faraday material losses such as "E+S" that have been found to make up the majority of the total material loss by all mechanisms;
- The highest corrosion rates for the impingement zones have been in aerated conditions and indicate possibility of severe corrosion in impingement sections of pipelines containing aerated fluids;
- The Inhibitor has been shown to reduce the total material loss by all mechanisms "T", the material loss by electrochemical mechanisms "C" and the combined erosion and synergy component "E+S";
- The inhibitor has shown sensitive concentration effects with optimum efficiency dependent on conditions. The two impingement zones require 150 ppm for optimum efficiency with the outer zones requiring 100 ppm;
- Provided that the optimum inhibitor concentration is achieved, the inhibitor has shown the capability to work well over a range of shear stresses.
- Increasing inhibitor concentration above the optimum value has been shown to have detrimental effects on the corrosion rate and inhibitor efficiency. This has been the case with the inhibitor increasing "T", "E+S" and in some cases "C". The

overall effect has been determined from "T", the total material loss from all mechanisms;

- CO_2 environments have shown variable film formation with the lower velocity conditions having the least protective films. This has been linked to the degree of supersaturation influenced by local concentrations of Fe^{2+};
- CO_2 films have been shown to form in regions where there are higher amounts of Fe^{2+} concentration provided by the pre-corrosion before film formation;
- Shear stresses below 6 Pascals have been shown to have no major effect on inhibitor efficiency as 100 ppm was the optimum concentration for all values up to 6 pa. Shear stresses of 15 Pascal's and 183 Pascal's have been shown to require higher concentrations at 150 ppm in order to achieve peak efficiency;
- The inhibitor has been found to be effective at reducing the galvanic activity between the hydrodynamic zones considered. The inhibitor has also been found to reduce the amount of preferential corrosion by switching the anode between the zones. This mechanism would ensure more uniform corrosion activity instead of preferential corrosion within one zone leading to large cumulative metal losses within the zone. It is also noticed that during the switch, the cathode is also benefiting from a cathodic protection effect which would help reduce the corrosion damage

9.2 Recommendations and Further Work

In light of the conclusions within this project, the following recommendations are made:

- A review of corrosion monitoring techniques in situations involving flowing corrosive fluids is recommended. This should include similar assessments using other laboratory systems used to simulate flow such as the Rotating cylinder and Rotating disk electrodes;
- If corrosion inhibition is used as a mitigation technique for internal corrosion of pipelines, a comprehensive test program to establish the inhibitor optimum concentration should always be conducted and in conditions that best simulate actual field conditions;

- More studies are required in order to establish the amount of non-Faraday material loss in flowing corrosive fluids. Such studies should then be used to develop correlations to account for the non-Faraday material losses encountered in solid-free corrosive flow.

- Further work on non-Faraday related material losses in solid-free flow should be carried out. In addition, such work should involve other methods of simulating flow such as the rotating cylinder and rotating disk;

- Correlations for the non-Faraday material losses should be established and used alongside electrochemical monitoring techniques;

- A similar study involving sour (H_2S) environments should be conducted;

- Studies such as XPS should be carried out to identify films formed in various hydrodynamic zones with and without inhibitor;

- Linkage of galvanic effects due to welding and galvanic effects due to hydrodynamic activity should be considered.

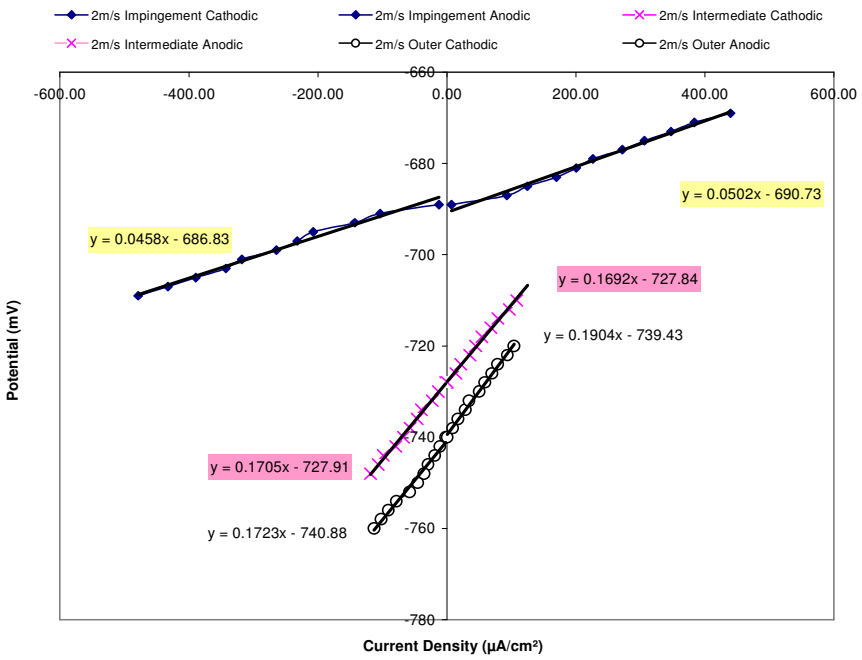

Figure A 1. 4 hour linear polarisation scans, 2 m/s, aerated.

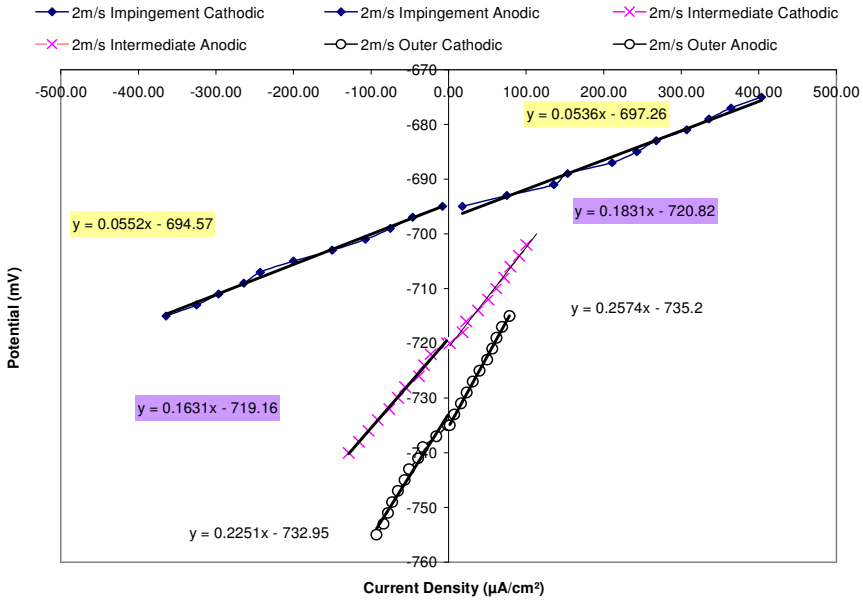

Figure A 2. - 15 hour linear polarisation scans, 2 m/s, aerated.

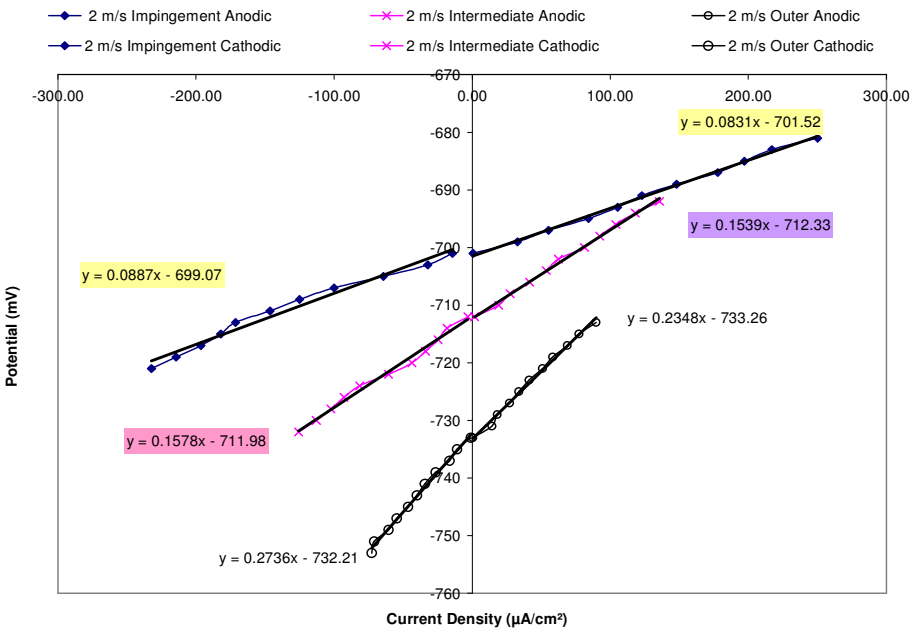

Figure A 3. - 24 hour linear polarisation scans, 2 m/s, aerated

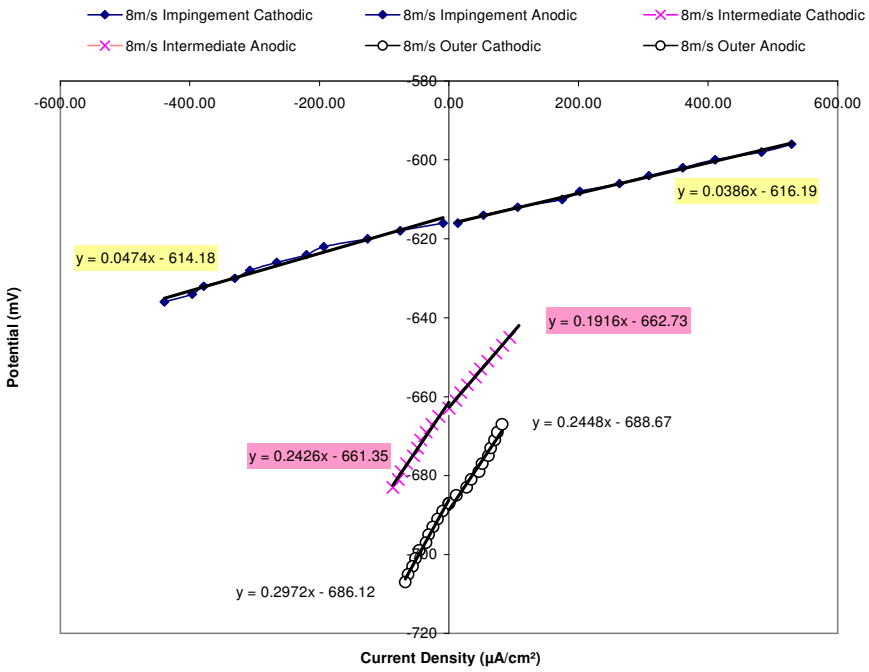

Figure A 4. - 4 hour linear polarisation scans, 8 m/s, aerated.

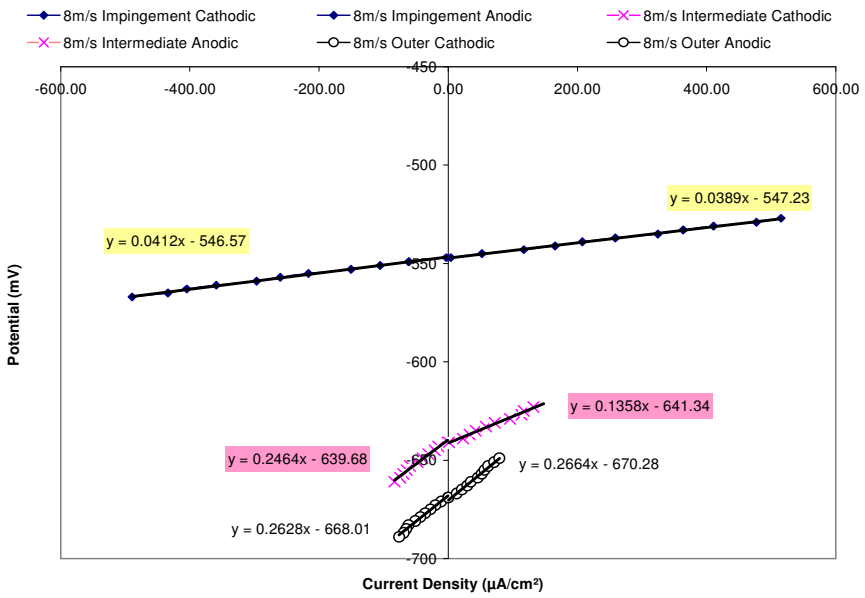

Figure A 5. – 15 hour linear polarisation scans, 8 m/s, aerated.

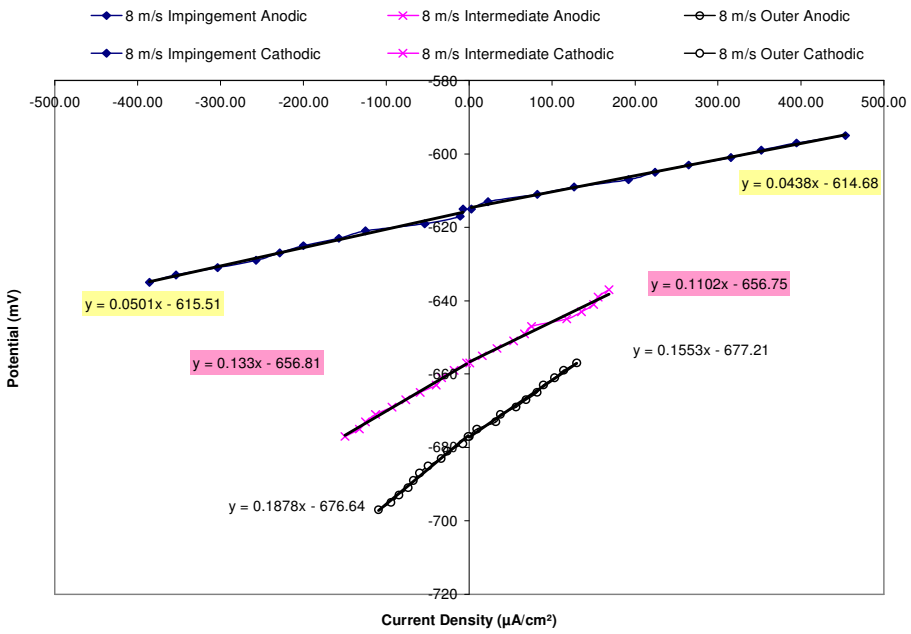

Figure A 6. - 24 hour linear polarisation scans, 8 m/s, aerated

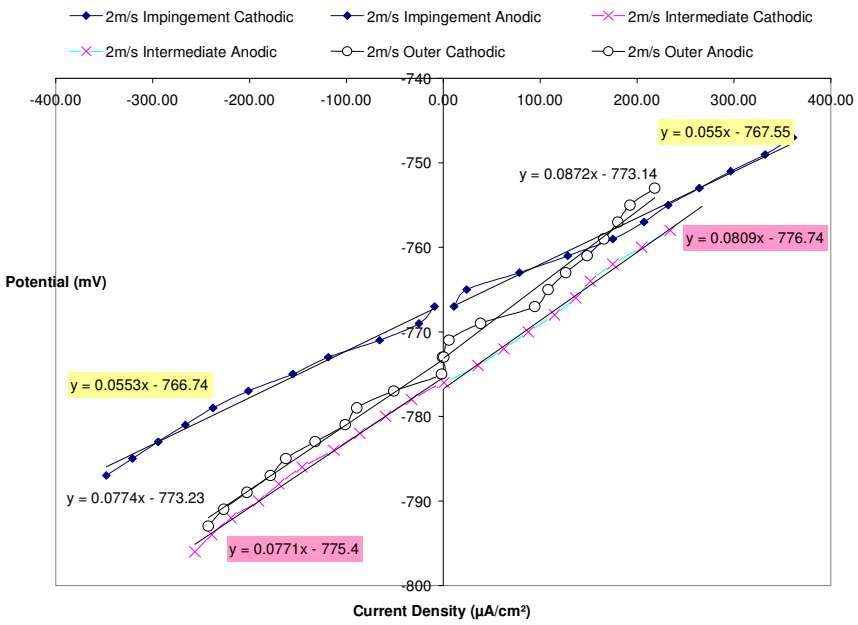

Figure A 7. - 4 hour linear polarisation scans, 2 m/s, CO_2

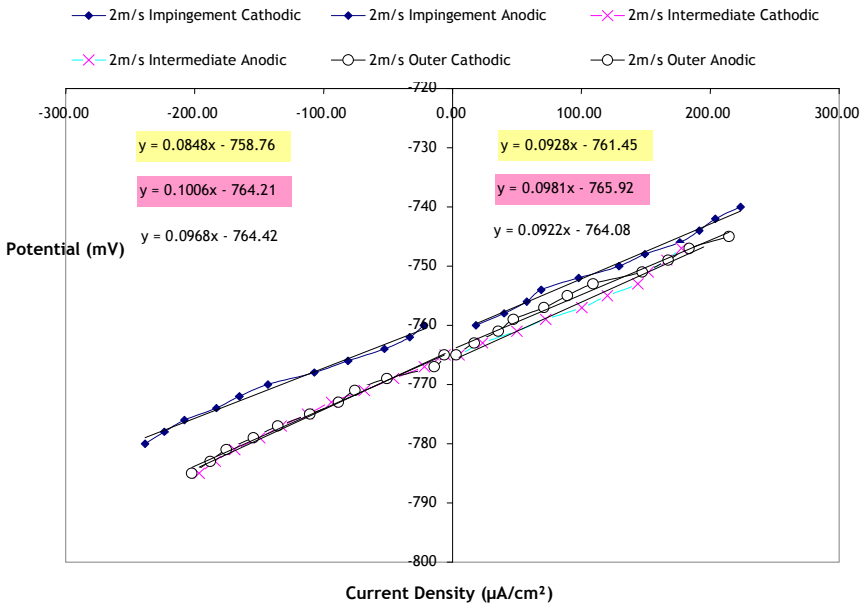

Figure A 8. - 15 hour linear polarisation scans, 2 m/s, CO_2

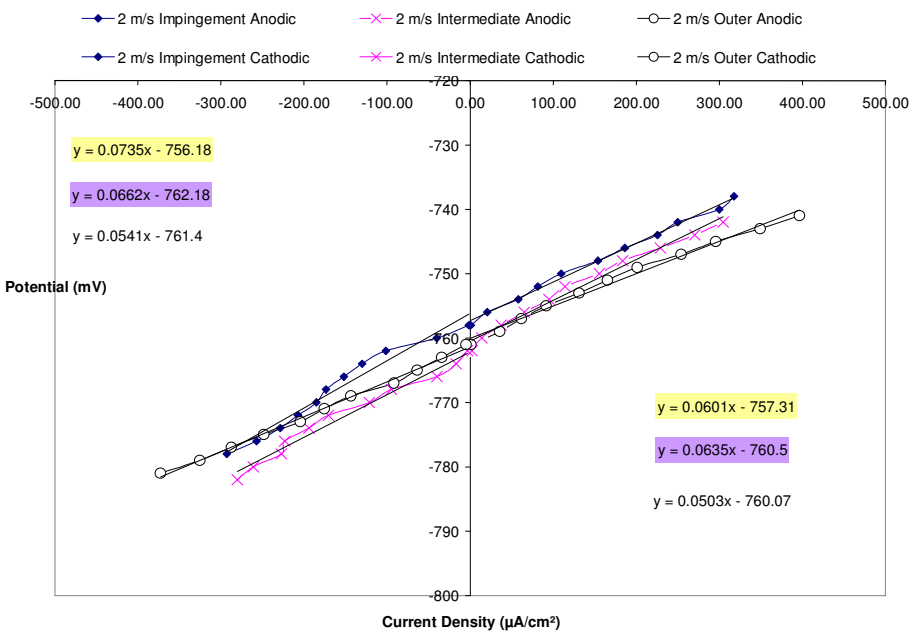

Figure A 9. - 24 hour linear polarisation scans, 2 m/s, CO_2

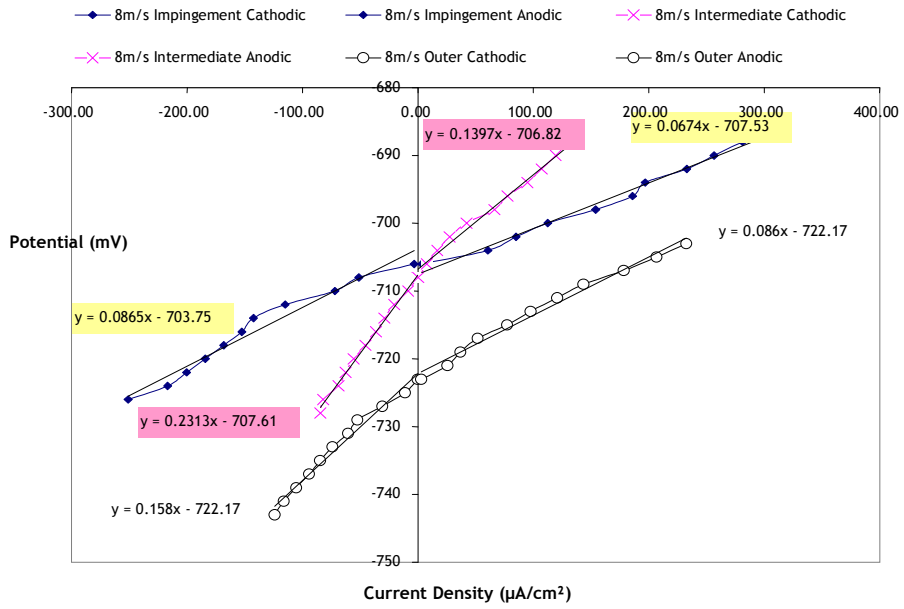

Figure A 10. - 4 hour linear polarisation scans, 8 m/s, CO_2

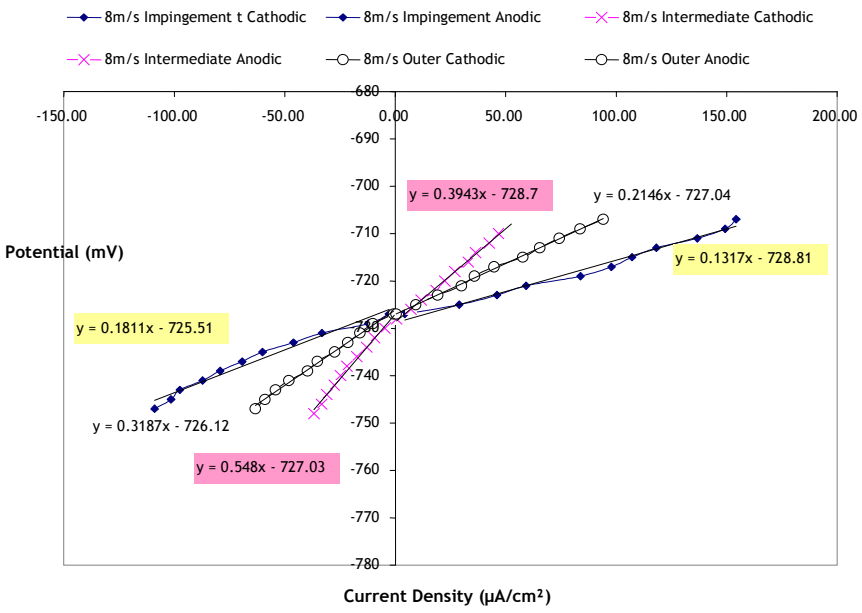

Figure A 11. - 15 hour linear polarisation scans, 8 m/s, CO_2

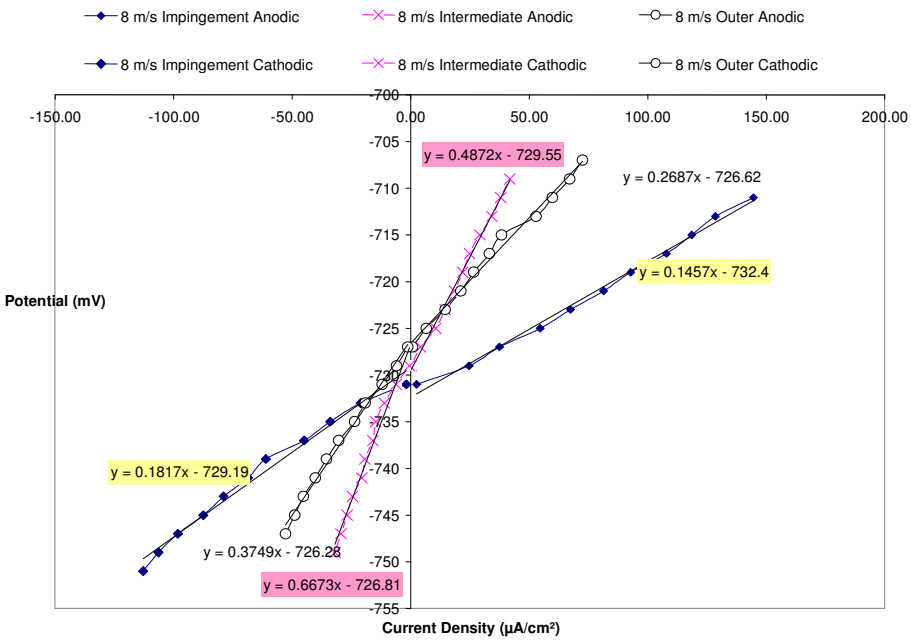

Figure A 12. - 24 hour linear polarisation scans, 8 m/s, CO_2

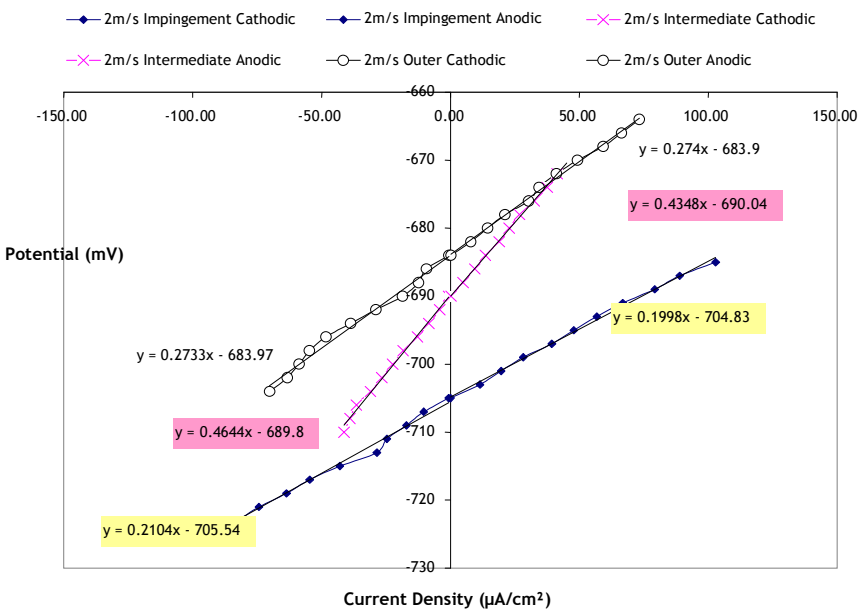

Figure A 13. - 4 hour linear polarisation scans, 2 m/s, CO_2 with 100 ppm inhibitor

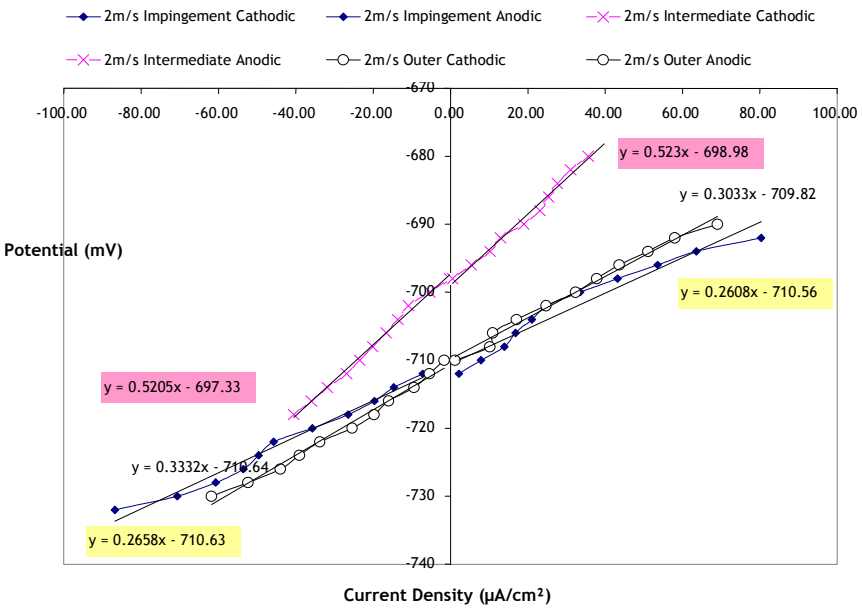

Figure A 14. - 15 hour linear polarisation scans, 2 m/s, CO_2 with 100 ppm inhibitor

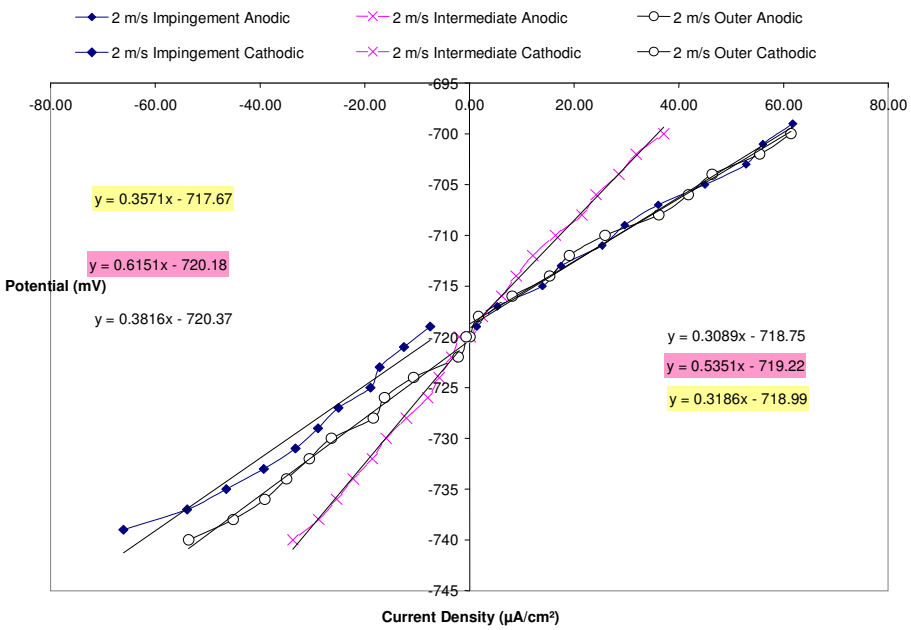

Figure A 15. – 24 hour linear polarisation scans, 2 m/s, CO_2 with 100 ppm inhibitor

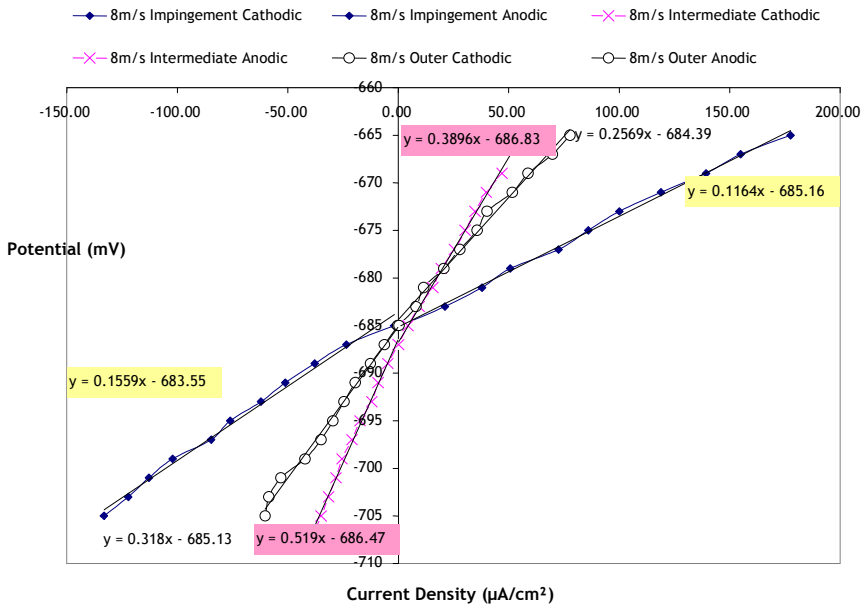

Figure A 16. – 4 hour linear polarisation scans, 8 m/s, CO_2 with 100 ppm inhibitor

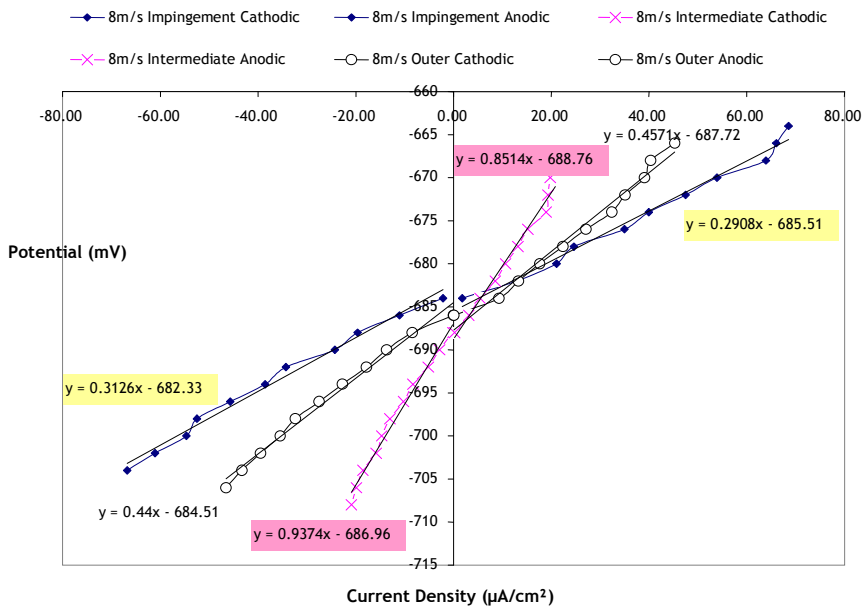

Figure A 17.– 15 hour linear polarisation scans, 8 m/s, CO_2 with 100 ppm inhibitor

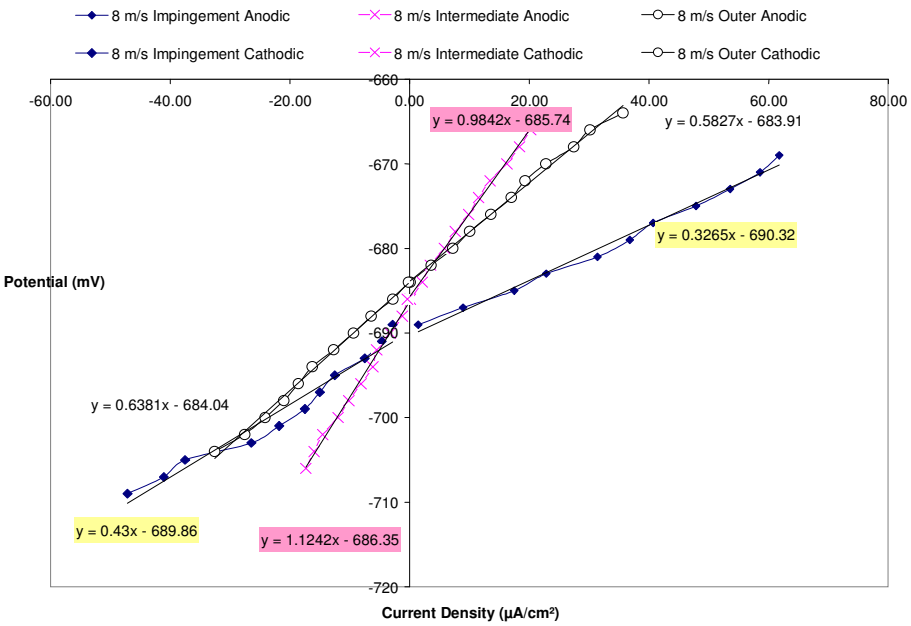

Figure A 18. – 24 hour linear polarisation scans, 8 m/s, CO_2 with 100 ppm inhibitor

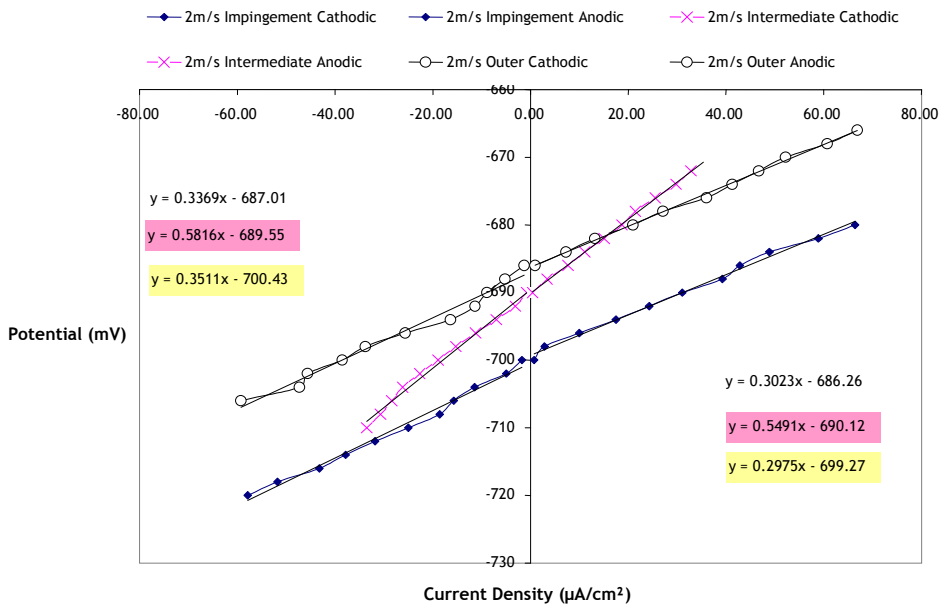

Figure A 19. – 4 hour linear polarisation scans, 2 m/s, CO_2 with 150 ppm inhibitor

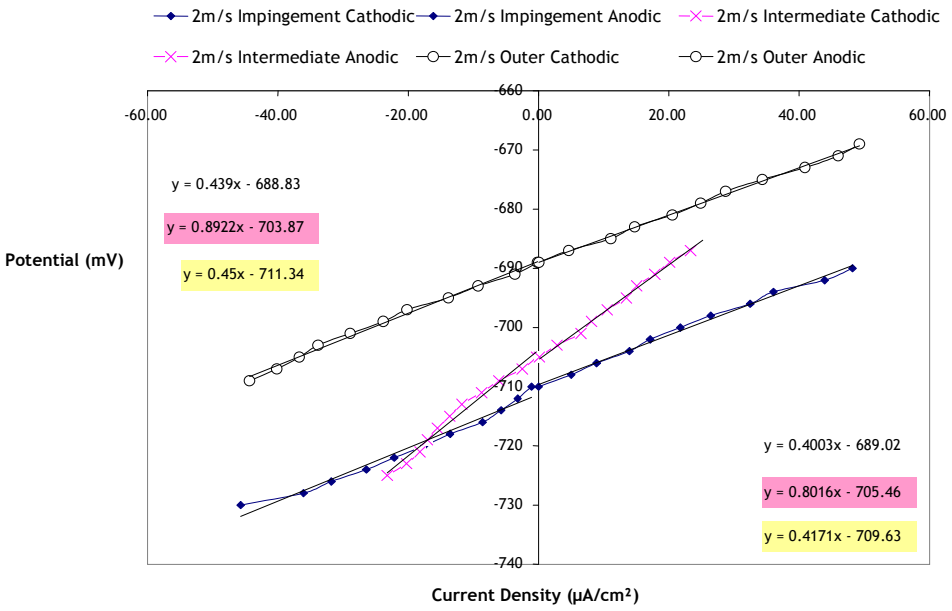

Figure A 20. – 15 hour linear polarisation scans, 2 m/s, CO_2 with 150 ppm inhibitor

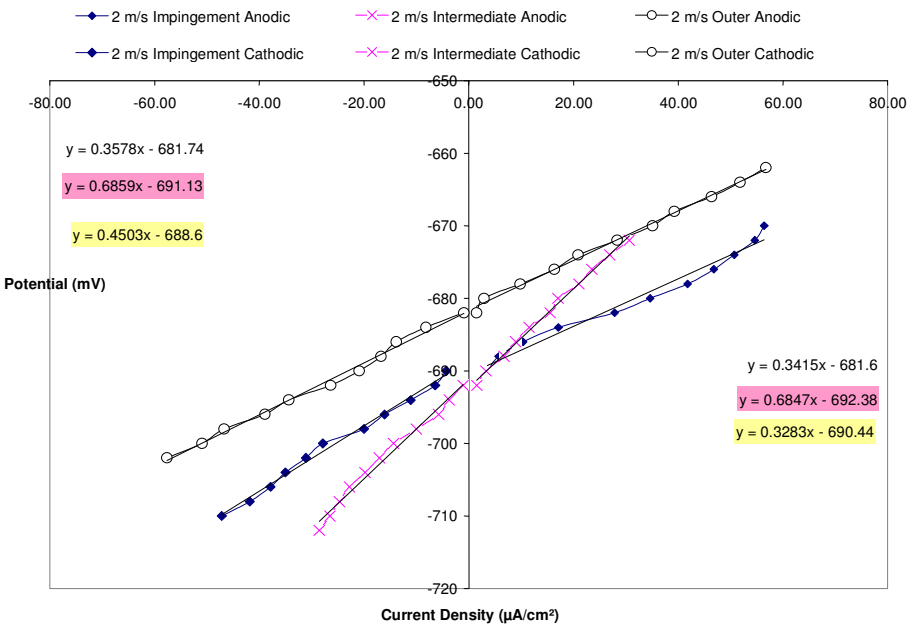

Figure A 21. – 24 hour linear polarisation scans, 2 m/s, CO_2 with 150 ppm inhibitor

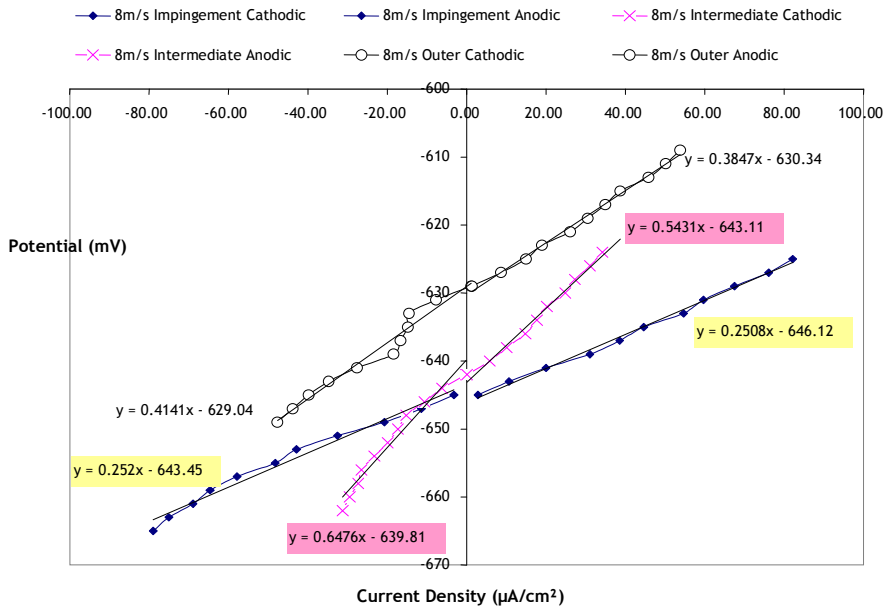

Figure A 22. – 4 hour linear polarisation scans, 8 m/s, CO_2 with 150 ppm inhibitor

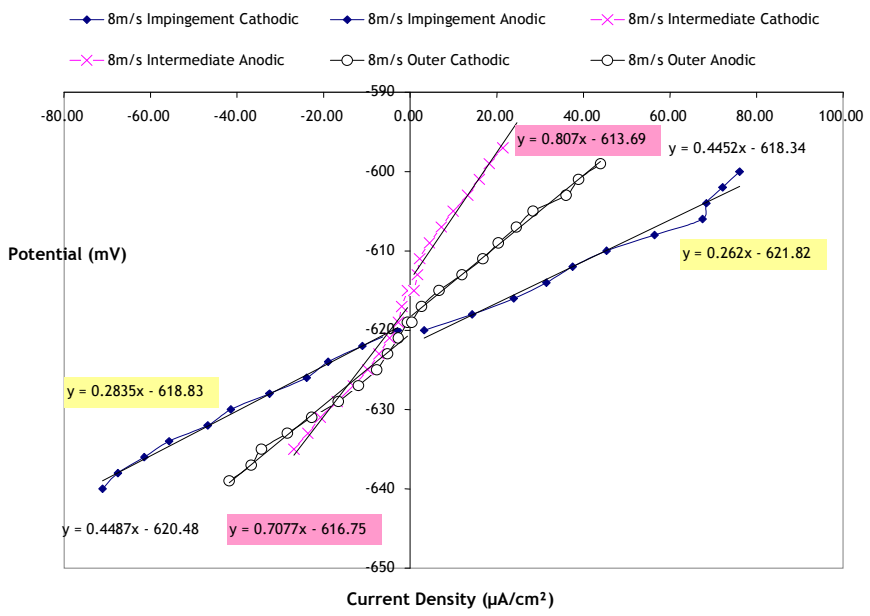

Figure A 23. – 15 hour linear polarisation scans, 8 m/s, CO_2 with 150 ppm inhibitor

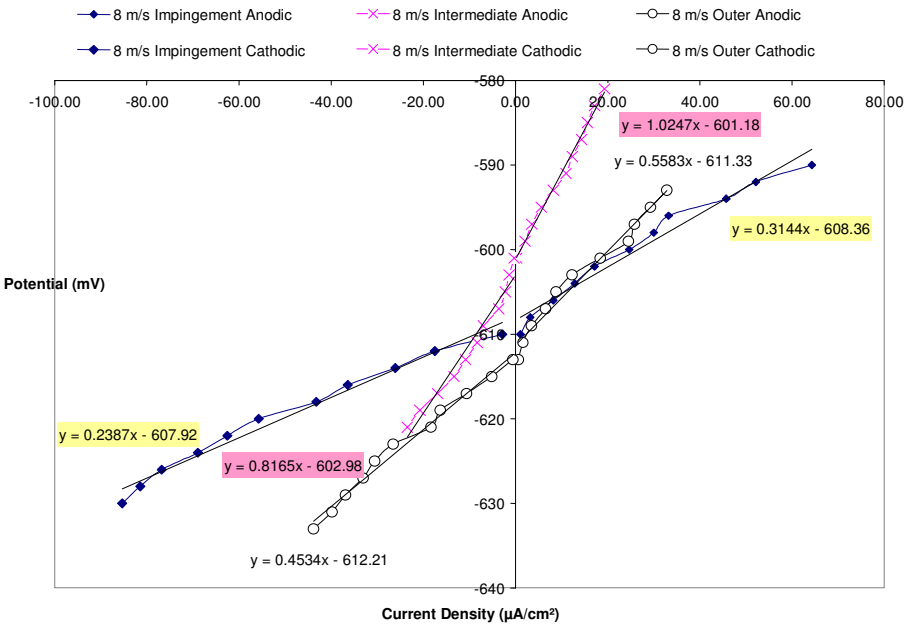

Figure A 24. – 24 hour linear polarisation scans, 8 m/s, CO_2 with 150 ppm inhibitor

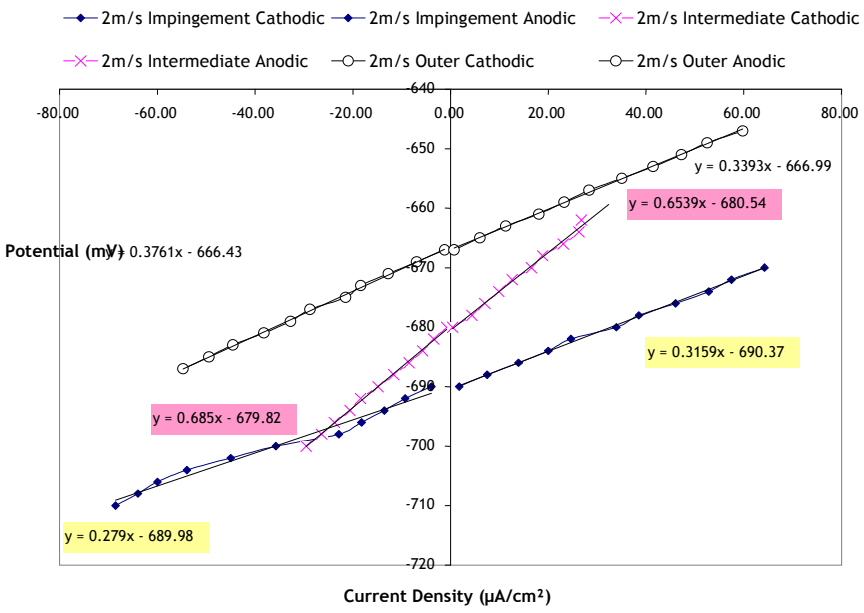

Figure A 25. – 4 hour linear polarisation scans, 2 m/s, CO_2 with 200 ppm inhibitor

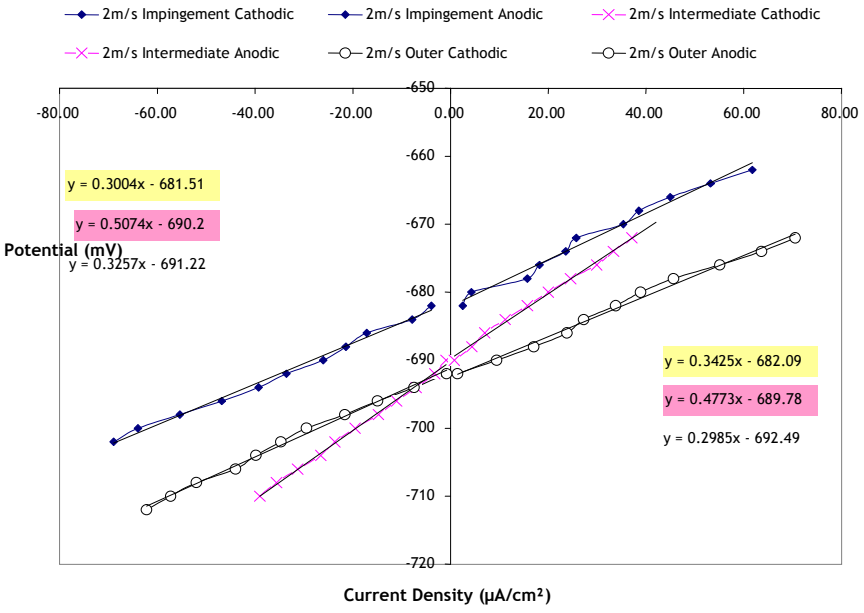

Figure A 26. – 15 hour linear polarisation scans, 2 m/s, CO_2 with 200 ppm inhibitor

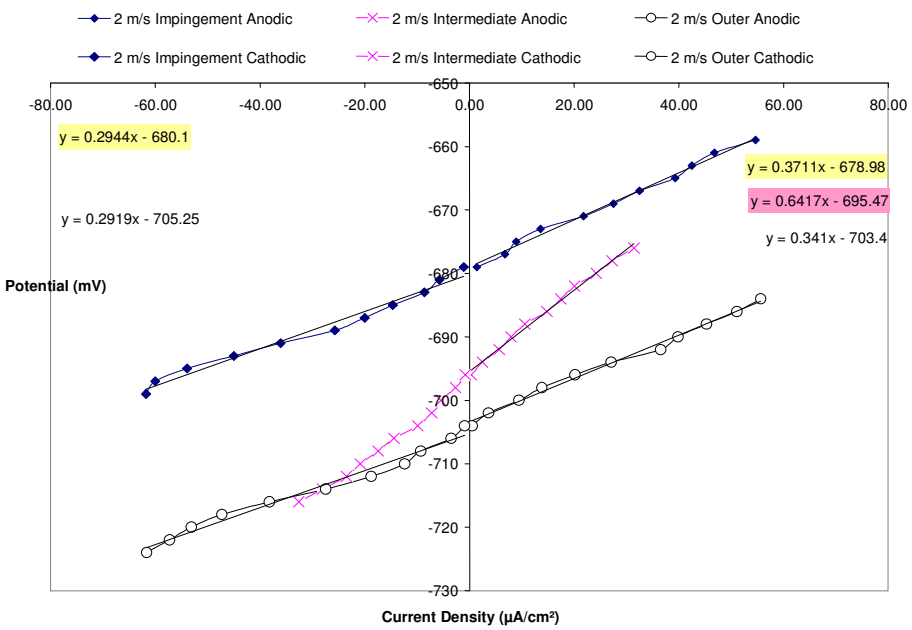

Figure A 27. – 24 hour linear polarisation scans, 2 m/s, CO_2 with 200 ppm inhibitor

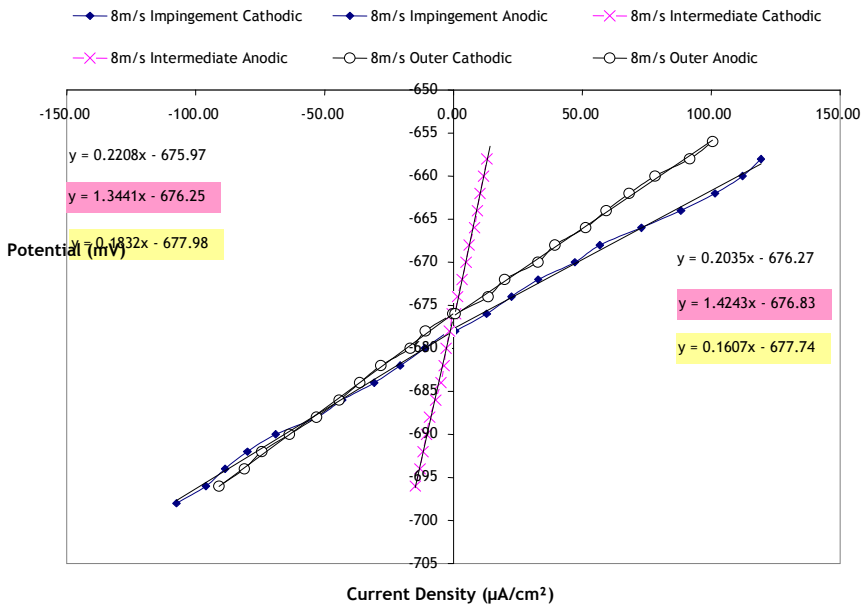

Figure A 28. – 4 hour linear polarisation scans, 8 m/s, CO_2 with 200 ppm inhibitor

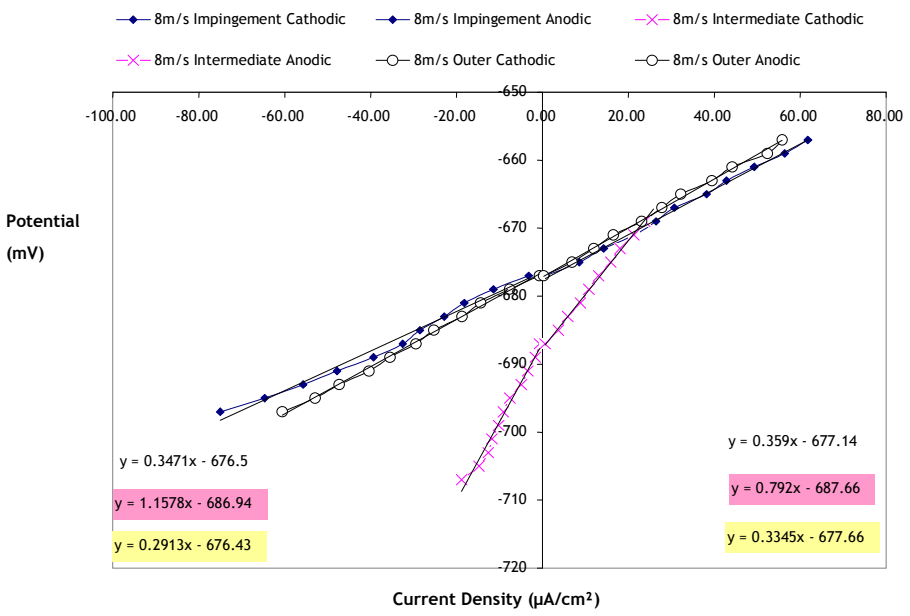

Figure A 29. – 15 hour linear polarisation scans, 8 m/s, CO_2 with 200 ppm inhibitor

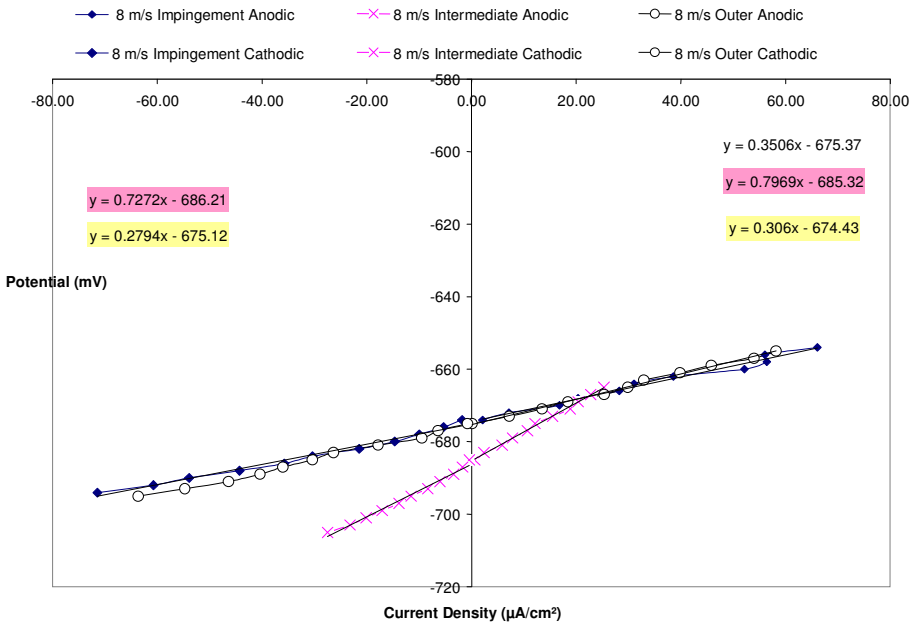

Figure A 30. – 24 hour linear polarisation scans, 8 m/s, CO_2 with 200 ppm inhibitor

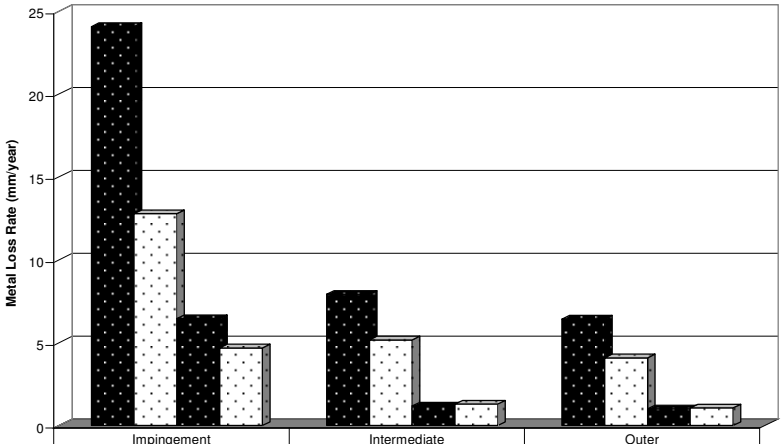

	Impingement	Intermediate	Outer
8 m/s Gravimetric "T"	24.06	7.91	6.41
2 m/s Gravimetric "T"	12.78	5.16	4.08
8 m/s Electrochemical Corrosion "C"	6.44	1.17	1
2 m/s Electrochemical Corrosion "C"	4.68	1.29	1.05

Figure B 1. Metal loss rates obtained by mass loss "T" and electrochemistry "C" in aerated conditions.

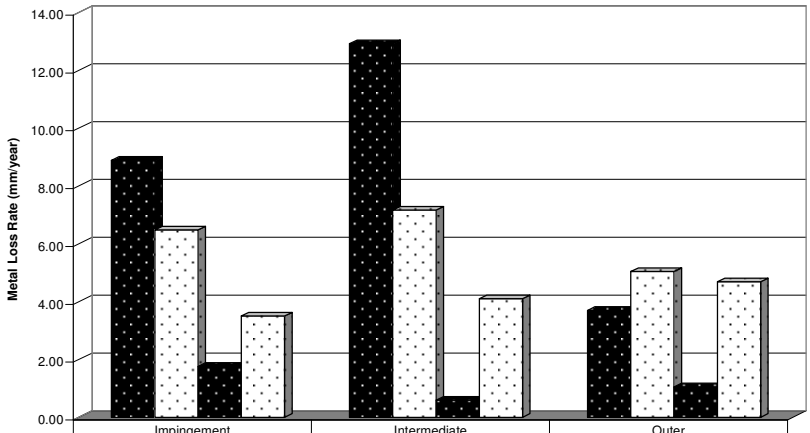

	Impingement	Intermediate	Outer
8 m/s Gravimetric "T"	8.88	12.92	3.69
2 m/s Gravimetric "T"	6.48	7.16	5.04
8 m/s Electrochemical Corrosion "C"	1.76	0.59	1.05
2 m/s Electrochemical Corrosion "C"	3.50	4.10	4.68

Figure B 2. Metal loss rates obtained by mass loss "T" and electrochemistry "C" in CO_2 saturated conditions.

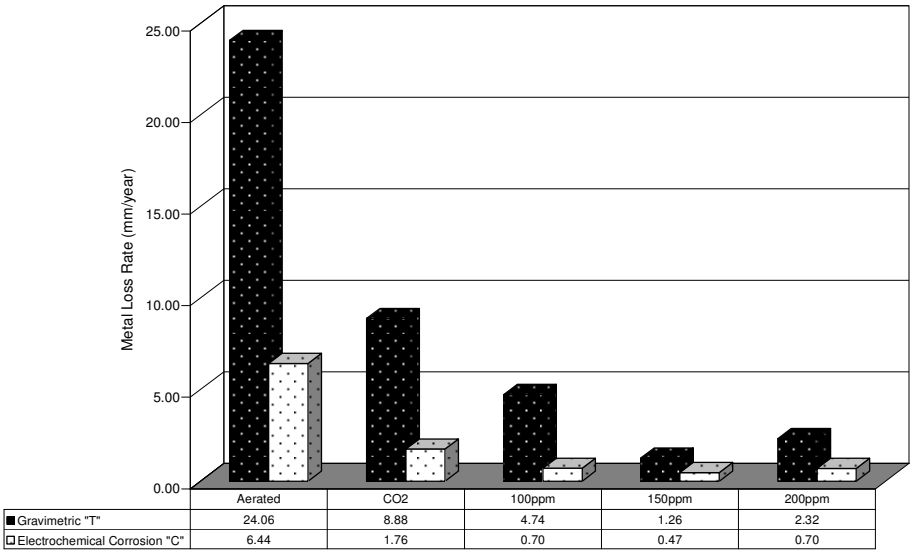

	Aerated	CO2	100ppm	150ppm	200ppm
Gravimetric "T"	24.06	8.88	4.74	1.26	2.32
Electrochemical Corrosion "C"	6.44	1.76	0.70	0.47	0.70

Figure B 3. Metal loss rates obtained by mass loss "T" and electrochemistry "C" in various conditions for the impingement zone at 8 m/s.

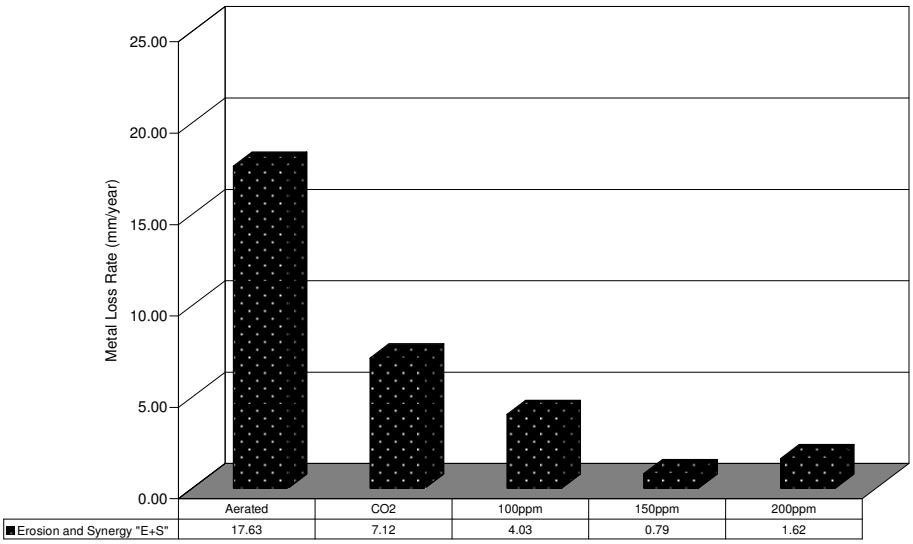

	Aerated	CO2	100ppm	150ppm	200ppm
Erosion and Synergy "E+S"	17.63	7.12	4.03	0.79	1.62

Figure B 4. Combined erosion and synergy "E+S" component in the impingement zone at 8 m/s.

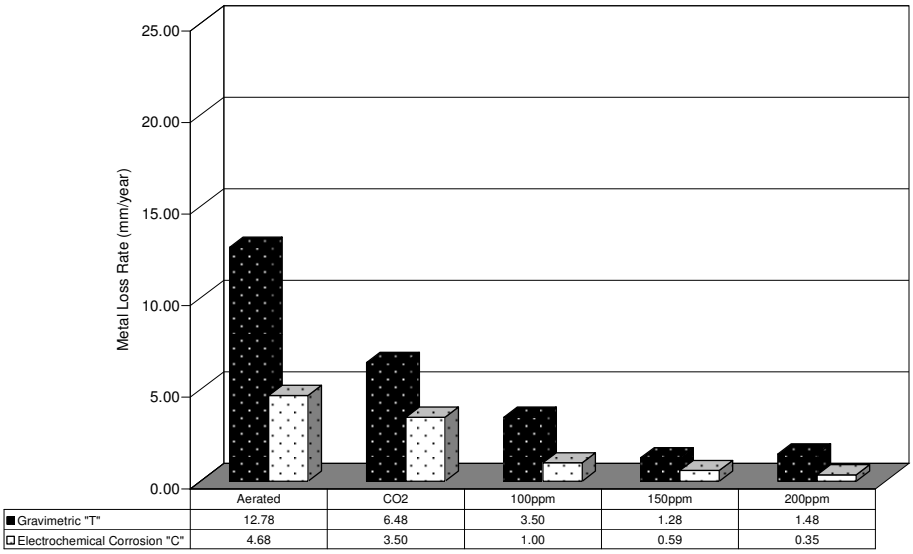

Figure B 5. Metal loss rates obtained by mass loss "T" and electrochemistry "C" in various conditions for the impingement zone at 2 m/s.

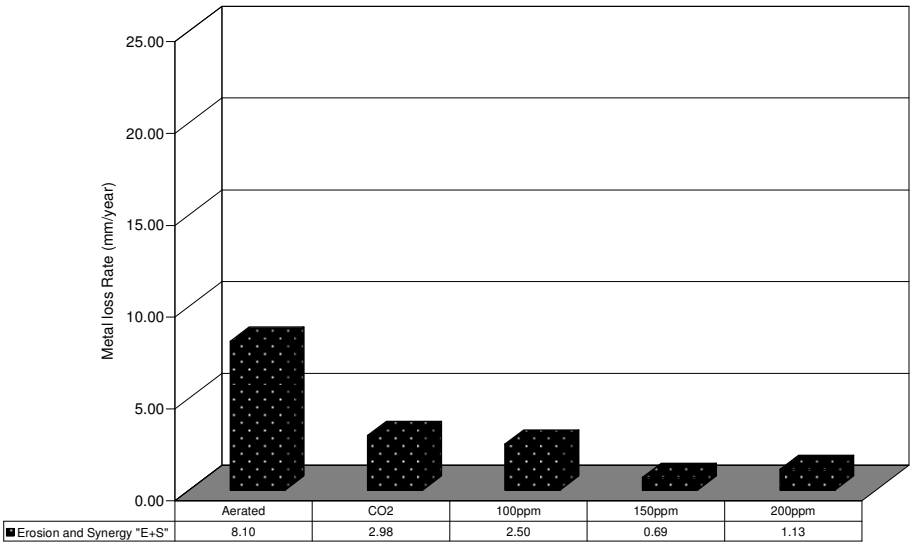

Figure B 6. Combined erosion and synergy "E+S" component in the impingement zone at 2 m/s.

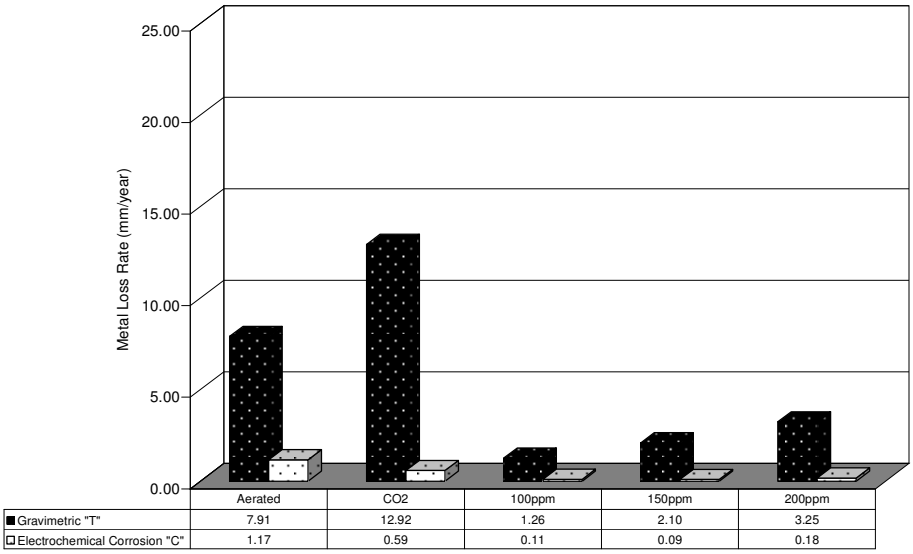

Figure B 7. Metal loss rates obtained by mass loss "T" and electrochemistry "C" in various conditions for the intermediate zone at 8 m/s.

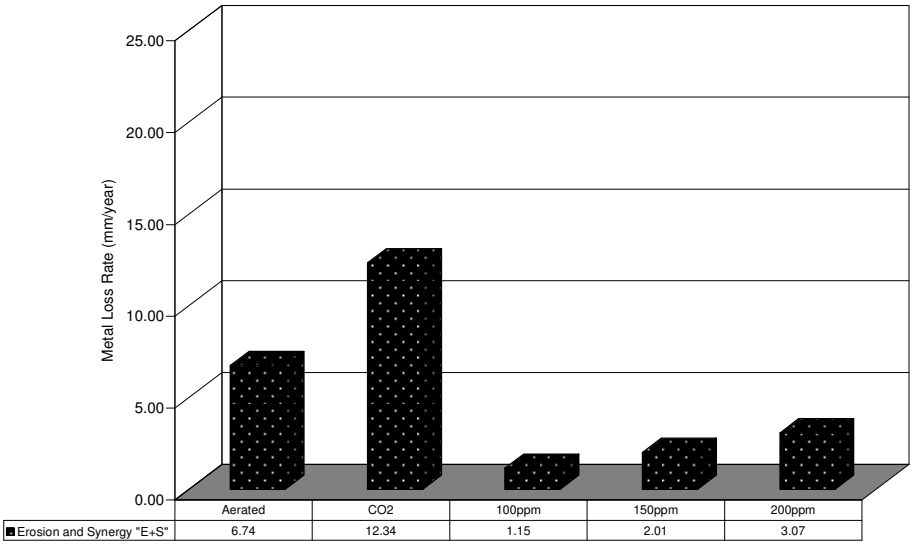

Figure B 8. Combined erosion and synergy "E+S" component in the intermediate zone at 8 m/s.

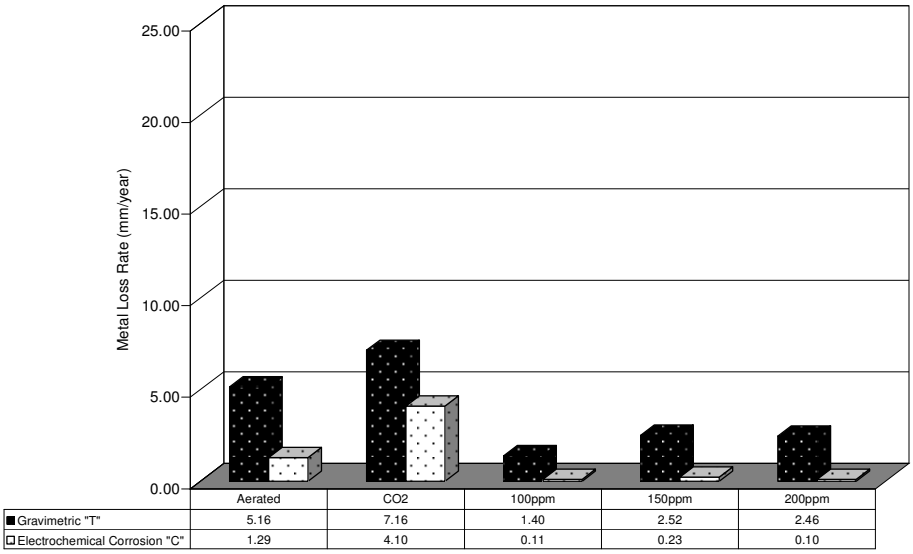

	Aerated	CO2	100ppm	150ppm	200ppm
Gravimetric "T"	5.16	7.16	1.40	2.52	2.46
Electrochemical Corrosion "C"	1.29	4.10	0.11	0.23	0.10

Figure B 9. Metal loss rates obtained by mass loss "T" and electrochemistry "C" in various conditions for the intermediate zone at 2 m/s.

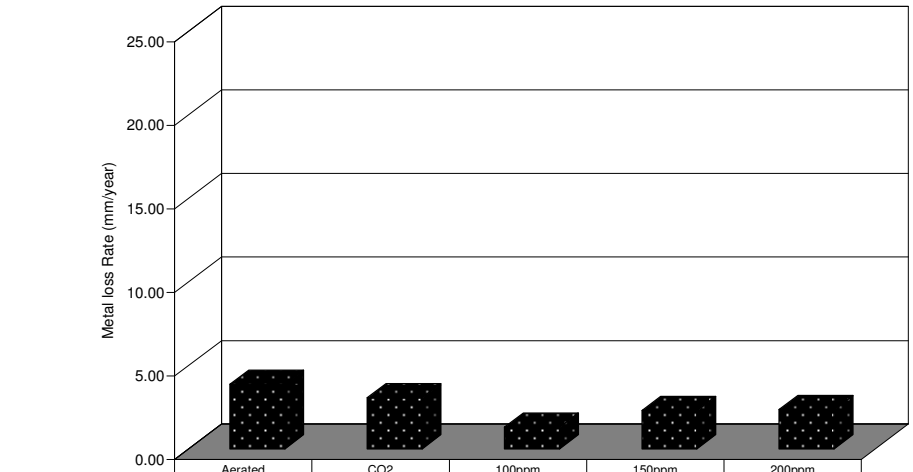

	Aerated	CO2	100ppm	150ppm	200ppm
Erosion and Synergy "E+S"	3.87	3.06	1.29	2.29	2.36

Figure B 10. Combined erosion and synergy "E+S" component in the intermediate zone at 2 m/s.

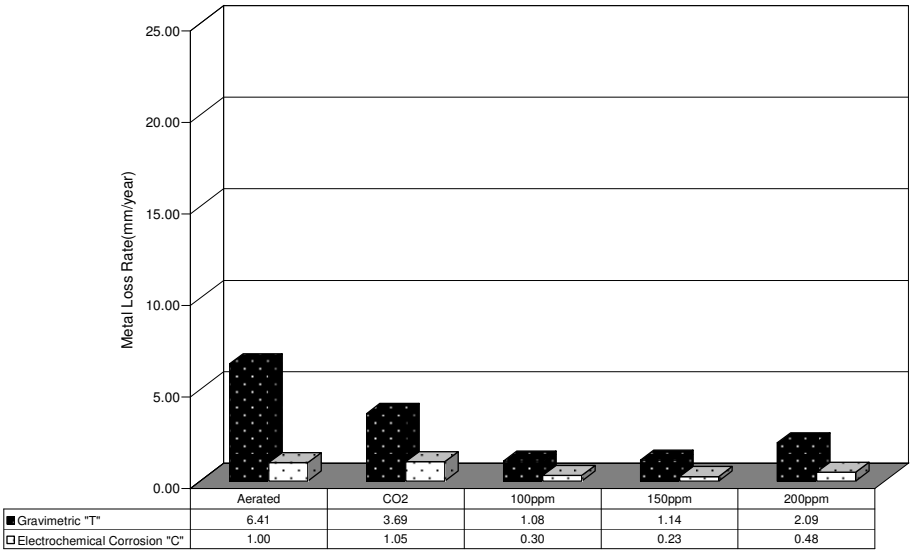

	Aerated	CO2	100ppm	150ppm	200ppm
Gravimetric "T"	6.41	3.69	1.08	1.14	2.09
Electrochemical Corrosion "C"	1.00	1.05	0.30	0.23	0.48

Figure B 11. Metal loss rates obtained by mass loss "T" and electrochemistry "C" in various conditions for the outer zone at 8 m/s.

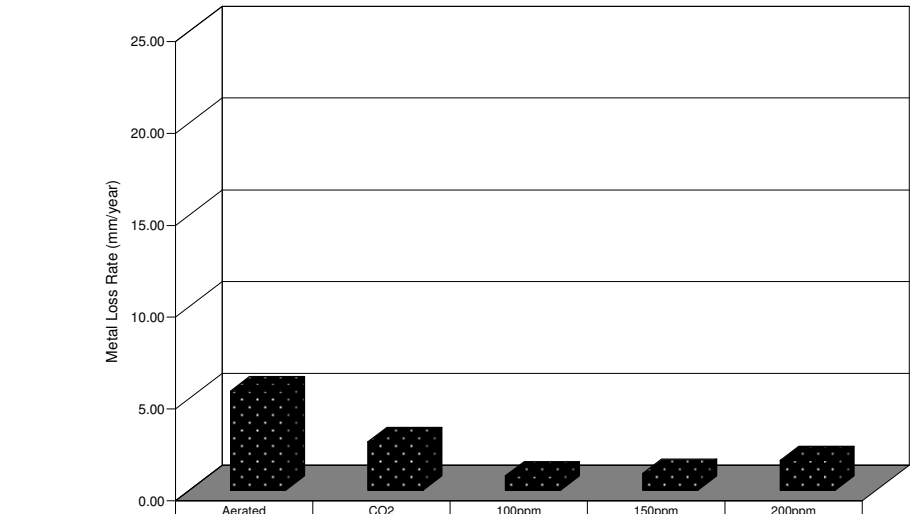

	Aerated	CO2	100ppm	150ppm	200ppm
Erosion and Synergy "E+S"	5.41	2.63	0.78	0.91	1.61

Figure B 12. Combined erosion and synergy "E+S" component in the outer zone at 8 m/s.

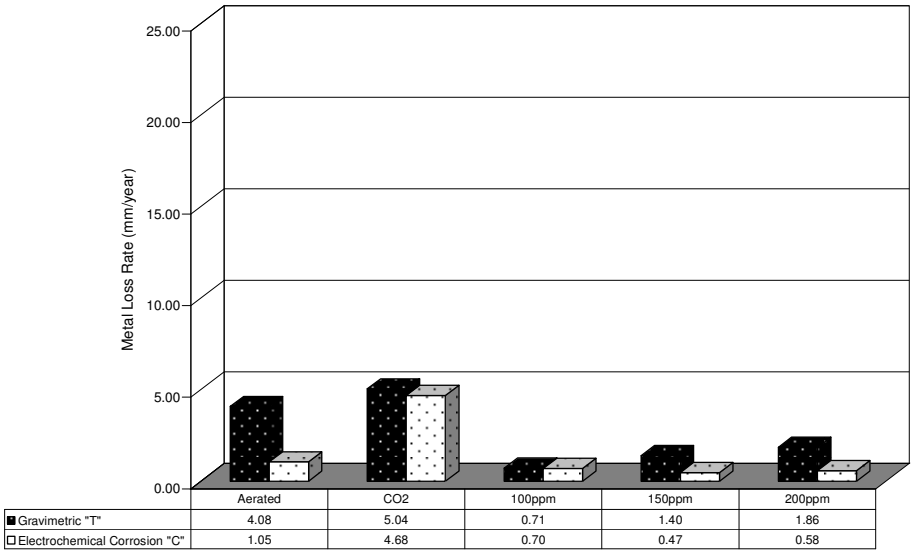

Figure B 13. Metal loss rates obtained by mass loss "T" and electrochemistry "C" in various conditions for the outer zone at 2 m/s.

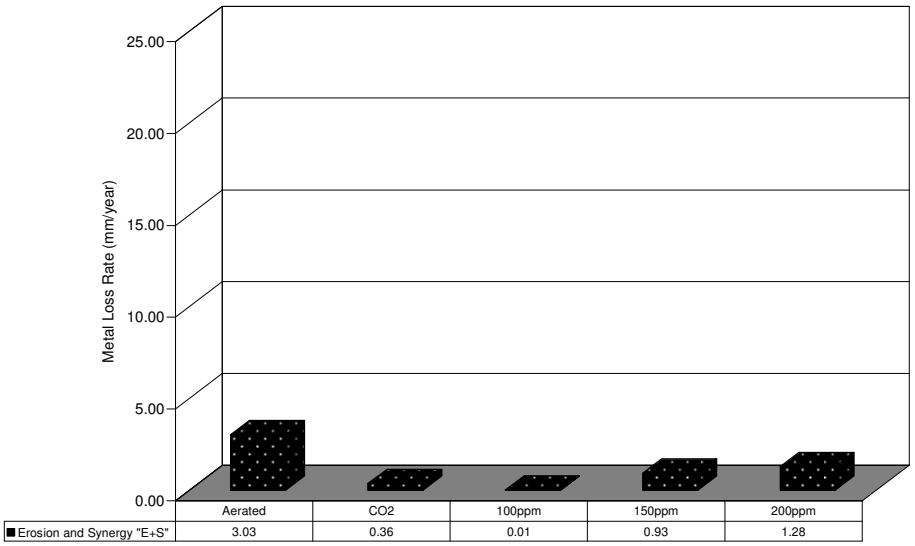

Figure B 14. Combined erosion and synergy "E+S" component in the outer zone at 2 m/s.

Alawadhi K., Robinson M., Chalmers A., & Winning I. (2008). Inhibition of weld corrosion flowing brines containing Carbon Dioxide. *Corrosion 2008* , Paper No. 08622.

Ali S., El-Shareef R., Al-Ghamadi R., & Saeed M. (2005). The isoxazolidines: the effects of steric factor and hydrophobic chain length on the corrosion inhibition of mild steel in acidic medium . *Corrosion Science 47* .

Altoe P., Pimenta G., Moulin C., Diaz S., & Mattos O. (1996). Evaluation of oilfield corrosion inhibitors in CO_2 containing media: A kinetic study. *Electrochimica Acta, Vol 41* , Nos 7/8.

Andrews P., Illson T., & Mathews S. (1999). Erosion-corrosion studies on 13 Cr steel in gas well environments by jet impingement . *WEAR 233-235* , 568-574.

Bommersbach P., Alemany-Dumont C., Pierre Millet J., & Normand B. (2006). Hydrodynamic effect on the behaviour of a corrosion inhibitor film: Characterisation by electrochemical impedence spectroscopy. *Electrochimica Acta, 51* .

Chen Y., Hong T. G., & Jepson W. (2000). EIS studies on corrosion inhibitor behaviour under multiphase flow conditions. *Corrosion Science 42* .

Chokshi K., Sun W., & Nesic S. (2005). Iron carbonate scale growth and the effect of inhibition in CO_2 corrosion of mild steel. *Corrosion 2005* , Paper 05285.

Dave K., Roberts K., Shadley J., Ramachandran S., & Rybicki E. J. (2008). Effect of a corrosion inhibitor for oil and gas wells when sand is produced. *Corrosion 2008* , Paper No. 08570.

Dayalan E., de Moraes F., Shadley J., Shirazi S., & Rybicki E. (1998). CO_2 corrosion prediction in pipe flow under $FeCO_3$ scale-forming conditions. *Corrosion 98* , Paper No 51.

de Waard C. (1993). Prediction of CO_2 corrosion of carbon steel. *Corrosion 93* , Paper No. 69.

Demoz A., Dabros T., Michaelian K., Papavinasam S., & Revie W. (2004). A new impinging jet device for corrosion studies. *Corrosion Vol 60* , 455-464.

Duda Y., Govea-Rueda R., Galicia M., Beltrn H., & Zamudio-Rivera L. (2005). Corrosion Inhibitors: Design, performance and computer simulations. *The Journal of Physical Chemistry B* , 22674-22684.

Dugstad A. (1998). Mechanism of protective film formation during CO_2 Corrosion of carbon steel. *Corrosion 98* , Paper no 31.

Dugstad A., Hemmer H., & Seiersten M. (2001). Effect of Steel Microstructure on Corrosion Rate and Protective Iron Carbonate Film Formation. *Corrosion, Vol 57* , 369-378.

Efird K. (2000). Jet impingement testing for flow accelerated corrosion. *Corrosion 2000* , paper 00052.

Efird K., Wright E., Boros J., & Hailey T. (1993). Correlation of steel corrosion in pipe flow with jet impingement and rotating cylinder tests. *Corrosion* , 992-1003.

Fajardo V., Canto C., Brown B., Young D., & Nesic S. (2008). The effect of acetic acid on the integrity of protective iron carbonate layers in CO_2 corrosion of mild steel. *Corrosion 2008* , Paper No 08333.

Fang H., Nesic S., & Brown B. (2006). General CO_2 corrosion in high salinity brines. *Corrosion 2006* , Paper 06372.

Feyerl J., Mori G., Holzleinther S., Haberl J., Oberndorfer M., Havlik W., et al. (2008). Erosion-corrosion of carbon steels in laboratory-three-phase flow. *Corrosion, Vol 64* , Paper 2.

Foss M., Gulbrandsen E., & Sjoblom J. (2009). Effect of corrosion inhibitors and oil on carbon dioxide corrosion and wetting of carbon steel with ferrous deposits. *Corrosion Science, Vol 65* , Paper No. 1.

G119-09 ASTM, Standard guide for determining synergism between wear and corrosion. *American Society for Testing and Materials* .

Garber J., & Sangita K. (1998). Factors affecting iron carbonate scale in gas condensate wells containing CO_2. *Corrosion 98* , Paper No. 19.

George K., & Nesic S. (2004). Electrochemical investigation and modelling of carbon dioxide corrosion of carbon steel in the presence of acetic acid. *Corrosion 2004* , Paper No. 04379.

Giralt F., & Trass D. (1976). Mass transfer from crystalline surfaces in a impingementimpinging jet, Part 2: Erosion and Diffusional Transfer. *Canadian Journal of Chemical Engineering* , Vol 54.

Gulbrandsen E., & Dugstad A. (2005). Corrosion loop studies of preferential weld corrosion and its inhibition in CO_2 environments. *Corrosion 2005* , Paper No. 05276.

Gulbrandsen E., Nesic S., & Burchardt T. (1998). The effect of pre-corrosion on the performance of inhibitors for CO_2 corrosion of carbon steel. *Corrosion 98* , Paper No. 13.

Guo H., Lu B., & Luo J. (2006). Non-Faraday material loss in flowing corrosive solution. *Electrochimica Acta* , 5341-5348.

Guo, X., & Tomoe, Y. (1999). The Effect of Corrosion Product Layers on the Anodic and Cathodic Reactions of Carbon Steel in CO2-saturated MDEA solutions at 100 deg C. *Corrosion Science, Vol 41* , 1391-1402.

Han J., Yang Y., Brown B., & Nesic S. (2007). Electrochemical investigation of localised CO_2 corrosion of mild steel. *Corrosion 2007* , Paper 07323.

Han J., Yang Y., Nesic S., & Brown B. (2008). Roles of passivation and galvanic effects in localized CO_2 corrosion of mild steel. *Corrosion 2008* , Paper 08332.

Hedges B. (2005). A prophetic CO_2 corrosion tool - But when is it to be believed. *Corrosion 2005* , Paper No. 05552.

Hedges B., Paisley D., & Woolman R. (2000). The corrosion inhibitor availability model. *Corrosion 2000* , Paper No. 00034.

Hedges W. (1996). The continuing development of environmentally friendly corrosion inhibitors for petroleum production. *Corrosion 96* , Paper 96151.

Heeg B., Moros T., & Klenerman D. (1998). Persistency of corrosion inhibitor films on C-Steel under multiphase flow conditions. Part 1: The Jet Cylinder Arrangement. *Corrosion Science* , 1303-1311.

Heitz E. (1996). Mechanistically based prevention strategies of flow-induced corrosion. *Electrochimica Acta* , 503-509.

Henry k., Meyer R., Hicks K., & Horsup D. (2005). The design and synthesis of improved corrosion inhibitors . *Corrosion 2005* , Paper 05282.

Hesjevick S., & Olsen S. (2003). Corrosion at high CO_2 pressure. *Corrosion 2003* , Paper 03345.

Heuer J., & Stubbins J. (1999). An XPS characterisation of $FeCO_3$ films from CO_2 corrosion. *Corrosion Science 41* , 1231-1243.

Hodgkiess T., & Vassiliou G. (2005). Complexities in the erosion corrosion of copper-nickel alloys in saline water. *Desalination Vol 183* , 235-247.

Hu X., & Neville A. (2004). An examination of electrochemical characteristics of two stainless steels (UNS S32654 and UNS S31603) under liquid-solid impingement. *WEAR 256* , 537-544.

Hu X., & Neville A. (2002). Assessing the role of corrosion in erosion-corrosion of high grade alloys in aggresive marine environements . *Corrosion 2002* , Paper No. 02189.

Hu X., & Neville A. (2003). In-situ measurements of corrosion charactersitics of high alloy stainless steels in saline liquid-solid impingement conditions. *Corrosion 2003*, 03264.

Hu X., & Neville A. (2008). Prediction of erosion-corrosion in oil and gas - a systematic approach. *Corrosion 2008*, Paper No. 08540.

Hussain E., & Robinson M. (2007). Erosion Corrosion of 2205 Duplex stainless steel in flowing seawater containing sand particles. *Corrosion Science 49*, 1737-1754.

Hussain H., & Hussain A. (2005). Erosion-corrosion of duplex stainless steel under Kuwait marine condition. *Desalination 183*, 227-234.

Jambunathan K., Lai E., Moss M., & Button B. (1992). A review of heat transfer data for single circular jet impingement. *International Journal of Heat and Fluid Flow, Vol 13* , 106-115.

Jeyaprabha C., Muralidharan S., Jayaperumal D., Venkatachari G., & Rengaswamy N. (1998). Studies on corrosion inhibitors for oil-well tubular material in acid environments . *Anti-Corrosion Methods and Meterials* , 148-152.

Jiang X., Zheng Y., & Ke W. (2005). Corrosion inhibitor performances for carbon dioxide corrosion of N80 steel under static and flowing conditions. *Corrosion, vol 61* , Paper No. 4.

Jiang X., Zheng Y., & Ke W. (2005). Effect of flow velocity and entrained sand on inhibition of two inhibitors for CO_2 corrosion of N80 steel in 3% NaCl solution. *Corrosion Science Vol, 47* .

Jovancicevic V., Ramachandran S., & Prince P. (1998). Inhibition of CO_2 corrosion of mild steel by imidazolines and their precursors. *Corrosion 98* , Paper No. 18.

Kolts J., Joosten M., & Humble P. (1998). Aspects of corrosion inhibitor selection at elevated temperatures. *Corrosion 98* , Paper No. 37.

Linter B., & Burstein G. (1999). Reactions of pipeline steels in carbon dioxide solutions. *Corrosion Science 41* , 117-139.

Lopez D., Schreiner W., de Sanchez S., & Simison S. (2003). The Influence of carbon steel microstructure on corrosion layers. An XPS and SEM characterisation. *Applied Surface Science 207* , 69-85.

Lopez D., Simison S., & Sanchez S. (2005). Inhibitors performance in CO_2 corrosion EIS studies on the interaction between their molecular structure and steel microstructure . *Corrosion Science 47* .

M-506, (2005). *CO2 Corrosion Rate Calculation Model.* NORSOK.

Marsh J., & Teh T. (2007). Conflicting Views: CO_2 corrosion models, corrosion inhibitor availability philosophies, and the effect on subsea systems and pipeline design. *Offshore Europe, Aberdeen* , SPE 109209.

McMahon A., & Paisley D. (2007). Corrosion Prediction Modelling . *A guide to the use of corrosion prediction models for risk assessment in oil and gas production and transportation facilities* , Sunbury Report No. ESR.96.ER.066.

Menendez C., Weghorn S., & Ahn Y. (2005). Electrochemical evaluations of high shear corrosion iInhibitors using jet impingement. *Corrosion 2005* , Paper 05331.

Meng H., Hu X., & Neville A. (2007). Study of corrosion in erosion-corrosion of two stainless steels in simulated marine conditions via experimental design. *Corrosion 2007* , Paper No. 07254.

Moiseeva L. (2005). Carbon Dioxide corrosion of Oil and Gas field equipment. *Protection of Metals, Vol 41* , 82-90.

Mora-Mendoza J., & Turgoose S. (2002). Fe_3C influence on the corrosion rate of mild steel in aqueous CO_2 systems under impingementflow conditions. *Corrosion Science, Vol 44* , 1223-1246.

Nafday O., & Nesic S. (2005). Iron carbonate scale formation and CO_2 Corrosion in the presence of acetic acid. *Corrosion 2005* , Paper No. 05295.

Nesic S., & Solvi G. E. (1995). Comparison of the rotating cylinder and pipe flow tests for flow-sensitive carbon dioxide corrosion. *Corrosion, Vol 51* , 773-787.

Nesic S., Cai J., & John Lee K-L. (2005). A multiphase flow and internal corrosion prediction model for mild steel pipelines. *Corrosion 2005* , Paper No 05556.

Nesic S., John Lee, K-L., & Ruzic V. (2002). A mechanistic model of iron carbonate film growth and the effect on CO_2 corrosion of mild steel. *Corrosion 2002* , Paper No. 02237.

Nesic S., Nordsveen M., Nyborg R., & Stangeland A. (2003). A mechanistic model for carbon dioxide corrosion of mild steel in the presence of protective iron carbonate films - Part 2: A Numerical Experiment. *Corrosion, Vol 59* , 489-497.

Nesic S., Postlethwaite J., & Olsen S. (1996). An electrochemical model for prediction of corrosion of mild steel in aqueous carbon dioxide solutions. *Corrosion Vol 52* , 280-294.

Nesic S., Wang J., Cai J., & Xiao Y. (2004). Intergrated CO_2 model - mulitphase flow model . *Corrosion 2004* , Paper No. 04626.

Nesic S., Wang S., Cai J., & Xiao Y. (Aberdeen 2004). Intergrated CO_2 corrosion - multiphase model. *Society of Petroleum Engineers (SPE) 1st International Symposium on Oilfield Corrosion* , Paper No. SPE 87555.

Nesic S., Wilhelmsen W., Skjerve S., & Hesjevik S. (1995). Testing of inhibitors for CO_2 corrosion using electrochemical techniques. *Proceedings of the 8th European Symposium on Corrosion Inhibitors (8 SEIC)* .

Neville A. H., & Xu H. (1999). An elecrochemical and microstructural assessment of erosion-corrosion of cast Iron. *WEAR 233-235* , 523-534.

Neville A., & Hu X. (2001). Mechanical and electrochemical interactions during liquid-solid impingement on high-alloy stainless steels. *WEAR 251* , 1284-1294.

Neville A., & Reza F. (2004). Assessing MMC's for corrosion and erosion-corrosion applications in the oil sands industry . *Corrosion 2004* , Paper No. 04125.

Neville A., & Reza F. (2007). Erosion-corrosion of cast white irons for application in the oilsands industry. *Corrosion 2007* , Paper No. 07678.

Neville A., & Wang C. (2009). Erosion corrosion mitigation by corrosion inhibitors - an assessment of mechanisims. *WEAR, Vol 267* .

Neville A., Hodgkiess T., & Dallas J. (1995). A study of the erosion-corrosion behaviour of engineering steels for marine pumping applications. *WEAR 186-187* , 497-507.

Neville A., Hu X., & Reyes M. (2000). Corrosion and erosion-corrosion behaviour of a CO-Based alloy in Ni containing austenitic cast iron. *Corrosion 2000* , Paper No. 00628.

Neville A., Wang C., Ramachandran S., & Jovancicevic V. (2003). Erosion-corrosion mitigation using Chemicals. *Corrosion 2003* , Paper No. 03319.

Nordsveen M., Nesic S., Nyborg R., & Stangeland A. (2003). A mechanistic model for carbon dioxide corrosion of mild steel in the presence of protective iron carbonate films - Part 1: Theory and Verification. *Corrosion Vol 59* , 443-456.

Olsen S. (2005). CO_2 corrosion prediction model - Basic Principles. *Corrosion 2005* , Paper No 05551.

Petersen A., Klenerman D., & Hedges W. (2004). Evaluation of the effect of carbon dioxide corrsion inhibitors on cavitation damage caused during ultrasonic test. *Corrosion, Vol 60* , Paper No. 2.

Place Jr M. (1998). Corrosion inhibitor development for subsea wells. *Corrosion 98* , Paper No. 9.

Postlethwaite J., Wang Y., Adamopoulos G., & Nesic S. (1994). Relationship between modelled turbulence parameters and corrosion product film stability in disturbed single-phase aqueous flow. *Modelling Aqueous Corrosion* , 297-316.

Pots B., & Hendriksen E. (2000). CO_2 corrosion under scaling conditions - The special case of Top-of-Line corrosion in wet gas pipelines. *Corrosion 2000* , Paper No. 00031.

Poulson B. (1993). Advances in understanding yydrodynamic effects on corrosion. *Corrosion Science* , 655-665.

Poulson B. (1990). Mass transfer from rough surfaces. *Corrosion Science* , 743-746.

Pritchard A., & Webb P. (1998). Use of the FSM technique in the laboratory to measure corrosion inhibitor performance in multiphase flow. *Corrosion 98* , Paper No. 8.

Ramachandran S., & Jovancicevic, V. (1998). Molecular Modelling of the Inhibition of Mild Steel CO2 Corrosion By Imidazolines. *Corrosion 98* , Paper no. 17.

Ramachandran S., Ahn Y.B., Jovancicevic V., & Bassett J. (2005). Futher advances in the development of erosion corrosion inhibitors. *Corrosion 2005* , Paper No. 05292.

Ramachandran S., Campbell S., & Ward M. (2000). The interactions and properties of corrosion inhibitors with by product layers. *Corrrosion 2000* , Paper No. 00025.

Ramachandran S., Ward M., Bartrip K., & Jovancicevic V. (2002). Inhibition of the effects of particle impingement. *Corrosion 2002* , Paper No. 02498.

Ramakrishma R., Nesic S., & Gulino D. (2006). Erosion-corrosion and synergistsic effects in disturbed liquid-particle flow. *Corrosion 2006* , 06594.

Rincon H. (2008). Erosion-corrosion of corrosion resistant alloys used in the oil and gas industry . *Corrosion 2008* , Paper No. 08571.

Rippon I. (2001). Carbon steel pipeline corrosion engineering: life cycle approach. *Corrosion 2001* , 01055.

Schmitt G., Werner C., & Bakalli M. (2005). Fluid mechanical interactions of impingementflowing fluids with the wall - Revisited with a new electrochemical tool. *Corrosion 2005* , Paper No. 05344.

Seal S., Sapre K., Kale A., Desai V., Gopal M., & Jepson P. (2000). Effect of multiphase flow on corrosion of C-Steel in presence of inhibitor: a surface morphological and chemical study. *Corrosion Science 42* .

Shadley J., Shirazi S., Dayalan E., & Rybicki E. (1998). Prediction of erosion-corrosion penetration rate in CO_2 environments with sand. *Corrosion 98* , Paper No. 59.

Song F., Kirk D., Graydon J., & Cormack D. (2004). Predicting carbon dioxide corrosion of bare steel under an aqueous boundary layer. *Corrosion, Vol 60* , 736-748.

Sun W., & Nesic S. (2006). Basics Revisited: Kinetics of iron carbonate scale precipitation in CO_2 Corrosion. *Corrosion 2006* , Paper No. 06365.

Sun W., & Nesic S. (2008). Kinetics of Corrosion Layer Formation: Part 1 - iron carbonate layers in carbon dioxide corrosion. *Corrosion, Vol 64* , 334-345.

T-5A-31, (1995). *State-of-the-Art Report on Controlled-Flow Laboratory Corrosion Tests.* NACE Publication 5A195.

Tan Y., Bailey S., & KinsellaB. (1996). The monitoring of the formation and destruction of corrosion inhibitor films using electrochemical noise analysis. *Corrosion, Vol 38* .

Tang X., Xu L., & Cheng Y. (2008). Electrochemical corrosion behaviour of X65 steel in simulated oil-slurry. II: Synergism of erosion and corrosion. *Corrosion Science 50* , 1469-1474.

Tebbji K., Bouabdellah I., Aouniti A., Hammouti B., Oudda H., Benkaddour M., et al. (2007). N-benzyl-N, N-bis[(3,5-dimethyl-1H-pyrazol-1-yl)methyl]amine as corrosion inhibitor of steel in 1 M HCl. *Materials Letters 61* , 799-804.

Turgoose J., Palmer J., & Dicken G. (2005). Preferential weld corrosion of 1% Ni welds: Effect of solution conductivity and corrosion inhibitors. *Corrosion 2005* , Paper No. 05275.

van Hunnik E., & Pots B. H. (1996). The formation of protective $FeCO_3$ corrosion product layers in CO_2 corrosion. *Corrosion 96* , Paper No. 6.

Vera J., & Shirah D. (2009). Laboratory evaluation of galvanic CO_2 corrosion and inhibition of carbon steel piping partially clad with Alloy 625. *Corrosion 2009* , Paper No. 09566.

Villarreal J., Laverde D., & Fuentes C. (2006). Carbon steel corrosion in multiphase slug flow and CO_2. *Corrosion Science Vol 48* , 2363-2373.

Wang C., & Neville A. (2004). Understanding the action of inhibitors in mitigating erosion-corrosion in impinging flows. *Corrosion 2004* , Paper No. 04658.

Wang C., Neville A., Ramachandran S., & Jovancicevic V. (2005). Allevation of erosion-corrosion damage by liquid-sand impact through use of chemicals. *WEAR 258* , 649-658.

Wang J., Shirazi S., Shadley J., Rybicki E., & Dayalan E. (1998). A Correlation for mass transfer coefficients in elbows. *Corrosion 98* , Paper 42.

Wang S., & Nesic S. (2003). On coupling CO_2 corrosion and multiphase flow models. *Corrosion 2003* , Paper No. 03631.

Wen J., Gu T., & Nesic S. (2007). Investigation of the effects of fluid flow on SRB Biofilm. *Corrosion 2007* , Paper 07516.

Wood R. (2006). Erosion-corrosion interactions and their effect on marine and offshore materials. *WEAR 261* , 1012-1023.

Yapici S., Kuslu S., Ozemetin C., Ersahan H., & Pekdemir T. (1999). Surface shear stress for a submerged jet impingement using electrochemical technique. *Journal of Applied Electrochemistry 29* , 185-190.

Zhang G., Lu M.C., & Wu Y. (2006). Effect of HCO_3^- concentration on CO_2 corrosion in oil and gas fields. *Journal of University of Science and Technology Beijing* , 44-49.